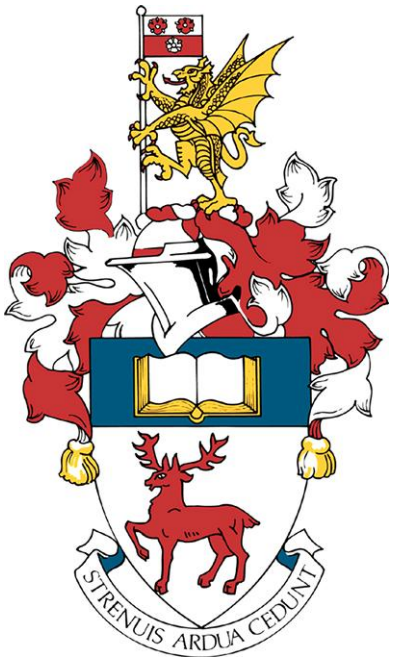

UNIVERSITY OF SOUTHAMPTON

Faculty of Medicine

Human Development and Health

Bubbles for Bone: Acoustic Stimulation for Drug Delivery in Fracture Repair

Supervisors:
Dr Dario Carugo
Dr Nicholas D. Evans

PhD Thesis
Sara Ferri

Academic Year 2020/2021

Declaration of Authorship

I, Sara Ferri, declare that this thesis entitled "Bubbles for bone: acoustic stimulation for bone delivery in fracture repair" and the work presented in it is my own and has been generated by me as the result of my own original research. I confirm that:

1. This work was done wholly while in candidature for a research degree at this University;
2. Where any part of this thesis has previously been submitted for a degree or any other qualification at this University or any other institution, this has been clearly stated;
3. Where I have consulted the published work of others, this is always clearly attributed;
4. Where I have quoted from the work of others, the source is always given. With the exception of such quotations, this thesis is entirely my own work;
5. I have acknowledged all main sources of help;
6. Where the thesis is based on work done by myself jointly with others, I have made clear exactly what was done by others and what I have contributed myself;
7. Parts of this work have been published as: [1]

Signature: Date: 22/02/2021

Acknowledgements

I would like to express my gratitude to my supervisors Dr Dario Carugo and Dr Nick Evans, who gave me the opportunity to be a PhD candidate and supported and guided my research with their knowledge, patience and motivation throughout the years. I was very lucky to have you for supervisors and mentors. Thank you to all my research group: Anastasia Polydorou, Dr Jonathan May, Dr Qiang Wu and Dr Eleanor Stride; your insightful and different perspectives in all our bubble meetings were fundamental for brainstorming, analysing our experiments and results and coming up with new ideas to enrich this project. Thank you to MRC and IfLS for funding my research.

My PhD journey wouldn't have been the same without all the amazing friends I made along the way. Thank you to my office colleagues and friends, in particular to Erik and Gareth. I will never forget all the time we spent decorating our office for Christmas, finding an unusual and extravagant theme every year (starting with Alice in Wonderland, moving to dinosaurs and ending with Harry Potter), all the battles with the office nerf guns and the support through good and bad times. Thank you to the first two people I met here in Southampton: Andrea and Elisabetta. During our first lunch together, I didn't know I had just met two friends. I will never forget all the coffees and almonds I had at Pret's with Andrea while talking about all sort of things and the New Year's Eve I spent skiing with Eli.

I would like to thank two special friends supporting me with frequent and endless phone calls from Milan: Paolé and Mutto. Distance was never a problem for us!

Although my PhD is about bubbles, little did I know when I started that bubbles would become so important in the final year of my PhD... An extra special thank you to my support bubble, my Italian family in England: Chiari, AntoooOOOoOOo and Sebisebi. Thanks to you, my lockdowns have been full of laughs, hugs, pizzas and gourmet food.

Last, but not least, I will always be grateful to my family: to my grandparents for being so proud to have another Engineer in the family, to my brother Ste for being there to support me in his personal and alternative way, and to my Mum and Dad, Mu and Pi, for always believing in me. If I'm here, it's because of you.

Grazie

Abstract

Impaired fracture healing causes a major financial burden for healthcare services; 10% of bone fractures result in costly and debilitating conditions like delayed or nonunion fractures. Common treatments are invasive, with a significant impact on a patient's quality of life. In this study, we aim to overcome this limitation by using acoustically-stimulated microbubbles (MBs) and nanodroplets (NDs) as non-invasive ultrasound responsive vehicles for the targeted delivery of osteogenic compounds.

MBs and NDs safety and efficacy depend on their size and stability; in this study, formulation protocols were optimised and the effects of production, storage and handling parameters assessed. A microscope-compatible water-tank incorporating a passive cavitation detector was also developed to study the acoustic behaviour of MBs and NDs within a model bone fracture.

A method was established to produce MBs and NDs, which were stable upon storage. The optimal formulation conditions for MBs were to produce them in a biocompatible viscous medium, store them at low temperature (4^{o}C) and label them with DiI at a concentration < 2.14 μM. As for NDs, the optimal conditions were to produce them with a percentage of PFP equal to 10% v/v and to perform the sonication step for 60 seconds with an intensity of 72 W to achieve a narrow size distribution. MBs cavitation and NDs vaporisation were achieved and evaluated using the developed acoustic stimulation apparatus.

Further studies will investigate the relationship between MB and ND acoustic response and the release of osteogenic compounds.

Detailed summary

Background

Ten percent of bone fractures result in costly and debilitating conditions such as delayed or nonunion fractures, where the bone fails to heal properly. The ultimate aim of this project is to promote bone repair using gas-filled, lipid-coated microbubbles (MBs) or perfluorocarbon nanodroplets (NDs), which are designed to carry bio-active compounds and release them upon exposure to ultrasound (US). An optimal agent for this application should combine several desirable characteristics, including stability during storage, handling and administration; since all these aspects significantly affect their acoustic response upon US stimulation and thus their therapeutic effectiveness *in vivo*. Therefore, this thesis will investigate initially how different physico-chemical conditions may influence the stability and dimensional properties of ultrasound-responsive agents, and secondly the acoustic response of these agents within a bone fracture model.

Method

Tests were performed to characterise the static and dynamic behaviour of MBs and NDs over time, by studying their size and particle concentration. These properties give an indication of the relative stability, safety and therapeutic effectiveness of these agents upon administration. Different parameters used to produce MBs and NDs were varied (chemical formulation, production method, batch handling) to establish a reproducible method to generate MBs and NDs, which were stable upon storage. Once having established an effective production protocol, an ultrasound setup was designed and built to characterise the acoustic behaviour of these ultrasound-responsive agents. This allowed study of how the agents responded to different US stimulation conditions,

and how their responses changed in the presence of a bone fracture.

Phospholipid MBs were stabilised by lipid shell consisting of a 9:1 molar ratio of 1,2-distearoyl-sn-glycero-3- phosphocholine (DSPC) to polyoxyethylene(40) stearate (PEG40s) and they were produced by sonication. To test the stability of MBs, media with different viscosity (5-10 times greater than phosphate buffer saline, PBS) were prepared, comprising different proportions of PBS, glycerol and propylene glycol. MBs were then stored at 4^{o}C or incubated in a 37^{o}C, 95% humidity and 5% CO_2 environment. Stability was measured in terms of mean diameter and concentration over a period of 6 days. Finally, the effect of the incorporation of a lipophilic fluorescent dye, 1,1'-dioctadecyl-3,3,3',3'-tetramethylindocarbocyanine perchlorate (DiI), was determined as it enables MB tracking *in vivo* and *in vitro*. Concentrations of DiI in the range 2.14-21.42 μM were tested.

Phospholipid-coated NDs with a perfluoro-n-pentane (PFP) core stabilised by 9:1 molar ratio of DSPC to PEG40s were fabricated in PBS by sonication. To optimise the ND size, the following parameters were investigated: different proportions of PFP (in the range 5-15% v/v in PBS), sonications with different intensity (in the range 24-72 W) and duration (in the range 20-60 seconds), and the effect of the incorporation of a lipophilic fluorescent dye (concentrations of DiI in the range 2.14-21.42 μM). The stability of NDs was assessed at either 4^{o}C or 37^{o}C. Finally, the phase transition to microbubbles was demonstrated using an acoustofluidic device designed and built for this purpose.

A microscope-compatible water-tank incorporating a passive cavitation detector (PCD) was developed to study the acoustic behaviour of MBs and to quantify their cavitation activity upon US stimulation. The device was designed using SOLIDWORKS (Solidworks Applications Limited, Oldbury, West Midlands, UK), evaluated using COMSOL Multiphysics (COMSOL Inc., Burlington, MA, USA), and tested *in vitro*. This apparatus was employed to investigate the behaviour of MBs and NDs when embedded in a 2% agarose gel, which was injected within physical models of bone fracture of different geometry. The model was composed of a PDMS manifold accommodating two fragments of bone with a gap in between, where the sample of MBs or NDs was loaded. Bone was modelled using a material with comparable acoustic impedance (Z = 5.41 x 10^6 kg/m^{2}s, Sawbones, Washington, USA). Different fracture gaps (3.5-5.5 mm), thicknesses (2 and 4 mm), and inclination angles (45^{o} and 90^{o}) were evaluated. Ultrasound stimulation experiments were performed at

either 1 or 2 MHz US frequency, duty cycle of 1-5%, acoustic pressure of 0.03-0.95 MPa, and exposure time of 30 s. A PCD was used to detect the signal emitted, and a frequency-domain analysis (i.e. Fast Fourier Transform, FFT) was performed to extract the content in frequency of the detected signal.

Results

Stability tests revealed that temperature had a significant effect on MBs mean diameter and concentration. At 37°C, the diameter increased over two hours from 4.67 ± 1.45 to 18.24 ± 11.63 μm, while MB volumetric concentration decreased from 2.65 x 10^8 to 4 x 10^6 MBs/mL. In contrast, at 4°C, the mean diameter increased from 3.9 ± 0.42 to 10.72 ± 0.7 μm while concentration decreased from 2 x 10^8 to 4 x 10^6 MBs/mL over six days. An increase in the viscosity of the medium (from 1.58 to 15.38 cP) led to smaller MBs, with mean diameter of 2.92 ± 2.88 vs 3.66 ± 2.89 μm (just after production) and 4.06 ± 4.49 to 6.26 ± 5.05 μm (after 1 day). Incorporation of the lipophilic dye, DiI, significantly affected MB size. The mean diameter increased, with increasing viscosity, from 4.99 ± 3.8 to 5.48 ± 2.99 μm, after production. Whereas, at day 6 the mean diameter increased from 13 ± 11.82 to 17.94 ± 14.74 μm with increasing DiI:MB ratio.

Concerning the production of NDs, by increasing the percentage of PFP from 5% to 15% v/v in PBS, the initial ND diameter increased from 162.87 ± 49.42 to 308.17 ± 76.01 nm. An increase in the intensity of sonication from 48 to 72 W led to a decrease in ND size from 354.65 ± 127.21 to 315.01 ± 100.56 nm. A sonication of 60 seconds generated NDs with a diameter of 249.74 ± 9.67 nm. Finally, the addition of DiI at different molar ratios did not affect ND size. Importantly, NDs were stable at both 4°C (up to 6 days) and at 37°C (up to 110 minutes); however, some evidence of ND-to-MB phase transition was observed after 40 minutes at 37°C. Using the acoustofluidic device, it was demonstrated that DSPC:PEG40s NDs transitioned into MBs upon acoustic stimulation (frequency = 1.75 MHz, driving voltage = 15 Vpp).

Numerical simulations showed that the experimental setup generated an acoustic pressure field at the target plane (that also corresponds to the optical focal plane of the microscope) characterised by the presence of standing waves. The inclusion of a fracture model caused perturbations to the acoustic field, which were dependent on the architecture of the fracture (i.e. relative to the incident US field). US wave

reflection at the inner edges of the fracture gap resulted in the generation of a standing wave field, with 'hotspots' of higher acoustic pressure located within the fracture gap. Experiments were performed to investigate the acoustic behaviour of MBs within fracture models. FFT spectra show that the addition of MBs generated harmonics, subharmonics and ultraharmonics, likely corresponding to MB oscillations. When the bone fracture model was added to the apparatus, it was still possible to detect MB behaviour through the presence of harmonics and sub/ultraharmonics. The presence of the bone led to higher FFT amplitudes at the harmonic and ultraharmonic frequencies analysed. This increased response is likely due to the higher acoustic pressure developed in the hotspots present in the fracture gap. US experiments with NDs showed the presence of harmonics, ultraharmonics and broadband noise in the recorded signal, likely corresponding to ND phase transition into MBs.

Conclusions and Future Work

A method was established to produce MBs and NDs, which were stable upon storage. To achieve stability, the optimal conditions found for MBs were to produced them in a biocompatible viscous medium, stored them at low temperature (4^{o}C) and labelling them with DiI with a concentration below 2.14 μM. As for NDs, the optimal conditions found in this case were to produced them with a percentage of PFP equal to 10% v/v and to perform the sonication step for 60 seconds with an intensity of 72 W to achieve a narrow size distribution.

The developed setup allowed the generation of a relatively uniform acoustic field at the target plane; and revealed perturbations and hotspots generated in the fracture gap when a bone fracture model was tested. When MBs were added to the model, the FFT spectra exhibited harmonics, subharmonics and ultraharmonics; their intensity increased when tested in the bone fracture. These peaks likely correspond to ultrasound-induced MB oscillations. When NDs were added to the model, harmonics, ultraharmonics and broadband noise appeared, likely induced by ND phase transition.

Future work should focus on the loading and release of bioactive compounds.

Contents

List of Figures

List of Tables

List of Abbreviations and Definitions

3D	Three dimensional
ABC	Accelerated body clearance
ACD	Active cavitation detection
ADV	Acoustic droplet vaporisation
A/D	Analog-to-digital
ANOVA	One-way analysis of variance
BMD	Bone mineral density
BMP	Bone morphogenetic protein
BSA	Bovine Serum Albumin
CAD	Computer aided design
CCD	Charge-coupled device
CEHDA	Coaxial electrodynamic atomisation
CMC	Critical micellar concentration
CMOS	Complementary metal-oxide semiconductor
CO_2	Carbon dioxide
DAPI	4',6-diamidino-2-phenylindole
DiI	1,1'-dioctadecyl-3,3,3',3'-tetramethylindo carbocyanine perchlorate
DLS	Dynamic light scattering
DPCD	Double passive cavitation detection
DMEM	Dulbecco's Modified Eagle's Medium
DSPE	1,2-distearoyl-sn-glycero-3-phosphoethanolamine
DSPC	1,2-distearoyl-sn-glycero-3- phosphocholine
FBS	Fetal Bovine Serum
FDA	Food and Drug Administration

FFT	Fast Fourier Transform
FUS	Focused ultrasound
G	Glycerol
IQR	Interquartile range
LbL	Layer by layer
LIPUS	Low intensity pulsed ultrasound
MBs	Microbubbles
MG63	Homo sapiens bone osteosarcoma cell
μLAR	Microfluidic layered acoustic resonator
MLV	Multilamellar vescicles
MSC	Mesenchymal stem cell
MTF	Modulation transfer function
N2	Nitrogen
NDs	Nanodroplets
NO	Nitric Oxide
NTA	Nanoparticle tracking analysis
O_2	Oxygen
PBS	Phosphate buffer saline
PC	Phosphocoline
PCD	Passive cavitation detector
PDMS	Polydimethylsiloxane
PE	Polyethylene
PEG	Polyethylene glycol
PEG2000	Polyethylene glycol-2000
PEG40s	Polyoxyethylene(40)stearate
PES	Post-excitation signal
PFB	Perfluorobutane
PFC	Perfluorocarbon
PFP	Perfluoro-n-pentane
PG	Propylene glycol
pH	Potential for hydrogen
PLGA	Poly(lactic-co-glycolic acid)
PZT	Piezoelectric
RA	Room air

RES	Reticuloendothelial system
SD	Standard deviation
SPCD	Single passive cavitation detection
STFT	Short-time Fast Fourier Transform
SUV	Small unilamellar liposomes
T	Temperature
UCA	Ultrasound contrast agent
US	Ultrasound

Introduction

Bone fractures and nonunions impose an economic burden to the NHS in the UK, and there is no clinically approved systemic therapy for their treatment. It is estimated that fractures following falls have a cost of £2.3 billion, fragility fractures mainly due to osteoporosis impose a cost of £4.4 billion and hip fractures alone cost £2 billion per year [2]. Common therapeutic options include physical stimulation therapies and biological treatments; the former include mechanical fixation, plaster casts, prostheses and the use of low intensity pulsed ultrasound (LIPUS); while the latter embrace autograft, allograft and administration of hormones or protein [3]. Common treatments are therefore invasive and rely on the immobilisation of the fracture site and this immobilisation can lead to a decrease in a patient's quality of life; not only do patients have trouble performing work and other daily activities, but they are also at risk of side effects, including heart disease. Moreover, drugs are often administered orally or parenterally, where high drug dosages are used to reach a sufficient local therapeutic effect and overcome drug clearance by liver and kidneys. Consequently, this increase in systemic drug levels could lead to possible off-target side-effects [4]. Therefore, there is a need to develop novel treatments able to enhance the production of new bone mass in a targeted and non-invasive fashion.

The present study investigates the use of ultrasound-responsive drug delivery vehicles, such as gas microbubbles and perfluorocarbon nanodroplets, as a means to accelerate the bone fracture repair process. Microbubbles are used in the clinic as diagnostic agents (also known as ultrasound contrast agents, or UCAs) and, more recently, they have been investigated as therapeutic agents for the treatment of tumours, biofilm infections, neurological disorders, and blood clots [5]. Building upon their earlier therapeutic applications, it is anticipated that shelled microbubbles and nanodroplets can be loaded with bioactive compounds, delivered to the fracture site,

and stimulated with ultrasound to simultaneously induce the release of the compounds and mechanically stimulate cells [6].

In order to establish a therapeutic approach with the above characteristics, the present investigation is articulated into different sections. Firstly, a literature review is presented, discussing physiology and pathology of bone, current treatments for bone fracture, and recent advancements concerning the use of drug delivery vehicles. Subsequently, two chapters are presented to describe an experimental investigation of the production and characterisation of shelled microbubbles and nanodroplets, leading to the identification of suitable manufacturing protocols. Subsequently, a study of the acoustic response of these agents upon US stimulation in the presence or absence of a bone fracture model is reported.

A parallel, complementary and independent PhD project is focused on the study of the interaction between ultrasound-responsive agents and biological cells and tissues.

Chapter 1

Literature review

1.1 Physiology and Pathology of Bones

1.1.1 Bone Physiology

Bone is a highly specialised organ and the principle supporting framework of the body. In addition, the skeleton provides protection for vital organs, a safe environment for marrow (important for blood production), as well as contributing to the acid-base balance of our bodies and facilitates locomotion. It also acts as a mineral reservoir for calcium homeostasis, and as a reservoir for growth factors and cytokines, which are small proteins important in cell signalling.

Bone is composed of cells and bone matrix. The different cell types include osteoclasts, which are involved in bone resorption; osteoblasts, which are connected with bone matrix deposition and mineralisation; and osteocytes, which support bone structure and metabolism and have a putative, but not proven, role in mechanosensation [4]. The most popular theory regarding the major function of osteocytes is that they translate mechanical strain into biochemical signals between osteocytes and to cells on the bone surface to affect remodelling [7]. As for the bone matrix, it is constituted of an inorganic component (69% by mass) consisting mainly of hydroxyapatite, and an organic component (22% by mass) comprising mainly collagen and, in lower proportion, other structural proteins [8].

During a lifetime, bones grow both radially and longitudinally and are subject to the processes of modelling and remodelling, as shown in Figure 1.1. Modelling (also

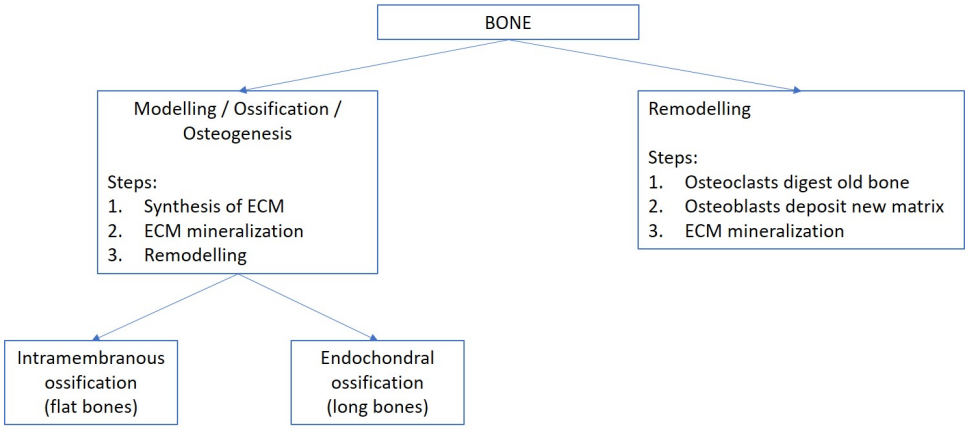

Figure 1.1: *Schematic representation of the processes leading to bone modelling and remodelling. Bone formation is involved in the process of bone modelling, while bone conservation is involved in bone remodelling.*

known as ossification or osteogenesis) is the process of new bone formation and mainly involves osteoblasts. It can be divided into three phases: (i) synthesis of extracellular organic matrix, (ii) matrix mineralisation, leading to the formation of bone, and (iii) bone remodelling, resulting from resorption and reformation. The formation of a physiological healthy bone occurs via both intramembranous and endochondral ossification, two processes occurring in parallel in different areas of the bone [8].

Intramembranous ossification mainly occurs in flat bones, during fetal development or as part of the natural healing of bone fractures. The main cell type involved in this process is the skeletal stem cell, an osteoprogenitor cell believed to remain dormant during adulthood and to activate in response to injury by differentiating into osteoclasts and osteoblasts. The primary sites of ossification are known as 'centres of ossification', in which skeletal stem cells proliferate and condense around a profuse capillary network. Subsequently, they differentiate into osteoblasts, which in turn create the osteoid (i.e. a non-mineral matrix of collagen and non-collageneous proteins) at the centre of the cell aggregate. Osteoblasts thus produce a bone matrix and become enclosed within the secreted collagen fibres, subsequently transforming into osteocytes. At this point, the osteoid becomes more and more mineralised, and the mature bone is formed.

Endochondral ossification (from the Greek *endon* and *chondros*, which mean 'within' and 'cartilage', respectively) mainly occurs in long bones, and plays an important role in both bone growth and fracture healing. It initiates in the cartilage, at specific sites

referred to as 'primary ossification centres'. In a first step of the process, a cartilage model is created, consisting of condensation of mesenchymal cells that differentiate into chondrocytes and secrete typical cartilage extracellular matrix components. Once formed, the cartilage model is invaded by blood vessels, osteoclasts, bone marrow cells, and osteoblasts, creating the so-called 'secondary centres of ossification'. Osteoblasts deposit bone on remnants of cartilage matrix, resulting in the formation of the mature bone [9].

During fetal development, bone modelling is the process by which bone is formed by osteoblasts without prior bone resorption. Bone remodelling instead occurs throughout a lifetime, and is the continuous replacement of discrete quantities of old bone (reabsorbed by osteoclasts) with newly synthesised matrix (deposited by osteoblasts), and the subsequent mineralisation of this matrix to form new bone. Physiological bone remodelling is based on a complementary and balanced activation of both bone resorption and bone formation, and it allows bones to change their overall shape in response to physiological factors or mechanical forces, leading to gradual adjustment of the skeleton to environmental conditions. These dynamic processes allow to maintain healthy bone tissue, repair damaged tissue, and regulate the homeostasis of the phosphocalcic metabolism. They also control the reshaping or replacement of bone during growth and following injuries, including fractures or microdamage. Remodelling also responds to the functional demands of mechanical loading. As a result, bone is added where needed and removed where it is not required [9].

1.1.2 Bone Pathology

The purpose of modelling and remodelling during growth is to achieve the skeleton peak strength, while bone remodelling during a lifetime maintains bone strength by replacing damaged bone. Abnormal bone remodelling can result in numerous skeletal disorders, the most common being osteoporosis. Osteoporosis, literally 'porous bone', is a very common metabolic disorder of the skeleton caused mainly by osteoblast and osteoclast dysfunction, due to senescence and hormonal factors. People affected by osteoporosis have a reduced bone mineral density (BMD), a disrupted bone microarchitecture, and an altered amount of noncollagenous proteins. All these pathological characteristics lead to increased bone fragility and risk of fractures [8]. There are two types of osteoporosis: primary and secondary. The former mainly occurs

during the postmenopausal and senile age, while the latter is associated with a low calcium and vitamin D diet [10], endocrine disorders, certain drugs, and malignant or chronic diseases like type 1 diabetes, rheumatoid arthritis, hyperthyroidism, celiac disease, asthma and multiple sclerosis [11].

Osteoporosis, and consequent bone fragility, is one of the main causes of bone fractures, of which fracture nonunions represent approximately 5-10% of all cases [12]. A fracture is a discontinuity in the geometry of bone, and there are different factors initiating and governing the healing of a fracture, classified as patient- or fracture-specific. Patient-specific factors include age, nutritional status, co-morbidities (i.e. diabetes mellitus), nicotine consumption, and other medications. Fracture-specific factors instead comprise the anatomical location, mechanical stability, bone integrity (i.e. osteoporosis) and comminution (i.e. how many bone fragments are present), infection, the presence of adjacent injuries, level of displacement and treatment method [13].

Fracture union occurs when the bone is repaired, so that fragments are stable and do not tend to displace, the bone is mechanically able to function and support the weight of the body, and the patient experiences absence of pain. An interruption in the repair process can result in a nonunion. According to the United States Food and Drug Administration (FDA), in order to diagnose a nonunion fracture, at least nine months must pass after the fracture, and there should not be signs of healing during the first three months. The main causes of fracture nonunion can be either patient-dependent or not. The former include advanced age, various medical co-morbidities, smoking, use of non-steroidal anti-inflammatory compounds, genetic disorders, metabolic diseases, and nutritional deficiency. Patient-independent factors include the fracture pattern, location, and displacement, severity of soft tissue injury, the degree of bone loss, quality of surgical treatment, and presence of infection [14].

Nonunions are difficult to treat and have a significant economic impact in terms of both direct and indirect costs, such as those associated with a loss in productivity. They represent an annual cost to the UK economy of about £2 billion and to the EU of €37 billion. It is therefore important to identify effective treatment options for nonunions to improve patients' quality of life and reduce the financial burden on both the healthcare providers and patients [13].

1.1.3 Treatments for Bone Fractures

There are different treatments available for fractures and nonunions, but they all suffer from invasiveness and there is currently no approved systemic therapy. Generally speaking, treatments can be divided into two categories: physical stimulation therapies and biological therapies. Among the clinically available therapies, mechanical fixation is the main approach to the treatment of fractures, normally via bone immobilisation with casts, but this can lead to joint stiffness of both muscles and periarticular structures due to the lack of mechano-stimulation.

Physical stimulation therapies are based on the evidence that prolonged immobilisation without stimulation leads to bone loss. To prevent this from occurring, mechanical stimuli could be applied to the site of injury enhancing the proliferation of bone cells and their mineralisation. Studies have suggested that osteocytes, osteoblasts and MSCs are mechanosensitive, but the mechanisms involved are not yet fully understood. It is commonly accepted that osteocytes are the main mechanosensory cells. Briefly, a load applied to the bone deforms the tissue and creates fluid flow within bone; this mechanical signal is detected by osteocytes and converted into a biochemical signal thanks to the ion channels and the integrin receptors on the external membrane of osteocytes. This signal conversion is called mechanotransduction, and involves different molecular signalling pathways and mediators. In addition, MSCs differentiate into fibroblasts, chondrocytes or osteoblasts and this can depend on the level (and type) of tissue strain at which they are subjected; in the case of a fracture, this response may lead to different healing outcomes[3].

Clinically, physical stimulation can be generated via internal fixation, which is the use of prostheses or mechanical devices to fix bone fragments together [15]. It allows the patient to load the site of injury, overcoming the detrimental effects of long immobilisation. Although it is associated with reduced hospitalisation, it requires surgical intervention. Other more experimental therapies under study are: electrical bone stimulation, extracorporeal shock waves [16], and low-intensity pulsed ultrasound (LIPUS) [17]. Electrical stimulation relies on the piezoelectric properties of the collagen matrix: compressions generate electronegative potentials and are associated with bone formation, while tensions lead to electropositive potentials and lead to bone resorption. It is thought that this electrical stimulation is the path through which bone forms in response to applied loads and this is the reason why electrical stimulation

treatments make use of electronegative potentials to achieve bone regeneration [16]. In extracorporeal shock wave therapy, high-intensity shock waves are produced to stimulate the formation of free radicals, mainly reactive oxygen species, which lead to the production of different growth factors. Finally, LIPUS is based on the evidence that ultrasound waves can generate micromechanical stresses within the fracture, thus stimulating and accelerating healing and preventing joint stiffness [18]. Unlike steady mechanical stimulation, LIPUS (1.5 MHz sinusoidal waves modulated in burst of 200 ms at a repetition frequency of 1 kHz and a spatial average-temporal average intensity of 30 mW/cm^2) subjects cells to a periodically varying load that may be better than a continuous load in the healing process of fractures [19]. It has been shown that LIPUS accelerates mineral nodule formation, reduces inflammatory responses, induces angiogenesis, and prevents joint stiffening in the case of joint immobilisation; however, the treatment outcome depends on factors like age and medical history of the patient, the site of the fracture and its nature. In addition, the governing mechanisms still need to be fully identified. It has been shown on human cadaveric specimens that LIPUS can produce nanomotion at the fracture site. For US to have a biological effect, the mechanical wave must be converted to a biomechanical signal within the cell. Integrins, the mechano-receptors of cells, become activated following mechanical stimulation and create focal adhesions, namely conglomerations of integrins. It is thought that these focal adhesions are able to initiate cellular pathways leading to the production of the enzyme COX2 (cyclo-oxygenase 2) that is essential for the induction of gene transcription for osteogenesis, remodelling and mineralisation [20]. Figure 1.2 shows the main steps of the LIPUS process. LIPUS is approved by NICE (National Institute for Health Care and Excellence) and in use for treatment of non-union fractures [21]. The clinical efficacy and underlying mechanisms of treatment, however, are still controversial; as a matter of fact, Schandelmaier et al. [22] performed a meta-analysis on different studies and concluded that LIPUS does not improve patient outcomes and probably has no effect on bone healing.

Biological therapies can be further classified into local or systemic treatments. Examples of clinically available local therapies are autografts, allografts and bone morphogenetic proteins (BMPs) [23]. The current gold standard for treating nonunions is the use of autologous bone grafts (autografts), and the preferred donor site is the patient's own iliac crest. The iliac crest is the most common donor site because of easy access and procurement. The ilium has osteogenic properties (inducible

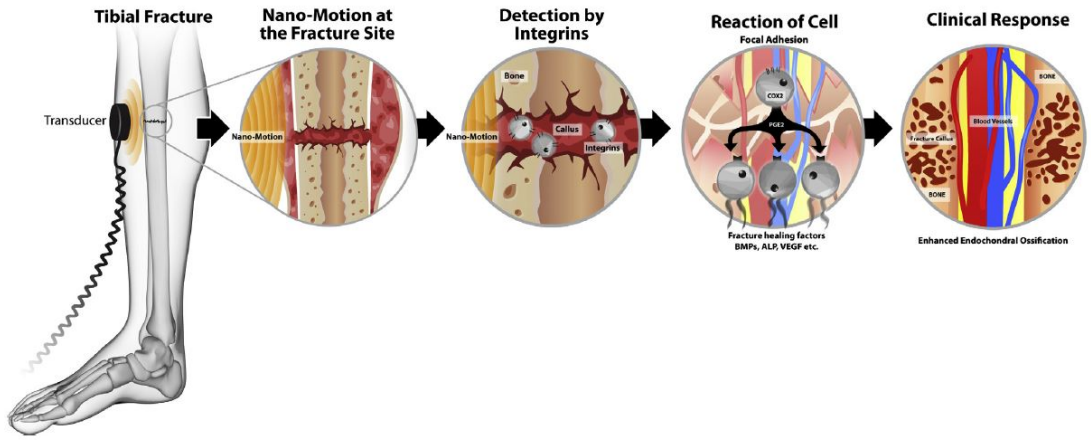

Figure 1.2: *The figure shows a schematic representation of the processes involved in LIPUS. The transducer is placed on the skin above the fracture and activated. LIPUS generates nanomotions at the fracture site that activate integrins, which in turn agglomerate in focal adhesions. These focal adhesions activate cellular pathways leading to the induction of osteogenesis, remodelling and mineralisation. [20]*

osteogenic precursor cells), osteoinductive properties (noncollagenous bone matrix proteins, including growth factors), and osteoconductive properties (bone mineral and collagen). Another donor site is the fibula. Bone tissue is transplanted from the donor site and grafted onto another part of the body to replace damaged tissue. Despite this technique is widely employed, it presents several drawbacks that are mainly associated with tissue harvesting, such as prolonged postoperative pain and site morbidity (i.e. bleeding and haematoma). Moreover, donor tissue is not always available. To overcome these limitations, allografts have been introduced, where the tissue is sourced from donors. However, allografts are associated with a higher failure rate and infection risk, due to their low osteogenic potential and subsequent creation of poor graft-host integration [24]. Another alternative for treating nonunions is the administration of recombinant human bone morphogenetic proteins (BMPs). However, BMPs are expensive and they are associated with several side effects, including infection, heterotopic bone formation, and immunogenic reactions. In order to reduce the negative consequences of BMPs, local targeted gene therapies are under preclinical investigation to be used to transiently overexpress osteogenic BMP genes, instead of administrating high doses of BMPs systemically [25].

Local targeted gene therapies currently in the preclinical phase include viral and nonviral vectors, *in vivo* electroporation or sonoporation. With respect to

viral and nonviral vectors, the former are efficient but they can cause malignancies and immunogenic reactions, while the latter are safer but less efficient. *In vivo* electroporation involves the use of high-intensity electric fields to permeabilise cell membranes. It has been employed to deliver a BMP gene into endogenous mesenchymal stem cells (MSCs). The method has proven to be successful; however, it is associated with high pain levels and tissue damage [23]. Finally, ultrasound-mediated cell and tissue permeabilisation (referred to as sonoporation) involves the use of ultrasound waves, often in combination with ultrasound-responsive agents, to enhance intracellular delivery of bioactive compounds. The safe and non-invasive nature of ultrasound, together with its ability to reach deep-lying tissues, make sonoporation an attractive (still unexplored) strategy for treating bone fractures. An example of a non-invasive, systemic therapy is the administration of parathyroid hormone, a regulator of mineral metabolism, but this has not been approved yet for fracture healing [25].

In conclusion, there are some clinically available options to treat bone fractures and nonunions; however, they all suffer from complications and drawbacks. The ideal treatment should combine the delivery of limited quantities of drugs to the site of injury, combined with mechanical stimulation of the site of injury [26]. At present, the majority of drugs are limited in their ability to reach the site of injury at sufficient concentrations, since they are cleared from the circulation mainly by liver and kidneys. Thus, high doses must be administered to achieve an acceptable therapeutic efficacy, but this results in increased systemic toxicity. Local drug delivery methods could be employed to overcome this limitation, and these are reviewed in the following paragraphs. In the context of this study, particular attention is devoted to ultrasound-responsive drug delivery vehicles, as a means to achieve a localised release of therapeutic compounds at the fracture site with simultaneous mechanostimulation of the fractured bone tissue. The combination of localised therapeutics and mechanostimulation is anticipated to enhance the bone repair process [27] [28].

1.2 Nanomedicine and Ultrasound Applied to Bone Fractures

1.2.1 Local Drug Delivery

Bone healing can be enhanced by the action of bioactive compounds, and this is usually achieved by administering them by local injection due to the lack of a validated systemic delivery method. The ideal drug dosage and administration method should take into account different parameters, including drug pharmacokinetics (i.e. the time course of drug absorption, distribution, metabolism, and excretion) and pharmacodynamics (i.e. the relationship between drug concentration at the site of action and the resulting effect, including the time course and intensity of therapeutic and adverse effects), therapeutic efficacy, possible off-target side-effects, short- and long-term outcomes. While systemic diseases, like osteoporosis and osteoarthritis, benefit from systemic administration of drugs; localised injuries, such as fractures and nonunions, would instead benefit from delivery *in situ*. Drug clearance mechanisms limit the spontaneous accumulation of most drugs at a treatment site, so a potential way to get around this is to load the drugs within protective carriers that are designed to passively or actively release the drug at the target organ or tissue [4].

Drug carriers require many desirable characteristics, including biocompatibility, high drug loading efficacy and an ability to retain the drug until reaching the target site where the payload should be released in a controlled fashion. In this way, optimal drug concentrations can be reached at the treatment site with minimal off-target side-effects [28] [29]. Administration of these drug carriers would normally be via a minimally invasive systemic route, such as intravenous injection. This is possible because drug distribution is governed by the physico-chemical characteristics of the carrier, rather than those of the drug, often leading to accumulation of drug-loaded carriers over time and maintaining high levels of drug at the target site for longer periods, enhancing treatment efficacy [4]. Carriers are usually composed of an outer shell encapsulating a core that can be either a liquid or a gas. Drugs can be encapsulated within the core of the carrier, incorporated in the shell, or connected to the shell through degradable linkers. Being able to control the release of a therapeutic compound both spatially and temporally would enhance tissue regeneration.

1.2.2 Nanoscale Carriers

Among the different types of carriers that could be employed to enhance healing processes, drug-loaded nanocarriers have attracted considerable interest. Notably, nanocarriers have a large surface area-to-volume ratio; thus, they can be loaded with a relatively high amount of drug, which is, then, protected from dispersion and degradation in the bloodstream. The blood circulation time of a compound is also increased, thanks to the protection provided by the external shell. Moreover, nanocarriers allow the transport of drugs across the cell membrane, which typically occurs via endocytosis, with possible enhancement of the drug's therapeutic effect [28] [29].

Nanocarriers are currently under investigation to be used for bone regeneration to treat bone diseases, such as osteoarthritis, bone metastases, osteosarcoma, bone infections, and inflammatory diseases. Two main classes of materials are used to produce the nanocarrier shell: inorganic and organic materials. The former have been employed to synthesise titanium nanotubes, gold nanoparticles, calcium phosphate nanoparticles, and mesoporous silica nanoparticles. As for the organic nanocarriers, chitosan nanoparticles, PLGA nanoparticles, and liposomes, have been largely investigated. The physico-chemical characteristics of the drug to be loaded, the targeted cell type, the required delivery rate, and the injury size are all factors influencing the choice of the materials to be used [28].

The release of drugs, within controlled temporal and spatial windows, can be achieved by applying stimuli of different nature to nanocarriers that are specifically designed to respond to these stimuli. For instance, it is known that some bone diseases are associated with a change in the physical and chemical properties of the local physiological environment, and this can be exploited to trigger the release of drugs. Figure 1.3 illustrates some of the main physical properties associated with bone diseases, which could be employed as stimuli for controlled drug release. It can be noted that each disease is associated with various stimuli; the choice of a stimulus is therefore a compromise between therapeutic outcome, cost, scalability, and reproducibility [4].

At present, stimuli-responsive nanocarriers have been designed to respond to changes in pH, redox conditions, temperature, enzymatic levels, and to different forms of energy, such as light, magnetic and ultrasound fields. For example, inflammation and

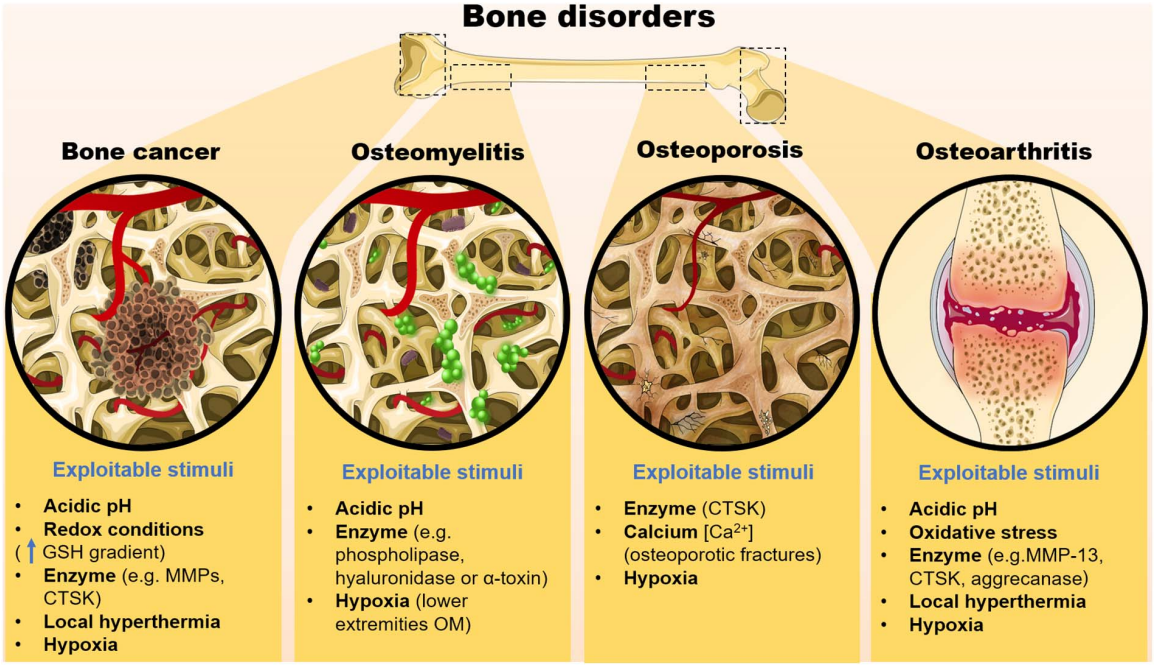

Figure 1.3: *The major diseases affecting bone are known to change some physiological characteristics of the local environment. These changes can be exploited as stimuli to allow the release of drugs by nanocarriers where needed. Reprinted from [4], with permission from Elsevier.*

tumours are usually associated with an increase in the local temperature, which can be further increased from the outside of the body, i.e. by using ultrasound, alternating magnetic fields, or hot water sacks. Coupling this with temperature-sensitive materials which are able to change their properties with temperature (in a non-linear fashion) could provide a good delivery strategy. As for magnetic fields, they can also be used to move functionalised magnetic nanoparticles to the site of interest. Consequently, drug concentration increases locally due to nanocarrier retention and this creates a favourable drug concentration gradient. This gradient is thought to translate into passive diffusion of the drug from the inside of the drug carrier to the outside. Regarding pH-mediated release, there are two alternative methods; (i) nanocarriers can be functionalised with pH-sensitive compounds by adding ionizable groups, like carboxylic acids and amines, to their shell. A change in the pH of the medium results in a sharp shift in the protonation of the ionizable groups, leading to the formation of discontinuities in the shell of the carrier and allowing the release of drugs. (ii) Drugs can alternatively be linked to stable shells via pH-sensitive linkers that hydrolise in response to changes in pH. Concerning ultrasound, it is already widely used in the clinical setting for non-invasive biomedical imaging as well as LIPUS therapy, as discussed in Paragraph 1.1.3. To further enhance the physical effects of ultrasound waves, ultrasound-responsive nanocarriers could be employed, which are known to volumetrically oscillate and collapse in response to ultrasound stimulation. In this way, drug release could be controlled both spatially and temporally in addition to the therapeutic effect of the stimulus itself [4].

This study focuses specifically on the use of ultrasound-sensitive particles, loaded with bioactive compounds. Lipid-shelled particles are a class of carriers characterised by high biodegradability and biocompatibility. Among the different types of ultrasound sensitive lipid-shelled particles, gas microbubbles and perfluorocarbon nanodroplets have attracted considerable interest from researchers. The former are mainly exploited for their echogenicity, while the latter also provide enhanced extravasion efficiency and circulation time. It is known that parameters like particle size, shape, rigidity, and composition influence stability, pharmacokinetics, pharmacodynamics, targeting ability, and cellular uptake; thus, it is important to find a trade-off between these characteristics in order to provide a functional solution for a given application [28] [30].

1.2.3 Ultrasound

Ultrasound (US) is a mechanical wave with a frequency exceeding the upper limit of human hearing, which is approximately 20 kHz (Figure 1.4).

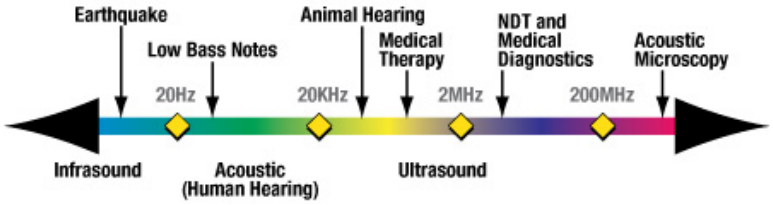

Figure 1.4: *Sound frequency spectrum. Ultrasound has a frequency higher than 20 kHz. [31]*

US is an acoustic pressure wave, meaning that it compresses and rarefies the medium through which it travels. Sound waves are classified as being longitudinal or transverse, depending on whether the vibration of each particle is parallel or transverse to the direction of propagation. US can be both longitudinal (as shown in Figure 1.5) and transverse [32].

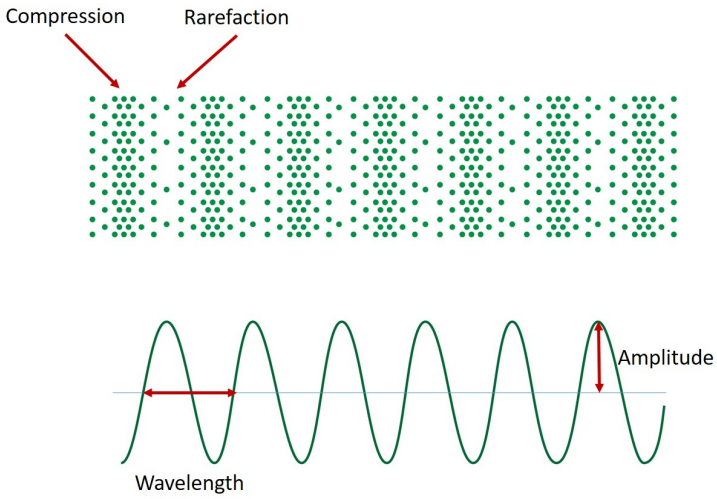

Figure 1.5: *An acoustic pressure wave creates compressions and rarefactions of the particles in the medium through which it travels. A pressure wave is characterised by a wavelength, namely the distance between one peak of a sine wave and the next peak, and by an amplitude, namely the maximum extent of the oscillation.*

The frequency f of the particle oscillation is related to the wavelength λ and the propagation velocity c as shown in Equation 1.2.1. Frequency is defined by the number of waves that passes a given point per second, the wavelength is the distance between

one peak of a sine wave and the next peak, while the propagation velocity is the speed at which the wave travels [33].

$$c = \lambda f \tag{1.2.1}$$

When a sound wave travels through a medium, it is possible to define the 'fundamental frequency' as the lowest resonant frequency of the vibrating medium. Building on this concept, a 'harmonic' and a 'ultraharmonic' are defined as an integer multiple of the fundamental frequency and a 'subharmonic' is defined as a fraction of the fundamental frequency. If a sound wave contains a wide range of frequencies, then the term used to define it is 'broadband noise'.

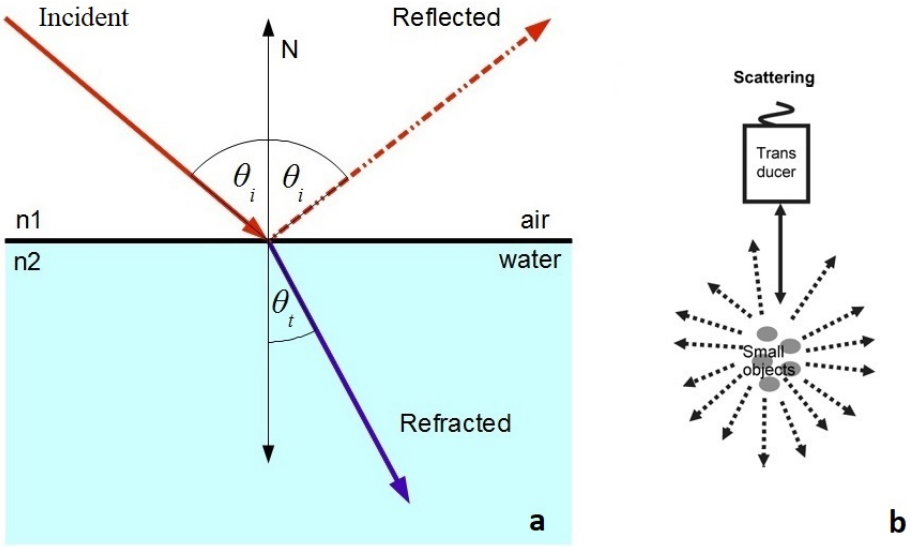

Figure 1.6: *a) When ultrasound crosses a surface dividing two media with different acoustic properties, part of the wave is reflected and part of it is refracted. [34] b) If the interface is small, waves are reflected in all directions and this phenomenon is referred to as scattering. [35]*

When a plane wave impinges on an infinitely large plane which is the interface between two media of different acoustic properties, reflection and transmission/refraction occur, meaning that part of the wave is reflected and part of the wave is transmitted or refracted, as shown in Figure 1.6.a. The amplitude of the reflected wave is proportional to the difference in acoustic impedance between the two media. Acoustic impedance is a physical property of the medium describing how much resistance an ultrasound

beam encounters as it passes through the medium itself. Equation 1.2.2 shows that acoustic impedance z is the product of the volumetric density ρ of the medium and the acoustic propagation velocity c in the medium.

$$z = \rho c \tag{1.2.2}$$

If the speed of sound in the two confining media is the same, the transmitted wave continues its propagation in the second medium maintaining its direction. If the speed of sound in the second medium is different with respect to the first one, then refraction occurs and the refracted wave continues its propagation in the second medium in a different direction.

If the physical interface between the two media is small relative to the ultrasound wavelength or if the surface is very irregular, then scattering takes place. The scattered wave propagates in all directions in a spherical manner. Thus, a component of the scattered wave will travel towards the ultrasound source, as shown in Figure 1.6.b. The latter is denoted as 'backscattering'. Reflection, transmission/refraction and scattering, together with absorption (namely, the transfer of energy from the sound beam to the medium and, ultimately, its degradation into heat), cause attenuation of an ultrasound beam as it travels through different types of media [33].

1.2.3.1 Ultrasound as a Theranostic Stimulus

Ultrasound is widely used in medicine and is regarded as one of the safest imaging modalities, since it can be applied non-invasively and reach deep-lying tissues. The difference between the acoustic impedance of different soft biological tissues and organs is very small. Therefore, only a very small fraction of the ultrasound pulse is reflected, and most of the energy is transmitted. US frequencies used in clinical imaging lie between 1 and 30 MHz; the bandwidth chosen depends on the type of tissue to be imaged. The resolution obtained is higher with shorter wavelengths, with the wavelength being inversely proportional to the frequency as shown in Equation 1.2.1. However, the use of high frequencies is limited by their higher attenuation (i.e. loss of signal strength) in tissue, and thus their shorter depth of penetration [36].

Another diagnostic use of ultrasound can be found in the orthopaedic field. By applying the so-called 'axial transmission technique', it is possible to study the propagation of US waves along the cortical shell of long bones and obtain information

about the bone healing process of fractures. Indeed, the velocity of propagation of US depends on the material where it travels [37] [38]. The gap of a bone fracture and the subsequent stages of fracture healing from bone callus to re-mineralisation are all associated with different mechanical characteristics (notably, a gradual increase in the stiffness, load at failure, strength and Young's modulus) of the structure involved and, hence, different velocities of propagation of the US wave. The speed of sound is not only affected by the stiffness, but also by the dimension and geometry of the fracture gap and by the thickness of the bone involved [39].

Apart from being used for diagnostic applications, ultrasound can also be used as a therapeutic stimulus. As discussed earlier, ultrasound waves can be used in combination with drug-loaded carriers, such as microbubbles or nanodroplets, to achieve controlled drug release and local stimulation of cells.

1.3 Gas Microbubbles

Microbubbles (MBs) consist of a gas core surrounded by a shell that provides stability, in terms of their concentration and mean diameter. There are several compositions available for both the entrapped gas and the shell, and each microbubble formulation has its own characteristics and functions. As shown in Figure 1.7, microbubbles can also be loaded with drugs and they can be used as gas carriers - for sonodynamic therapy (O_2 MBs) or antimicrobial treatments (NO MBs) [40] [41].

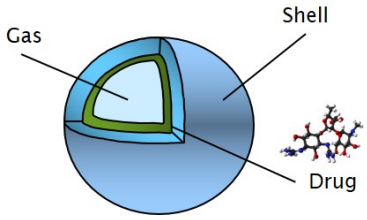

Figure 1.7: *The figure shows the structure of a microbubble: a gas core surrounded by a shell that provides stability. Microbubbles can be loaded with drugs and act as drug carriers. Republished with permission of Royal Society of Chemistry, from [42]; permission conveyed through Copyright Clearance Center, Inc.*

Usually, about 95% of microbubbles used in the clinic have a diameter smaller than 10 μm and a mean diameter of approximately 3 μm. Therefore, they have approximately the same size as erythrocytes, and share similar rheology in microvessels and capillaries

[43]. This is one of the main reasons why microbubbles are already in use as ultrasound contrast agents (UCAs), and as a means of transporting drugs and bioactive gases (i.e. oxygen or nitric oxide). UCAs are usually injected intravenously and, despite having a gas core, the quantity of gas is so limited (typically less than 200 μL per injection) that it is not hazardous in terms of possible embolisms [5]. They usually have a vial concentration of approximately 10^8 to 10^9 MBs/mL and are typically administered to patients by intravenous injection of a 1-2 mL suspension, giving an average blood concentration of around 10^5 to 10^6 MBs/mL, which is sufficient to produce strong contrast enhancement even at low ultrasound intensities [44]. Being able to maintain stability of both size and concentration with respect to time is fundamental to both MB safety and efficacy. Notably, MBs should not occlude blood vessels and their concentration should be high enough to provide a desirable therapeutic effect.

The gas core of MBs is fundamental for their ultrasound responsiveness, and ultimately for their therapeutic function. The compressibility of the gas cores gives MBs the ability to compress and expand in response to US; these volumetric oscillations generate harmonic echoes much stronger than the tissue echoes, and this phenomenon is at the basis of the use of MBs as ultrasound contrast agents. The amplitude of these oscillations depends on the US frequency, pressure and pulse duration as well as MB shell and size [45]. The gases normally incorporated in MBs are room air [46], fluorocarbons [47] [48], oxygen [40] or nitric oxide [41]. Table 1.1 shows the main gases usually incorporated in MBs and their molecular weights. Different gases may also have different diffusion coefficients and this can have an influence on the stability of microbubbles. Gases with lower molecular weights usually diffuse faster than gases with higher molecular weights.

Table 1.1: *Gases most often used as the core of microbubbles and their molecular weight.*

Gas	Molecular Weight [g/mol]
Room air	28.96
Perfluorobutane PFB	238.03
Oxygen O_2	31.99
Nitric Oxide NO	30.01

Gas microbubbles without a shell are highly unstable, and cannot be used for drug delivery purposes. Many different shell constituents have been investigated; including

proteins, polymers, lipids, or a combination of these.

As for the protein-shelled microbubbles, they are mainly used in contrast ultrasound imaging. Different types of proteins, such as albumin, lysozyme and avidin [49], can be used to coat the gas core, providing a very active surface thanks to their amphipathic nature, i.e. the characteristic of having both hydrophilic and hydrophobic moieties.

In polymer-shelled microbubbles, the gas core is stabilised by a thick coating layer consisting of cross-linked or entangled polymers. Polymers make the shell more resistant to compression and expansion during US stimulation, and this reduces MB echogenicity and potentially its ability to deliver drugs.

Finally, lipid-shelled microbubbles are the most commonly used formulation in both biomedical imaging and drug delivery, hence they are the focus of this study. In these microbubbles, phospholipids organise themselves spontaneously so that their hydrophobic acyl chains face the gas core, and their hydrophilic headgroups face external aqueous environment of the bubble, as shown in Figure 1.8.

Figure 1.8: *The figure shows the monolayer structure of a microbubble shell. Phospholipids organise spontaneously so that their hydrophobic acyl chains face the gas core, and their hydrophilic headgroups face the surrounding aqueous environment of the bubble. [50]*

Lipid shells show enhanced stability, due to different physico-chemical factors. Firstly, the lipid monolayer organises itself so as to have a low surface tension, and this increases the stability of the microbubble. Secondly, lipids in the monolayer are pack together tightly thanks to both hydrophobic and Van der Waals interactions. In addition, there are some weak physical forces among the phospholipids, which allow expansion and compression to occur during exposure to ultrasound [51].

Lipid shells are typically composed of two constituents: a primary lipid and an

emulsifier. The primary lipid is often a phosphocholine (PC) with twin saturated acid fatty tails. In order to offer sufficient resistance to gas diffusion through the shell, the phospholipid tail length (i.e. the number of carbon atoms) should be of at least 16 carbons; while PC-lipids with 24 carbon atoms are the longest acyl chains currently commercially available [52]. The longer these hydrophobic chains are, the more stable are the microbubbles, thanks to enhanced attractive dispersion forces between the hydrophobic tails of adjacent lipid molecules in the shell of the bubble. This is also associated with lower gas permeability through the shell. Moreover, increasing the hydrophobic chain length decreases the surface tension of the microbubble. The primary lipid fraction should be at least 70 mol% of the total lipid content, to enhance stability. As for the emulsifier, it is usually a polyethylene (PE) of similar tail length to the phospholipid molecule, with a long polyethylene glycol (PEG) group. It has both hydrophilic and hydrophobic groups and this facilitates its intercalation within the microbubble shell, while still being soluble in water. It is used to encourage the initial lipid absorption in the shell and to prevent non-specific protein absorption, lipid dispersion, and phagocytosis *in vivo*. Moreover, it prevents microbubbles from coalescing, and this happens through a steric repulsive force between different microbubbles. Bubble fusion can happen only if microbubbles collide with high inertia, or if contact between them is long enough to allow the emulsifier to diffuse away from the point of contact. The concentration of surfactant used should be higher than its critical micellar concentration (CMC), which is the threshold concentration at which the surfactant aggregates and forms micelles. Examples of surfactants are polyethilene glycol stearate (e.g. PEG40s) and PEGylated phospholipids (e.g. DSPE-PEG) [53].

Despite the use of PEGylation as a means of increasing resistance of MBs to immunologic clearance, recent studies have shown that when the immune system is exposed to PEG molecules, these can be recognised and therefore the immune system adapts by producing anti-PEG antibodies. Moreover, an increase in the presence of anti-PEG antibodies has been detected in more than 70% of the general population who has never been treated with PEGylated compounds. This may be due to the increasing low-level exposure to PEGylated compounds present in household goods. The presence of anti-PEG antibodies leads to an accelerated blood clearance (ABC) and altered pharmacokinetics of PEGylated particles, a decrease in the therapeutic effect, and possible adverse effects [47]. Furthermore, PEGylated

compounds also seem to induce accelerated blood clearance by the activation of other immunologic processes. Notably, once in the body, particle surfaces interacts with the local environment (e.g. blood) and absorb a complex corona of proteins, which influences the interaction between particles and the surrounding tissue. In the presence of PEG, anti-PEG antibodies bind to the surface of the particle, enhancing their interaction with macrophages and their clearance from the body. Interestingly, although antibodies alter the clearance of PEGylated particles, the pharmacokinetics of free PEG is not affected [54] [55]. Therefore, further studies are needed to better understand these immunologic processes, and patients should be pre-screened and monitored to check the level of anti-PEG antibodies in their blood and alternatives to PEGylated compounds should be considered if needed.

The composition of MB shell, together with the final size of the microbubble and US parameters used, influence microbubble behaviour upon ultrasound stimulation. Different MB responses are used for different purposes in the biomedical field, as discussed in the following paragraph [56].

1.3.1 Microbubble Response to Ultrasound

Since the propagation of sound is slower in gases than in liquids, and gases and liquids have very different densities, an acoustic impedance mismatch occurs between blood and microbubbles. Microbubbles can thus effectively reflect the ultrasound energy, which makes them a useful tool in contrast imaging. Moreover, during ultrasound stimulation, the gas core undergoes volumetric oscillations, by expanding during the rarefaction phase of the pressure wave and contracting during the compression phase. These oscillations can also be exploited for imaging purposes and to mechanically stimulate cells. The oscillation is due to two phenomena that drive the liquid-gas interface in opposite directions: (i) the resistance against compression of the gas inside the MB on one side, and (ii) the inertia of the surrounding liquid on the other. The temporal dynamics of these competitive effects is such that, at a certain frequency called resonance frequency, the oscillation synchronises with the US wave and results in a maximal radial response. The resonance frequency is directly related to the MB size; hence, to obtain a maximal response from a sample, the MB size dispersity should be as small as possible so that US matches the resonance frequency of the majority of MBs [45].

The oscillation MBs undergo is called cavitation, and it can be classified as stable or inertial. The former is the repetitive and controlled oscillation of the gas core, and has been shown to directly affect cell membrane ion channels and receptors, and potentially cause secondary effects on membrane permeability and action potential; while the latter is a chaotic oscillation leading to microbubble rupture and producing a series of mechanical effects including shock waves and microjets. The final MB behaviour strongly depends on the acoustic pressure and frequency used. As shown in Figure 1.9, there can be six different behaviours based on the level of acoustic pressure used; the acoustic pressure being the difference between the pressure caused by a sound wave and the ambient pressure of the media the sound wave is travelling through.

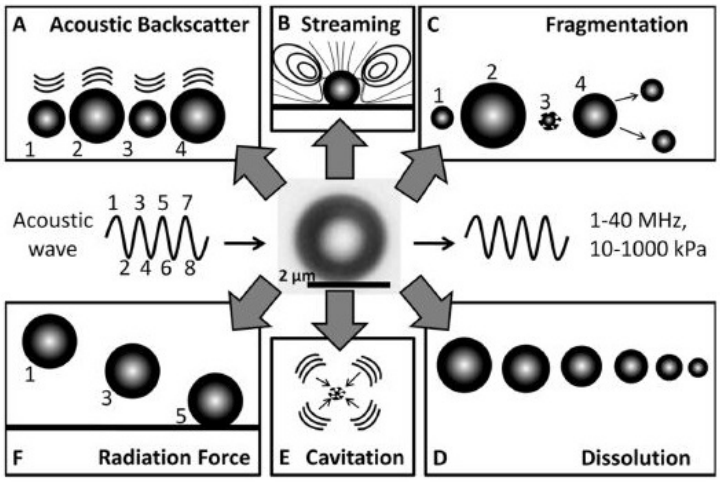

Figure 1.9: *Different intensities of ultrasound lead to different microbubble responses. A) At low acoustic pressures, microbubbles act as a UCA. B) The stable oscillation of microbubbles creates streaming of fluid that mechanically stimulates cells. C) Moderate acoustic pressures lead to fragmentation. D) Just before fragmentation, dissolution occurs. E) High acoustic pressures and lower frequency lead to inertial cavitation. F) Sonication at low pressure and at a resonance frequency of the environment where MBs are placed allows microbubble manipulation. [51]*

At low acoustic pressures (<15 kPa) and near the MB resonance frequency, a microbubble stimulated with ultrasound responds with a backscattered echo (Figure 1.9.A) that can be used to detect and locate the microbubble (this principle is at the basis of ultrasound contrast imaging). The echo that is re-radiated mainly contains the fundamental driving frequency of the incoming US wave. Microbubbles with a small diameter (few µm) resonate at frequencies in the range 1-10 MHz, which is the

same range used in biomedical imaging. Moreover, stable MB oscillations can drive a steady flow in the MB vicinity (also referred to as cavitation microstreaming) [57]. Microstreaming can enhance local mixing of chemical species, by promoting convection, and generates shear forces over a cell membrane (Figure 1.9.B). Ultrasound also creates a net force on the microbubble, moving it in the direction of the propagating US wave; this force is known as 'radiation force' (Figure 1.9.F). Furthermore, since MBs themselves act as a secondary source of US waves when they cavitate, they will also exert secondary forces onto neighbouring bubbles. As a result, MBs oscillating in phase in close vicinity to each other will experience a net attractive force that can result in MB aggregation and coalescence and eventually lead to collapse.

Increasing the excitation pressure above 15 kPa leads to an increase in the amplitude of the radial oscillations, which also become non-linear and non-spherical since the expansion and compression phases of the oscillation are no longer equal. When MBs oscillate in a non-linear fashion, the echo contains both the fundamental driving frequency and its harmonics and subharmonics.

At higher acoustic pressures (approximately >300 kPa), oscillation can cause instability of the interactions between shell constituents resulting in fragmentation, whereby the original microbubble divides into daughter bubbles (Figure 1.9.C). At acoustic pressures just below the fragmentation threshold, dissolution occurs since a small amount of gas escapes from the core through the shell to the outside during the expansion phase of each cycle (Figure 1.9.D).

At high acoustic pressures, inertial cavitation takes place after a prolonged expansion phase. The volumetric changes of the microbubbles no longer follow the frequency of the incoming US wave, but are dominated by the inertia of the surrounding liquid. The resulting implosion creates a shockwave (and fluid jets) that can be potentially useful to enhance the transport of macromolecules in cells (Figure 1.9.E). During collapse, high temperatures and pressures can be generated in the centre of the MB core. The occurrence of inertial cavitation in a volume can be detected acoustically by the elevated broadband noise level that occurs during bubble collapse. The threshold between stable and inertial cavitation is not well-defined in terms of acoustic pressure, MBs can start to cavitate inertially between 200 and 500 kPa and this depends on different characteristics like MB size and shell stiffness. Moreover, the direct relationship between acoustic pressure and MB response only holds when the resonance frequency is used; at other frequencies the response is variable [51].

A main focus of this study is on the behaviour of microbubbles when stimulated with low acoustic pressures (at a frequency close to the MB resonance frequency), and on their interaction with biological tissues. Low pressure may be more beneficial than high pressure to limit the potential side effects associated with higher pressures. Inertial cavitation and collapse are usually unpredictable and cause high local pressures and temperatures. As a consequence, high-speed microstreaming and microjets are induced and these can cause cell and tissue damage. Apart from cell damage and death, high temperatures can also cause abnormal cell migration, altered gene expression, and cell membrane dysfunction. Stable cavitation induced by lower acoustic pressures is considered to be more beneficial to injured tissue and likely does not cause cell damage [58] [59].

1.3.2 Interaction between MBs and Biological Systems

Ultrasound stimulation affects not only the behaviour of microbubbles, but also the way in which cavitating microbubbles interact with cells and tissues. When a sound wave propagates through a suspension of ultrasound-responsive particles in a fluid, three physical phenomena occur: acoustic streaming and cavitation microstreaming on one side and radiation forces on the other. Acoustic streaming is defined as a steady fluid flow generated by the viscous attenuation of an acoustic wave (i.e., an ultrasound wave in this study). When particles are added to this scenario and undergo cavitation, further streaming of fluid called 'cavitation microstreaming' can be generated. The characteristics of streaming flow, namely velocity, length scale and flow features, depend on the physical and geometrical characteristics of the fluid and the particles, and on the characteristics of the acoustic wave. Cavitation microstreaming has a velocity in the order of μm/s, the length scale is in the order of μm and the flow geometry depends on different variables, such as acoustic pressure amplitude, viscosity of the medium, and the amount of surface-active material present in the fluid surrounding the bubble. By analysing a bubble on a surface, four characteristic streaming regimes can be observed. If the viscosity and the acoustic pressure amplitude are low, the streaming pattern usually comprises two major toroidal vortices and four smaller circular vortices, as shown in Figure 1.10.A. When the driving amplitude and/or the liquid viscosity increase, the toroidal and circular vortices can become more marked and the final pattern can be more similar to the one shown in Figure 1.10.B. The third regime shown in Figure 1.10.C usually occurs in low viscosity liquids,

but it can also occur in high viscosity ones if the driving pressure is sufficiently high. The fourth geometry illustrated in Figure 1.10.D is associated with high driving amplitudes and low medium viscosity. In the third and fourth cases, microbubble surface movements appear too [60] [61].

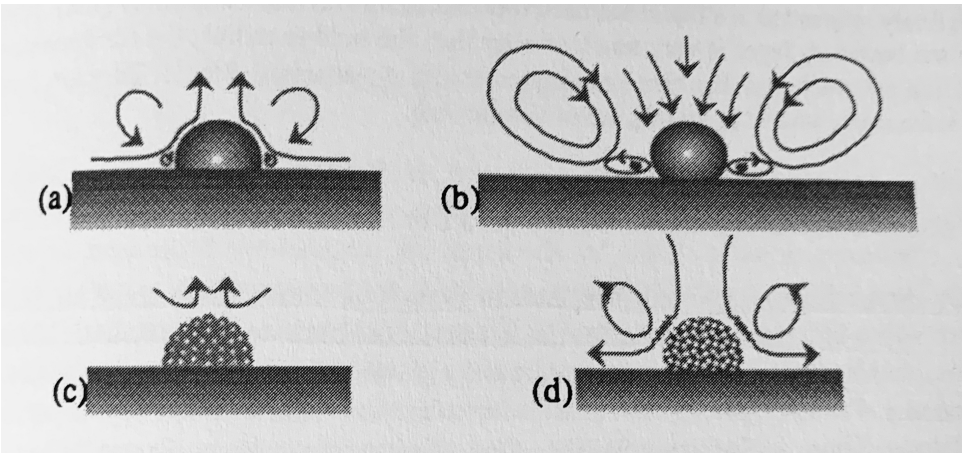

Figure 1.10: *Cavitation microstreaming creates a fluid flow that can have different patterns according to the acoustic pressure amplitude and the viscosity of the fluid. A,B) Patterns occurring when low acoustic amplitudes and viscosities are present. C) Pattern present with low viscosity fluids, or high viscosity ones with a high driving force. D) Pattern present at high driving amplitudes and low viscosities. [60]*

Pereno et al. [62] proposed a microfluidic layered acoustic resonator (μLAR) to simultaneously perform US stimulation, acoustic emission monitoring and optical microscopy of samples. By adding fluorescent tracer beads to a sample of SonoVue MBs, the cavitation microstreaming flows induced by MBs were imaged. Figure 1.11 shows the setup used to perform the imaging experiments and the pictures obtained: the μLAR consists of a single piezoelectric element, a ceramic carrier, a fluid cavity and a glass reflector. The device is designed to be operated at the resonance frequency of the layered structure and has an acoustic pressure minimum located at the reflector-air boundary so that no pressure nodes are developed in the fluid cavities, which may affect MB behaviour.

Microstreaming generates mechanical shear stress on nearby cells that can result in cell deformation and the creation of small, temporary openings in the cell membrane and between cells. Such openings can lead to enhanced uptake of drug molecules when these they are co-administered with MBs [45].

Radiation forces are steady forces generated as a result of a sound wave impinging

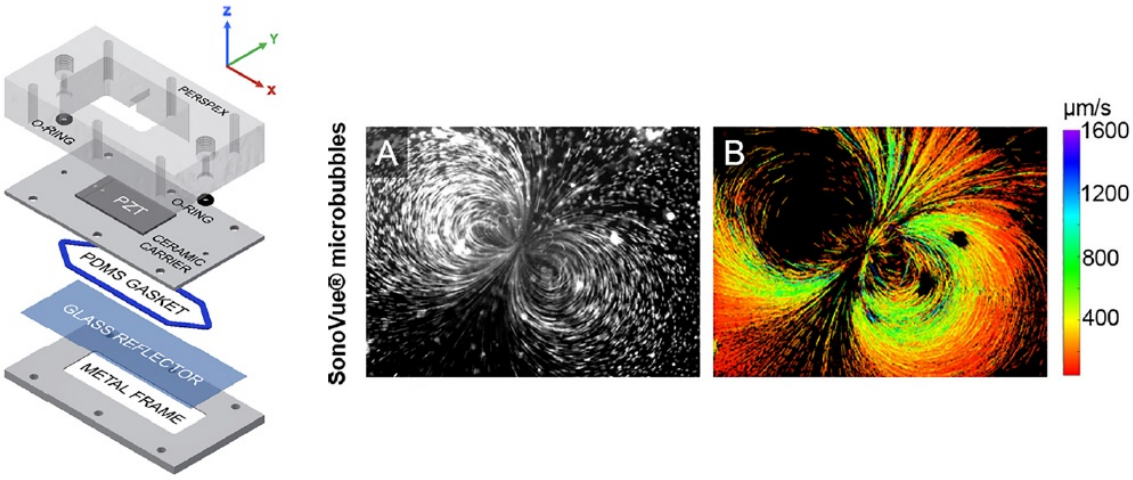

Figure 1.11: *The schematic shows the µLAR device used to simultaneously perform US stimulation, acoustic monitoring and imaging of cavitating microbubbles. The device consists of a single piezoelectric element, a ceramic carrier, a fluid cavity and a glass reflector. A) Cavitating SonoVue MBs. B) Velocimetry performed on the video of cavitating SonoVue MBs. Reprinted from [62], with the permission of AIP Publishing.*

on a surface, which are proportional to the acoustic power of the sound wave. Radiation forces create a displacement of the particles suspended in the fluid. Acoustic radiation forces are a physical phenomenon resulting from the interaction of an acoustic wave with an obstacle placed along its path, and they can be divided into primary and secondary forces. The former consists of forces that direct particles away from the acoustic source, which could improve both drug and gene carrier extravasation from the vessel in the direction of wave propagation. The latter instead are a form of 'attractive' force between particles and would increase aggregation between individual bubbles [63].

As a result of both microstreaming and acoustic radiation forces, when ultrasound is applied to a blood vessel in which microbubbles are circulating, MBs are pushed against the wall of the vessel, as shown in Figure 1.12 [64]. Generally, acoustic streaming dominates in large vessels and decreases with decreasing vessel diameter; radiation forces dominate in microvessels instead [65].

In addition to this, the oscillation of MBs close to cells can create transient perturbations to the cell membrane resulting in temporary and reversible openings, which provide a pathway for extracellular substances to travel into the intracellular milieu through the membrane. It can also enhance the uptake of extracellular

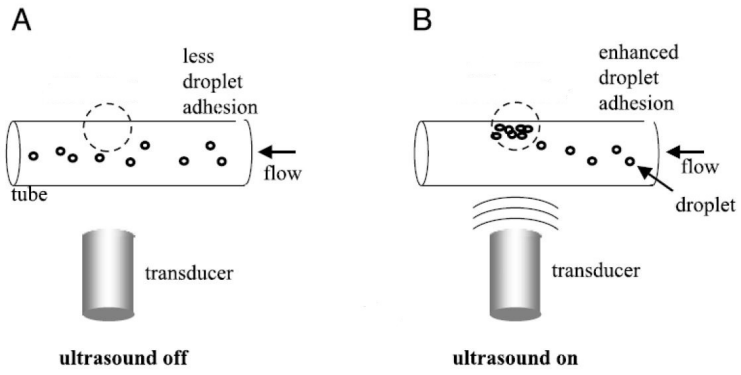

Figure 1.12: *Radiation forces allow the accumulation of microbubbles near the endothelial wall of a blood vessel. [64]*

substances, by promoting cell endocytosis [63].

As the skeletal system has an abundant blood supply, combined gene or drug injection with ultrasound irradiation is a promising approach for site-specific therapy and to reduce undesired side effects. Capillaries are fenestrated with a pore size between 60 and 80 nm, depending on the tissue, to allow nutrients and waste exchange between blood and cells [66]. Blood vessels in bones have an average pore sizes up to 80 nm, hence microbubbles are too big to extravasate. However, ultrasound and microbubbles may induce an increase in the permeability of the endothelial vasculature allowing small molecules bigger than the fenestration threshold to exit the bloodstream and travel into tissues. As a matter of fact, cavitation leads to alternating invagination and distension of the blood vessel wall. These movements damage the endothelial lining and temporarily increase blood vessel permeability. High-speed microscopy used to observe microbubble dynamics in *ex vivo* vessels showed that large blood vessels are mainly subject to invaginations, while small vessels experience both invaginations and distensions. In small vessels, MBs contacted with the vessel wall during expansion, and the dilation of the vessel was larger than the invagination induced by MB collapse. For large blood vessels, MBs did not make contact with the vessel wall during expansion, and generated much less dilation than invagination [67]. Passive extravasation of microbubbles is inefficient; however, when coupled with the presence of ultrasound, efficiency is increased. Once extravasation has occurred, it is thought that the expansion and contraction of microbubbles near a cell, causing cavitation streaming, can enhance US-mediated intracellular drug delivery.

Drug transport into cells normally occurs by diffusion, namely the movement of drug molecules driven by a gradient in their concentration, which suffers from limited drug penetration into tissue. In the case of microbubbles, different mechanisms have been associated with increased cellular drug uptake, including: (i) hyperpolarization of the membrane leading to endocytosis of external macromolecules, (ii) potential exchange or fusion of the phospholipid MB shell with the phospholipid bilayer of a cell membrane, (iii) activation of membrane pathways that allows the movement of molecules between the inside and the outside of the cell, and (iv) sonoporation (i.e. formation of transmembrane pores) [43] [28].

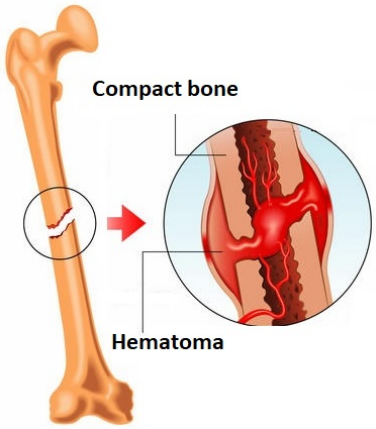

Figure 1.13: *In the early stages of a fracture, haematoma occurs. Fractures are usually associated with damaged blood vessels, favouring the extravasation of blood and potentially of drug carriers. [68]*

The ultimate aim of this research is to deliver US-responsive carriers to bone fractures, in order to release drugs at the point of treatment and enhance the bone healing process. Extravasation at a fracture site is enhanced thanks to the local characteristics of the bone vasculature. Firstly, bone is a highly perfused tissue as it receives between 5.5 and 11% of the cardiac output [69]; thus, administration of carriers through the bloodstream represents a suitable delivery route. Secondly, skeletal vessels are fenestrated with a pore size up to 80 nm. Furthermore, fractures in their early stages are usually associated with locally damaged vasculature and haematoma; the presence of discontinuities in the blood vessel wall thus leads to enhanced extravasation of blood, as shown in Figure 1.13. It is therefore hypothesised that it would lead to the extravasation of systemically injected microbubbles (of micron or sub-micron diameters), and their passive accumulation at the fracture site. Notably, a previous

work by Wang et al. [70] showed passive accumulation of functionalised nanoparticles with a size range of 40-70 nm at a fracture site in mice, demonstrating the feasibility of the aforementioned aim.

1.3.3 Production of Microbubbles

Microbubbles can be produced by using different processes that can mainly be divided into two major categories based on the physics of formation: stochastic and deterministic approaches. Stochastic methods result in the generation of a highly concentrated suspension of stable microbubbles; however, they are limited in their ability to control the MB size. Consequently, the MB size distribution is relatively broad. On the other hand, deterministic-based methods allow controlling the size of the produced bubbles by adjusting the boundary conditions and the geometry of the device used, as well as the physical and chemical properties of the fluids. The main drawback of such methods is that the final MB concentration is relatively low, and devices suffer from limited lifetime. There are also some additional methods that lie in between these two categories [71].

Sonication and mechanical agitation

One of the most commonly used methods to produce microbubbles is sonication, which is a mechanical agitation method also known as emulsification. In this process, a hydrophobic phase (generally a gas) is dispersed within an aqueous surfactant solution, by using high-intensity ultrasound (in the frequency range 20-25 kHz). The production process is often divided into two steps. Initially, a first sonication of the solution is performed to destabilise the air-water interface and to induce cavitation within the fluid of the gas bubbles that are forming due to the low pressure. Such instability allows large gas bubbles to form into the liquid solution. Secondly, a further sonication favours cavitation of the pre-formed large bubbles, which then divide into microbubbles.

The final size of the produced microbubbles depends on several factors, such as frequency, power and pulsation regime of sonication. The final MB size distribution obtained is broad, typically ranging from 1 to 10 μm, and the shell thickness is variable. At present, there are no established means to control the size using this production method. Before using these microbubbles for intravascular biomedical applications,

filtration is required to remove any bubble greater than 10 μm in diameter [72].

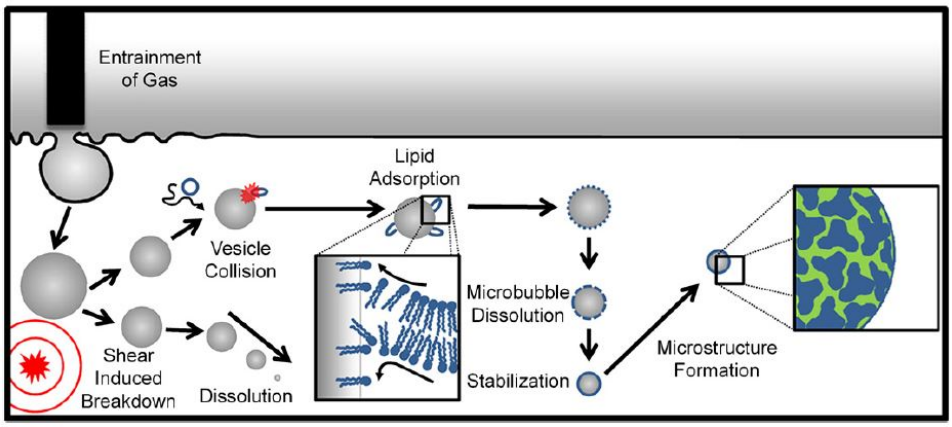

Figure 1.14: *Process of production of lipid-shelled microbubbles by sonication. Reprinted from [73], with permission from Elsevier.*

In the case of lipid-shelled microbubbles, the process is outlined in Figure 1.14. A first sonication is used to disperse the lipids; in this process, multilamellar vesicles (MLVs) form small unilamellar liposomes (SUVs). During the second sonication, unshelled gas microbubbles form at the liquid-gas interface and they collide with the SUVs in suspension. Provided that the inertia of the collision is high enough, then the liposome shell immediately adsorbs at the gas-liquid interface of the bubbles. The newly established surface tension helps liposomes to unravel their structure and spread their lipid molecules on the shell of the microbubble. Lipid molecules previously packed in bilayers can now organise to form a monolayer coating; the lipid shell of the microbubble is thus formed thanks to the adsorption of lipids. The hydrophobic acid tails of phospholipids spontaneously orient to face the gas core. The process of adsorption continues while counterbalanced by the dissolution of the bubble driven by the Laplace pressure (discussed in Paragraph 1.3.5) until an equilibrium is reached. Lipid molecules are now packed together providing stability to the newly formed lipid-shelled microbubble [73] [52].

Thanks to the convenient trade-off between cost, the rate of MB production and MB size dispersity, sonication was the chosen production method for this project.

Laser ablation

The laser ablation method is based on chemical reactions. A solid aluminium surface is placed into a container filled with water and is subject to an ultraviolet laser with a wavelength λ of 248 nm. A chemical reaction takes place between the aluminium of the surface and the oxygen dissolved in water: aluminium oxidises and creates Al_2O_3 nanoclusters. Simultaneously, during the process, some unshelled bubbles at the upper gas-water interface are created. Bubbles and nanoclusters merge and this process allows stable microbubbles to be obtained. This method is stochastic, thus the MB size distribution cannot be controlled [71].

Forced extrusion methods

In this process, the components used to create microbubbles (i.e. gas, surfactant in liquid, lipids or proteins or polymers) are forced one or more times through a porous membrane with a set stiffness and wettability. Gas bubbles are formed in the solution, and are stabilised due to the addition of emulsifiers. Different parameters influence the process, among them the shear stress applied over the bubbles imparted by the fluid flow, the buoyancy force and the surface tension of microbubbles, the flow velocity, the emulsifier used, the transmembrane pressure drop, the porosity and chemical/mechanical properties of the membrane. Some of these characteristics can be controlled to obtain the desired bubble size. For example, if a hydrophilic membrane is used, it is more likely that microbubbles produced have a smaller size because they detach more rapidly from the membrane itself. Conversely, hydrophobic membranes are associated with the production of larger bubbles with a broad size distribution, since the good wettability of the gaseous phase to the hydrophobic surface causes bubble coalescence before detachment of the bubbles from the membrane surface [42] [71].

Template layer-by-layer deposition

Layer-by-layer (LbL) deposition is a process that can be used to create polymeric-coated microbubbles with very controlled size distribution. In this process, polymeric beads are used as a sacrificial template for the core of the microbubble. Polymers with an opposite charge with respect to the beads can be adsorbed on the surface of the beads resulting in the formation of multilayers of polymers, due to strong

electrostatic interactions among the anionic and cationic components. These layers of polymer represent the shell of the resulting bubbles. After this first phase of the process, internal beads are chemically removed by using strong acidic solutions, leaving a hollow shelled microbubble. Whilst the size of the microbubbles can be finely controlled with this method, microbubble stability is relatively low because the multilayer polymer shell has low mechanical properties: the structure easily collapses upon a small shear stress or bending force [71].

Coaxial electrohydrodynamic atomisation

Coaxial electrohydrodynamic atomisation (CEHDA) is an evolution of conventional electrohydrodynamic atomisation. In the latter, electricity is used to create a jet of liquid that breaks up and creates bubbles. In CEHDA, two immiscible fluids are used to create a coaxial jet that is then atomised to create uniform bubbles. To produce microbubbles, two needles are used to supply gas and a suspension of the coating material, respectively, then a high electrical potential difference is applied between these two needles and an earthed ringed electrode positioned below. This method offers good size control of MBs, but the production rate is limited [42].

Microfluidic devices

Microfluidic devices are used to achieve superior control over the size of MBs, by tuning the hydrodynamic boundary conditions (such as pressure and flow rate). Devices have an orifice where a jet of gas comes into contact with one or more streams of liquid. At a set point from the orifice, the interface between the gas and the liquid becomes unstable, and this results in the break-up of gas bubbles. There are two main types of microfluidic devices, namely flow focusing systems produced using soft lithography techniques and mechanically assembled units composed of capillaries inserted in a polymeric matrix to form a T-junction. The limitations of microfluidic devices are connected to their low production rate and low device lifetime [42].

1.3.4 Microbubbles for Drug Delivery

Microbubbles can also be used as drug delivery agents, since they can be loaded with drugs. The drug delivery action is enhanced by the MB responsiveness to US

waves. It was suggested that MB shell shedding could play an important role in the release of a therapeutic payload: during the compression phase of the oscillation of MBs, the surface area reduces and this leads to an oversaturation of the lipid shell material resulting in the shedding of lipid material and - potentially - the release of drugs [45] [74]. Thanks to their echogenic properties, MBs could also be visualised and their acoustic activity monitored during treatment. MBs can be described, then, as theranostic agents since they combine diagnostic and therapeutic activities thanks to their ability to be imaged and deliver drug.

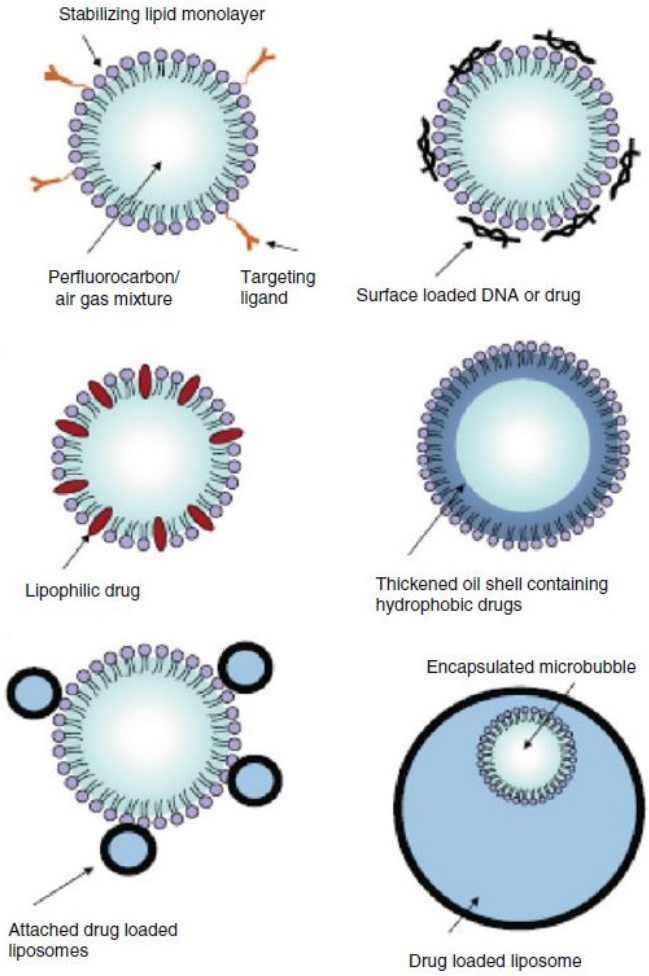

Figure 1.15: *Drugs can be loaded onto microbubbles in different ways. For instance, they can be linked to the external shell, embedded within the shell itself, or inserted in a layer of oily material located between the gas core and the lipid shell. [43]*

Figure 1.15 shows the main alternative methods available to load microbubbles

with drugs. The choice of a loading method depends on the chemical characteristics of the drug. Drugs can be connected to the outer surface of microbubbles either directly, thanks to electrostatic interactions, or indirectly by using ligands (mainly antibodies or short peptide sequences). When drugs are on the external surface, it is fundamental to ensure that their bioavailability and biological activity are not compromised due to the unwanted interaction with blood constituents. Hydrophobic drugs can be incorporated into the lipid shell or possibly even placed in an oil layer between the gas core and lipid shell. Another alternative is to load drugs into nanoliposomes, and attach them to the outer MB surface via modifications to the PEGylated lipid. This strategy is particularly convenient for delivering hydrophilic drugs because liposomes have aqueous cores suitable for loading hydrophilic drugs. Alternatively, a recently developed procedure allows the creation of giant liposomes with a diameter of around 5 µm, which can then be encapsulated with both drugs and microbubbles in the liposome core. This technique allows the potential delivery of a large amount of drug for each liposome; however, being so large their biodistribution may be limited and their therapeutic effect must be assessed [43] [75].

1.3.5 Stability of Microbubbles

It is possible to refer to a microbubble suspension as an emulsion, namely a mixture of two or more liquids in which one is present as droplets, of microscopic or ultramicroscopic size, distributed throughout the other. Emulsions are not always thermodynamically stable and their instability can be related to different physical phenomena, including Ostwald ripening, coalescence, and collapse [76].

Ostwald ripening, also known as disproportionation, isothermal distillation, or molecular diffusion, is governed by the Epstein-Plesset law and the Laplace pressure [77]. An emulsion comprises two different phases: a dispersed phase (i.e. the gas bubbles) and a bulk phase (i.e. the solution in which bubbles are suspended). The solubility of the gas contained in bubbles is inversely proportional to the radius of curvature of the bubbles themselves. As a consequence, the gas contained in smaller bubbles usually dissolves into the bulk phase. This creates local areas of supersaturation in the fluid, which consequently drive the gas into larger bubbles. The whole process does not need the bubbles to be in contact with each other, as it relies on the transport of dissolved matter through the dispersion solution.

The rate of ripening can be explained as the velocity of change in the cube of the average radius of a bubble with time, and it is directly proportional to the Laplace pressure. The Laplace pressure, also known as Young-Laplace pressure, describes the relation between the equilibrium pressure across the membrane of a bubble, the surface tension, and the radius of the bubble. This relation relies on the assumption that a thin spherical membrane containing a fluid, that can either be gas or liquid, is under pressure. Since the pressure of the gas core is higher than the pressure acting on the membrane from the outside, the volume of the bubble tends to increase and this is balanced by the surface tension that applies a force acting from the outside towards the centre of the bubble, keeping it in a spherical shape. To analyse the equilibrium of forces acting on the bubble, consider one half of the sphere (referred herein as a 'semi-bubble'). It is known that the internal pressure is higher than the external pressure, so there is a force (ΔP) acting on the external surface of the semi-bubble and pointing outwards, as shown by Figure 1.16.b. The force vectors are in a direction normal to the surface. By projecting all vectors in a XY plane, it can be observed that all the horizontal components of the force cancel out; the only active forces are the vertical components of the pressure force ΔP, and these are acting on the cross-sectional area of the bubble and they point upwards. Simultaneously, the surface tension is acting on the perimeter of the semi-bubble and it points downwards, as shown in Figure 1.16.c [78]. In the case of lipid-shelled microbubbles, a typical value of surface tension is around 25 mV/m [73].

Equation 1.3.1 and Equation 1.3.2 show the upward and downward forces, and Equation 1.3.3 shows the Laplace pressure.

$$F_{up} = \Delta P \pi R^2 \tag{1.3.1}$$

Where ΔP is the pressure acting on the semi-bubble surface and πR^2 is the area of the semi-bubble surface with radius R.

$$F_{down} = \gamma 2\pi R \tag{1.3.2}$$

Where γ is the surface tension acting on the perimeter of the semi-bubble and 2πR is the perimeter of the the semi-bubble with radius R. The Laplace pressure is finally obtained by defining that the upward forces are equal to the downward forces. By readjusting the equation, the following is obtained:

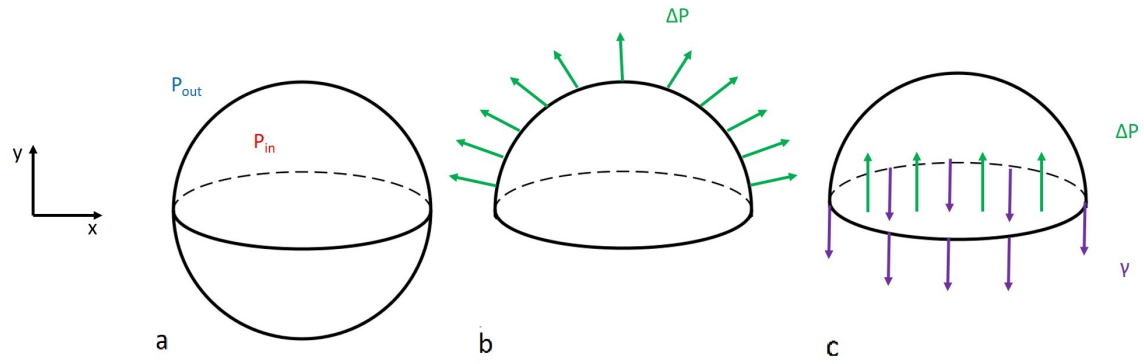

Figure 1.16: *Equilibrium of forces in a bubble. a) In a bubble there is a pressure acting from the inside of the bubble, and one acting over the external surface. b) The pressure within the bubble is higher than the one acting on the outside, hence the net pressure acting over the microbubble shell surface points outward. By considering half of the shell, it can be inferred that the horizontal components of the net pressure cancel out. c) The remaining vertical components of the net pressure act on the cross-sectional area of the bubble pointing upwards, and they are counterbalanced by the surface tension of the shell acting on the perimeter of the semi-bubble and pointing downwards.*

$$\Delta P = \frac{2\gamma}{R} \tag{1.3.3}$$

The smaller the radius of the bubble, the higher the ΔP, hence smaller bubbles have a higher Laplace pressure and are less stable; thus, the gas tends to diffuse out of the small bubbles until it's fully dissolved and diffuses into the larger ones. This leads to an overall increase in the average size of the bubble suspension and to an overall decrease in the number of bubbles. The Epstein-Plesset theory highlights that the dissolution of bubbles accelerates with the radius reduction; thus, a bubble is expected to dissolve quickly when dissolution starts. A model was developed describing the dissolution rate of a bubble without a shell, due to the gas diffusion process (within a steady degassed solution) [73]. Equation 1.3.4 shows how the MB radius changes with respect to time:

$$-\frac{dR}{dt} = H\frac{1 - f + \frac{2\sigma}{P_a}R}{1 + \frac{4\sigma}{3}P_a R}\left(\frac{D_w}{R} + \sqrt{\frac{D_w}{\pi t}}\right) \tag{1.3.4}$$

where R is the radius of the bubble, H is the Ostwald coefficient (i.e. a coefficient expressing the gas solubility), f is the ratio of partial pressure of the solution with

respect to the pressure at gas saturation, σ is the surface tension at the bubble-water interface, P_a is the ambient pressure, and D_w is the diffusivity of the gas investigated in the medium. Borden et al. added a term to this expression, to account for the resistance to mass transfer offered by a monolayer shell. Equation 1.3.5 is the final adapted Epstein-Plesset equation they derived:

$$-\frac{dR}{dt} = \frac{H}{\frac{R}{D_w} + R_{shell}} \frac{1 - f + \frac{2\sigma}{P_a}R}{1 + \frac{4\sigma}{3}P_a R} \tag{1.3.5}$$

where R_{shell} is the mass transfer resistance of the shell. In lipid-shelled microbubbles, the Laplace pressure favours the dissolution of the bubble until the lipids are fully condensed and packed together. During the packing of the membrane, the surface tension γ diminishes, and reaches a point where it can be considered negligible. At this point, dissolution stops and the bubble can be considered stable from the point of view of the gas core [79] [80]. As gas molecules dissolve, they release free energy; a portion of this free energy is used to pack the lipid shell and part of it is stored in the compression state of the shell. The stored free energy is the cause of the dissolution of the bubble driven by the lipid molecules; indeed, the system tends to reach a thermodynamic equilibrium by using the free energy to make lipids desorb from the shell and reform liposomes in the solution surrounding the microbubbles [52].

Besides Ostwald ripening, coalescence can occur when two bubbles are in contact with each other and their membranes break, resulting in two smaller bubbles merging and creating a larger one. Usually, coalescence is the dominant physical phenomenon in an emulsion where bubbles are not shelled.

Lipid encapsulation can be used to decrease both surface tension and gas dissolution. Generally, surface tension enhances dissolution since it both increases the Laplace pressure and decreases the number of gas particles reaching the gas-liquid interface by reducing the interfacial area. If the surface tension of a bubble is too low, then the membrane is compressed above the equilibrium and this can result in the collapse of the membrane. Firstly, buckling occurs and microscopic folds appear. These microscopic folds then merge to create macroscopic ones, finally resulting in the collapse of the bubble [73].

As a whole, short-term stability is mainly influenced by coalescence while long-term

stability is predominantly affected by Ostwald ripening [81]. Generally, bubbles are considered to be stable when two conditions are fulfilled: (i) the solution in which they are dispersed is fully saturated, and (ii) the surface tension is low.

The stability of MBs *in vivo* is further influenced by clearance mechanisms caused by two phenomena: dissolution and phagocytosis. Once injected into the bloodstream, MBs exchange their gas core with dissolved gases found in the blood, mainly N_2, O_2 and CO_2, until they reach an equilibrium at which point they will have undergone complete dissolution. Phagocytosis, on the other hand, has been observed to occur primarily in the lung, liver and spleen. Interestingly, phagocytosed microbubbles are more stable against dissolution than freely circulating microbubbles, potentially due to the more regulated gas composition in the surrounding cell microenvironment [44].

1.4 Phase-shift Nanodroplets

Nanodroplets (NDs) are an alternative to the use of microbubbles. The main differences between microbubbles and nanodroplets lie in their size and composition. Microbubbles are gas-filled spherical particles with a mean diameter ranging between 3-10 μm, while nanodroplets are liquid-filled spherical particles with a smaller mean diameter of about 100-500 nm [43]. Microbubbles and nanodroplets are related systems, as phase transition can occur between the two forms. Following an increase in temperature or upon ultrasound stimulation, the liquid core of NDs vaporises and this phase transition leads to the formation of gas-filled MBs. Nanodroplets are at least five times smaller than the microbubbles resulting from their phase transition. Unlike microbubbles, which have a circulation time of minutes (half-life < 5 min [44]), nanodroplets have a half-life in the order of 2-6 hours for imaging applications [82].

Since microbubbles are relatively large, they experience only very limited extravasation when administered *in vivo*, which in turn hinders their ability to penetrate within a target tissue. Using nanodroplets as an alternative to microbubbles provides not only enhanced extravasation, but also increased stability to pressure and mechanical stress imparted by the blood flow. Nanodroplets are also more stable against dissolution in blood. Due to high acoustic impedance, both PFP droplets and bubbles manifest echogenic properties; however, the main drawback of nanodroplets with respect to microbubbles is that they manifest much lower echogenicity than bubbles, resulting in weaker US contrast. This is usually overcome by using a suspension containing both

nanodroplets and microbubbles. Co-administration of microbubbles and nanodroplets could also promote ND extravasation. Indeed, when microbubbles are stimulated with ultrasound, their response could further enhance extravasation of nanodroplets and lower their vaporisation threshold [83] [65].

Nanodroplets are currently being studied for a range of different applications, among these: embolotherapy, gene delivery, enhanced thermal ablation, phase aberration correction, targeted drug delivery, ultrasound imaging, theranostics, thermal therapy, and histotripsy [84] [85].

The composition of nanodroplet shells are comparable to the ones used for microbubbles, while many different perfluorocarbons have been used as suitable cores. Examples from the literature, with their phase transition temperatures, are summarised in Table 1.2. Phillips et al. [82] and Kawabata et al. [86] also showed that the phase transition temperature and stability can be modulated by mixing of different perfluorocarbons.

Table 1.2: *Main perfluorocarbons used as core for nanodroplets with their abbreviation, chemical formula and transition temperature. [87]*

Name	Abbreviation	Chemical formula	Phase transition temperature
Octafluoropropane	OFP	C_3F_8	-36.7°C
Decafluorobutane	DFB	C_4F_{10}	-1.7°C
Perfluoropentane	PFP	C_5F_{12}	29°C
Perfluorohexane	PFH	C_6F_{14}	56.6°C
Perfluoroheptane	FC84	C_7F_{16}	80°C
Perfluorooctane	PFO	C_8F_{18}	101°C
Decafluoropentane	DFP	$C_5H_2F_{10}$	55°C
Perfluoro(2-methyl-3-pentaone)	PFMP	$C_6F_{12}O$	49°C
Perfluoro-15-crown-5-ether	PFCE	$C_{10}F_{20}O_5$	146°C

Nanodroplets are an active area of study, and there are still some open questions representing a barrier to clinical translation. On one side, it is still not known which are the best chemicals to use for shell and core to enhance stability and efficacy; on the the other side, there are still discrepancies between *in vitro* and *in vivo* results and vaporisation *in vivo* is more difficult to achieve. More *in vivo* studies of nanodroplets are needed [88].

The perfluorocarbon chosen for this work is PFP since it has a phase transition

temperature just above ambient temperature (29^{o}C), meaning that it is in its liquid phase at ambient temperature. Once in the droplet configuration, its phase transition temperature increases, as explained in Paragraph 1.4.1, and it can be vaporised at relatively low mechanical indices in the diagnostic range (MI $<$ 1.9 as approved by FDA for diagnostic imaging; the mechanical index being a measure of acoustic power defined as the peak negative acoustic pressure in MPa over the square root of the frequency in MHz) [89] [90]. The lipid shell chosen for this work is composed of DSPC and PEG40s in a molar ratio 9:1, which is the same lipid composition used for the microbubbles studied here, allowing direct comparisons between the two formulations.

1.4.1 Nanodroplets Response to Ultrasound

Once NDs have reached the site of interest, they can be converted into microbubbles either by increasing the local temperature or by stimulating them with ultrasound. By using one of these two forms of energy, the liquid perfluorocarbon core vaporises and microbubbles are formed. By selecting the appropriate PFC core, it is possible to control the ultrasound properties or temperature needed to promote phase transition.

As a matter of fact, the boiling point of nanoscale particles is related to the acoustic energy required to vaporise them. The Clausius-Clapeyron Equation (1.4.1) shows that the phase-transition temperature is inversely proportional to the pressure exerted on the particle itself.

$$\frac{\mathrm{dp}}{\mathrm{dT}} = \frac{\mathrm{L}}{\mathrm{T}\Delta\mathrm{V}} \tag{1.4.1}$$

In the equation, p is the pressure acting on the shell of the particle, T is the temperature, L is the specific latent heat and V the specific volume change during phase transition. The smaller the droplet, the higher the phase transition temperature [91] [92]. Figure 1.17 shows the relationship between droplet diameter and vaporisation temperature for droplets with different interfacial energy. The droplets that will be used in this study have a lipid shell composed of DSPC and PEG40s, they have a mean diameter smaller than 1 μm and they display an interfacial energy around 25-30 mN/m; hence, their phase transition temperature is predicted to be around 70^{o}C, as shown by the red line in the graph. The bigger the ND, the easier it is to obtain phase transition since lower temperatures and pressure magnitudes are needed. Given a normal distribution of NDs size and at low pressures, the upper tail of the size

distribution will be subject to most of the droplet vaporisation activity, with very little activation of smaller droplets [93] [65].

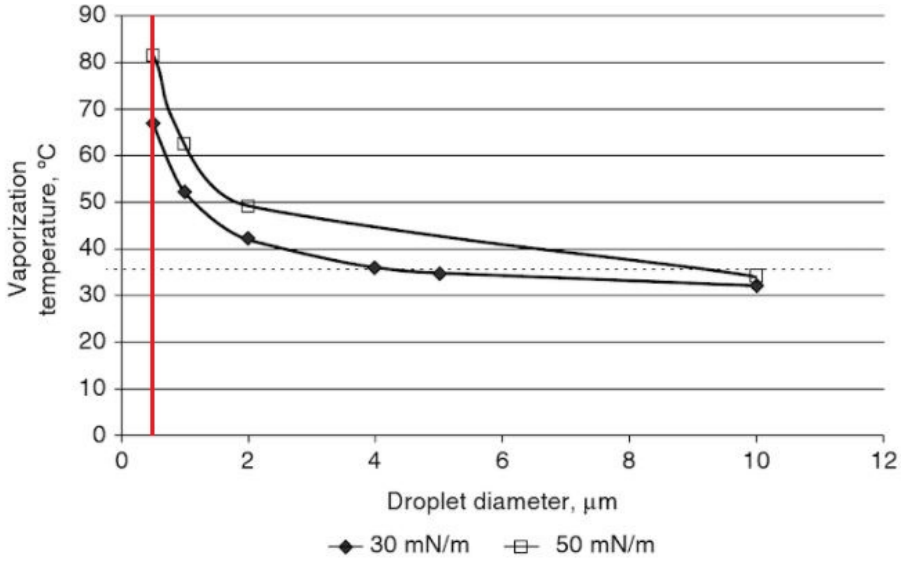

Figure 1.17: *The graph shows how the phase transition temperature of PFP droplets changes according to the droplet size, for two different values of interfacial energy, namely 30 and 50 mN/m [43]. The red line indicates the approximate size range of NDs produced in this study*

The transition from nanodroplet to microbubble due to US is referred to as 'acoustic droplet vaporisation' (ADV) and depends on the vapour pressure (or boiling point) of the liquid core, which is a function of temperature. The vapour pressure is defined as the pressure exerted by a vapour in thermodynamic equilibrium with its condensed phases (solid or liquid), at a given temperature and in a closed system. It can be visualised as the pressure of solid or liquid molecules trying to transition into the gas phase. When the pressure of the fluid is higher than the vapour pressure, the fluid remains in a condensed form; but when the pressure of the surrounding fluid is lower, then a phase transition of the inner fluid into gas occurs. ADV occurs because of the effect of acoustic waves on the local fluid pressure. In nanodroplets, Laplace pressure is also present due to surface tension, and this increases the vapour pressure. When a sound wave is applied to a solution containing nanodroplets, it generates a pressure wave (comprising compression and expansion phases) in the fluid. In the expansion phase of the wave, the pressure of the surrounding fluid decreases; when it becomes lower than the vapour pressure, transition to MBs can occur [94].

In addition to having a surrounding pressure lower that the inner vapour pressure

of the liquid core, a nucleation event is also required to trigger ADV. When a liquid remains in its liquid state, even when the temperature is above their boiling point, it is called 'superheated'. For phase transition to occur, the formation of a nanoscopic cavity of gas is needed and its appearance is random and stochastic, with an activation energy barrier that is related to the amount of superheating and the interfacial energy of the gas-liquid boundary. The gas nucleation site can develop in three different areas: in the core of the droplet, adjacent to the surfactant shell (either inside or outside of the droplet) or external to the droplet within the bulk fluid phase in the direction of US propagation. If MBs are present in the surrounding fluid of NDs, their cavitation can act as an external nucleation site and trigger phase transition [94].

Usually, the distance between the transducer used to stimulate NDs and the sample itself is in the order of few cm and this can cause distortions in the US wave due to nonlinear propagation. These distortions can create ultraharmonics with wavelengths of the order of the droplet size. The presence of ultraharmonics, together with the spherical shape of the droplet, give rise to a focusing of the wave on a specific spot inside the droplet, which can become a nucleation site of ADV [95]. Focusing is also due to the fact that the speed of sound in perfluorocarbon liquids is significantly lower than that in water or tissue, the acoustic mismatch leads to refraction of the incident wave at the interface between these fluids, and the spherical shape of the droplet gives rise to wave focusing. This interpretation has been validated with experimental data showing positions of the nucleation spots captured with an ultrahigh-speed camera. The combined effects of non-linear propagation and diffraction lead to an amplification of the peak negative pressure in the micrometer-sized droplet, which triggers droplet vaporisation [96].

Three different phases can be observed during vaporisation. Before the appearance of the nucleation site, shape deformations and oscillatory translations of the droplet appear. The second phase is characterised by the creation of the first nucleation site and by perturbations due to successive vaporisation and condensation cycles driven by the applied ultrasound. Finally, the third phase is a continued growth of the vapour bubbles obtained [85].

After vaporisation, the resulting MB is in theory approximately 5 times bigger than the original ND; therefore, a 500-nm diameter droplet would generate a 2.5-μm bubble upon complete vaporisation. Larger MBs appear too, and these are secondary bubbles developing due to different phenomena like: coalescence between newly formed MBs

or between MBs and NDs, and diffusion of dissolved air from small bubbles into larger bubbles (i.e. Oswald ripening) [49]. Ostwald ripening may also play a predominant role in gel or solid matrices, where droplet and bubble diffusion and collisions are restricted or stalled. The expansion is, hence, hard to control and some bubbles may become larger than expected. After vaporisation, larger MBs usually survive in their new state, while sub-micron agents may recondense back to the liquid state [93].

1.4.2 Interaction between NDs and Biological Systems

Blood vessels in normal tissues have tight interendothelial junctions, which do not allow extravasation of nanoparticles. When ultrasound is applied, it generates local tissue heating that leads to modifications of the biological environment; of particular interest are increases in the permeability of blood capillaries and vasodilation. In addition, ultrasound creates shear stress, which may open inter-endothelial cell gaps. Acoustic streaming and radiation force (already presented in Paragraph 1.3.1) can also force nanoparticles through blood capillary walls, thus enhancing extravasation of drug carriers [89] [65].

1.4.3 Production of Nanodroplets

In a similar way to microbubbles, nanodroplets can be produced with both stochastic and deterministic methods. Stochastic approaches result in the generation of a highly concentrated suspension of nanodroplets; however, they are limited in their ability to control the uniformity of the batch size. As a consequence, size distribution of NDs produced with this method is relatively broad. To overcome this, sometimes size-separation techniques are used in combination; however, they present high variability in size reduction, and often require differential centrifugation, which adds time to the manufacturing process and is challenging to execute at scale. On the other hand, deterministic-based methods allow control of the ND size by adjusting the boundary conditions and the geometry of the device used, as well as the physical and chemical properties of the fluids. The main drawback of such methods is that the final ND concentration is relatively low, and devices suffer from limited lifetime. So far, each of these methods is technically challenging and has its own weaknesses [97].

Sonication and mechanical agitation

Nanodroplets are normally produced via sonication or high speed mechanical agitation in the presence of a liquid perfluorocarbon, that forms the ND liquid core. Batches produced in this way normally display a broad size distribution. Furthermore, both agitation and sonication techniques can cause the emulsion to heat up. Careful consideration of the temperature sensitivity of the droplet structure and the encapsulated therapeutic is thus required with this method.

When sonication is used, a hydrophobic phase is dispersed within an aqueous surfactant solution, by using high-intensity ultrasound (in the frequency range 20-25 kHz). Using a tip sonicator is a simple and popular approach, but can be compromised by cross contamination between samples and the introduction of metallic particulates into the emulsion as the tip erodes with use [88].

During sonication, cavitation bubble alternatively undergo contraction and dilatations and are broken-up by the successive implosions. The fragmentation of the PFC droplets gradually decreases their average diameter [98].

Microfluidic devices

To achieve a narrower ND size dispersity, the use of microfluidic devices has been investigated. These devices allow control of the ND size by regulating gas pressure, liquid flow rate and device geometry; their main drawback is the low rate of production when compared to sonication.

To generate smaller droplets, a first approach involved reducing the microfluidic channel size to the nanometer range. When the channel dimension is reduced to the submicron range though, the device is relatively difficult to fabricate and is likely to be clogged by impurities. The second approach was to use microfluidic systems to generate monodisperse precursor microdroplets and then convert them into nanodroplets by condensation or solvent evaporation. Another strategy to make droplets in the submicron range is to form a tip-streaming (thread forming) mode in a flow-focusing configuration, in which the formed droplet size is not limited by the minimum feature size of the microfluidic channels. In the tip-streaming phenomenon a very thin thread is pulled from the tip and breaks up into a series of tiny droplets that are one order of magnitude smaller than the primary thread. Furthermore, increasing the viscosity of the continuous phase through the addition of glycerol greatly enhanced

the ability to drive droplet production stably in the sub-micrometer regime at high pressures [99] [100].

Condensation

Nanodroplets can also be produced from microbubbles by condensation: through a combination of decreased environmental temperature and increased environmental pressure it is possible to turn MBs into NDs. The reduction in size to the nanometer scale increases the Laplace pressure that then stabilises the droplets against re-expansion until an external trigger, such as US or heat, is applied [87] [101].

It is hypothesised that during condensation, the monolayer lipids may fold into bilayer strands on the surface of the droplet, which then goes back to be a monolayer after vaporisation [102].

Micelles

A different approach to the generation of drug-loaded PFC nanodroplets was suggested in the works by Rapoport's group [89]. Here, drug-loaded polymeric micelles were used as a precursor for generating nanoemulsions. The simplicity of manufacture, absence of toxic solvents and increased drug loading capacity are attractive features of this technology. In addition, amphiphilic block copolymer micelles (if they are present in the formulation) may exert relevant biological effects by preventing development of drug resistance.

Polymeric micelles are formed by self-assembly of individual amphiphilic block copolymer molecules (unimers) in a liquid medium. Hydrophobic blocks form micelle cores, while hydrophilic blocks (usually PEG) form micelle shells. PEG shells are important for suppression of nanodroplet uptake by reticuloendothelial system cells. Lipophilic drugs are often solubilised in the micelle core. However, micelles on their own are limited by their short stability.

To produce nanodroplets, a PFC compound is then introduced into the micellar solution, as shown in Figure 1.18. At low concentration, PFC is dissolved in the micelle core (Figure 1.18, zone 1). When the PFC concentration exceeds a limit of solubility in the micelle core, nanodroplets transition into a separate phase. In some ranges of PFC/copolymer concentration ratios, micelles coexist with nanodroplets (Figure 1.18, zone 2). In this process, former micelle cores turn into droplet shells. A

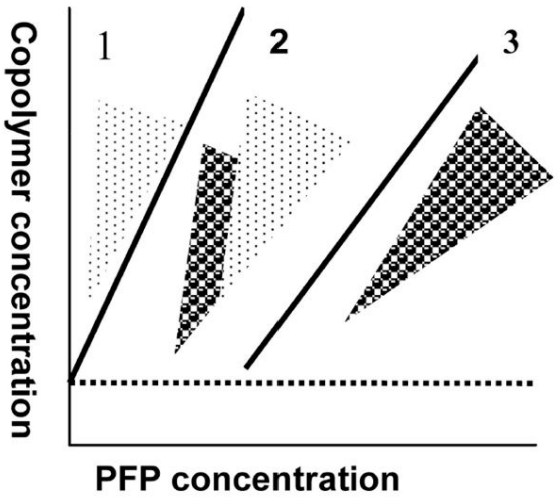

Figure 1.18: *Schematic representation of a phase diagram of a micelle/nanoemulsion system. In zone 1, micelles are present with dissolved perfluoropentane; in zone 2 there is a coexistence of micelles and nanodroplets; in zone 3 only nanodroplets are present. Reprinted from [103], with permission from Elsevier.*

nanodroplet shell contains two layers: the inner layer, formed by a hydrophobic block of a block copolymer, and the outer layer, formed by a hydrophilic block, usually PEG, as shown schematically in Figure 1.19. A lipophilic drug initially encapsulated in micelle cores moves with the hydrophobic block into the inner layer of a droplet shell.

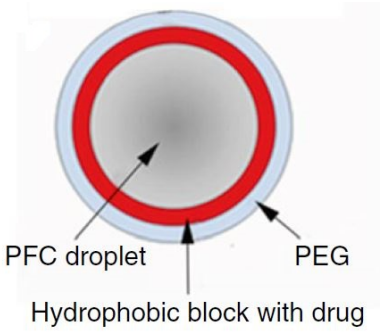

Figure 1.19: *Schematic representation of a drug loaded ND. Reprinted by permission from [89]*

As PFC concentration increases, the whole block copolymer is used for droplet stabilisation and micelles disappear; only droplets are observed in this phase (Figure 1.18, zone 3). The droplet size in PFC nanoemulsions ranges from 200 to 750 nm depending on the type of the stabilising copolymer, perfluorocarbon-to-copolymer

concentration ratio and emulsification conditions. The size and number of nanodroplets may be controlled by a copolymer/PFP ratio. As a general rule, for a fixed PFP concentration, the higher the copolymer concentration, the smaller the droplet size; for a fixed copolymer concentration, the higher the PFP concentration, the larger the droplet sizes [89] [103].

1.4.4 Nanodroplets for Drug Delivery

For drug-loaded nanodroplets, pharmaceutical dosage is an important parameter to control. A trade-off between a concentration high enough to provide a therapeutic effect and low enough to prevent toxicity is needed. Size, concentration and loading capabilities need to be optimised and tailored for a chosen specific application, to ensure a safe and effective treatment strategy [88].

Drug delivery is based on two mechanisms. Firstly, after extravasation, US can enhance the contact between the membranes of droplets and cells. This, together with the local increase in temperature caused by US, promotes fluidisation of membranes and fusion between cell membranes and phospholipid coated nanodroplets, which results in drug transfer from nanodroplets into the interior of the cell [89]. Drug uptake may be connected to cavitation-induced effects on cell membrane too. Secondly, upon phase transition, the nanoparticle volume increases, while the thickness of the shell decreases and, as a result, the drug is released from the ND, as shown in Figure 1.20. The process by which the drug is released and taken up by cells is still under investigation. [43] [65] [71]. The stability of bubbles generated from ND vaporisation has not been completely investigated yet, but it's known to be lower than the one of microbubbles obtained directly by sonication [104]. This could be caused by a different quantity and organisation of lipids in the shell. During sonication, lipids reorganise themselves to reach a low energy configuration where they are packed together and stable; during phase transition, NDs expands into MBs and the quantity of available lipids creating the shell could be lower than in pre-formed microbubbles, leading to a lower stability of the structure.

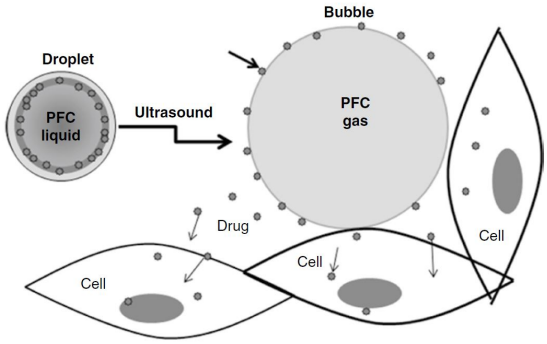

Figure 1.20: *The gas-to-liquid phase transition of perfluorocarbon induced by temperature or ultrasound, leads to the conversion of a nanodroplet into a microbubble. Such transition can also favour the release of drugs and their delivery into cells. [43]*

1.4.5 Stability of Nanodroplets

The stability of NDs can be analysed from two points of view: intrinsic, which solely depends on the ND properties, and extrinsic, which depends on the interaction with the surrounding environment.

As for the intrinsic stability, the size of NDs inhibits the effect of gravitational forces to the benefit of Brownian motion, and induces the predominance of steric stabilisation between droplets. As a consequence, Ostwald ripening is the primary process that can affect ND stability. If the batch presents sufficiently narrow size distribution, this may inhibit Ostwald ripening since the difference in Laplace pressure between the larger and smaller droplets is reduced.

As for the extrinsic stability, when nanodroplets are injected systemically and circulate in the body, they eventually enter the heart through the vena cava, then travel in the pulmonary circulation and back to the heart through the pulmonary veins. They are then conveyed into the arterial circulation through the aorta. Because of the size (typically < 600 nm), NDs do not present risk of pulmonary embolism (which may occur if the particle size is above 10 μm). ND elimination is predominantly performed by the macrophages of the reticuloendothelial system (RES), most notably in the liver and spleen and eliminated in the bile, although very small particles (< 10 nm) are filtered by the kidneys. Before macrophage uptake by phagocytosis, nanoparticles are recognised through opsonisation, by fixation onto their surface of a blood protein called opsonin. Two parameters are known to affect this phenomenon, the size of the particle and the chemical properties of its surface. Indeed, the limit of 100 nm is generally

considered as a threshold for RES recognition, which can also inhibited by adding hydrophilic polymers like polyethylene glycol (PEG) to the surface of the particle. [98] A study by Yarmoska et al. [97] showed that, by increasing the molar ratio of PEG with respect to the other lipid used, it is possible to enhance stability with respect to time and to obtain smaller nanodroplets, which were also more consistent between batches. Their data also showed that the relation between increased lipid shell PEGylation and reduced droplet size is non-linear. It is possible that there is a critical concentration of PEG necessary to achieve sufficient steric stabilisation such that increasing PEGylation further will not have a demonstrable impact on reducing nanodroplet coalescence.

1.5 Acoustic Characterisation of Ultrasound Responsive Agents

The most common methods used to characterise microbubble acoustic behaviour are optical and acoustic. Optical methods allow MB volumetric changes to be observed; however, such analysis requires very high temporal and spatial resolution, and the number of bubbles that can be simultaneously analysed is limited. Alternatively, acoustic methods can be used, which are often more representative of the whole sample response, although with limited resolution. Acoustic methods can be active or passive. Active cavitation detection (ACD) uses a secondary low-pressure pulse to investigate changes caused by a primary pulse [105]. Even if the measurement pulse has lower energy than the stimulating pulse, it can influence the cavitation process, hence this approach is not optimal. Passive cavitation detection (PCD) instead uses a transducer to 'listen' passively to the acoustic emissions of microbubbles without interfering with the MB oscillation. In this study, attention is devoted to the PCD method, as it has been demonstrated to provide more reliable and comprehensive results [106].

1.5.1 Passive Cavitation Detection

Passive cavitation detection (PCD) is a method used to characterise the acoustic behaviour of microbubbles. In this method, microbubbles are stimulated by ultrasound emitted from a transducer, and one or two transducers are employed to passively

detect the acoustic emissions originating from MB cavitation. In the first case, the method is called single passive cavitation detection (SPCD); while in the latter case, it is called double passive cavitation detection (DPCD). The main advantage of DPCD is that it can provide a spatial intensity map of the emissions received.

The oscillation of microbubbles results in the generation of acoustic waves. The detectors record the pressure wave emitted by the cavitating bubbles. These waves bring information about the periodicity and stability of the microbubble response and the pressure recorded is proportional to the second temporal derivative of the volume of the bubble. Consequently, spectral peaks in the pressure emissions are linked to spectral peaks in the volumetric oscillation [107].

When microbubbles are exposed to ultrasound at their resonance frequency, their temporal response can be classified into two different phases. Firstly, while microbubbles are stimulated, they have a primary response that consists of an initial harmonic behaviour: their volume grows and shrinks in response to ultrasound in a periodic way and with a fixed frequency. Secondly, after 1-5 μs from the end of the excitation, there can be a post excitation signal (PES), which is a second broadband response.

A key aspect of the PCD technique is the possibility of determining the threshold between stable cavitation, inertial cavitation, and destruction. Defining MB destruction is challenging, since the term can be associated with different events such as fragmentation, cavitation, rupture and collapse. The ability to distinguish between these MB behaviours is important, as each MB behaviour may lead to different cell stimulation 'regimes', such as microstreaming or jetting. If the acoustic pressure is low, microbubbles oscillate linearly and they emit waves at the stimulating frequency. By increasing the acoustic pressure, harmonics, subharmonics and ultraharmonics appear, and these are characteristics of stable cavitation of microbubbles. In addition, the appearance of broadband noise emissions on the background noise level is indicative of inertial cavitation. An example of FFT spectra showing different MB acoustic behaviours can be found in Figure 1.21: in Figure 1.21.A, a low acoustic pressure was used and only the resonant frequency is present; in Figure 1.21.B, an increase in the acoustic pressure led to the appearance of harmonic components indicating the stable cavitation of MBs; in Figure 1.21.C, a further increase in the acoustic pressure led to the appearance of sub- and ultra- harmonics; finally, in Figure 1.21.D, the broadband noise level increases and the sub- and ultra- harmonic components are suppressed,

indicating inertial cavitation of MBs.

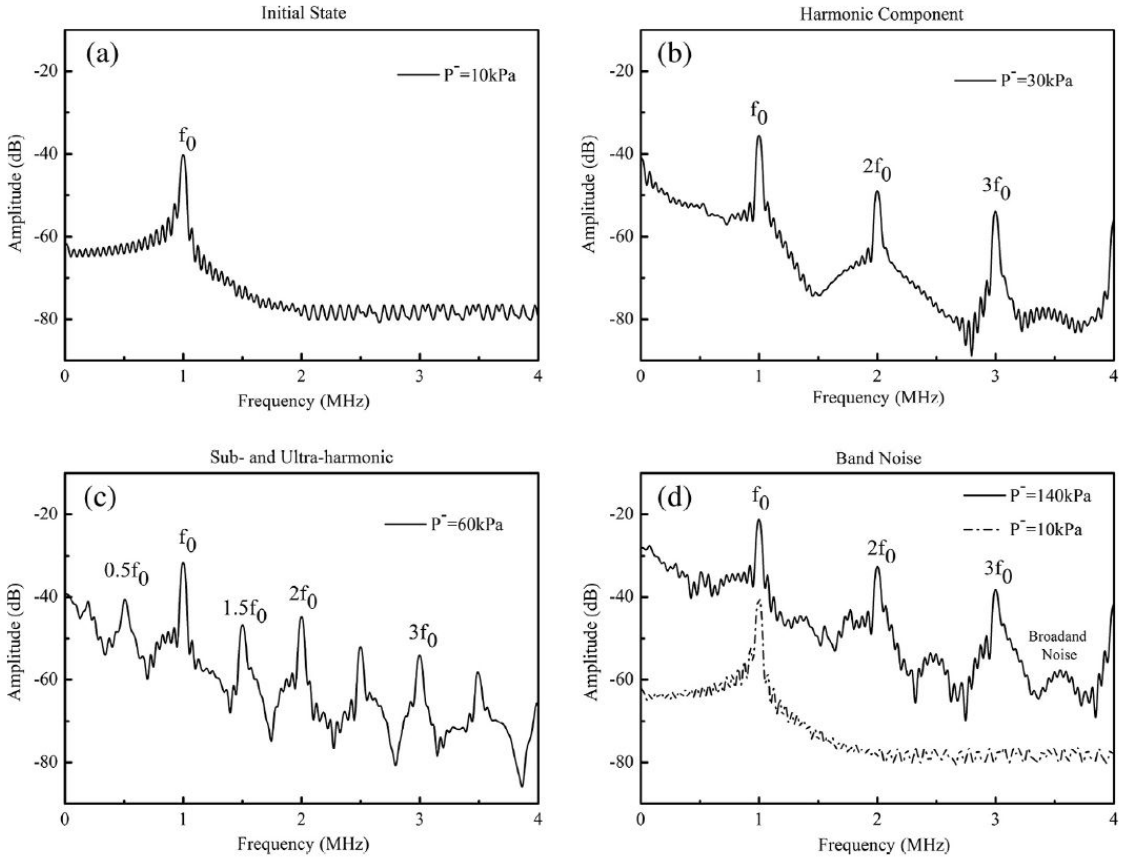

Figure 1.21: *The figure shows some FFT spectra obtained at different acoustic driving pressures connected to different behaviours of MBs. a) Only the driving frequency is present. b) Harmonic components appear indicating stable cavitation of MBs. c) Sub- and ultra-harmonic components appear. d) The broadband noise level increases and the sub- and ultra-harmonic components are suppressed. [108]*

In the literature, there are different methods to determine the threshold at which MBs undergo destruction. Giesecke and Hynynen [109] identified a value for the peak rarefactional pressure amplitude at which the broadband noise emission is greater than one standard deviation above the baseline noise. Chen et al. [110] used the peak rarefactional pressure fulfilling two requirements: the 5% of spikes in the recorded signal are higher than a chosen value, and the signal spectral amplitude increases between harmonics. Chang et al. [111] used the peak rarefactional pressure that destroyed all the microbubbles in the suspension. The main drawback of this approach is that the onset of destruction cannot be easily detected. Ammi et al. [112] analysed the emissions after 1-5 μs from the excitation, rather than the period of the stimulation

itself. These waves are the consequence of inertial cavitation of free microbubbles, and can be easily distinguished from all the other waves. Detecting the first of these waves means identifying the moment when the first shell breaks releasing its gas content, which in turn behaves as a free unshelled bubble. From the moment that the stimulating source is deactivated during detection, there is no additional noise to the signal. A last example is the one proposed by King et al. [106] [113]; who classified signals according to the presence or absence of post excitation signals PES, from the moment that PES is present only if microbubbles are free (i.e. indicating that the shell has been destroyed). However, the opposite does not hold as a bubble can disappear because of gradual diffusion of its inner gas into the suspension, without a sudden rupture.

Once having recorded the pressure emissions, the signals are processed using one of three methods: frequency-domain, time-domain, or time-frequency. The frequency-domain method is the most commonly used, in which a Fast Fourier Transform (FFT) of the spectrum is performed to determine the frequency content. Figure 1.22 shows how it is possible to shift from a time-domain to a frequency-domain to know the content in frequency of a recorded signal. Time-domain analysis is based on the study of the main characteristics of the waveform of the signal detected. Finally, to perform a time-frequency analysis, a short-time Fourier transform is employed (STFT).

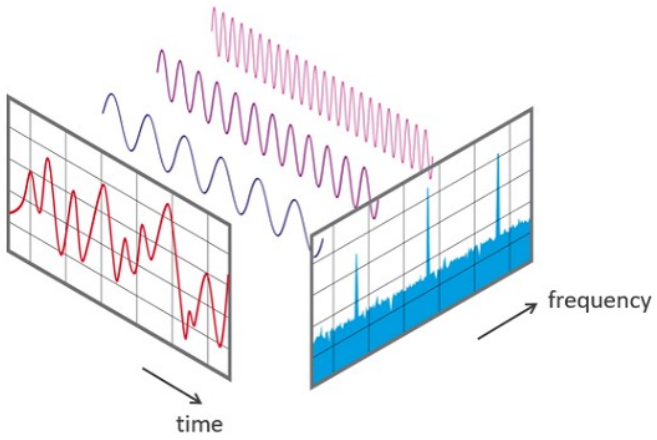

Figure 1.22: *By performing a Fast Fourier Transform (FFT) of a signal, it is possible to transition from the time-domain to the frequency-domain. This allows determining the frequency content of a signal. [114]*

1.6 Imaging

In this project, four different imaging modalities were used to visualise and characterise microbubbles and nanodroplets: bright field imaging, fluorescence imaging, B-mode ultrasound imaging and ultra-high speed imaging.

1.6.1 Bright field microscopy

Optical or light microscopes are devices used to magnify the structures of an object, displaying inherent complexity by using visible light as the source of illumination. The simplest microscopes are composed of a single lens that acts as a magnifying glass allowing magnifications up to 20x; while compound microscopes are composed of different lenses and components and allow magnifications up to 2000x. The four main components are: a light source, a condenser lens, an objective lens and an eyepiece. The condenser receives light rays from the light source and focuses them onto the specimen. Meanwhile, the objective lens forms a real, magnified aerial image of the object in the intermediate image plane. This real image is further magnified by the eyepiece to form the final image [115].

The two main categories of microscopes are transmission and reflection (or inverted). In the former, light is passed through the object under study to form an image; while in the latter an image is formed from light reflected from the surface of the object. The most common imaging technique in light microscopy is bright-field illumination. In this case, the light beam in focused onto the object thanks to a condenser-lens system [116].

While the human eye has a resolving power of approximately 150 μm, meaning that it can distinguish two points as separate if the distance between the two of them is at least 150 μm, the maximum resolving power of a compound light microscope is 0.2 μm [117].

1.6.2 Fluorescence microscopy

In fluorescence microscopy, the object itself acts as a light source thanks to its inherent fluorescence or added dyes. A substance is fluorescent when it absorbs light at a certain wavelength and immediately emits it at a longer one. Two commonly

used dyes are fluorescein, which emits a green light when excited with blue light, and rhodamine, that emits red light when excited with green/yellow light.

The fluorescence microscope is similar to the light microscope, apart from the presence of two sets of filters: the excitation and the barrier/emission filters. The former filters the light before it reaches the sample so that only the right wavelength is selected; while the latter blocks the emitting wavelength and only allows the emitted wavelength [115] [116].

1.6.3 US B-mode

Ultrasound is one of the most widely used modalities in medical imaging where the imaging is performed in real time with 20 to 100 images per second. In principle, the ultrasound transducer acts as both emitter and receiver. As the sound waves propagate towards the focal point, they reflect off any object with different acoustic impedance they encounter along their propagation path [118] [119].

The main modalities in which US can be used for imaging purposes are: A-mode, B-mode, Doppler and M-mode. A-mode (amplitude) is the oldest technique and is a 1D imaging modality that displays the amplitude of a recorded signal with respect to time. One single transducer is used and this modality is useful to measure distances between two points. B-mode (brightness) is an evolution of the A-mode. B-mode is a 2D imaging modality where brightness is used to represent the amplitude of the recorded signal with respect to time. Instead of a single transducer, a linear array of 100-300 piezoelectric (PZT) elements is used, and this provides the second dimension. The horizontal and vertical directions in the image represent real distances in tissue, whereas the intensity of the grey scale indicates echo strength. The Doppler modality is used to detect movement and it is based on the Doppler effect: in the presence of motion between the sound source and the sound receiver, a shift in the frequency or wavelength of the sound wave appears, and this can provide information about the phenomenon under study. Finally, M-mode consists of a single beam used to produce an image with a motion signal, where movement of a structure such as a heart valve can be depicted in a wave-like manner [118] [120].

1.6.4 Ultra High Speed Imaging

Ultra high speed imaging is becoming more and more important in many fields as it allows acquiring a series of image frames captured at high temporal resolution, providing more insightful information about the event under study [121]. Typical applications of high-speed imaging include car crash testing, air bag deployment, high-speed impact and materials testing, sport science, ballistics and nuclear detonation and explosions. Research fields in which ultra high speed imaging is used include: fluid dynamics and microfluidics, biomedicine, biomechanics and medicine [121]. In medicine, there are a number of events which need to be visualised at the nanosecond timescale. These include: shockwave lithotripsy for controlled kidney stone fracturing, cell membrane permeabilisation through acoustic streaming and sonoporation, the dynamics of oscillating microbubbles and nanodroplet vaporisation [104] [122]. The ability to record at sufficiently high frame rates to resolve these events has given invaluable insight into fundamental microbubble behaviour and their interaction with cells [123].

Among the most recent high-speed camera technologies are charge-coupled device (CCD) and complementary metal-oxide semiconductor (CMOS).

CCD chips are silicon semiconductor chips consisting of an array of M columns x N rows of photo-sensitive picture cells, called pixels. Every pixel contains electrons that receive photons and convert them into a charge. Every row of pixels is read out, pixel by pixel, and its content is preamplified, digitised and recorded. Subsequently, a digital image is built up row-by-row. The read-out of a normal video-rate CCD chip is 20 ms; whereas high-speed imaging CCD chips have a special chip and A/D conversion architecture with a typical throughput of up to 5 megapixels per millisecond, which corresponds to up to 5 gigapixel per second, which will then give origin to the different frames.

The more recent CMOS technology is less expensive, faster and require less energy to operate, but have a poorer image quality. Each CMOS pixel has its own read-out channel and can therefore be read individually, which reduces the time required because more actions are performed at the same time. CMOS chips allow up to 1 million complete frames per second. Since CMOS chips are noisier than CCD chips, their pixels are usually larger, to increase their sensitivity. Normally, CMOS and CCD chips only allow pictures in black and white; if colour is needed, a colour filter should

be used. Despite this, monochrome models are preferable since each colour filter uses blocks approximately 2/3 of the incoming light, so it goes at the expense of a factor 3 in sensitivity [121] [122].

Ultra high speed imaging has been fundamental in the study of MB behaviour. US frequencies used to stimulate microbubbles and their subsequent oscillation are in the order of 1-5 MHz; hence, ultra-high-speed imaging at a frame rate exceeding 10 Mfps is required. Using this technology, Van der Meer et al. [124] recorded a bubble's resonance curve within a single run of the camera by changing the insonation frequency in each segment and this method was later called 'microbubble spectroscopy'. Later on, shell buckling [125], nonspherical oscillations [126] and subharmonic oscillations [127] were visualised for the first time too, along with the study of drug delivery, release, and uptake of drugs by cultured cells [128].

1.7 Tissue mimicking phantoms for MBs and NDs acoustic characterisation

To characterise microbubbles and nanodroplets from an acoustic point of view, it would be beneficial to tailor and standardise the acoustic properties and phantom configurations of the environment in which they are located. Since the 1960s, different ultrasound tissue-mimicking materials and phantom fabrication techniques have been developed and tested to model both soft and hard tissues. Acoustic properties control the propagation of ultrasound through a medium and therefore a close matching is a prerequisite before translating knowledge reliably to the clinical setting. Tissue-mimicking phantoms are commonly used in therapeutic ultrasound for dosimetry, *in vitro* research, transducer characterisation and quality assurance [129] [130] [131].

When developing a tissue mimicking phantom for acoustic characterisation, the main acoustic properties and mechanical parameters that should be tailored to most accurately reproduce the tissue environment include: characteristic acoustic impedance, speed of sound, ultrasonic attenuation, back-scattering coefficient, non-linearity parameter, and Young's modulus [131]. One challenge in this process is the intra-variability and intervariability of real biological tissues, meaning that there are differences in the properties of tissues between persons and within different body

compartments of a single person. This stands mainly for hard tissues, since soft tissues have much more comparable acoustic characteristics, with a sound attenuation coefficient in the range 0.5 to 1.5 dB/cm/MHz and a 8% variation in speed of sound. Since the main objective of this work is to produce drug-loaded microbubbles and nanodroplets for bone fracture repair, a phantom simulating both soft tissue in a fracture gap and the fractured bone is needed [130] [132] [133].

1.7.1 Soft tissues

Soft tissues includes muscles, tendons, ligaments, fat, fibrous tissue, synovial membranes, nerves and blood vessels; and they are usually modelled as isotropic and homogeneous. Soft tissue mimicking materials include: water, hydrogels (i.e., gelatin-based materials, agarose-based materials) oil gel–based tissue substitutes (with propylene glycol in different proportions to achieve different speeds of sound and attenuations), open cell foam (like polyurethane foam and a NaCl water solution). An advantage of this latter material is that localised zones mimicking tissue pathologies or variations can be created within the material by removing regions of foam before preparation, therefore allowing for the creation of simple dishomogeneous phantoms. Other materials include synthetic polymer substitutes, silicone-based products, and organic materials like tofu or animal tissue [129] [130].

Agarose-based materials are the most widely used to manufacture soft tissue substitutes, since they are easy to fabricate with desired chemical and geometrical characteristics, and are resistant to high temperature, nontoxic, biocompatible, safe and cost-effective [130] [129]. Agarose gels can be employed as soft tissue substitutes (having a sound attenuation coefficient in the range 0.04-1.4 dB/cm/MHz) and as biomaterial/scaffold in regenerative medicine. Their performance is well characterised, leading to repeatable outcomes in experiments; under ideal storage conditions, agar gels can remain stable up to two and a half years [130] [134].

Agarose is a linear polysaccharide extracted from marine red algae, and consists of β-1,3 linked D-galactose and α-1,4 linked 3,6-anhydro-αL-galactose residues, as shown in Figure 1.23.

Agarose forms a gel when a homogeneous solution is cooled from 99^{o}C to a temperature below the sol-gel transition point (coil-helix transition), which depends on the proportion of agarose in the gel, as shown in Figure 1.24. The gel is formed

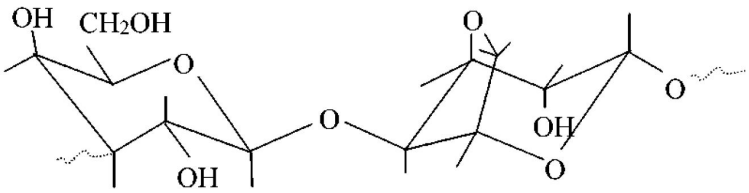

Figure 1.23: *Fundamental unit of agarose. [135]*

when an infinite three-dimensional network of agarose fibers, formed by helices of agarose, develops. The melting of agarose gels occurs at a relatively high temperature, around 85°C [135] [134].

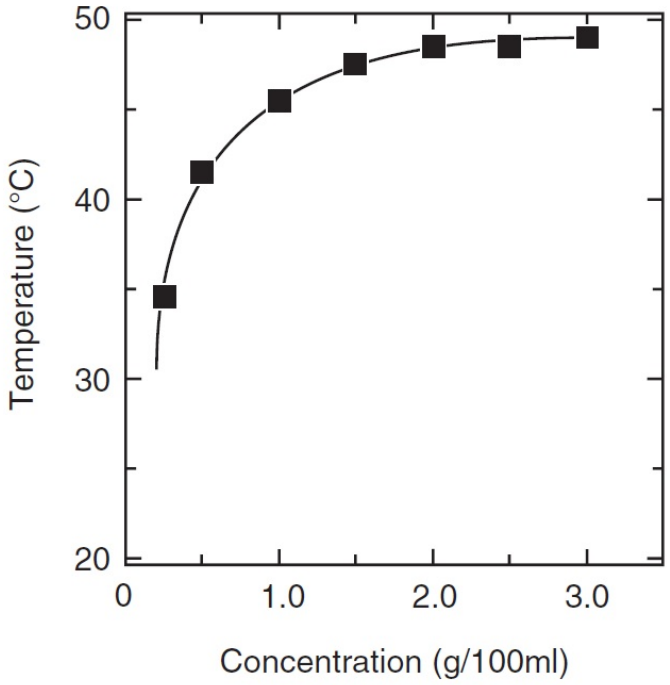

Figure 1.24: *Phase diagram of agarose solution, the closed squares represent sol-gel transition points at different agarose concentrations in water. Adapted from [136].*

In a study by Maxwell et al., a mixture of agarose gel and canine red blood cells in 0.9% isotonic saline was used as a tissue phantom to study cavitation-induced damage to tissue. The acoustic and mechanical properties of the gel phantom were found to be similar to soft tissue properties and the morphology of lesions generated in the phantom was very similar to that generated in the real tissue, at both macroscopic and cellular levels [131].

1.7.2 Hard tissues

Hard tissue includes all the mineralised tissues of our body, like cortical bone, trabecular bone, dental enamel and dentin. Mimicking hard tissues is more complex than mimicking soft tissues, due to their high variability in acoustic properties. Bone substitutes and phantoms are mainly needed to evaluate and calibrate ultrasound systems to detect bone pathologies [130].

The focus of this study is on the effects of a bone fracture on the acoustic stimulation and response of drug-loaded agents and, to achieve this, the most important acoustic characteristic to simulate is the characteristic acoustic impedance. Dodd et al. [137] used Sawbones material (Sawbones Europe, Krossverksgatan 3, Malmo, Sweden) to simulate a cortical bone and investigate the factors that determine how ultrasonic waves propagate across a simulated fracture. They compared these results with a real bovine cortical bone and concluded that the data obtained showed very similar characteristics. With material density and acoustic properties closer to human cortical bone, the Sawbones substitute, consisting of E-glass fibre epoxy resin, represents a better bone mimic in comparison to more commonly used plastics, such as acrylic.

1.8 Knowledge Gaps and Rationale of the Study

At present, clinically available treatments to heal bone fractures are invasive and suffer from complications at the systemic level. In recent years, ultrasound-responsive drug carriers have been proposed as an effective tool to perform local drug delivery upon external US stimulation. These include, but are not limited to, gas microbubbles and perfluorocarbon nanodroplets.

As for microbubbles, the literature is populated by studies using different chemical compositions and methods of production; however, there is no systematic study investigating how physico-chemical factors and production parameters affect MB characteristics, particularly their dimension and stability, which is important for applications where the MB size affects both their extravasation and safety (as it is the case for therapeutic applications targeted to bone fractures). It is therefore important to identify the optimal conditions and procedures leading to a stable MB-based agent, during storage, handling, and administration. Although it is known that MB stability is affected by the viscosity of the suspension medium, storage temperature, and production settings, there is no quantitative study that has evaluated their relationship yet. In addition, fluorescent labelling of MBs is commonly used to visualise them in applications *in vivo* and *in vitro*; however, it is not known whether the incorporation of a fluorophore within the MB shell can affect its dimension and stability with respect to time.

Nanodroplets are a more recently developed formulation when compared to microbubbles. Studies on NDs have been conducted using different chemical compositions and production processes, and it is generally accepted that mechanical agitation (i.e. via sonication) of a perfluorocarbon (PFC) emulsion in water leads is a viable method to produce NDs. However, little is known about the effect of production parameters on ND properties, which is an important prerequisite for administration *in vivo*. Knowing the size of nanodroplets and being able to tune it would be beneficial for applications where particle extravasation is strongly dependent on particle size, like in the case of bone fractures. For this reason, a systematic study of the quantitative relationship between production parameters and ND size is required.

A potential approach to achieve controlled drug release at a bone fracture, is to use ultrasound stimulation of an ultrasound-responsive agent. Earlier studies have utilised active or passive cavitation detection to study the acoustic response of drug-carriers

at a target site, upon exposure to different acoustic fields. The acoustic response is dependent on both the physical and mechanical properties of the drug carrier and of the surrounding environment. However, there is limited knowledge of how the geometrical and physical characteristics of a fracture can influence the acoustic response of drug carriers.

Finally, there are still open questions about the identification of the optimal drug for achieving the desired therapeutic outcomes, namely a quicker bone mass production and a decrease in the inflammation of the injured area making the bone fracture healing process quicker. The type of drug will determine the coupling mechanism with an ultrasound-responsive carrier. This knowledge gap needs to be addressed first, in order to subsequently assess the effect of ultrasound on the drug release kinetics.

1.9 Aims and Objectives

The main aim of this work is to develop therapeutic agents for application in bone fracture repair. The focus is on the study of both microbubbles and nanodroplets to be employed as drug carriers, for delivering a therapeutic payload upon ultrasound stimulation and promoting healing of bone fractures. To achieve this final aim, the following objectives will have to be addressed.

- Production of microbubbles and assessment of their stability.
  A first objective of the project involves the production of microbubbles, and the investigation of how different parameters influence their characteristics and stability. The aim is to demonstrate if and how different production, storage and manipulation conditions, including those replicating some characteristics of the *in vivo* environment, can influence MB stability. Once microbubbles are produced, it is fundamental that their size and number is maintained with respect to time, to provide therapeutic effect and preserve safety once injected in the bloodstream.

- Production of nanodroplets and assessment of their characteristics.
  A second objective of the project involves the assessment of a production protocol for nanodroplets, and the investigation of how different parameters (regarding production, storage and manipulation, including those replicating some characteristics of the *in vivo* environment) influence their characteristics.

Once nanodroplets are produced, it is fundamental to know their stability with respect to time and to assess their phase transition to microbubbles.

- Analysis of the acoustic behaviour of drug carriers in a model fracture.
  A third objective of the project focuses on the study of the behaviour of both microbubbles and nanodroplets upon ultrasound stimulation, since it affects therapeutic outcomes. The aim is to design a model that replicates the acoustic field in a bone fracture and to evaluate conditions that are relevant to clinical administration. Experimental systems may comprise both *in vitro* and *ex vivo* models.

Chapter 2

Evaluation of the effects of suspension medium, production parameters and storage conditions on microbubble stability

Acoustically stimulated microbubbles (MBs) have been extensively studied for therapeutic and diagnostic applications over the last 60 years. They were firstly proposed as an ultrasound contrast agent (UCA) in 1968 by Gramiak and Shah, when MBs were formed unintentionally in a saline solution used during a vascular ultrasound imaging procedure [138]. Apart from being used as UCAs, they can also be exploited as therapeutic agents and are under investigation as a tool for breaking blood clots [43] and kidney stones [139], and to deliver gases and drugs [19].

Microbubbles consist of a gas core surrounded by a shell that provides stability, in terms of concentration and mean diameter. Being able to maintain both MB size and concentration with respect to time is fundamental to their safety and efficacy; MBs should not occlude blood vessels and their concentration should be high enough to provide a therapeutic effect. Usually, about 95% of microbubbles used in the clinic has a diameter smaller than 10 μm and a mean diameter of approximately 3 μm [43]; it is advisable that the diameter is kept smaller than 10 μm to avoid vascular embolism [140].

There are several compositions available for both the entrapped gas and the shell, but, to the best of the author's knowledge, there is no systematic study quantitatively assessing the influence of different production parameters on MB stability for the same MB chemical composition. Studying a single MB chemical composition could give an idea of the relative impact that every paramenter has on stability. Moreover, there is no previous study quantitatively investigating the stability (in terms of both concentration and diameter) of MBs at 37^{o}C, which replicates the temperature occurring *in vivo*. The main parameters qualitatively studied in the literature are: (i) composition and (ii) viscosity of the dilution suspension, and (iii) storage temperature. As for composition of the suspension fluid, Kaya et al. [48] concluded that the use of glycerol and propylene glycol could enhance stability of MBs, and that this could be due to changes in viscosity. Kwan and Borden [73] also suggested that an increase in the viscosity of the dilution medium may partially hinder film drainage and coalescence between MBs. Furthermore, Shih and Lee [141] observed that viscosities >3 cP led to smaller MBs and decreased coalescence among MBs. Concerning the medium's temperature, Rovers et al. [142] showed that an increase in storage temperature led to a faster decrease in MB concentration. Owen et al. [143] demonstrated that the concentration with respect to time of DSPC/PEG40s MBs was comparable to DSPC/DSPE-PEG2000 MBs at 37^{o}C, while DSPC/DSPE-PEG2000 MBs maintained a greater concentration over time when compared to DSPC/PEG40s MBs at 4^{o}C.

This work addresses a key absence in understanding MB stability and diameter change at storage and body temperature as a result of (i) production and storage parameters, (ii) environmental conditions, and (iii) manipulation. Sonication is a stochastic process known to generate highly concentrated suspensions of MBs, but with a poor control over their size [42]; hence identifying parameters that influence the characteristics of MBs is important. MBs are formed upon two sonication steps, where the first step leads to the formation of liposomes in the suspension medium (i.e. the precursors of MBs), and the second results in the formation of gas-filled MBs [73].

In a first phase of the study presented in this thesis, it was investigated whether it was possible to control the MB size by changing the size of their precursors. Subsequently, MBs were diluted in media with different viscosity (ranging between 1.58-5.26 cP) composed of different proportions of phosphate buffered saline (PBS), glycerol (G) and propylene glycol (PG), to assess the influence of viscosity on stability.

A second phase of the thesis focused on the effect of environmental parameters on

MB stability. To gain a better understanding of MB behaviour *in vitro*, MBs were produced in PBS or cell medium and subsequently diluted in cell medium. To simulate both *in vitro* and *in vivo* conditions, MBs were stored in an incubator (T = 37°C, humidity = 95%, [CO_2] = 5%) and their stability assessed.

In a third phase of the work presented in this thesis, MBs were labelled with different molar fractions of a chosen fluorescent dye. Labelling of MBs is useful both for applications *in vitro*, i.e. to study MB uptake by cells, and *in vivo*, i.e. to visualise and localise particles in a model organism. It is known that lipophilic cell labelling dyes like DiI, DiO and DiD are useful for tagging lipid-coated MBs, but little is known about how the presence of these dyes can affect the size and stability of MBs. [44] [144]

2.1 Materials and Methods

The experiments performed to characterise and study microbubbles are presented in Figure 2.1.

Both size and concentration of MBs are fundamental parameters that can affect their safety and therapeutic efficacy. Notably, in order to be administered *in vivo*, MBs should have a diameter smaller than 10 μm to avoid obstruction of blood vessels. In addition, MB concentration should be maintained over time to provide the right dose of drug to the injured site and to achieve a predictable acoustic response.

The first series of tests described in this Chapter mainly focused on the generation of microbubbles. Firstly, tests were performed to establish a method to manufacture microbubbles and assess their stability during storage. Different formulations of suspension medium were tested, and a systematic study of the influence of medium viscosity on MB stability was performed. Subsequently, conditions relevant to MB application *in vitro* and *in vivo* were evaluated. Finally, a study was performed to investigate whether MB size could be controlled during production.

2.1.1 Generation of Microbubbles

A series of experiments were performed in order to investigate the effect of different physical parameters on microbubble stability. These included the composition of the saline medium used to suspend microbubbles, the type of encapsulated gas, the

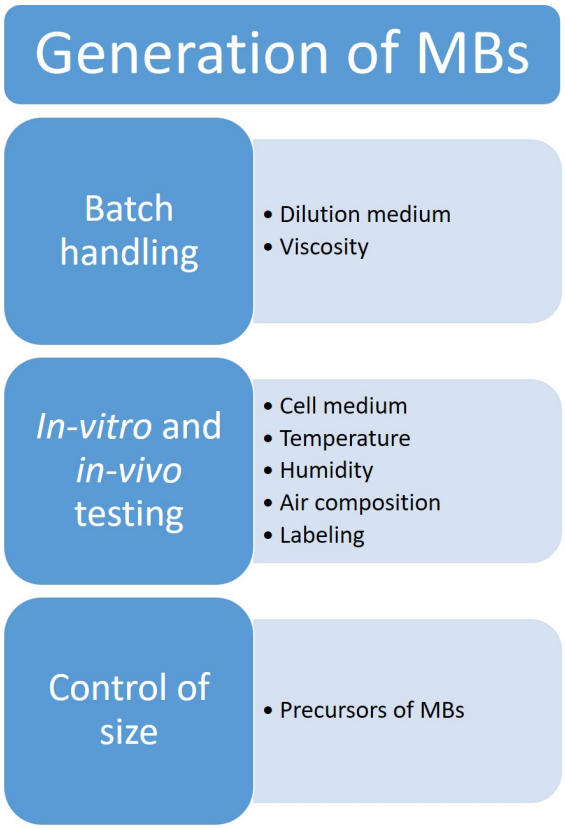

Figure 2.1: *The tests described in this Chapter can be divided into three main sections: MB batch handling, MB stability at conditions relevant to administration in vitro and in vivo, and control of MB size. Each section includes different studies to achieve a comprehensive characterisation of MBs.*

conditions in which microbubbles are stored, and the incorporation of a fluorescent dye within the MB shell.

Method

To produce lipid-shelled microbubbles, two constituents were selected: a phosphocholine PC and a polyethylene with a long polyethylene glycol (PEG) group. In this study, the lipid and the emulsifier used to produce microbubbles were 1,2-Distearoyl-sn-glycero-3-phosphocholine (DSPC, Avanti, Alabaster, Alabama, USA) and polyoxyethylene(40)stearate (PEG40s, Sigma-Aldrich, Saint Louis, Missouri, USA), as reported in earlier studies [46] [144] [143] [145]. The process of MB production was performed within a fume hood. Prior to production, it was necessary to determine the desired sample volume and lipid concentration, as these will define the amount of DSPC and PEG40s to be employed. In this study, a sample volume of 2 mL with a total lipid concentration of 4 mg/mL was selected; with DSPC and PEG40s present at 31.64 mM and 4.88 mM respectively, corresponding to a molar ratio of 9:1 [143]. Since the stock solutions of DSPC and PEG40s had concentrations of 25 mg/mL and 10 mg/mL (in chloroform) respectively, 249 µL of DSPC and 179 µL of PEG40s were added to a 10 mL glass vial (inner diameter: 2 cm) and gently mixed. A glass vial was employed, as it was inert to chloroform.

A glass syringe (1 mL Glass Tight Luer Lock Syringe, Supelco, Bellefonte, PA, USA) was used to transfer the lipid solutions to the vial. The syringe was washed by flushing with chloroform three times, at the beginning of the MB production protocol and in between lipid injections. The scale of the syringe has a resolution of 0.20 mL; however, small changes in the quantity of DSPC used did not affect the final result [143]. The mixture in the glass vial was covered with parafilm, which was then pierced a number of times to allow for the solvent to evaporate overnight within a fume hood, at environmental temperature.

The obtained dry lipid film was hydrated using 2 mL of a chosen medium to a final concentration of 3.94 mM and 0.44 mM for DSPC and PEG40s, respectively. The medium was composed of different proportions of phosphate buffered saline (PBS, Sigma-Aldrich, Saint Louis, Missouri, USA), glycerol (Sigma-Aldrich, Saint Louis, Missouri, USA), and propylene glycol (Sigma-Aldrich, Saint Louis, Missouri, USA). PBS is a salty buffer solution commonly used in biological research containing

sodium chloride, sodium phosphate, and (in some formulations) potassium chloride and potassium phosphate. The buffer helps to maintain a constant pH. The osmolarity and ion concentrations of the solution usually match those of the human body (isotonic). Glycerol and propylene glycol are used to increase the viscosity of the medium.

The hydrated lipid film was placed for 30 minutes on a hot plate (Fisher Scientific, Hampton, New Hampshire, USA) set at 95°C, and mixed using a magnetic stirrer set at 700 rpm. Among all the production methods presented in Paragraph 1.3.3, sonication was the chosen method as it is cost-effective and allows to obtain a high concentration of MBs in a short time frame. Lipids were then homogeneously dispersed for 150 seconds using a sonicator with a 3.22 mm diameter tip (Fisher Scientific, Hampton, New Hampshire, USA) at 48 W, with the tip completely immersed in the liquid. Microbubbles were subsequently formed by placing the sonicator tip at the air-liquid interface, for 30 seconds at 84 W (f = 22.5 kHz). The sonication process was performed under a fume hood, with the glass window of the hood fully closed. During sonication, millimetre-sized bubbles filled with room air are pinched off from the surface and then fragmented into microscale gas bubbles by cavitation. The process is rapid if the tip of the sonicator is placed at the interface between liquid and air; but can be slower if the tip is immersed in the liquid. [73] The temperature of the fluid during MB production must be higher than the phase transition temperature of lipids, to allow lipid molecules to organise themselves in a new low-energy arrangement. Considering that the phase transition temperature of DSPC is 55°C and the one of PEG40s is 37°C, hydration of the lipid film was performed on a hot plate set at 95°C, to ensure that the fluid temperature was >55°C during sonication.

Immediately after production, the vial containing the microbubble suspension was capped and placed in ice (or water containing an ice pack) for approximately 5 minutes. This step is required to lower the fluid temperature below the phase transition temperature of DSPC, reducing the diffusion rate of the gas through the MB shell. Stability of microbubbles was assessed by measuring MB size and concentration with respect to time. Since MBs are filled with gas, they float in a suspension and their position in the vial is dependent on their size. To obtain a representation of all MBs in the suspension, vials were manually shaken before collecting an aliquot of 10 µL with a pipette, to be imaged. Each sample was then placed on a haemocytometer (Neubauer improved, Marienfield, Germany) and a coverslip was placed on the top. Microbubbles were imaged using an inverted microscope (Helmut Hund, Wetzlar,

Germany) integrated with a camera GXCAM-Hichrome SII (GT Vision, Stansfield, UK). To allow statistical studies, three vials were produced for each MB formulation, and 10 pictures of every single vial were taken at each time point investigated. The approximate number of MBs detected in 10 pictures was around 5 x 10^4.

Figure 2.2 shows the main steps taken to produce microbubbles by sonication.

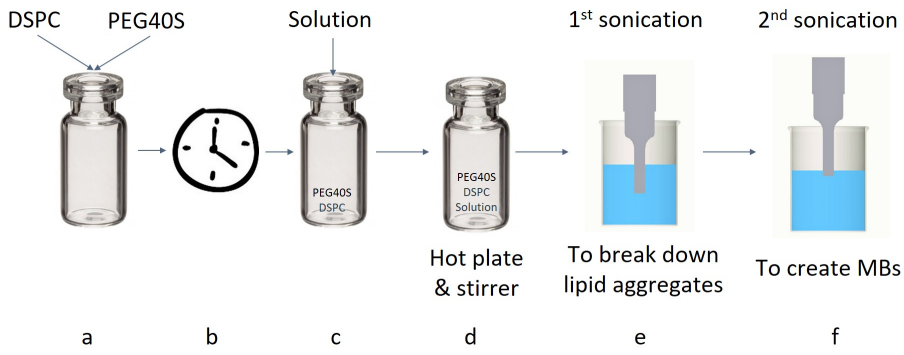

Figure 2.2: *Main steps of the MB production process based on sonication. a) DSPC and PEG40s dissolved in chloroform were placed in a glass vial at a desired molar ratio. b) Chloroform was let to evaporate overnight. c) The lipid film was hydrated. d) The solution was mixed and heated using a hot plate and stirrer. e) A first sonication was performed with the tip completely immersed in the liquid, to break down lipid aggregates. f) A second sonication was performed with the tip at the air-liquid interface, to generate microbubbles.*

Images were taken at different time points, and then processed with ImageJ (National Institutes of Health, USA) to determine the number of bubbles in each picture and the diameter of each bubble.

Figure 2.3 shows a representative microscope image of the produced microbubbles taken with a 10x magnification lens.

Each microscope image was converted into a 8-bit image format and a threshold was applied. To recognise bubbles that are in contact with each other as separate entities, the binary function 'Watershed' was applied, and to detect all bubbles the function 'Analyze Particles' was used, which is based on the edge detection of microbubbles. It works by scanning the image until it finds the edge of an object; it then outlines the object and measures its size. Such function allowed obtaining an image showing the outlines of the detected bubbles (Figure 2.4), and generated a data file containing the number of detected bubbles and their area (in pixels x pixels).

To convert pixels into μm, a dimensional calibration of the images was performed using the haemocytometer grid as a reference. By taking a microscope image of the

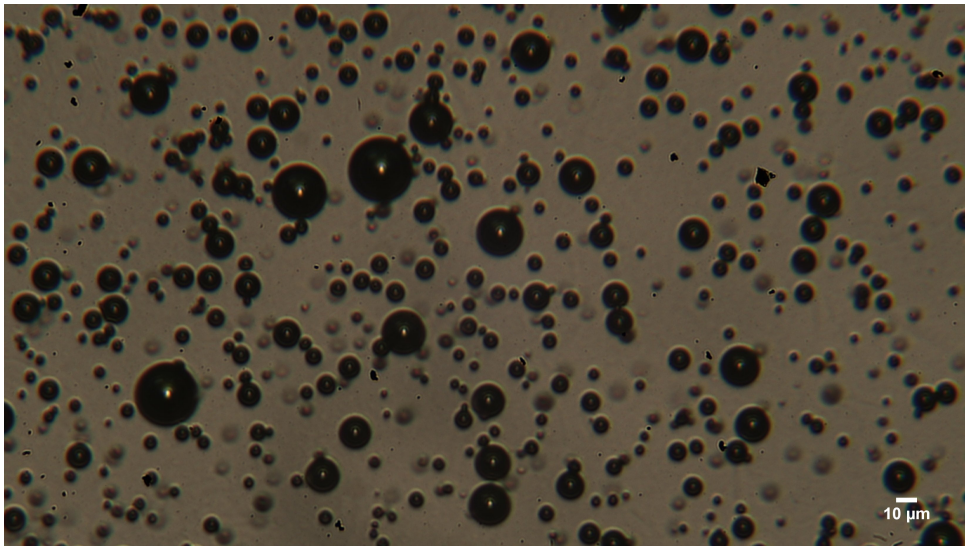

Figure 2.3: *Image of microbubbles taken with an inverted optical microscope (Helmut Hund, Wetzlar, Germany) with a 10x magnification lens. The image was taken one day after production, with microbubbles suspended in 2 mL of a medium composed of 70% PBS, 20% glycerol and 10% propylene glycol.*

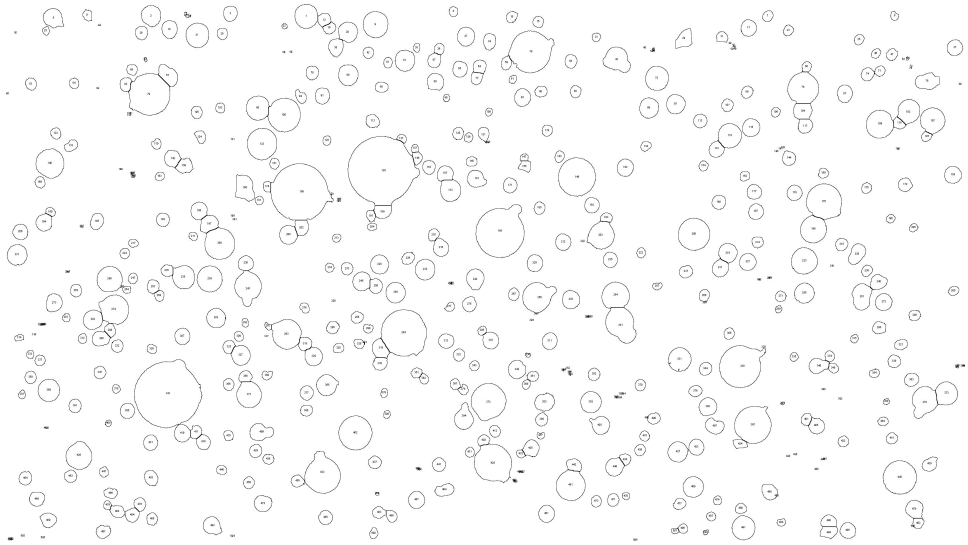

Figure 2.4: *Outlines of microbubbles obtained from image processing using ImageJ. The microscope image of MBs was taken one day after production, with microbubbles suspended in 2 mL of a medium composed of 70% PBS, 20% glycerol and 10% propylene glycol.*

grid, and knowing the physical length (in μm) of the segments of the grid, it was possible to determine a scaling factor between pixels and μm. Given that the software provides the area of detected MBs, it was then possible to determine their diameter. In addition, by knowing the x-y dimension of the image and the thickness of fluid between the haemocytometer and the coverslip, it was possible to calculate the volume of the sample in an image. This information was necessary to calculate the concentration of MBs in [MBs/mL].

A graph showing the size distribution of microbubbles at each time point was then created using the software Origin 2017 64 bit (Electronic Arts, Northampton, Massachusetts, USA). As an example, Figure 2.5 shows a typical size distribution obtained by analysing microbubble images taken just after production. The graph shows that the distribution of MB diameter is skewed, and this information will be used for future statistical analyses. The graph only shows MBs with a diameter greater than 1 μm. Even if submicron MBs were likely present in suspension, the microscope used did not have sufficient spatial resolution to resolve them. It was is also known that oxygen and nitrogen nanobubbles have a very short lifetime [146]; thus, the MB detection threshold was set at 1 μm. Figure 2.6 shows how the size distribution of microbubbles changes over time; the number of microbubbles drastically decreases, while the peak of the distribution moves to the right hand side of the graph, indicating an overall increase in MB size.

In addition to the size distribution, it was important to evaluate the change in MB concentration and mean diameter over time. Representative plots are shown in Figure 2.7 and Figure 2.8.

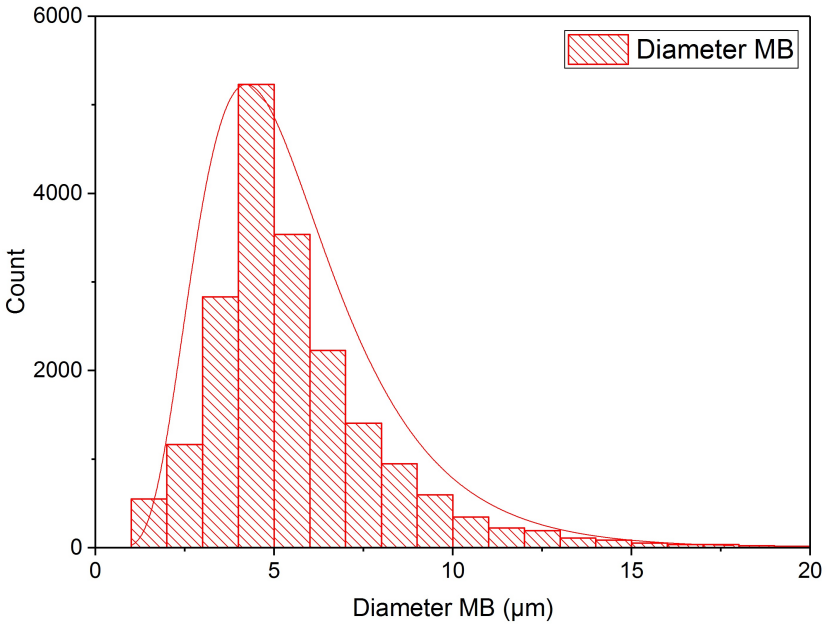

Figure 2.5: *Example of a typical MB size distribution graph. The graph corresponds to one day after production, with microbubbles suspended in 2 mL of a medium composed of 70% PBS, 20% glycerol and 10% propylene glycol.*

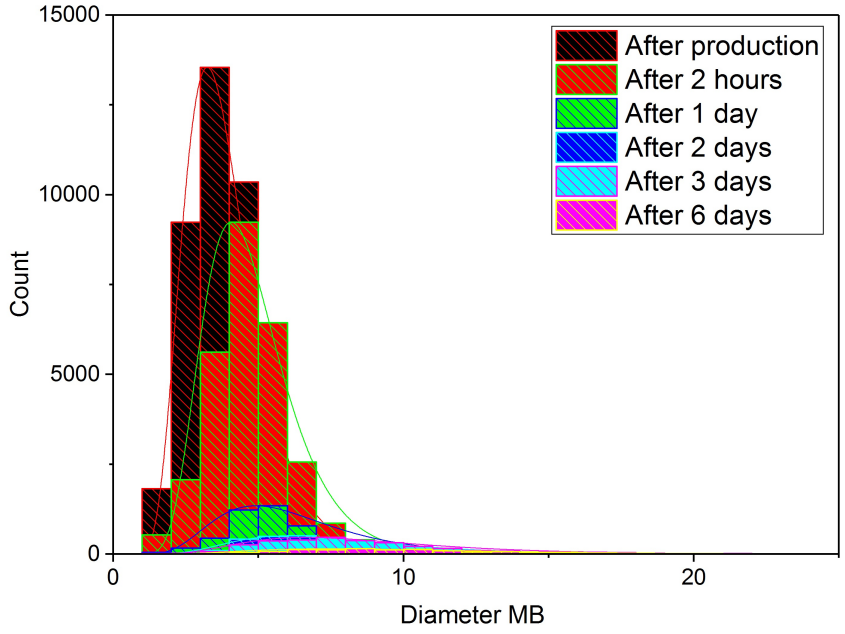

Figure 2.6: *Example of a typical MB size distribution graph over time. The graph corresponds to one day after production, with microbubbles suspended in 2 mL of a medium composed of 70% PBS, 20% glycerol and 10% propylene glycol.*

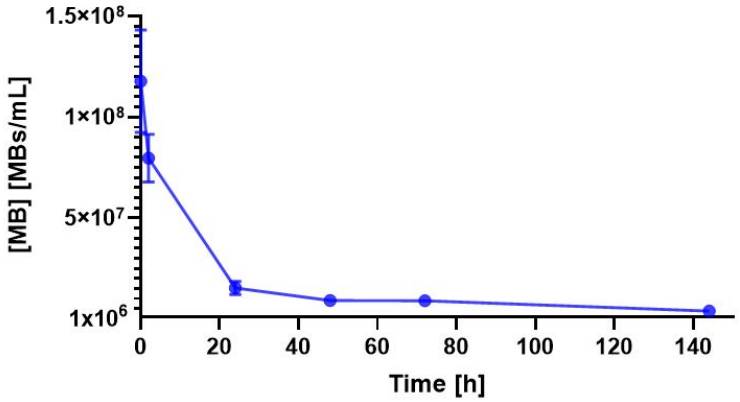

Figure 2.7: *Example of a graph showing how the concentration of microbubbles changes with respect to time. MBs were suspended in 2* mL *of a medium composed of 80% PBS, 10% glycerol and 10% propylene glycol. Three independent measurement (N = 3) of the same formulation are represented on the graph.*

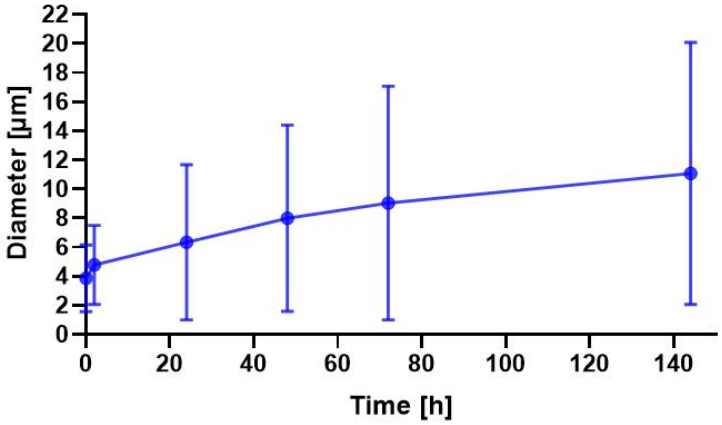

Figure 2.8: *Example of a graph showing how the mean diameter of microbubbles changes with respect to time. MBs were suspended in 2* mL *of a medium composed of 80% PBS, 10% glycerol and 10% propylene glycol. Three independent measurement (N = 3) of the same formulation are represented on the graph.*

Statistical Analysis

Following the experimental tests, statistical analysis was performed on the results obtained. Two types of statistical test were performed in this study: independent-samples t-test and one-way analysis of variance (ANOVA). The software used was SPSS (IBM Analytics, Armonk, New York, USA).

The independent-samples t-test was used to compare the concentration of MBs obtained for different formulations with respect to one chosen as a reference, at each time point tested. As a matter of fact, the independent-samples t-test compares the means between two independent groups on the same variable to determine whether there is a statistically significant difference between them. The null hypothesis H_0 for the independent t-test is that the population means u_1 and u_2 from the two unrelated groups are equal (Equation 2.1.1).

$$H_0 : u_1 = u_2 \tag{2.1.1}$$

The aim of the test is to reject the null hypothesis H_0 and accept the alternative hypothesis H_1, which is that the population means are not equal (Equation 2.1.2).

$$H_1 : u_1 \neq u_2 \tag{2.1.2}$$

To do this, a significance level α is set to either reject or accept the alternative hypothesis. The significance level is the likelihood of two means being different due to chance alone, so it is the probability of rejecting the null hypothesis when it is true. Most commonly, this value is set at 0.05, which indicates a 5% risk of concluding that a difference exists, but which is only due to chance. In addition, some assumptions must be met before performing the test: variables should be measured on a continuous scale, and there should be independence of observation between the observations in each group and between the groups themselves; where two observations are defined as 'independent' if the occurrence of one observation provides no information about the occurrence of the other observation. Furthermore, there should be no outliers because they reduce the validity of results, and variables should be approximately normally distributed.

The test provides a t-value with a two-tail significance, meaning that it defines if there is a statistical difference or not, but it does not provide information about how

different groups can be ordered (if one is greater/lower than the other). To define the presence of the order, the t-value provided by the result of the test can be used to perform a one-sided (upper or lower) comparison.

The ANOVA test was used to compare the diameter of MBs obtained for different formulations at each time point. ANOVA is used to determine whether there are any statistically significant differences between the means of three or more independent groups. The null-hypothesis is that the population means μ of all the N groups are equal (Equation 2.1.3).

$$H_0 : \mu_1 = \mu_2 = \mu_3 = ... = \mu_N \tag{2.1.3}$$

The aim of the test is to reject the null hypothesis H_0 and accept the alternative hypothesis H_1, which is that there are at least two group means that are statistically significantly different from each other. However, the ANOVA test does not define which are the specific groups that are different and, to do so, a post hoc test should be used. The post hoc test performed in this study is the Tukey's honestly significant difference (HSD).

Some assumptions should be met before running the ANOVA test: variables should be normally distributed in each group and observations should be independent. In the case of the diameter of MBs, Figure 2.5 shows that the distribution is skewed and not normal. In this case, the ANOVA test can still be performed, but data must undergo a logarithmic transformation before the test to normalise the data distribution. [147] [148]

2.1.1.1 Reproducibility of the MB production and sizing method

As stated in Paragraph 2.1.1, every time a new condition was tested, three vials (N=3) of MBs were produced to allow statistical analyses and comparisons. At each time point tested, 10 images for each produced vial were taken and analysed separately, before combining the results. The method used to produce microbubbles, i.e. sonication, is a stochastic one, thus it is not possible to finely control the final MB size. However, this does not imply that the method is not reproducible. To assess method's reproducibility, eight vials of microbubbles were produced all with the same standard method (Paragraph 2.1.1), and 10 MB images of every vial were taken after production. The MB counting method was applied to every image to determine the

mean MB size per image. Thus, 10 values of the mean MB diameter were obtained for each vial. A one-way ANOVA was performed to define the presence or absence of a statistical difference between the eight vials produced and a Scheffe post-hoc test was used to identify which groups were statistically different. This test was chosen because it is the only multiple comparison test that is entirely coherent with ANOVA and it is more conservative than the other post-hoc tests, hence it is suitable for unplanned comparisons between a large number of cases. [149]

2.1.1.2 Effect of physical properties of the suspension medium on MB stability

2.1.1.2.1 Effect of different suspension media

The effect of the viscosity of the MB suspension medium on microbubble stability was investigated. Phospholipid-shelled MBs were produced by sonication, using saline media with different viscosity. The underlying hypothesis was that an increase in medium viscosity would lead to increased MB stability, due to the fact that the diffusivity of a gas is inversely proportional to the viscosity of the fluid in which diffusion occurs. Chemicals used to produce the suspension medium, together with their relative amount and the net medium viscosity in centipoise cP, are reported below:

- 100% PBS, $\mu = 1.58$ cP
- 90% PBS + 10% glycerol, $\mu = 2.18$ cP
- 80% PBS + 20% glycerol, $\mu = 3.18$ cP
- 70% PBS + 30% glycerol, $\mu = 4.92$ cP
- 80% PBS + 10% glycerol + 10% propylene glycol, $\mu = 3.36$ cP
- 70% PBS + 20% glycerol + 10% propylene glycol, $\mu = 5.26$ cP

The choice of using glycerol and propylene glycol was based on solutions already used *in vitro* in the literature [48] [150] [151], and their concentration was varied to achieve different viscosities.

After production, MBs were stored at 4^{o}C in between microscope acquisitions and their stability was assessed by microscopy analysis, as described earlier. Three

independent repeats were performed for each medium composition. For each repeat, ten microscope images were taken at 2 hours, and 1, 2, 3 and 6 days after MB production.

2.1.1.2.2 Effect of medium viscosity

Upon completion of the tests described in Paragraph 2.1.1.2.1, a more systematic study of the influence of medium viscosity on the stability of microbubbles was performed. Considering that the viscosity μ of a solution composed of 100 % PBS is equal to 1.58 cP, increasing amounts of glycerol were added to PBS in order to achieve a medium bulk viscosity equal to five and ten times the viscosity of PBS. Chemicals used to produce the suspension medium, together with their relative amount and the net medium viscosity, are reported below:

- 60% PBS + 40% glycerol, $\mu = 8.26$ cP
- 50% PBS + 50% glycerol, $\mu = 15.38$ cP

After production, MBs were stored at 4^{o}C in between microscope acquisitions and their stability was assessed by microscopy analysis. Three vials of each composition were produced. Ten pictures of every vial were taken after production, after five hours and after 1 day.

2.1.1.2.3 Effect of fluorescent labelling

The effect that the incorporation of a fluorophore within the MB shell has on MB stability was investigated. Notably, fluorescent labelling of MBs is often performed during applications *in vitro*, i.e. to study MB uptake by cells or transfer of material from the MB shell to the cell membrane, and *in vivo* to quantify MB biodistribution upon administration in a living organism [144]. The underlying hypothesis was that the addition of a dye could alter the physical characteristics of the MB shell, and in turn affect MB size and stability.

To produce fluorescently-labelled microbubbles, the protocol described in Paragraph 2.1.1 was used. The only difference was in the hydration of the lipid film, during which the lipid analogue dye 1,1'-Dioctadecyl-3,3,3',3'-Tetramethylindocarbocyanine Perchlorate (DiI, Life Technologies, Carlsbad, California, USA) was added to the lipid suspension. Three vials containing 2 mL of PBS were produced, containing

DiI concentrations of 2.14, 10.71 and 21.42 μM, corresponding to molar ratios DSPC:PEG40s:DiI of 0.89:0.101:0.00025, 0.9:0.101:0.0012, and 0.9:0.101:0.0025, respectively. Talu et al. [144] showed that a molar ratio of 0.9:0.101:0.000196 is sufficient to allow for MB detection via fluorescence microscopy. Ten microscope images of every vial (N=3 for each condition) were taken at time intervals of 2 hours, and 1, 2, 3 and 6 days after MB production.

2.1.1.2.4 Effect of the conditions of a cell incubator

Experiments were performed to investigate MB stability at environmental conditions relevant to their application *in vitro* and *in vivo*. These tests are an important pre-requisite before investigating the interaction between cells and microbubbles. The underlying hypothesis was that a change in the temperature, humidity, and gas composition of the environment could affect MB stability, and that varying some formulation-related parameters could help enhancing MB stability.

Following the production of microbubbles, vials were stored in an incubator (NuAire, Plymouth, Minnesota, USA) with a temperature of 37°C, a humidity of 95%, and a percentage CO_2 of 5% to simulate conditions *in vivo*. Four different tests were performed: microbubbles were either filled with room air or nitrogen (Boc, UK) and diluted in either PBS or cell medium (DMEM, Lonza), and they were placed in the incubator with the vial either open or closed with a lid. Nitrogen was used as an alternative gas core with respect to room air to see if this could have an impact on MB stability.

To produce nitrogen-filled (N_2) microbubbles, a nitrogen cylinder (BOC, Guildford, Surrey, England, UK) was employed to supply the gas. The protocol used is the same as the one described earlier for the production of bubbles filled with room air (RA). The only difference lied in the use of a needle connected to the nitrogen cylinder, which was used to saturate the vial with nitrogen prior to the sonication at the gas-liquid interface.

Figure 2.9 shows the vials produced for these tests, indicating the medium in which MBs were diluted and the gas used for the core. In this way, it was possible to study both the influence of temperature, humidity and percentage CO_2 on the stability of microbubbles, and the influence of temperature alone. Ten microscope images of every vial (N = 3 for each condition) were taken after production, and every 15 minutes until two hours from production.

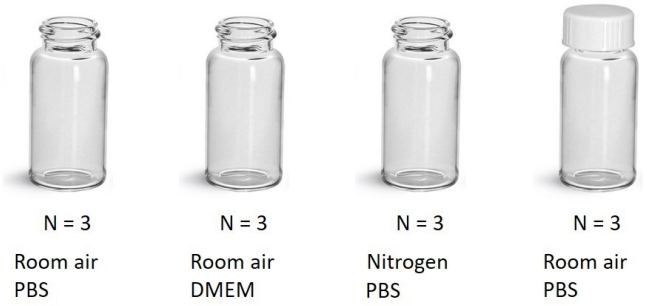

Figure 2.9: *Six vials containing room air MBs (three with MBs suspended in phosphate buffered saline PBS and three with MBs suspended in cell medium, or Dulbecco's Modified Eagle Medium DMEM) and three vials containing nitrogen microbubbles were placed in the incubator without lid. The remaining three vials containing room air MBs were placed in the incubator, in a vial closed with a lid.*

2.1.1.2.5 Effect of producing and/or suspending MBs in cell medium

Experiments were performed to investigate the effect of cell medium on MB stability at environmental conditions relevant to their application *in vitro* and *in vivo*. The underlying hypothesis was that producing or diluting MBs in cell medium could have an impact on the size and stability of MBs, due to the chemical composition of cell medium.

PBS is a buffer composed of different salts frequently used in biological applications to stabilise both osmolality and pH during experiments. When cells are cultured, they need amino acids, vitamins and other supplementary components to live and proliferate, and these are supplied by the medium. One of the most common media used is DMEM (Dulbecco's Modified Eagle's Medium), which is sometimes enriched with 10% FBS (Fetal Bovine Serum). Since they both contain amino acids, which are the components of proteins, using these media instead of PBS in the MB production or dilution processes could have an impact on the final product. Microbubbles could have some proteins in the shell, as well as lipids, and this could change their size and stability with respect to time.

Microbubbles were either produced in PBS and then diluted 1:2 and 1:5 in PBS, DMEM, or DMEM with FBS, or directly produced in DMEM or DMEM with FBS instead of PBS. Three vials (N=3) of each composition were produced (total of 27 vials). Following the production of microbubbles, vials were stored in an incubator (NuAire, Plymouth, Minnesota, USA) with a temperature of 37^{o}C, a humidity of

95%, and a percentage CO_2 of 5% to simulate conditions *in vivo*. Ten microscope images of every vial were taken after production, every 15 minutes until two hours from production.

2.1.1.2.6 Effect of the lipid shell formulation

In this step of the study, MBs were produced with a different lipid shell to investigate the influence of acyl chain length of the lipid constituent on MB stability. Instead of DSPC and PEG40s, 2,6-Di-tert-butyl-4-methylphenol, 2,6-Di-tert-butyl-p-cresol, BHT, Butylated hydroxytoluene, Butylhydroxytoluene (DBPC, Avanti, Alabaster, Alabama, USA) and 1,2-distearoyl-sn-glycero-3-phosphoethanolamine-N-[amino(poly -ethylene glycol)-2000] (DSPE-PEG2000, Avanti, Alabaster, Alabama, USA) were used with a molar ratio 9:1. The DBPC/DSPE-PEG2000 formulation has been already employed in previous studies [152] [153], and the hypothesis at the base of this experiment is that the longer chain of DBPC with respect to DSPC could increase MB stability. The phospholipids and the molar ratios were chosen to be complementary to other studies being undertaken within the wider research group.

The protocol used to produce DBPC-containing microbubbles is similar to the one used for DSPC MBs, with some adjustments to account for the different chemistry of the lipids.

Prior to MB production, it is necessary to determine the desired sample volume and lipid concentration, as these will define the amount of DBPC and DSPE-PEG2000 to be employed. In this study, a sample volume of 3 mL with a total lipid concentration of 4 mg/mL was selected; with DBPC and DSPE-PEG2000 present at a molar ratio of 9:1. Since the stock solutions of DBPC and DSPE-PEG2000 had concentrations of 10 mg/mL (in chloroform) respectively, 357 μL (11.08 mM) of DBPC and 308 μL (3.56 mM) of DSPE-PEG2000 were added to a 10 mL glass vial (inner diameter: 2 cm) and gently mixed. A glass vial was employed, as it is inert to chloroform.

Following evaporation of chloroform and lipid hydration (with 3 mL of PBS to reach final concentrations of 1.32 mM and 0.36 mM of DBPC and DSPE-PEG2000, respectively), the hydrated lipid film was placed for 1 hour on a hot plate (Fisher Scientific, Hampton, New Hampshire, USA) set at 100°C, and mixed using a magnetic stirrer set at 700 rpm. The heating step was longer and at a greater temperature with respect to DSPC MB production, since DBPC has a greater phase transition temperature of 69°C (versus 55°C for DSPC). Lipids were then homogeneously

dispersed for 4 minutes (instead of 2 minutes and 30 seconds, as for DSPC) using a 3.22 mm diameter sonicator tip (Fisher Scientific, Hampton, New Hampshire, USA) at 48 W, with the tip completely immersed in the liquid. A second heating step at 100^{o}C for 5 minutes was then carried out, to ensure that the fluid temperature was kept above the phase transition temperature. Microbubbles were subsequently formed by placing the sonicator tip at the air-liquid interface, for 30 seconds at 84 W (f = 22.5 kHz).

Three vials of room air DBPC/DSPE-PEG2000 MBs, three vials of nitrogen DBPC/DSPE-PEG2000 MBs and three vials of oxygen DBPC/DSPE-PEG2000 MBs were produced. Oxygen MBs were tested as recent studies by Esmaeili et al. [154] and ongoing parallel studies have shown that microbubbles are capable of promoting oxygen penetration and boosting the wound healing process by supplying adequate oxygen. Following the production of microbubbles, vials were stored in an incubator (NuAire, Plymouth, Minnesota, USA) with a temperature of 37^{o}C, a humidity of 95%, and a percentage CO_2 of 5% to simulate conditions of a standard cell incubator. Ten microscope images of every vial were taken after production, and every 15 minutes until two hours from production.

2.1.2 Precursors of Microbubbles

In this step of the study, the dimensions of microbubble precursors (i.e. liposomes or other supra-molecular structures) that were generated during the lipid film hydration step were determined. This was performed to get a more pervasive understanding of the MB production process, and to also evaluate whether MB size distribution could be influenced (and potentially controlled) by the sonication process.

Method

The protocol used to produce the MB precursors was the same as the one described earlier in Paragraph 2.1.1. After heating and stirring of the hydrated lipid film (composed of DSPC and PEG40s with a molar ratio 9:1, hydrated with PBS), fluid samples were taken before and after lipid dispersion (performed using a sonicator, as described earlier). Sizing of the supra-molecular particulate structures present in the fluid was performed using a Dynamic Light Scattering (DLS) machine (Zetasizer Nano, Malvern Panalytical Ltd, Malvern, UK) and the Zetasizer Software (Malvern

Panalytical Ltd, Malvern, UK). To perform the measurements, the software required the following data characterising the sample: dynamic viscosity μ, refractive index n, and dielectric constant k of the dispersant, temperature T of the sample, type of cuvette used, and equilibrating time t needed. The measure of the diameter is a function of the temperature of the sample; therefore, during the measurement, the temperature of the cuvette has to be stable. For this reason, an equilibration step of the temperature of the cuvette is introduced prior to the measurement. When sizing the MB precursors, the input data were: $\mu = 1.31$ cP, $n = 1.335$, $k = 0.1$, $T = 10^{o}$C, $t = 120$ s and the volume of the cuvette was 1 mL (Fisherbrand FB55147, Fisher Scientific, UK). The sample was transferred from the glass vial into the cuvette by using a 1 mL pipette. The DLS machine measures the sample three times, and every time runs different measurements. The number of measurements is automatically set depending on the the concentration and transparency of the sample.

2.1.2.1 Effect of the duration of sonication on liposome dimension

MB precursors were sized before and after the first sonication step. When sonication was applied, the sonicator was set at a power of 48 W, and the tip was completely immersed in the lipid dispersion. Different lengths of sonication and sonication regimes (pulsed vs. continuous) were investigated:

- 30 seconds
- 1 minute
- 2 minutes
- 2 minutes and 30 seconds
- 3 minutes
- 4 minutes
- 5 minutes
- 2 minutes and 30 seconds with pulse (pulsation of 4 seconds, with 50% duty cycle)

The underlying hypothesis was that an increase in the length of sonication could lead to smaller MB precursors with a lower size dispersity, in turn leading to smaller and more uniform microbubbles. Three vials for each experimental condition were produced and analysed.

2.1.2.2 Effect of a pulsed sonication on the diameter of MBs

In this test, liposomes obtained using a pulsed sonication of 2 minutes and 30 seconds, with a pulsation of 4 seconds and duty cycle of 50%, were used to produce microbubbles in order to investigate whether pulsation had an effect on the average MB size. After production, microbubbles were stored at 4^{o}C in between experiments, and MB stability was assessed by microscopy. Three vials were produced for each condition tested. For each repeat, ten microscope images were taken at 2 hours and 1 day after production.

To study the effect of sonication on the MB size in a more systematic way, MBs were produced by applying different sonication conditions, and their size was measured only after production. The hypothesis was that using larger precursor liposomes would result in the production of larger microbubbles. In particular, microbubbles were produced using liposomes obtained without sonication, with a continuous sonication of 2 minutes and 30 seconds, and with a pulsed sonication of 2 minutes and 30 seconds (with pulsation of 4 seconds and duty cycle of 50%).

2.2 Results

This paragraph presents the results obtained from the tests described in Paragraph 2.1. Results can be categorised into two main groups, relating to either the generation of microbubbles or of MB precursors. As for the tests relating to MBs, they aimed at investigating the influence of MB formulation and batch handling on their stability for applications *in vivo* and *in vitro*. As for tests relating to MB precursors, they aimed at assessing whether MB size distribution could be influenced and potentially controlled by varying the sonication process parameters.

2.2.1 Generation of Microbubbles

2.2.1.1 Reproducibility of the MB production and sizing method

Microbubbles produced with the protocol described in Paragraph 2.1.1 were analysed, and their mean diameter and standard deviation are presented in Figure 2.10 and in Table 2.1. The aim of this experiment was to show the repeatability of fabrication method.

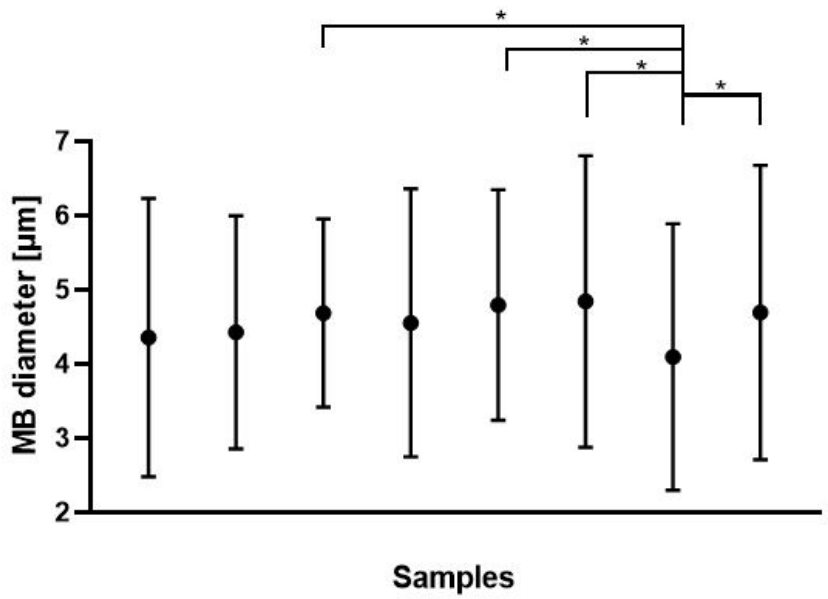

Figure 2.10: *The graph shows the mean diameter and standard deviation of eight vials of microbubbles, produced with the protocol described in Paragraph 2.1.1 and measured just after production. The bars on the top of the graph indicate the groups that are statistically different (*$p < 0.05$).*

Table 2.1: *Mean diameter, standard deviation (SD) and median diameter of eight vials of microbubbles produced with the protocol described in Paragraph 2.1.1 and measured just after production.*

	Mean Diameter [μm]	Standard deviation	Median Diameter [μm]
Vial 1	4.35	1.87	4.23
Vial 2	4.43	1.57	4.35
Vial 3	4.69	1.27	4.69
Vial 4	4.55	1.81	4.57
Vial 5	4.79	1.70	4.78
Vial 6	4.84	2.02	4.81
Vial 7	4.09	1.79	4.12
Vial 8	4.69	1.98	4.65

A one-way ANOVA was performed, showing that there were some statistical differences between samples ($p < 0.05$). A Scheffe post-hoc test showed that there was a statistical difference between vial 7 and vials 3, 5, 6 and 8 ($p < 0.05$), while there was no statistical difference between all the other samples. Overall, statistical difference was found only in 15% of all comparisons with a maximum difference in mean diameter of 15.49%. Together this data indicate that the methodology for producing bubbles of a consistent size distribution is robust and sufficiently reproducible.

2.2.1.2 Effect of the physical properties of the suspension medium on microbubble stability

2.2.1.2.1 Effect of different suspension media

Experiments were performed to identify a suitable suspension medium that preserved microbubble stability during storage, in terms of MB concentration and diameter with respect to time.

As it can be observed in Figure 2.11, MB concentration reduced with respect to time, from an average value of 1.5 x 10^8 MBs/mL after production to 7 x 10^6 MBs/mL after six days for all suspension media investigated. As it can be observed in Figure 2.12, MB diameter increased with respect to time, from a mean value across all media tested of 3.9 μm after production to 10.48 μm after 6 days for all suspension

media investigated. Table 2.2 shows the mean diameter of microbubbles suspended in different media, with respect to time.

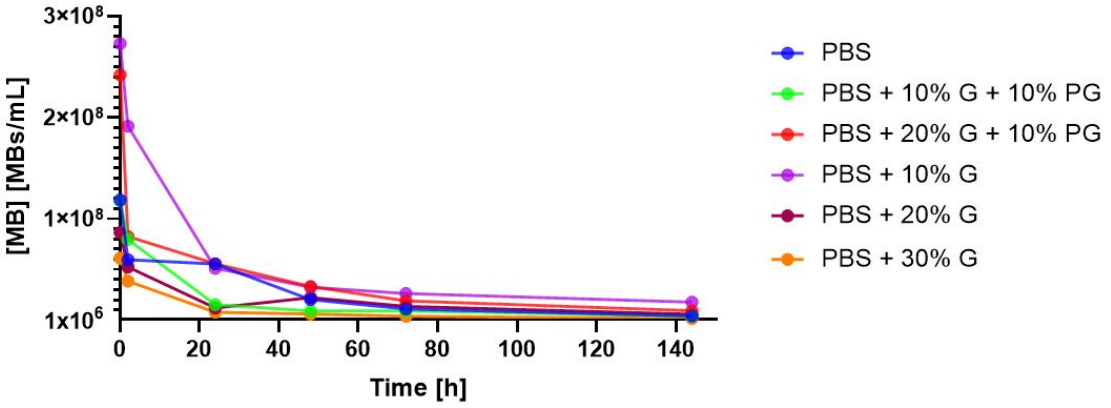

Figure 2.11: *The graph shows the concentration of microbubbles diluted in media with different composition, with respect to time. The average concentration of MBs decreased over time from a mean value for all the composition tested of 1.5 x 10^8 MBs/mL (just after production) to 7 x 10^6 MBs/mL after six days. PBS: phosphate buffered saline; G: glycerol; PG: propylene glycol. Every line represents the mean of measurements performed on three independent vials (N = 3) of the same formulation.*

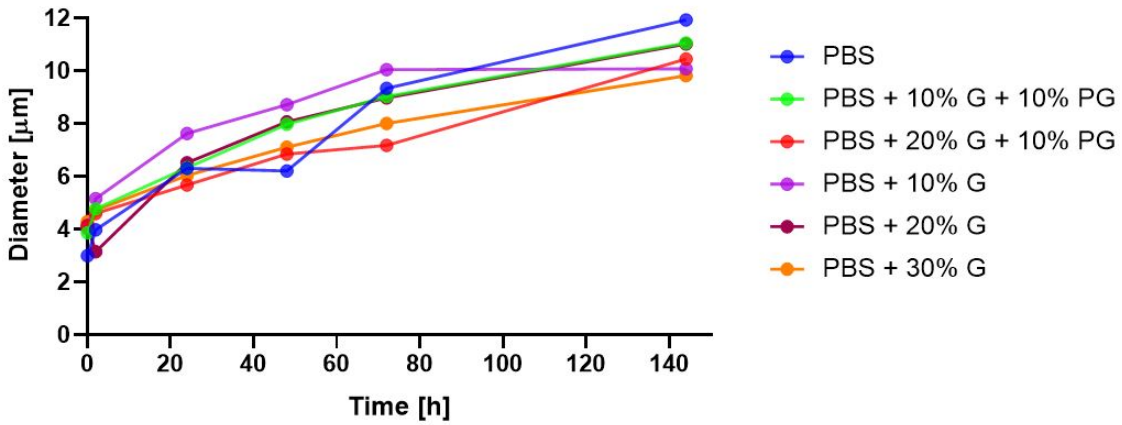

Figure 2.12: *The graph shows the diameter of microbubbles diluted in suspension media with different composition, with respect to time. The mean diameter increased from 3.9 µm (just after production) to 10.48 µm after 6 days. PBS: phosphate buffered saline; G: glycerol; PG: propylene glycol. Every line represents the mean of measurements performed on three independent vials (N = 3) of the same formulation.*

Table 2.2: *Mean MB diameter with respect to time, obtained by suspending microbubbles in different media. PBS: phosphate buffered saline; G: glycerol; PG: propylene glycol.*

	After production [μm]	After 2 hours [μm]	After 1 day [μm]
100% PBS	2.99 ± 2.45	3.97 ± 4.15	6.31 ± 6.14
10% G	4.01 ± 3.19	5.15 ± 4.11	7.62 ± 7.42
20% G	4.13 ± 3.28	3.14 ± 3.23	6.51 ± 4.09
30% G	4.28 ± 3.89	4.71 ± 3.69	6.03 ± 4.76
10% G 10% PG	3.86 ± 2.30	4.76 ± 2.71	6.32 ± 5.33
20% G 10% PG	4.09 ± 2.92	4.59 ± 3.80	5.67 ± 5.02

	After 2 days [μm]	After 3 days [μm]	After 6 days [μm]
100% PBS	6.20 ± 5.15	9.34 ± 7.58	11.92 ± 10.66
10% G	8.71 ± 8.71	10.04 ± 10.00	10.07 ± 10.00
20% G	8.06 ± 5.65	8.97 ± 6.83	11.01 ± 8.01
30% G	7.10 ± 5.21	8.00 ± 6.78	9.81 ± 5.54
10% G 10% PG	7.97 ± 6.41	9.02 ± 8.03	11.05 ± 9.00
20% G 10% PG	6.84 ± 8.26	7.17 ± 6.38	10.44 ± 9.01

An ANOVA test was performed on the MB diameter vs. time data, to evaluate whether there was any statistical difference between mean values. There was a statistically significant difference between all experimental groups at all time points investigated ($p<0.05$). The suspension medium did not affect MB diameter after production and after 2 hours; however, results obtained at 1, 2 and 3 days after production showed that an increase in the medium viscosity from 1.58 cP to 5.25 cP resulted in MBs that were at least 1 μm smaller.

A t-test was performed on the MB concentration vs. time data, to evaluate whether there was any statistical difference between mean values. The t-test showed no statistical difference between the concentrations of the different groups tested at different time points ($p>0.05$).

This first experimental characterisation suggested that the composition of the suspension medium may influence MB stability. Since a physical property that differs across the media investigated is their dynamic viscosity, further tests were performed to systematically investigate the influence of medium bulk viscosity on MB stability.

2.2.1.2.2 Effect of medium viscosity

To systematically investigate the effect of the viscosity of the suspension medium, microbubbles were suspended in media with different bulk viscosity following the protocol described in Paragraph 2.1.1.2.2. Microscope images of MBs were taken after production, and at 5 and 24 hours from production.

Table 2.3 and Figure 2.13 show the mean diameter of microbubbles with respect to time. It can be observed that an increase in the viscosity of the medium resulted in MBs maintaining a diameter comparable to their initial one, for a longer time period. While MBs diluted in 100% PBS experienced an increase in diameter of 2.6 μm over 1 day; MBs diluted in the most viscous medium tested (50% PBS and 50% glycerol) only increased their diameter by 0.18 μm.

Figure 2.14 shows the concentration of microbubbles with respect to time. The greater the viscosity of the dilution medium, the lower was the decrease in concentration over time. After 24 hours, there were still 53% of MBs present in the most viscous medium, while there were only 32% of MBs in the least viscous one. At higher viscosities, the main mechanism connected to MB decrease in concentration is thought to be at the solution-air interface where gas exchange takes place; while, at lower

Table 2.3: *The table shows the mean diameter and standard deviation of microbubbles with respect to time, obtained by suspending microbubbles in media with different bulk viscosity. PBS: phosphate buffered saline; G: glycerol.*

	After production [μm]	After 5 hours [μm]	After 24 hours [μm]
100% PBS, μ = 1.58 cP	3.66 ± 2.90	5.15 ± 3.33	6.27 ± 5.06
60% PBS 40% G, μ = 8.26 cP	3.48 ± 4.51	3.15 ± 3.79	3.85 ± 4.35
50% PBS 50% G, μ = 15.38 cP	2.93 ± 3.53	2.77 ± 2.69	3.11 ± 3.72

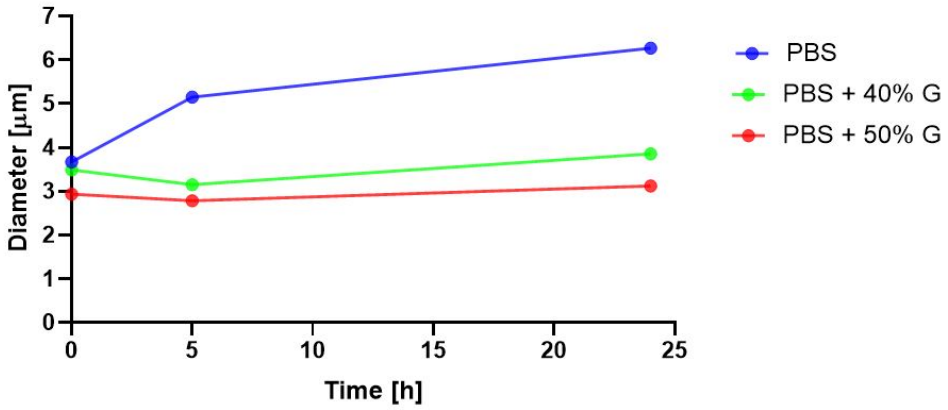

Figure 2.13: *The graph shows the time evolution of MB mean diameter, where microbubbles were suspended in media with different viscosity. Increasing the viscosity of the suspension medium resulted in more stable MBs. MBs diluted in the most viscous medium (50% PBS and 50% Glycerol) maintained a diameter close to their original size of approximately 3 μm, over one day; while MBs diluted in the least viscous medium (100% PBS) increased their size by 3 μm over 1 day. PBS: phosphate buffered saline; G: glycerol. Every line represents the mean of measurements performed on three independent vials (N = 3) of the same formulation.*

viscosities, gas exchange across the lipid shell and into the solution may be the main mechanism. MBs diameter remained unaltered at higher viscosities thanks to a lower interaction between MBs, while concentration decreased anyway because MBs concentrated at the solution-air interface and broke releasing their inner gas into the surrounding atmosphere.

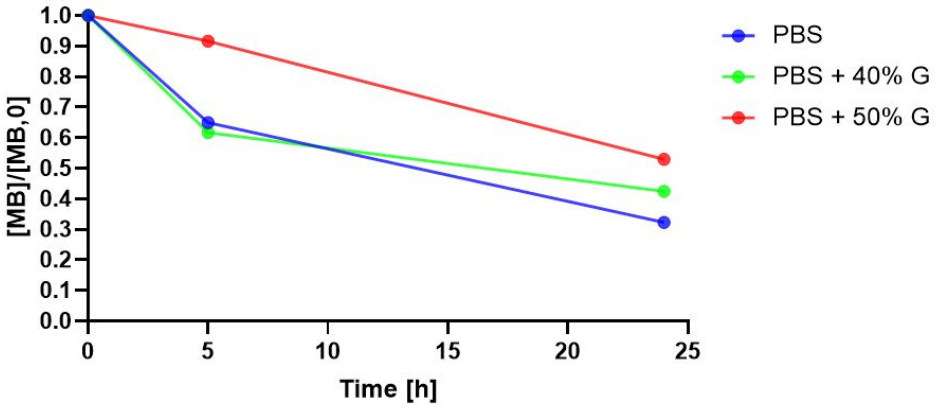

Figure 2.14: *The graph shows the time evolution of MB normalised concentration, where microbubbles were suspended in media with different viscosity. The greater was the viscosity of the dilution medium, the lower was the decrease in MB concentration with respect to time. PBS: phosphate buffered saline; G: glycerol. Every line represents the mean of measurements performed on three independent vials (N = 3) of the same formulation.*

A one-way ANOVA test was performed on the mean diameters at the different time points investigated. It determined that there was a statistically significant difference ($p < 0.05$) between the four groups at each time point.

A t-test was also performed on the data related to the concentration of MBs with respect to time, to evaluate whether there was any statistical difference between mean values. The result of the t-test shows that there is no significant difference between the concentrations of the different groups tested at different time points ($p > 0.05$).

2.2.1.2.3 Effect of fluorescent labelling

Experiments were performed to evaluate the effect of a lipophilic fluorescent label on MB diameter and concentration. DiI was added with concentrations of 2.14, 10.71 and 21.42 μM corresponding to molar ratios DSPC:PEG40s:DiI of 0.89:0.101:0.00025, 0.9:0.101:0.0012, and 0.9:0.101:0.0025 respectively. Figure 2.15 shows an image of the fluorescent microbubbles labelled with 2.14 μM DiI. Images demonstrate that this

amount of DiI is sufficient for static imaging of MBs, similarly to the concentration used by Talu et al. [144], who used a molar ratio of 0.9:0.101:0.000196.

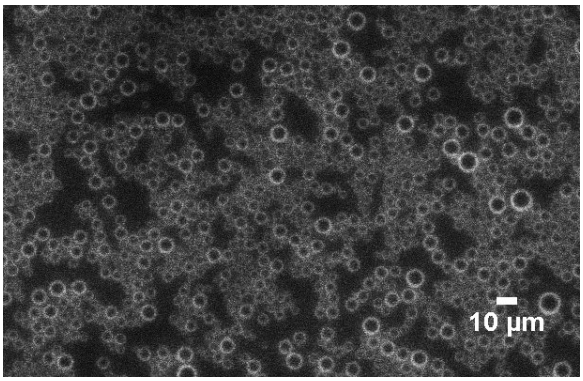

Figure 2.15: *Microscope image of fluorescent MBs labelled with 2.14 µM DiI. The picture was taken with an IX71 Olympus microscope, with a magnification lens of 10x.*

Figure 2.16 shows the diameter of microbubbles with respect to time. Higher concentrations of DiI led to larger mean MB diameter, at all time points tested. After production, the presence of Dil increased the mean diameter from 4.99 ± 3.8 up to 5.48 ± 2.99 µm; while after 6 days from production, the increase was from 13 ± 11.82 to 17.94 ± 14.74 µm.

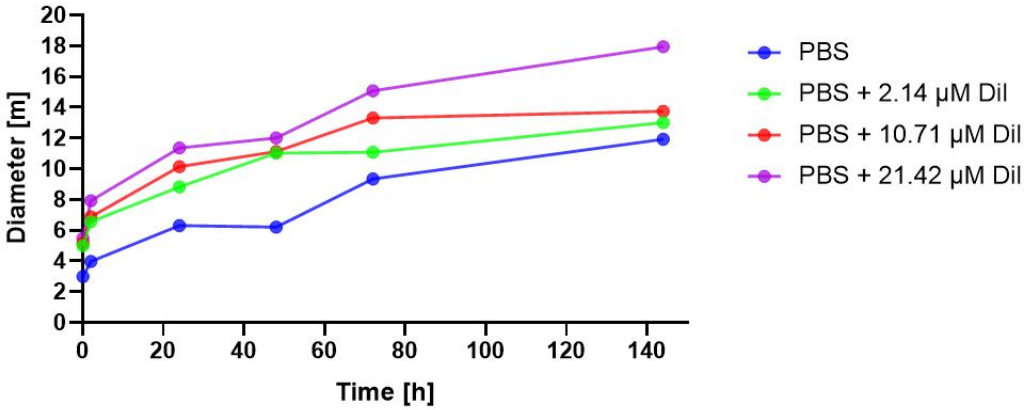

Figure 2.16: *The graph shows the diameter of microbubbles labelled with different molar quantities of DiI, with respect to time. An increase in the quantity of DiI led to an increase in the mean MB diameter, at each time point tested. Every line represents the mean of measurements performed on three independent vials (N = 3) of the same formulation.*

Figure 2.17 shows the concentration of microbubbles with respect to time, for the different shell compositions tested. It can be observed that increasing the amount of DiI did not have a marked effect on MB concentration.

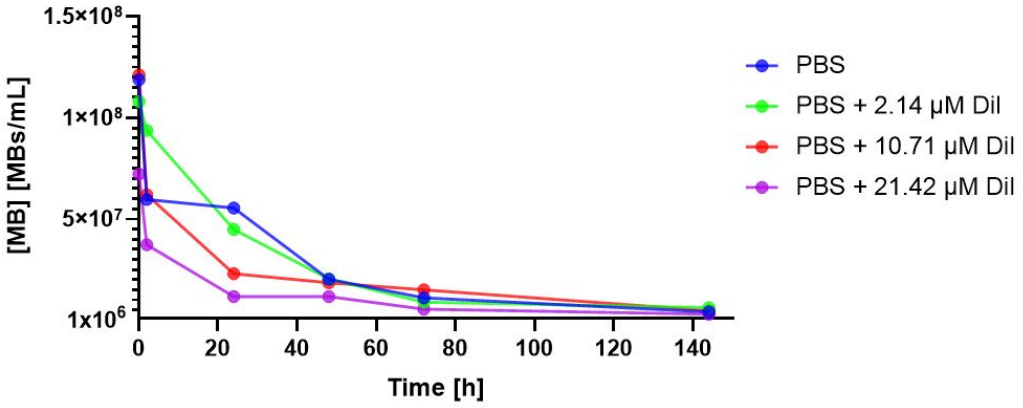

Figure 2.17: *The graph shows the average concentration of microbubbles labelled with different quantities of DiI with respect to time. Every line represents the mean of measurements performed on three independent vials (N = 3) of the same formulation.*

A one-way ANOVA test was performed to determine if different molar amounts of DiI led to MBs having different mean diameter. The test revealed that there is sufficient evidence ($p < 0.05$) to conclude that the mean diameter of the four groups belongs to different populations, at each time point. Moreover, increasing the amount of DiI resulted in a statistically significant increase in the mean diameter of microbubbles at all time points. Table 2.4 shows the time evolution of the mean MB diameter, for different molar amounts of DiI.

Table 2.4: *The table shows the mean MB diameter with respect to time, for MBs labelled using different concentrations of DiI.*

	After production [µm]	After 2 hours [µm]	After 1 day [µm]
0 µM	2.99 ± 2.45	3.98 ± 4.15	6.31 ± 6.14
2.14 µM	4.99 ± 3.80	6.56 ± 4.59	8.82 ± 5.56
10.71 µM	5.15 ± 3.23	6.86 ± 4.23	10.14 ± 8.08
21.42 µM	5.47 ± 2.99	7.92 ± 4.86	11.36 ± 8.26

	After 2 days [μm]	After 3 days [μm]	After 6 days [μm]
0 μM	6.20 ± 5.15	9.34 ± 7.58	11.92 ± 10.66
2.14 μM	11.02 ± 8.07	11.07 ± 9.09	13.00 ± 11.82
10.71 μM	11.13 ± 8.47	13.31 ± 10.27	13.73 ± 12.52
21.42 μM	12.01 ± 8.08	15.07 ± 11.12	17.94 ± 14.74

Generally, increasing the concentration of DiI in the MB formulation led to an increase in the mean diameter, but this difference was only significantly higher at the highest concentration (molar ratio of DSPC:PEG40s:DiI equal to 0.9:0.101:0.0025) compared to PBS ($p < 0.05$; at each time point)

2.2.1.2.4 Effect of the conditions of a cell incubator

Experiments were made to investigate the effect of environmental conditions on MB stability, and particularly different temperatures, humidities and concentrations of CO_2 were tested, as described in Paragraph 2.1.1.2.4.

Figure 2.18 shows the diameter of microbubbles with respect to time. It can be observed that the storage temperature had a major effect on the size of MBs, while the other conditions tested, namely the dilution medium and the type of inner gas, did not alter the stability significantly. Notably, the mean diameter of MBs stored at 37°C after 2 hours was 15.88 μm, which was greater than the diameter of MBs stored at 4°C (5.54 μm).

Figure 2.19 shows the concentration of microbubbles with respect to time, for all the different conditions tested. Temperature was the parameter with the highest impact on concentration. The concentration of MBs stored at 4°C slightly decreased from 3.09 x 10^8 MBs/mL to 7.49 x 10^7 MBs/mL over 2 hours; while the concentration of MBs stored at 37°C decreased from 2.8 x 10^8 MBs/mL to 6.57 x 10^6 MBs/mL over 2 hours. The other conditions tested, namely the dilution medium and the inner gas, did not have a marked impact on the concentration of MBs with respect to time.

A one-way ANOVA test was run to assess the presence of a statistical difference between the diameters of MBs stored in different conditions, at different time points. This test demonstrated that all groups were significantly different at all time points ($p < 0.05$).

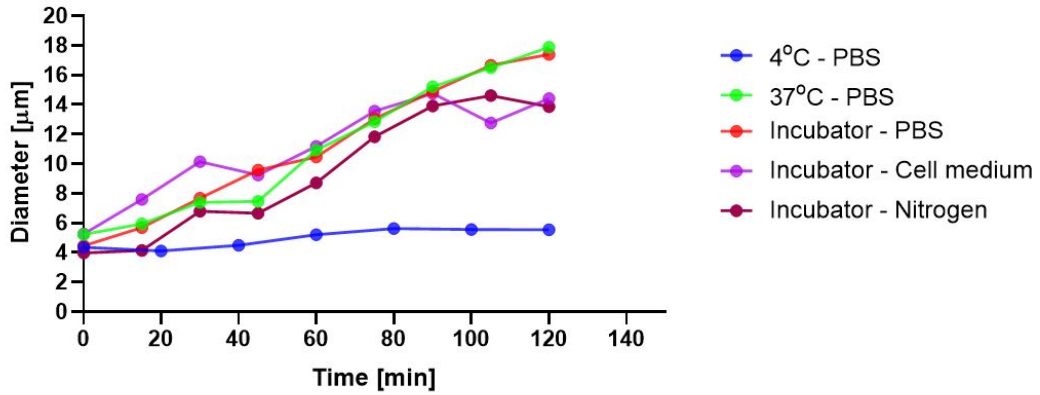

Figure 2.18: *The graph shows the diameter of MBs stored in different environmental conditions with respect to time. The storage temperature had a major effect on the size of MBs. The mean diameter of MBs stored at 37°C after 2 hours is 15.88 µm, which is bigger than the diameter of MBs stored at 4°C (equal to 5.54 µm). Every line represents the mean of measurements performed on three independent vials (N = 3) of the same formulation.*

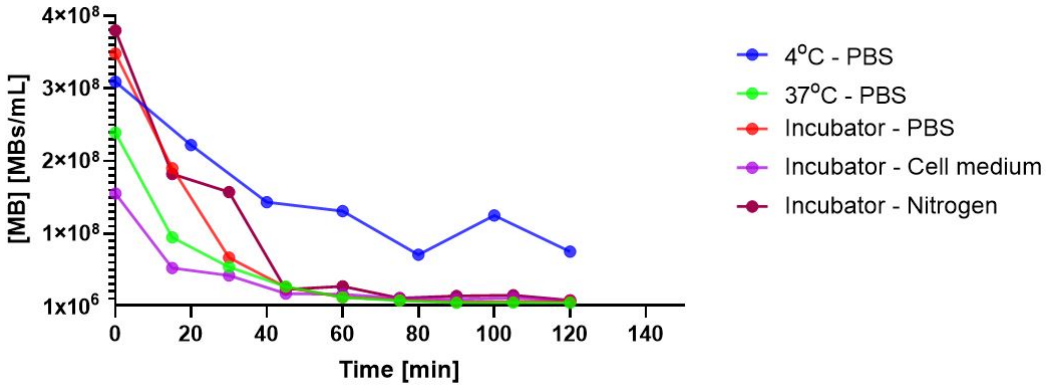

Figure 2.19: *The graph shows the concentration of MBs stored in different environmental conditions with respect to time. Temperature was the parameter with the highest impact on concentration. Indeed, the concentration of MBs stored at 4°C slightly decreased from 3.09 x 10^8 MBs/mL to 7.49 x 10^7 MBs/mL over 2 hours; while the concentration of MBs stored at 37°C decreased from 2.8 x 10^8 MBs/mL to 6.57 x 10^6 MBs/mL over 2 hours. Every line represents the mean of measurements performed on three independent vials (N = 3) of the same formulation.*

A t-test was performed on the data related to the concentration of MBs with respect to time to evaluate whether there was any statistical difference between mean values. The test demonstrated that the concentration of MBs stored in the fridge at 4°C was always statistically higher than the ones stored in the incubator ($p < 0.05$). The other results of the test are inconsistent with the idea that there are significant differences between the groups of MBs stored in the incubator ($p > 0.05$); thus producing MBs in PBS or cell medium and filling the gas core with room air or nitrogen did not alter the stability of MBs.

2.2.1.2.5 Effect of producing and/or suspending MBs in cell medium

Experiments were performed to investigate the effect of producing and/or diluting MBs in cell medium instead of PBS on MB stability, as described in Paragraph 2.1.1.2.5.

Figures 2.20 and Table 2.5 show the diameter of MBs produced in PBS and then measured without being diluted or with a volumetric dilution equal to 1:2 or 1:5 in PBS. Figure 2.21 instead shows their concentration with respect to time. The greater the dilution, the larger is the mean diameter of microbubbles at each time point, suggesting that dilution has an effect on the size of MBs. MBs not diluted had an initial mean diameter of 4.45 ± 3.29 μm, 2.05 μm smaller than the ones diluted 1:5 in PBS (6.50 ± 6.41 μm). As for the MB concentration, no conclusion can be drawn on the relationship between dilution and the rate of decrease in the number of bubbles. Indeed, MBs diluted 1:2 in PBS maintained a higher concentration with respect to time (15% higher after one hour of observation) compared to the two other cases (diluted and diluted 1:5 in PBS), suggesting that there is not an obvious relationship between dilution and concentration.

Table 2.5: *The table shows the mean MB diameter with respect to time for MBs produced in PBS and then diluted at different ratios in PBS.*

	After production [μm]	After 15 min [μm]	After 30 min [μm]	After 45 min [μm]	After 60 min [μm]
1	4.45 ± 3.29	5.68 ± 5.3	7.67 ± 7.09	9.57 ± 7.05	10.46 ± 7.98
1:2	6.82 ± 6.29	7.98 ± 7.63	9.18 ± 7.54	10.53 ± 7.98	11.50 ± 7.81
1:5	6.50 ± 6.41	10.17 ± 8.68	11.11 ± 7.99	12.81 ± 8.50	11.65 ± 10.58

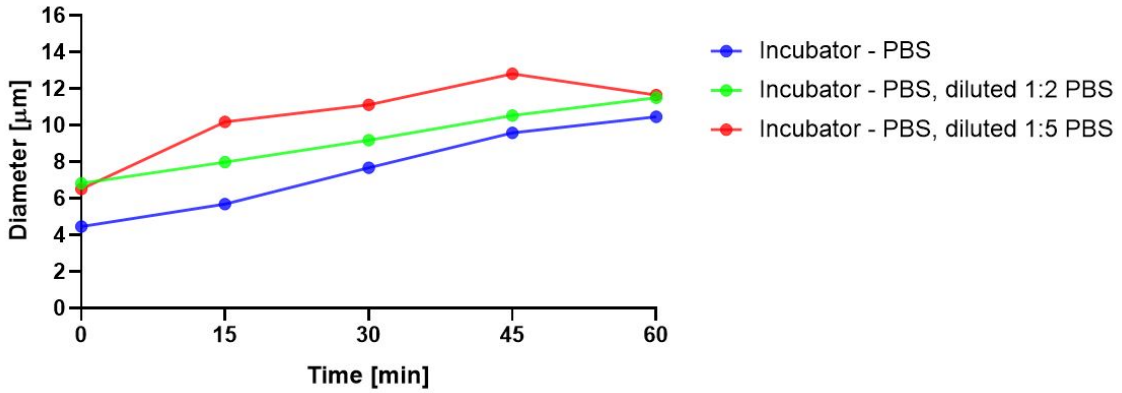

Figure 2.20: *The graph shows the diameter of microbubbles produced in PBS without dilution and produced in PBS and then diluted 1:2 and 1:5 by volume in PBS. After production, MBs were stored in a cell incubator at 37°C. The greater the dilution of MBs in PBS, the larger their mean diameter at different time points. Every line represents the mean of measurements performed on three independent vials (N = 3) of the same formulation.*

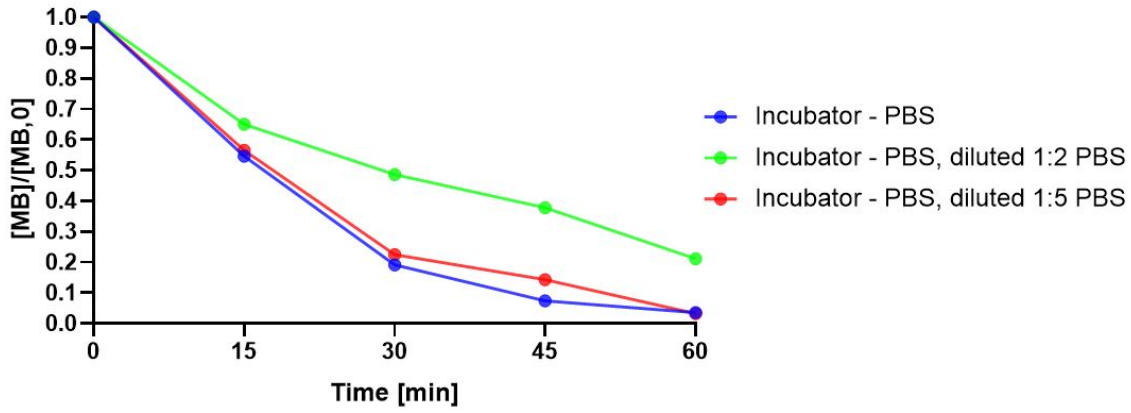

Figure 2.21: *The graph shows the normalised concentration of microbubbles produced in PBS without dilution, and produced in PBS and then diluted 1:2 and 1:5 in PBS. The normalisation is performed with respect to the initial concentration of MBs for each condition tested. After production, MBs were stored in a cell incubator at 37°C. Every line represents the mean of measurements performed on three independent vials (N = 3) of the same formulation.*

Figures 2.22 and Table 2.6 show the diameter of MBs produced in DMEM, or produced in PBS and then diluted 1:2 or 1:5 in DMEM. Figure 2.23 instead shows their concentration with respect to time. Results show that greater MB dilutions led to larger MBs at each time point. The mean diameter of microbubbles diluted 1:5 was 2.5 μm larger than undiluted MBs (7.77 ± 7.24 μm vs 5.26 ± 6.13 μm). In the case of the 1:5 dilution, after 30 minutes there were only few bubbles left and, for this reason, the data at this time point are not reliable. After 45 minutes no microbubble could be detected. As for the MB concentration, the most diluted MB sample displayed the quickest rate of decrease in concentration; after 15 minutes, only 10% of the initial MBs were present.

Table 2.6: *The table shows the mean MB diameter with respect to time for MBs produced in DMEM and undiluted, and produced in PBS and then diluted at different volume ratios in DMEM.*

	After production [μm]	After 15 min [μm]	After 30 min [μm]	After 45 min [μm]	After 60 min [μm]
1	5.26 ± 6.13	7.59 ± 6.94	10.14 ± 9.00	9.24 ± 8.73	11.17 ± 9.94
1:2	6.12 ± 5.57	7.19 ± 5.84	10.58 ± 16.84	11.14 ± 11.54	15.11 ± 11.13
1:5	7.77 ± 7.23	12.01 ± 10.55	9.03 ± 10.74	-	-

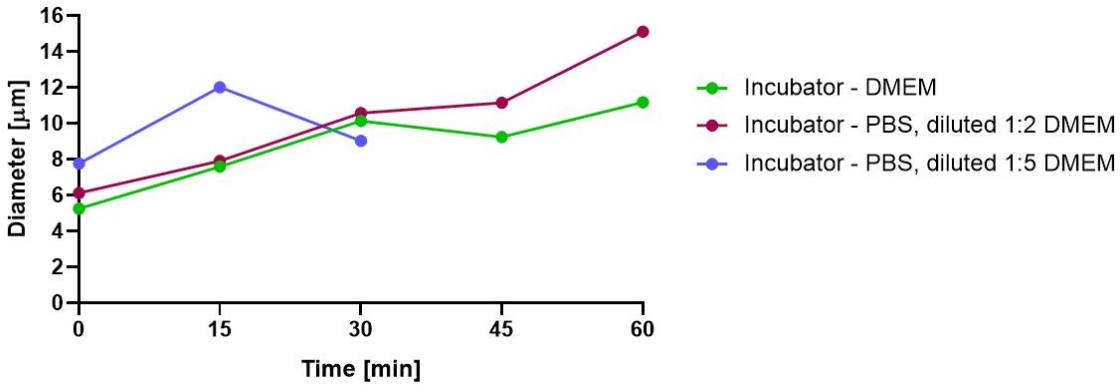

Figure 2.22: *The graph shows the diameter of microbubbles produced in DMEM without dilution, and produced in PBS and then diluted 1:2 and 1:5 in DMEM. After production, MBs were stored in a cell incubator at 37°C. Every line represents the mean of measurements performed on three independent vials (N = 3) of the same formulation.*

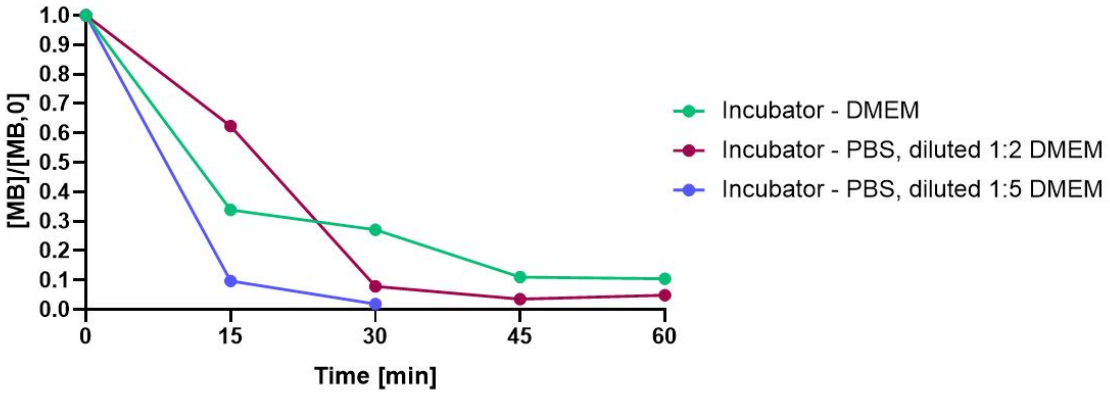

Figure 2.23: *The graph shows the normalised concentration of microbubbles produced in DMEM without dilution, and produced in PBS and then diluted 1:2 and 1:5 in DMEM. The normalisation is performed with respect to the initial concentration of MBs for each condition tested. After production, MBs were stored in a cell incubator at 37°C. Every line represents the mean of measurements performed on three independent vials (N = 3) of the same formulation.*

Figures 2.24 and Table 2.7 show the diameter of MBs produced in DMEM with an addition of 10% FBS, or produced in PBS and then diluted 1:2 or 1:5 in DMEM and 10% FBS. Figure 2.25 instead shows their concentration with respect to time. Results show that increasing the MB dilution led to an increase in the mean MB diameter, at each time point. The mean diameter of microbubbles diluted 1:5 was 4.79 μm greater than the one of undiluted MBs. After 45 minutes there was no microbubble left. As for MB concentration, the most diluted MBs shows the quickest rate of decrease of concentration over time: after 15 minutes only the 7% of MBs are still in the solution vs the 55% in the undiluted case.

Table 2.7: *The table shows the mean MB diameter with respect to time for MBs produced in DMEM and 10% FBS, and undiluted and produced in PBS and then diluted at different ratios in DMEM and 10% FBS.*

	After production [μm]	After 15 min [μm]	After 30 min [μm]	After 45 min [μm]	After 60 min [μm]
1	4.95 ± 4.06	6.21 ± 6.07	7.56 ± 6.60	8.33 ± 7.55	9.58 ± 8.96
1:2	5.93 ± 5.60	7.32 ± 6.63	10.47 ± 8.33	10.83 ± 8.82	11.51 ± 9.91
1:5	9.74 ± 7.22	12.09 ± 12.19	14.06 ± 12.75	-	-

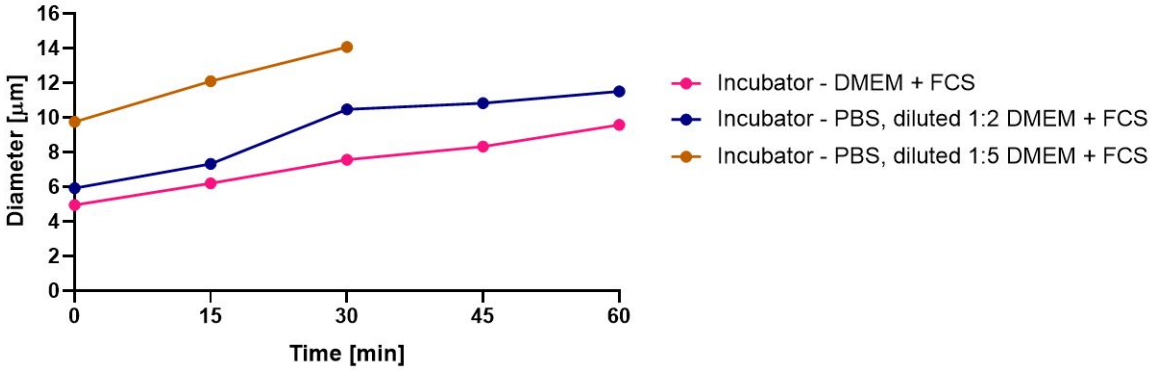

Figure 2.24: *The graph shows the diameter of microbubbles produced in a solution composed of DMEM and 10% FBS without dilution, and produced in PBS and then diluted 1:2 and 1:5 in DMEM and 10% FBS. After production, MBs were stored in a cell incubator at 37 degrees. The higher the dilution, the larger the mean diameter with respect to time; i.e. the mean diameter of microbubbles diluted 1:5 is 4.79 µm greater than the one of undiluted MBs. Every line represents the mean of measurements performed on three independent vials (N = 3) of the same formulation.*

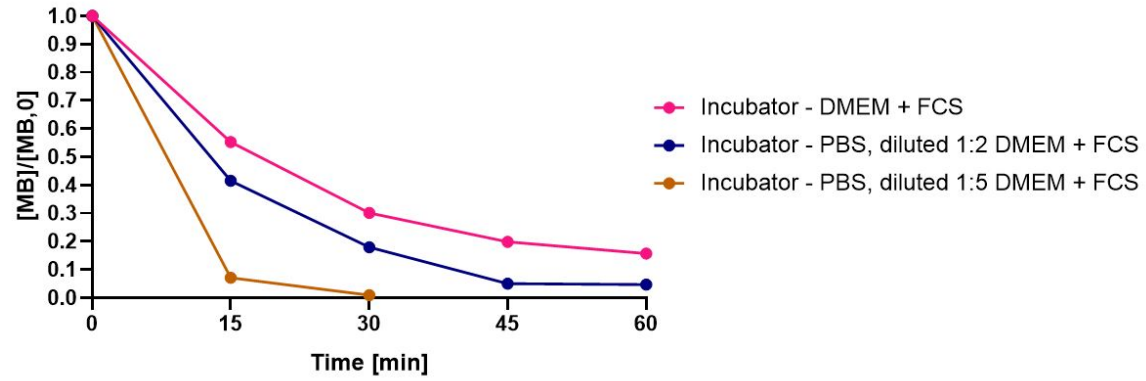

Figure 2.25: *The graph shows the normalised concentration of microbubbles produced in a solution composed of DMEM and 10% FBS without dilution, and produced in PBS and then diluted 1:2 and 1:5 in DMEM and 10% FBS. The normalisation is performed with respect to the initial concentration of MBs for each condition tested. After production, MBs were stored in a cell incubator at 37°C.Every line represents the mean of measurements performed on three independent vials (N = 3) of the same formulation.*

The difference in diameter between undiluted and diluted MB suspensions can be observed in the microscope images, as shown in Figure 2.26.

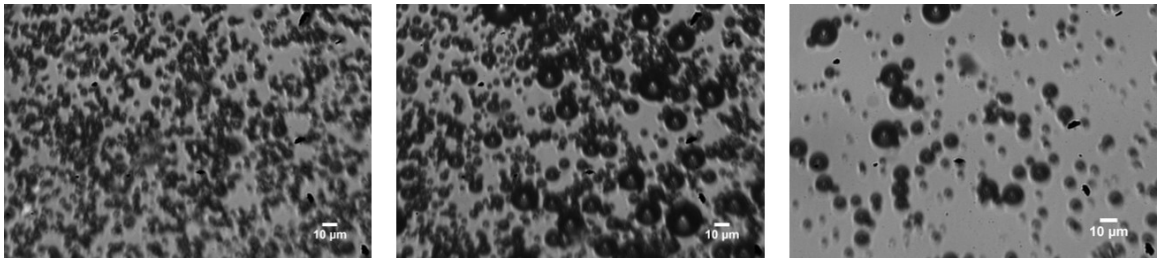

Figure 2.26: *Microscope image taken with a 10x objective of A) MBs produced in PBS, B) MBs produced in DMEM and diluted 1:2 in DMEM, and C) MBs produced in DMEM and diluted 1:5 in DMEM. The greater the dilution, the larger is the mean diameter of microbubbles.*

Overall, increasing the dilution led to larger MBs and lower MB concentration with respect to time. The same behaviour was observed for all the three different dilution media tested, suggesting that the composition of the medium does not have as much as an impact as the dilution itself.

2.2.1.2.6 Effect of the lipid shell formulation

Experiments were performed to assess the influence of different MB shell constituents on the stability of microbubbles with respect to time. MBs were produced with a lipid shell composed of DBPC/DSPE-PEG2000 (molar ratio 9:1) and compared to DSPC/PEG40s (molar ratio 9:1).

Figures 2.27 and 2.28 show respectively the MB concentration and diameter with respect to time. Microbubbles were produced as described in Paragraph 2.1.1.2.6, and stored at 37^{o}C for two hours.

Results show that DBPC/DSPE-PEG2000 MBs are more stable in terms of size and concentration than DSPC/PEG40s. As for their concentration, the former are able to maintain their initial concentration of approximately 4 x 10^8 MBs/mL for two hours at 37^{o}C, while the latter decreased their concentration of a factor of 10^2 MBs/mL. As for the MB diameter, DBPC/DSPE-PEG2000 MBs were able to maintain their initial diameter of approximately 5 µm for two hours, while their counterparts, with a DSPC/PEG40s shell, increased their diameter from 4.45 to 17.39 µm.

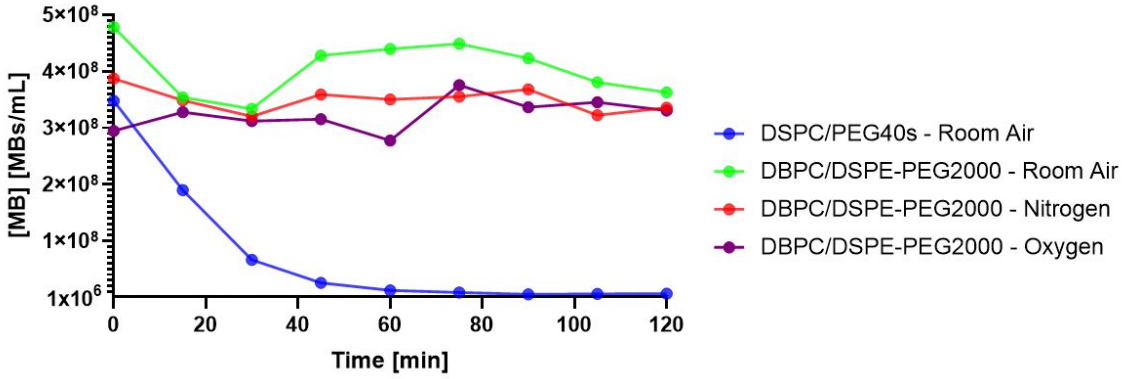

Figure 2.27: *The graph shows the concentration of MBs with respect to time. Results correspond to MBs having a lipid shell composed of DBPC/DSPE-PEG2000 and filled with either room air, nitrogen or oxygen (green, red and purple lines). These formulations are compared with DSPC-PEG40s microbubbles (blue line), filled with room air. Every line represents the mean of measurements performed on three independent vials (N = 3) of the same formulation.*

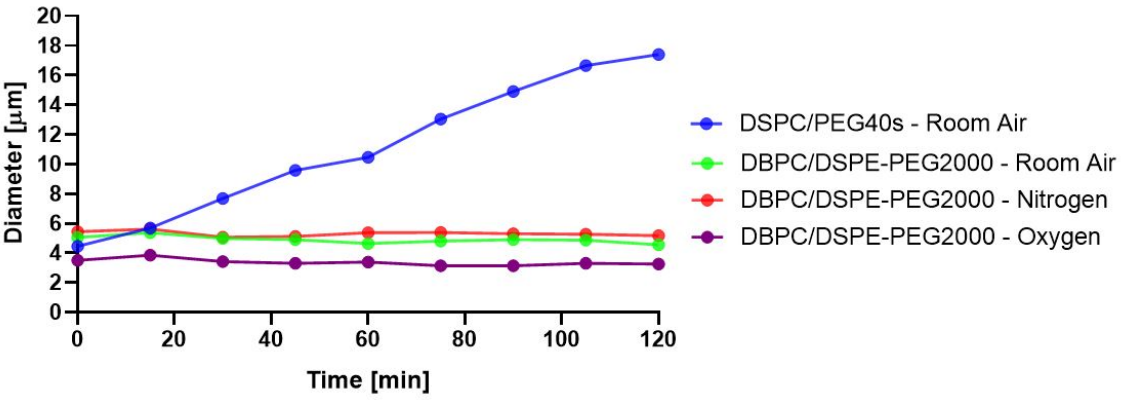

Figure 2.28: *The graph shows the diameter of MBs with respect to time. Microbubbles represented by the green, red and purple line have a lipid shell composed of DBPC/DSPE-PEG2000 and are filled with room air, nitrogen or oxygen, respectively. MBs represented by the blue line have a lipid shell composed of DSPC-PEG40s and are filled with room air. Every line represents the mean of measurements performed on three independent vials (N = 3) of the same formulation.*

2.2.2 Precursors of Microbubbles

As explained in Paragraph 2.1.2, experiments were carried out to investigate the size of microbubble precursors (i.e. in the form of liposomal structures) obtained at different stages of the MB production process. Liposome size was obtained through DLS measurements.

2.2.2.1 Effect of the duration of sonication on liposome dimension

Figure 2.29 and Table 2.8 show the diameter of liposomes obtained using different sonication protocols. There was a statistically significant difference between liposomes obtained without sonication (i.e. from lipid hydration only) and the ones obtained with sonication. Moreover, there was a statistically significant difference between liposomes obtained with a pulsed sonication, and the ones obtained with a continuous sonication. The statistical difference was determined by a one-way ANOVA test ($p < 0.05$). However, there was no statistical difference between the diameter of liposomes obtained by continuous sonication of different durations.

Table 2.8: *Mean diameter and standard deviation of MB precursors (liposomes), obtained after different sonication protocols.*

	Diameter [nm]
No sonication	229.76 ± 27.64
30 seconds	59.32 ± 6.33
1 minute	53.51 ± 10.06
2 minutes	49.49 ± 6.09
2 minutes 30 seconds	55.75 ± 6.87
3 minutes	65.20 ± 6.11
4 minutes	54.67 ± 8.72
5 minutes	60.37 ± 5.66
Pulsed	98.45 ± 16.98

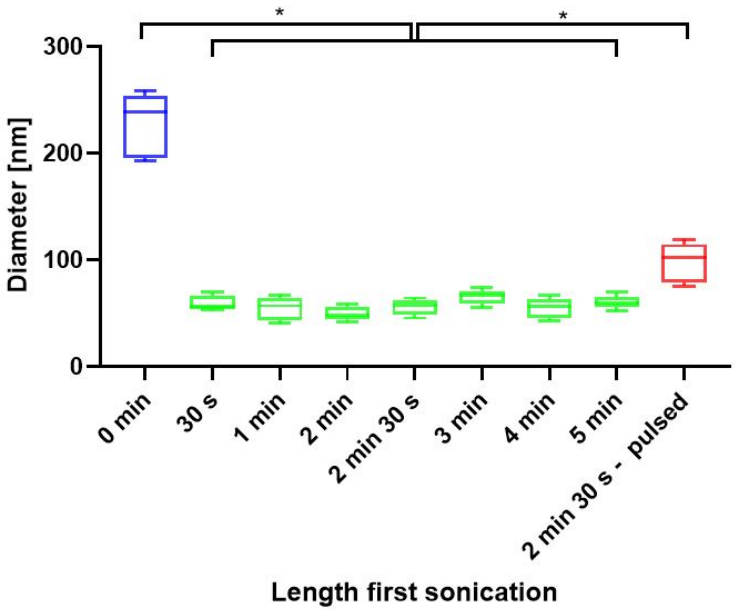

Figure 2.29: *The boxplots show the size distribution of liposomes obtained from different sonication protocols. Liposomes have comparable size, except for the ones that were either not sonicated or sonicated using a pulsed wave (4 seconds, with 50% duty cycle). The bars on the top of the graph indicate the groups that are statistically different (*$p < 0.05$). Every boxplot represents the mean of measurements performed on three independent vials ($N = 3$) of the same formulation.*

2.2.2.2 Effect of a pulsed sonication on the diameter of MBs

Given the statistically significant difference between the dimensions of liposomes produced without sonication, continuous sonication and pulsed sonication, gas MBs were produced using these three types of liposomes to assess whether the size of MB precursors affected the actual MB size.

Figure 2.30 shows the diameter of microbubbles produced with a continuous sonication (2 minutes and 30 seconds) and with a pulsed sonication (2 minutes and 30 seconds, pulsation of 4 seconds with 50% duty cycle) over a period of 6 days. By performing a one-way ANOVA test on these data, it was found that all data points were statistically different ($p < 0.05$); however, it was not possible to define a trend since there was not a sonication that led to smaller MBs with comparison to the other one at all time points.

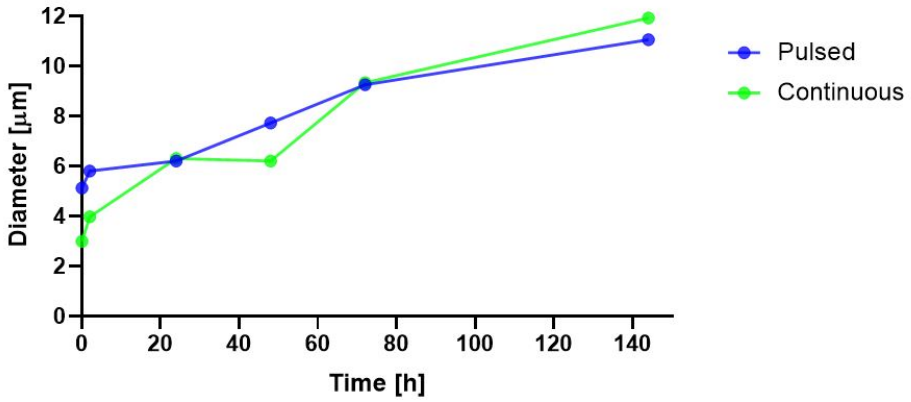

Figure 2.30: *The graph shows the diameter of microbubbles obtained using liposomes produced using continuous or pulsed sonication. The mean MB diameter increased from 4.06 to 11.48 µm over six days. Every line represents the mean of measurements performed on three independent vials (N = 3) of the same formulation.*

Figure 2.31 shows the concentration of microbubbles with respect to time. A first pulsed sonication led to a higher concentration of microbubbles after production and after two hours, compared to the concentration of MBs obtained with a continuous sonication. However, the difference in the stated concentrations reduced after one day.

To investigate the difference between producing microbubbles using precursors obtained without sonication, with a continuous sonication or a pulsed sonication (pulsation of 4 seconds with 50% duty cycle) in a more systematic way, a further

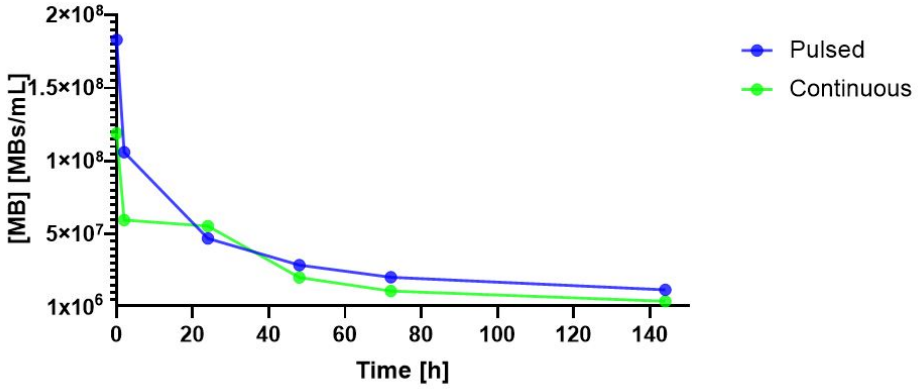

Figure 2.31: *The graph shows the concentration of microbubbles obtained using liposomes generated with a continuous (2 minutes and 30 seconds) or pulsed (2 minutes and 30 seconds, pulsation of 4 seconds with 50% duty cycle) sonication. Every line represents the mean of measurements performed on three independent vials (N = 3) of the same formulation.*

test was performed analysing the diameter and concentration of microbubbles after production. Figures 2.32 and 2.33 show respectively the diameter and the concentration of microbubbles after production. A one-way ANOVA test was performed on these data, and it showed that MBs obtained from unsonicated liposomes are different from the ones obtained from the sonicated ones ($p < 0.05$). As for the MB diameter, Figure 2.32 and Table 2.9 show that the difference between a continuous and a pulsed sonication was negligible, while the difference between these two groups and the unsonicated group was significant.

Table 2.9: *The table shows the mean diameter and standard deviation of microbubbles (after production), obtained from MB precursors generated with different sonication protocols.*

	Diameter [μm]
No sonication	6.44 ± 3.70
Continuous sonication	4.72 ± 2.17
Pulsed sonication	4.71 ± 2.48

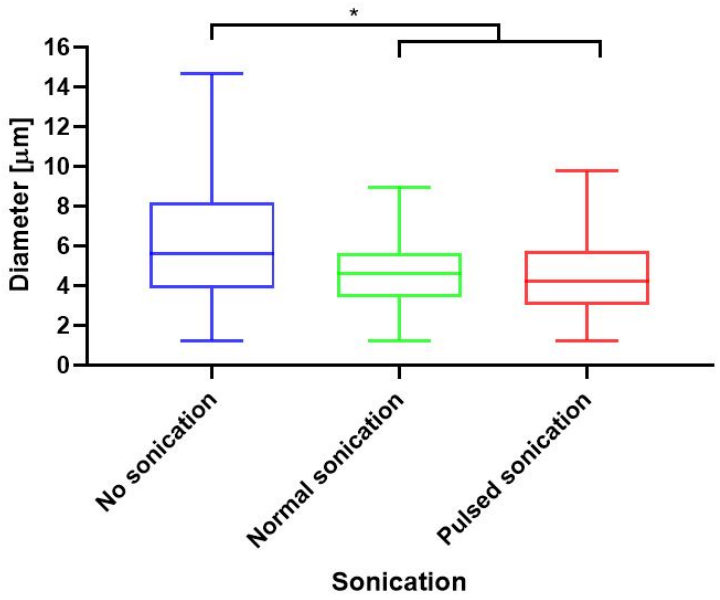

Figure 2.32: *The boxplots show the size distribution (after production) of microbubbles obtained from liposomes generated without sonication (hydration only), with a continuous sonication, and with a pulsed sonication. MBs obtained from unsonicated liposomes were statistically different from the ones obtained from the sonicated ones (*$p < 0.05$). Every boxplot represents the mean of measurements performed on three independent vials ($N = 3$) of the same formulation.*

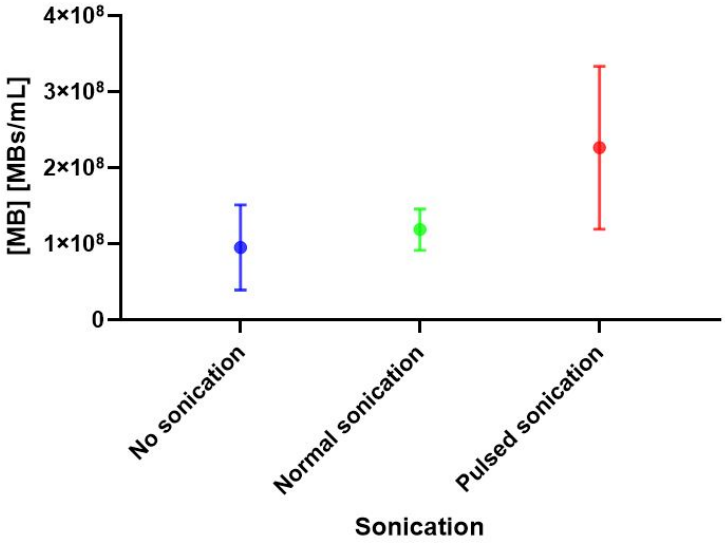

Figure 2.33: *The graph shows the concentration (after production) of microbubbles obtained from liposomes generated without sonication (hydration only), with a continuous sonication, and with a pulsed sonication. Three repetitions were performed for each case.*

Microbubble precursors generated with a pulsed sonication led to a greater MB concentration than those produced by continuous sonication. Producing microbubbles from precursors generated without sonication instead led to a lower MB concentration. These differences can be appreciated from the MB size distribution, as shown in Figure 2.34. From this graph, it can be observed that MB median diameter and the shape of the size distribution was comparable between the three protocols; however, the number of microbubbles was much greater for MBs generated from the sonicated batches compared to the unsonicated one.

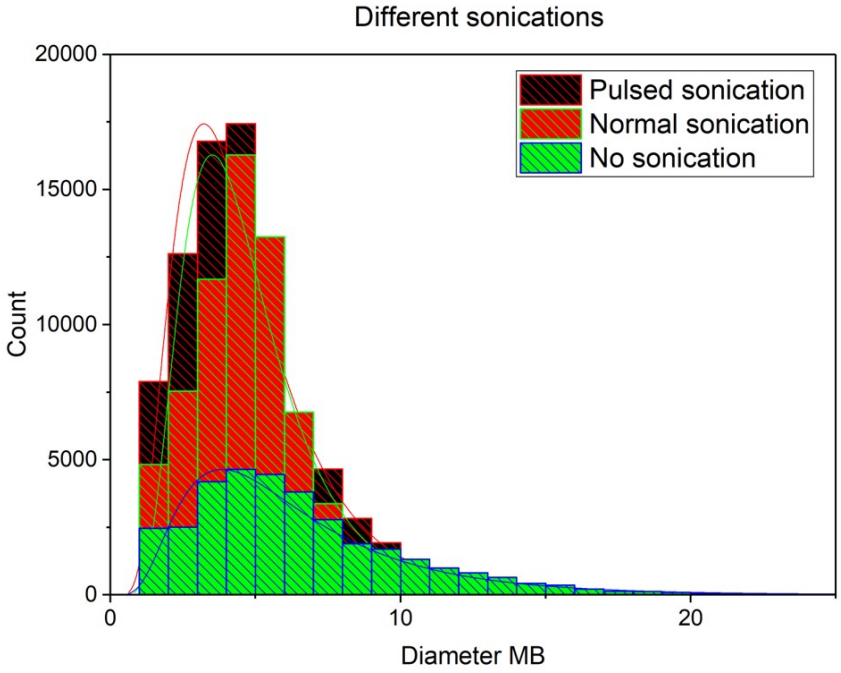

Figure 2.34: *The graph shows the size distribution (after production) of MBs obtained from liposomes generated without sonication (hydration only), with a continuous sonication (2 minutes and 30 seconds), and with a pulsed (2 minutes and 30seconds, pulsation of 4 seconds with 50% duty cycle) sonication.*

2.3 Discussion

In order to develop ultrasound-responsive agents providing desirable and controllable therapeutic performance, both *in vitro* and *in vivo*, it is fundamental to first evaluate the behaviour of microbubbles alone and the influence of different physico-chemical parameters on their stability. Microbubbles should be stable, in terms of their mean dimension and concentration, and their size dispersity should be limited. The MB size should be kept below the safety limit of 10 μm to avoid obstructing blood vessels [140]. A high concentration is desirable to allow a therapeutic dose of drug to reach the injury site and act locally [28]; while low size dispersity is desirable to allow for comparable drug loading and acoustic response across different MBs in a suspension [155].

Different studies in the literature suggest that there is a relation between production parameters of microbubbles and their final size and stability, but the majority of these previous studies is not quantitative. In addition to this, microbubbles have been mainly developed for application in cancer treatment, while limited attention has been paid to their use in bone therapies. The knowledge gaps that will be addressed in the next paragraphs regard the quantitative effects of medium viscosity, storing conditions, labelling of MBs and MB chemical composition on their stability in terms of their size and concentration with respect to time.

2.3.1 Generation of Microbubbles

2.3.1.1 Reproducibility of the MB production and sizing method

As shown in Paragraph 2.2.1.1 (page 86), the process of microbubble production by sonication and the MB sizing process can be considered reproducible, as only in a minor proportion of repeats MBs were statistically different from each other. A previous study in the literature by Feinstein et al. [156] had previously shown that sonication allows to obtain reproducible batches of MBs in terms of size; however 25 to 50 trial runs were necessary for the operator to produce repeatable MB batches.

Repeating the sonication process several times allows obtaining similar batches and, as shown in Figure 2.10 on page 86, this stage has been reached in this study. In addition, knowing that the produced batches share similar physical characteristics, provides confidence for using this manufacturing methods and the produced samples

in future investigations both *in vitro* and *in vivo*.

2.3.1.2 Effect of viscosity on MB stability

In order to preserve safety and efficacy, MB size and concentration should be maintained over time. It is known that one of the main physical phenomena affecting stability is Ostwald ripening, namely the diffusion of the inner gas of smaller microbubbles into the surrounding medium and the subsequent diffusion of this gas into larger MBs. Since the diffusivity of the gas is inversely proportional to the viscosity of the fluid in which diffusion occurs, the quantitative effect of diffusion on MB stability was tested.

In a first experiment, MBs were produced in media composed of different quantities of PBS, glycerol and propylene glycol, with viscosity ranging between 1.58 and 5.26 cP. The choice of glycerol and propylene glycol was driven by the fact that they are already used in the literature to prevent microbubble coalescence [150] [151].

Figure 2.11 (page 88) shows the concentration of microbubbles produced in different media composed of PBS, glycerol and propylene glycol with respect to time, as described in Paragraph 2.2.1.2.1, revealing a marked drop in the number of MBs between the time of production and two hours after production. This observation is consistent with prior studies reported in the literature by Kaya et al. [48].

It was however not possible to draw any relevant conclusion from these tests. The data shown in Figure 2.12 (page 88) suggest that after 1, 2 and 3 days from production, an increase in the viscosity of the suspension medium led to smaller bubbles. However, this dependency did not apply to MB diameter measured just after production, after 2 hours, and after 6 days from production. For this reason, further tests were required to evaluate the influence of viscosity on the stability of microbubbles.

A more systematic study of the influence of medium viscosity on the stability of microbubbles was performed. Viscosity was varied between 1.58 and 15.38 cP by adding glycerol. In Paragraph 2.2.1.2.2, Figure 2.13 (page 91) shows that an increase in the viscosity of the medium led to smaller microbubbles. The viscosity of the suspension had little effect on the diameter just after production; however, media with viscosity 5 and 10 times greater than PBS (μ = 1.58 cP) maintained a smaller microbubble diameter after 5 and 24 hours. While MBs diluted in 100% PBS experienced an increase of 2.6 μm over 1 day; MBs diluted in the most viscous

composition tested (50% PBS and 50% glycerol, $\mu = 15.38$ cP) only increased their diameter by 0.18 μm, suggesting that these MBs can be stored for longer periods while still maintaing their size, and hence their safety. These findings suggest that a glycerol content (by volume) greater than 40% ($\mu > 8.26$ cP) preserved the MB size more effectively than lower amounts. Increased medium viscosity can slow down the rate of MB dissolution, because of slower gas diffusion. Increased viscosity may also inhibit film drainage and decrease the probability of MB coalescence [73]. These findings may also suggest that a limiting viscosity has been reached at $\mu = 8.26$ cP, since there was only a small difference between microbubble diameters at 5 hours and 24 hours, for both $\mu = 8.26$ cP and $\mu = 15.38$ cP. This behaviour is consistent with other studies in the literature by Dayton et al. [150] and by Pancholi et al. [157] suggesting that increased medium viscosity leads to smaller bubbles, but only up to a certain viscosity value.

As for the concentration of microbubbles, Figure 2.14 (page 92) shows that an increase in the viscosity of the suspension medium led to a slower decrease in concentration with respect to time. This could be due to the fact that a greater fluid viscosity delays the dissolution of MBs by diffusion, thus maintaining a greater average MB concentration.

In conclusion, the desirable formulation for batch storage in the laboratory should have a glycerol content of 40%; in this way, the stability of phospholipid-shelled MBs is enhanced and MBs maintain their initial size of around 3 μm up to one day.

Glycerol is a biologically compatible substance, but high concentrations could raise immune responses by the organism; the normal dose allowed is 0.5 to 1 g/kg through intravenous injection [158]. Quantities suggested in this study do not represent an issue, but if the treatment is repeated over time, this could raise issues of ipersensibility. For these reasons, storage in glycerol is an effective strategy to maintain MB size and concentration over prolonged periods of time, but MB suspension should be centrifuged and resuspended in PBS prior to usage *in vivo*.

However, even if glycerol is a biologically compatible substance, such a high concentration could raise immune responses by the organism; the normal dose allowed is 0.5 to 1 g/kg through intravenous injection [158]. For these reasons, storage in glycerol is an effective strategy to maintain MB size and concentration over prolonged periods of time, but MB suspension should be centrifuged and resuspended in PBS prior to usage *in vivo*.

2.3.1.3 Effect of fluorescent labelling on MB stability

Labelling of MBs with fluorescent dyes allows performing multimodal imaging to better visualise and track MBs in living organisms [44] [159]; however, it can potentially affect MB size. In previous studies, lipophilic dyes such as DiI, DiO and DiD have been used to label lipid-coated MBs [44]. DiI has an excitation wavelenght $\lambda_{ex} = 550$ and an emission wavelength $\lambda_{em} = 590$; DiO has $\lambda_{ex} = 480$ and $\lambda_{em} = 520$; DiD has $\lambda_{ex} = 650$ and $\lambda_{em} = 690$. In a parallel complementary *in vivo* and *ex vivo* study of this project, it has been shown that DiO labelled MBs led to a low signal-to-noise ratio in the green emission channel. This is thought to be due to the fact that autoflourescence of tissues and blood in the emission range of the dye is too intense, hence distinguishing dye and tissue in these conditions is challenging. For this reason, DiO should be avoided and dyes with longer emission wavelengths like DiI or DiD are recommended and DiI was chosen to carry out experiments.

Figure 2.16 (page 93) shows that labelling microbubbles using the lipophilic dye DiI, in different molar ratios, had an effect on the mean diameter of microbubbles with respect to time. Greater molar amounts of DiI resulted in larger MBs over time. This observation could be due to the interaction between the dye and the MB shell constituents.

DiI is a lipophilic membrane stain with a high molecular weight (933.8793 g/mol) and it occupies a high volume due to its chemical structure, which is shown in Figure 2.35. Consequently, when it is integrated into the lipid shell of microbubbles, it may increase its overall diameter.

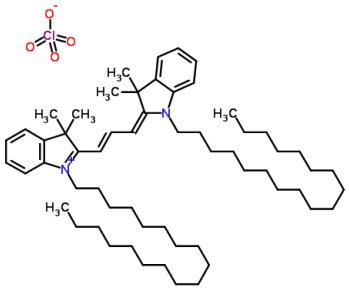

Figure 2.35: *Chemical structure of DiI.*

In lipid-shelled microbubbles, the emulsifier PEG40s is uniformly distributed on

the surface of the membrane, and this provides resistance to MB coalescence. It has been shown that DiI does not distribute uniformly on the shell, but rather forms domains that intercalate into the structure of the shell composed of PEG40s and DSPC. As a result, PEG40S is no more uniformly distributed and becomes less effective in preventing coalescence. The greater the quantity of DiI, the bigger the DiI domains; these clusters may hinder PEG40s from being uniformly distributed on the surface of the lipid shell. As a consequence, the ability of PEG40s to prevent coalescence diminishes, because there are areas of the shell where inter-bubble repulsive forces become weaker [160] [143]. This is the reason why labelled microbubbles undergo a faster increase in diameter, when compared to unlabelled ones, as shown in Figure 2.16 (page 93). In conclusion, a molar ratio of DSPC:PEG40s:DiI below 0.89:0.101:0.0002 (DiI < 2.14 μM) should be used, which is in line to what has been used in the literature to label MBs. [144]

2.3.1.4 Effect of *in vitro* conditions on MB stability

Experiments were performed to investigate MB stability at environmental conditions relevant to their application *in vitro* and *in vivo*. These tests are an important pre-requisite before investigating the interaction between cells and microbubbles. The underlying hypothesis was that a change in the temperature, humidity, and gas composition of the environment could affect MB stability, and that varying some formulation-related parameters could help enhancing MB stability.

MBs were stored in an incubator at 37°C and their stability was compared to the ones stored at 4°C. The storing conditions had a marked impact on the stability of microbubbles, as described in Paragraph 2.2.1.2.4. Figures 2.18 and 2.19 (page 96) show that both diameter and concentration of MBs were more stable over time, if MBs were stored in a fridge at 4°C. A marked decrease in their stability was observed upon storage in the incubator at 37°C. It is thought that an increase in temperature leads to a decrease in lipid packing density in the shell resulting in reduced surface tension and favouring diffusion of the gas [161]. In addition, the diffusion coefficient of molecules increases when temperature increases, independently from the behaviour of the shell. Enhanced diffusion leads both to an increase in the mean diameter of MBs and to a decrease in their number, hence their concentration. This behaviour is consistent with another study by Cavalli et al. [49] showing that MBs were more stable if stored at 4°C rather than room temperature. Shekhar et al. [162] have also

studied the effect of temperature, but the temperature values they used were not relevant for the aims of this study.

As for the other conditions tested in this experiment, namely diluting MBs in PBS or cell medium and filling MBs with room air or nitrogen, there is no statistical evidence showing that they affect the stability of microbubbles with respect to time. All groups of MBs are statistically different ($p < 0.05$), but it is not possible to define a clear trend showing that a certain experimental condition leads to an improvement or deterioration of MB stability.

Another possible challenge associated with the *in vitro* use of MBs is that, when MBs are administered to cells, they are diluted in cell medium and this could have some effect on the stability of MBs. Diluting MBs in media led to an increase in the mean MB diameter, independently on the type of medium used, as shown in Paragraph 2.2.1.2.5. This observation is thought to be a consequence of two phenomena: the mechanical stress to which MBs are subject during the dilution process on one side, and the effect of the physico-chemical properties of the dilution media on the other. During the dilution process, a sample of MBs is usually withdrawn using a 1 mL pipette with an orifice diameter of 1 mm and then injected into another vial. This process may impart mechanical stress on the MBs, both in the form of shear stress and static pressure, which could lead to MB rupture or coalescence. Diluted MBs were thus larger than the undiluted ones, and this difference was maintained throughout the observation. Since MBs are fragile, larger catheters or needles are generally preferred to avoid destruction during administration. Current clinical guidelines recommend using diameters of 20 gauges (nominal inner diameter of 0.603 mm) or larger. In the literature, it is known that using needles with orifices smaller than 25 gauges (nominal inner diameter of 0.26 mm) can significantly decrease the concentration and the acoustic response of microbubbles, but the exact threshold at which this decrease happens is formulation-dependent [163].

Moreover, Tables 2.5, 2.6 and 2.7 (page 97) show that the solution in which MBs are suspended may have an impact on their dimension. Notably, when MBs are diluted in DMEM or DMEM and 10% FBS, their diameter is bigger than the ones diluted in PBS. This could be due to the presence of amino acids and proteins in DMEM and FBS, which may interact with (or intercalate within) the MB shell.

As for MB concentration, greater dilutions led to a more rapid decrease in concentration with respect to time, as shown in Figures 2.21, 2.23, 2.25 (page 98). This

observation could be due to the concentration-dependence of MB dissolution. Because of Ostwald ripening and Laplace pressure, the gas contained in smaller bubbles is under greater pressure, and this drives its diffusion from within the bubble to the outer environment. This creates local areas of gas supersaturation. When MBs are highly concentrated, the gas present in these supersaturated areas diffuses into the larger bubbles, which become bigger over time. At lower concentrations, only part of this gas diffuses into the larger bubbles, while the majority of it redistributes in the liquid to reach an homogeneous concentration, hence microbubbles disappear and their concentration decreases more rapidly.

In conclusion, when MBs are stored at 37°C, temperature is the main parameter affecting their stability. When MBs are used in *in vitro* and *in vivo* conditions, they are often in a medium at 37°C, hence their ability to maintain their size and concentration may be compromised. In *in vitro* experiments, the focus is on the interaction between MBs and cells, so an increase in size is not an issue; however, in *in vivo* conditions, this behaviour could represent a safety concern (i.e., when MBs become too large) and could decrease the efficacy of treatment. A possible alternative to the injection of MBs in blood is the use of more stable nanodroplets, which are vaporising into MBs only at the site of injury. Moreover, to ensure that MBs maintain their original size and size distribution for longer periods of time, it is suggested that the stock solution is maintained without performing any dilution. If dilutions are necessary, then they should be performed just prior to the use of the sample. To the best of the author's knowledge, this is the first study that quantitatively investigated the effects of temperature and dilution of MBs in cell medium on their stability.

2.3.1.5 Effect of the lipid shell formulation on MB stability

MBs were produced with a different lipid shell to investigate the influence of acyl chain length of the lipid constituent on MB stability. MBs produced with a lipid shell composed of DBPC/DSPE-PEG2000 (molar ratio 9:1) were more stable at 37°C over 2 hours, compared to MBs with a lipid shell of DSPC/PEG40s (molar ratio 9:1), as shown in Figures 2.28 and 2.27 (page 103).

This result was anticipated, as DBPC has a longer carbon chain than DSPC (C22 vs C18) and this results in a more packed lipid shell since there is an increase in the attractive forces (namely, Van Der Waals attractions) between phospholipid molecules.

Overall, this enhances MB shell gas permeation resistance and its resistance against collapse. By increasing the acyl chain length, the thickness of the shell increases too, and this provides a thicker barrier for solute permeation. In addition, the longer chain of DBPC, hence the bigger steric effects, made microbubbles larger with respect to the ones produced with DSPC (5.04 vs 4.43 μm) [164]. Although the stability is different, acoustic studies performed on DSPC and DBPC MBs by Van Rooij et al. [165] showed that both compositions had similar acoustic response.

2.3.2 Precursors of Microbubbles

As explained in Paragraph 1.3.3, the sonication process to produce MBs involves two sonication steps: during the first one multilamellar vesicles are broken down to form smaller unilamellar vesicles, which then collide with gas bubbles forming during the second sonication step. During the collision, non-shelled gas bubbles merge with the lipid vesicles giving origin to lipid-shelled MBs [73]. Before and after the first sonication step of MB production, liposomes or other supra-molecular structures are generated. Knowing their size allows to gain a more pervasive understanding of the MB production process, and to also evaluate whether MB size distribution could be influenced (and potentially controlled) by the sonication process.

During the hydration of the lipid film, MB precursors (likely in the form of liposomes) with a mean diameter of 229.76 nm form. Figure 2.29 (page 105) highlights that performing a first sonication on the hydrated lipid solution and the type of sonication (i.e., continuous or pulsed) has an effect on the final liposome size. After hydrating the lipid film and mixing the resulting lipid dispersion using a magnetic stirrer, the generated liposomes had a larger mean diameter (229.76 nm), as reported in Table 2.8 (page 104). By sonicating these liposomes, their structure was broken down and it subsequently re-assembled [73], so that the newly formed liposomes had a smaller mean diameter of around 50 nm. As shown in Figure 2.29 (page 105), the length of the first sonication (in the range 30 seconds to 5 minutes) led to comparable sizes of liposomes in the range 53.51 - 65.20 nm, without statistical differences. Moreover, liposome size dispersity was not correlated to the sonication length, as can be noted from the standard deviation of the data. Performing a pulsed sonication on liposomes led to an intermediate liposome diameter (98.45 nm). This means that pulsed sonication partially hindered the breakage of the larger liposomes. It

is hypothesised that the interval between one pulsation and the following one provides sufficient time to lipids to rearrange in larger structures. In conclusion, results suggest that it is critical to perform the first sonication to break down lipid aggregates, and that a first sonication of 30 seconds is sufficient to obtain small liposomes. Tests to produce microbubbles in this work have been performed with a first continuous sonication of 2 minutes and 30 seconds, consistently with protocols reported in the literature [166]. To be consistent with these first tests performed, all further tests were performed with the same sonication time.

It is thought that bigger lipid unilamellar vesicles can give rise to bigger microbubbles, so the aim of this test was to investigate whether different precursors could lead to bubbles of different size, as a mean to control MB size.

Figure 2.30 (page 106) highlights that small differences in the dimension of liposomal MB precursors did not have an impact on the size of the microbubbles produced. An average difference of about 40 nm between liposomes generated with continuous sonication and the ones generated with pulsed sonication, did not impact on the final MB size. However, Figure 2.32 and Table 2.8 (page 108) show that when the difference was higher, the size of microbubbles was affected by the precursor size. A difference of about 170 nm between sonicated and non-sonicated liposomes resulted in an average difference of 1.7 μm in the MB size. Moreover, the size dispersity of MB precursors appeared to be directly correlated to the size dispersity of the obtained microbubbles. In addition, the concentration of microbubbles produced from sonicated liposomes was higher, as illustrated in Figure 2.33 (page 108). These observations confirm the importance of performing the first sonication process, since smaller liposomal precursors lead to smaller and less dispersed microbubbles; however, it is not possible to effectively control the final size of MBs by changing sonication parameters, as previously hypothesised.

2.3.3 Conclusions

MBs are widely used in the clinic as contrast agents in ultrasound imaging and, more recently, they have been investigated as therapeutic agents for the treatment of tumours, bacterial infections, neurological disorders and blood clots [5]. In this project, drug-loaded microbubbles were proposed as a new treatment for bone fracture healing. The specific aim of this study was to investigate the effect of different parameters

on the stability of lipid-shelled MBs produced by sonication, including those relating to (i) production and storage, (ii) environmental conditions, and (iii) manipulation. Experiments described in this Chapter have helped in establishing a sonication-based protocol to produce microbubbles that maximises their stability over time. In addition, it was also demonstrated that the methods used to produce and characterise MB size and concentration are robust and reproducible.

Experiments showed that it is fundamental to perform the first sonication step to obtain small liposomal precursors (< 60 nm) that, after the second sonication step, turn into small microbubbles. It was also found that the viscosity of the medium in which microbubbles are suspended, the storing conditions, and the labelling of microbubbles using fluorescent dyes all affect the stability of microbubbles in terms of their size and concentration over. To achieve maximum stability during storage, microbubbles should be produced in a biocompatible, viscous dilution medium ($\mu >$ 15 cP) and stored at 4^{o}C until usage. Since there is an increase in the diameter and a decrease in the concentration with respect to time, the storage time should be as short as possible (a maximum of 24 hours is advisable) to guarantee maximum safety. In addition, dilution of microbubbles should be avoided and, only if necessary, should be performed just prior to their usage. Finally, the visualisation of microbubbles *in vivo* and *in vitro* should be done adding low molar ratios of fluorescent dyes (< 2.14 µM), since greater quantities may lead to an increase in the MB mean diameter.

It was also shown that using a longer acyl chain (DBPC instead of DSPC) allows increasing the stability of MBs; however, further experiments are needed to investigate their acoustic response upon ultrasound stimulation. Although stability is different, acoustic studies performed on DSPC and DBPC by Van Rooij et al. [165] showed that both compositions had similar acoustic response.

In conclusion, this is the first study showing the quantitative impact of production, storage, environmental conditions, and manipulation on MBs stability, representing a novelty in the field of US responsive MBs.

Chapter 3

Evaluation of the effects of production parameters on nanodroplet stability and assessment of phase transition to microbubbles

Over the last decade, there has been an increasing interest in the use of liquid perfluorocarbon nanodroplets, which can be considered as the precursors of MBs as phase transition can happen between the two configurations. They are an order of magnitude smaller than microbubbles, and so are thought to extravasate more efficiently. They are also more stable in terms of concentration and diameter over time [71]. When compared to MBs, NDs have been shown to have a significantly longer circulation time *in vivo*, since having a liquid core instead of a gaseous one prevents gas dissolution. Unlike microbubbles which have a circulation time of minutes (half-life < 5 min [44]), nanodroplets have a half-life in the order of 2-6 hours for imaging applications [88]. Since microbubbles are relatively large, they experience only very limited extravasation when administered *in vivo*, which in turn hinders their ability to penetrate within a target tissue and stimulate the target cells. Using nanodroplets

as an alternative to microbubbles can provide enhanced extravasation. Nanodroplets are liquid spherical emulsions with a diameter range of 100-500 nm [43]. In addition to this, microbubbles and nanodroplets are related systems, as phase transitions can occur between the two conformations. Following an increase in temperature, mechanical stress or upon ultrasound stimulation, the liquid core of NDs vaporises and this phase transition allows to obtain gas-shelled MBs. Nanodroplets are at least five times smaller than the microbubbles resulting from their phase transition [167] [168]. By selecting the appropriate PFC core, it is possible to control the ultrasound field properties or the temperature that are needed to promote phase transition. Together, these properties make them particularly attractive as carriers for drug delivery that might be stimulated to release their cargo under extracorporeal US stimulation.

This project involves the use of drug loaded particles to enhance the bone fracture repair process. One potential approach is to manufacture drug loaded nanodroplets, inject them into the bloodstream, and rely on extravasation and passive accumulation at the site of fracture. Subsequently, upon US stimulation, NDs are induced to phase-transition into MBs. Exposure to US also drives MB cavitation, mechanically stimulating the surrounding cells and releasing their payload. Previous studies by Wang et al. [70], Stride et al. [26] and Rapoport et al. [169] have demonstrated extravasation of polymersomes and liposomes with a diameter <200 nm and paclitaxel loaded PFP PEG-PDLA nanodroplets with an average size of 250-300 nm, and their passive accumulation at a desired tissue through the use of appropriate molecular targets. The size of nanodroplets is an important factor for their use in *in vivo* applications; it is important to find a trade-off between a nanodroplet that is small enough to extravasate through the bone vasculature and big enough to vaporise into a microbubble at moderate mechanical indices. For instance, it is known that smaller NDs require higher acoustic pressure to phase-transition [43]. For these reasons, this study will aim to produce nanodroplets with a diameter in the range 200-300 nm, a dimension considered appropriate for achieving extravasation and subsequent therapeutic effects.

Since NDs have only been recently introduced, there is not a comprehensive quantitative characterisation of parameters affecting their size, stability, and acoustic behaviour, and these open questions have slowed down the clinical translation. [88] [82]

In order to address these knowledge gaps, this study aims at studying: (i) the

effects of production parameters on NDs size and size dispersity, and these can be influenced by (ii) conditions relevant for experiments *in vitro* and *in vivo*. (iii) The stability of NDs with respect to time at conditions relevant to storage and usage, and (iv) the acoustic parameters necessary to induce phase transition to MBs.

There is no available study in the literature investigating the effects of the amount of perfluorocarbon used and the sonication parameters. It was herein hypothesised that they could be varied in order to tune the ND size, and experiments were performed to validate this hypothesis. The chosen perfluorocarbon for this study was perfluoropentane (PFP) since its phase transition temperature is of 29^{o}C, so it is in its liquid phase at ambient temperature and it can be phase transitioned into gas with relatively low acoustic pressures. Concentrations of PFP in the range 5-15% (v/v in PBS) were tested. As for the sonication parameters, Bilati et al. [170] showed that the second sonication step, in particular its intensity and duration, is the most important in defining the size and dispersity of polymeric nanodroplets. The mean size of nanodroplets decreased with increasing sonication time and increasing intensity . We foresee a similar behaviour for lipid shelled nanodroplets, but no quantitative study is available. In this work, sonication length (in the range 20-60 seconds), modality (pulsed or continuous) and intensity (in the range 24-72 W) were varied, and their impact on size and size dispersity assessed.

As for conditions relevant to administration *in vitro* and *in vivo*, the effects of production and/or dilution in cell medium were tested, together with the effect of labelling using a lipophilic dye. It is known from the literature that NDs can be labelled with lipophilic dyes [171], but it is not known if this might change the ND dimension. In addition, it is not known whether producing NDs in cell medium (DMEM, DMEM and FBS or DMEM and BSA), or producing them in PBS and then diluting them in cell medium, could have an impact on their size due to the potential interaction between the lipids of the ND shell and the proteins and amino acids present in the medium.

As for the stability of NDs, it is known that they are more stable than MBs [167]; however, to the best of the author's knowledge, there is no quantitative study in the literature. For this reason, the stability of NDs was studied at 4^{o}C for a week and at 37^{o}C for 110 minutes.

The first section of this chapter describes the materials and methods used to produce nanodroplets with different characteristics; the second section describes the

results obtained and, finally, the third section provides a discussion of the results and compares them with relevant studies in the literature.

3.1 Materials and Methods

The tests performed to produce and characterise nanodroplets are presented in Figure 3.1.

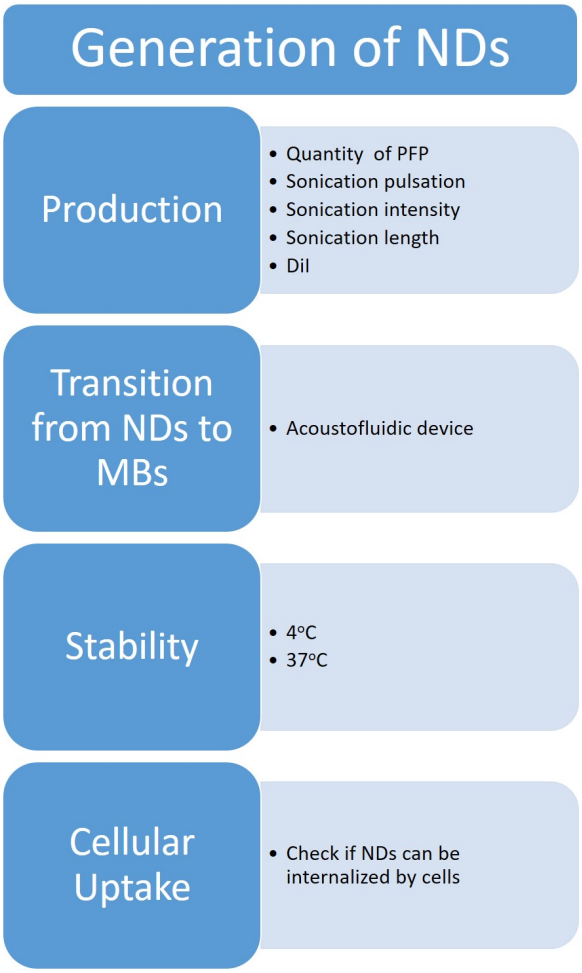

Figure 3.1: *The tests carried out to generate and characterise nanodroplets can be divided into four main categories: production, transition from MBs to NDs, ND stability and ND uptake by cells. Each category comprises of different studies to achieve a full characterisation of NDs.*

Thanks to their smaller (i.e. sub-micrometre) size, nanodroplets could be used as an alternative to MBs (or co-administered with MBs) to achieve greater extravasation

of the US-responsive agent and therapeutic compounds. Tests initially focused on the establishment of a method to generate stable nanodroplets. Since nanodroplets can be considered as MB precursors, additional tests were performed to assess their ability to phase transition. Finally, stability of NDs with respect to time was assessed and their uptake by cells was studied.

3.1.1 Generation of Nanodroplets

An experimental protocol was established in order to produce perfluorocarbon nanodroplets, and assess the influence of both the chemical formulation and the production protocol on their dimension and size dispersity. The size dispersity of droplets influences their acoustical response upon ultrasound stimulation and the amount of loaded drug; notably, if dispersity is low, the majority of nanodroplets will undergo vaporisation when exposed to the same acoustic field. If the sample has a large size dispersity, only a proportion of NDs may undergo vaporisation at a specific US stimulation regime; however, vaporised droplets can act as cavitation nuclei to facilitate vaporisation of droplets in close proximity [172] [88] [173]. In order to achieve reproducible therapeutic outcomes, the ND sample should thus have a low size dispersity. Following production, the stability of nanodroplets with respect to time was investigated. Nanodroplets can be considered as MB precursors; thus, tests were also performed to evaluate their ability to transition into a microbubble.

Method

To produce nanodroplets, a phospholipid, an emulsifier and a perfluorocarbon were used. The droplet coating was made of 1,2-distearoyl-sn-glycero-3-phosphocholine (DSPC, Avanti) and polyoxyethylene(40)stearate (PEG40s, Sigma-Aldrich, Saint Louis, Missouri, USA), while the droplet core was made of perfluoro-n-pentane (PFP, Strem, Newburyport, Massachusetts, USA). The choice of the coating material was coherent with the one used to produce microbubbles, as described in Paragraph 2.1.1. The protocol used to produce nanodroplets was similar to the one used to generate microbubbles, as described in Paragraph 2.1.1, with minor modifications. During nanodroplet production, the first sonication step (i.e. to homogeneously disperse lipids) was performed for a duration of 15 seconds at 48 W, with the tip completely immersed in the lipid solution. Sonication is known to increase the temperature of the liquid;

thus, since PFP has a phase transition temperature of 29°C, the lipid dispersion was placed in a fridge at 4°C for 30 minutes, prior to the addition of PFP. Subsequently, the lipid solution was pipetted into 1 mL plastic Eppendorf tubes (Starlab, Milton Keynes, UK) and PFP was added to the lipid dispersion. Tubes were shaken for 2 seconds to generate a micro-emulsion and placed inside a tube chiller (IsoFreeze).

Nanodroplets were subsequently formed by placing the sonicator tip within the tube and by applying a pulsed sonication; in this way the temperature of the liquid was kept below the phase transition temperature of PFP. The sonication process was performed under a fume hood.

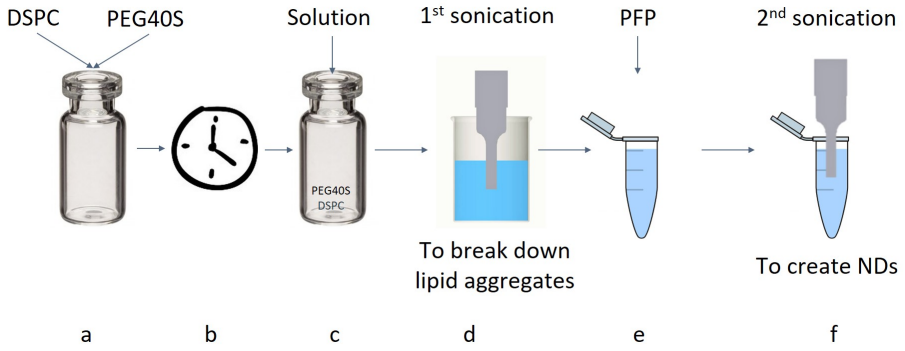

Figure 3.2: *Main steps taken to produce nanodroplets. a) DSPC and PEG40s were dissolved in chloroform and placed in a glass vial. b) Chloroform was left to evaporate overnight. c) The lipid film was hydrated. d) A first sonication was performed with the tip completely immersed in the fluid, in order to break down lipid aggregates. e) PFP was added to the lipid dispersion. f) A second sonication was performed with the tip fully immersed in the liquid, to generate nanodroplets.*

Figure 3.2 shows the main steps of the process used to produce nanodroplets.

The method used in this study to determine ND size was the dynamic light scattering (DLS) technique. Such technique is non-invasive and it is generally used for measuring the size of particles and other supra-molecular structures in the nanometre size range. The dimensions of nanodroplets were measured using both the DLS machine (Zetasizer Nano, Malvern Panalytical Ltd, Malvern, UK) and the Zetasizer Software (Malvern Panalytical Ltd, Malvern, UK). The following parameter were set on the software: $\mu = 1.31$ cP, n = 1.335, k = 0.1, T = 10°C, t = 120 s and the volume of the cuvette was 1 mL (Fisherbrand FB55147, Fisher Scientific, UK). The sample was transferred from the Eppendorf tube into the cuvette by using a 1 mL pipette. The DLS machine measures the sample three times, and every repeat comprises

several measurements. The number of measurements is automatically determined depending on the characteristics of the sample. Moreover, when the Zetasizer Nano applies the DLS technique to measure particle size, it provides an indication of the sample quality. The DLS provides both a mean size of the particles in the sample and their polidispersity index PdI, a dimensionless measure of the broadness of the size distribution ranging from 0 to 1. PdI < 0.08 indicates nearly monodisperse sample, $0.08 <$ PdI < 0.7 is the range over which the distribution algorithms best operate over and PdI > 0.7 indicates a very broad distribution of particle sizes [174].

The diameter distribution was plotted in the form of a boxplot, by showing the quartiles of the data distribution. Quartiles are a way of separating numerical data into four equal groups in terms of number of observations based on five key values: the minimum, represented by the bottom whisker; the first quartile, represented by the inferior line of the box; the median, represented by the central line of the box; the third quartile, represented by the superior line of the box; and the maximum, represented by the top whisker. The box thus illustrate the middle 50% of the data, also known as the interquartile range (IQR). The median of the values is depicted as a line splitting the box in two. The IQR illustrates the variability in the data: large IQR indicates a large spread in the values, while a smaller IQR indicates that most values fall near the centre value of the distribution. Boxplots also illustrate outliers as points extending beyond the whiskers. Finally, the cross within the box represents the mean value, which is often different from the median because the MB size distribution is skewed and not normal.

3.1.1.1 Effect of production parameters on nanodroplet dimension

3.1.1.1.1 Effect of the quantity of PFP

In these tests, different amounts of PFP were added to the lipid dispersion before performing the second sonication procedure, in order to study whether the amount of PFP can influence the final ND size. The hypothesis was that increasing the amount of PFP could lead to larger nanodroplets. Three concentrations of PFP were tested:

- 5% v/v in PBS
- 10% v/v in PBS
- 15% v/v in PBS

The second sonication step was 20 seconds long, at 72 W and pulsed. The pulse duration was 7 seconds with a duty cycle of 30%.

3.1.1.1.2 Effect of varying the sonication pulse length

The previous test was repeated, using different sonication conditions. In particular, the second sonication step was 20 seconds long at 72 W, but with a pulsation of 7 seconds and a duty cycle of 15%. The hypothesis was that shorter pulsations could prevent PFP evaporation.

3.1.1.1.3 Effect of the intensity of the second sonication

The intensity of the second sonication step, i.e. the one in which nanodroplets are formed, may influence the final ND size. To study the influence of sonication intensity on NDs dimension, 24 W and 48 W sonication powers were tested and compared with the one used previously (72 W). The underlying hypothesis was that an increase in sonication power would lead to smaller and less dispersed nanodroplets.

3.1.1.1.4 Effect of the length of the second sonication

After evaluating the effects of changing the sonication pulsation regime and intensity on NDs dimension and dispersity, different durations of sonication were also investigated. In these tests, nanodroplets were produced following the protocol described in Paragraph 3.1.1 and the length of the second sonication step was varied between 20 and 60 s. The hypothesis was that an increase in the sonication length would lead to smaller and less dispersed nanodroplets. A pulsation of 7 seconds with duty cycle of 30% was used.

3.1.1.1.5 Effect of production in cell medium

Experiments were performed to investigate the effect of cell medium on ND size, to study if and how the presence of amino acids and proteins influence ND characteristics and whether direct administration of droplets could be performed, using a biologically relevant medium and without dilution. The underlying hypothesis was that producing NDs in cell medium could have an impact on their size, due to the interaction with chemicals present in the medium.

Since cell medium contains aminoacids and proteins, it is possible that these compounds may coat PFP droplets, thus forming stable nanoemulsions even in the absence of phospholipids. To test this hypothesis, five different sample types were tested:

- PFP, DSPC and PEG40s (9:1) sonicated in DMEM
- PFP, DMEM and BSA sonicated in the absence of lipids
- PFP, DSPC and PEG40s (9:1) sonicated in DMEM and BSA
- PFP, DMEM and FBS sonicated in the absence of lipids
- PFP, DSPS and PEG40s (9:1) sonicated in DMEM and FBS

3.1.1.1.6 Effect of nanodroplet dilution in cell medium

Experiments were performed to investigate the effect of NDs dilution in cell medium on their size, to study how conditions relevant to applications *in vitro* and *in vivo* can influence ND characteristics. The underlying hypothesis was that diluting NDs in cell medium could have an impact on their size, due to the interaction with chemical constituents present in the medium.

To test this hypothesis, NDs were produced in PBS and diluted 1:2 or 1:5 by volume in DMEM or DMEM with 10% FBS.

3.1.1.1.7 Effect of storage temperature

Given that NDs are developed for intravascular administration, ND stability at 37^{o}C with respect to time should be studied. NDs were produced following the method described in Paragraph 3.1.1. After production, they were stored at 37^{o}C in an egg incubator (Kidsidol-UK) and transported to the DLS machine for analysis. Images of the samples were also taken every ten minutes with an optical microscope with a magnification of 50x (Olympus IX71, Olympus, Shinjuku, Tokyo, Japan), and their size was measured with a DLS machine (Zetasizer Nano, Malvern Panalytical Ltd, Malvern, UK). ND stability was studied over 2 hours, with measurements taken every 10 minutes. Three samples were measured at each time point tested.

3.1.1.1.8 Effect of the use of a fluorescent dye

Previous tests performed with microbubbles showed that the use of fluorescent dyes had an impact on the size and stability of microbubbles, as presented in Paragraph 2.2.1.2.3. In this test, nanodroplets were labelled with the dye 1,1'-Dioctadecyl-3,3,3',3'-Tetramethylindocarbocyanine Perchlorate (DiI, Life Technologies, Carlsbad, California, USA) and their size was determined. Nanodroplets were produced following the protocol described in Paragraph 3.1.1; the only difference was the addition of the dye, which was added to the lipid suspension. Three different tests with three different final concentrations of DiI were performed: 2.14, 10.71 and 21.42 μM, corresponding to molar ratios DSPC:PEG40s:DiI of 0.89:0.101:0.00025, 0.9:0.101:0.0012, and 0.9:0.101:0.0025.

3.1.1.2 Stability of nanodroplets with respect to time

As for gas microbubbles, it is important to study the stability of nanodroplets with respect to time, from both a storage and administration perspectives. Nanodroplets were produced following the protocol described in Paragraph 3.1.1 and were stored at 4°C between experiments. Three independent repeats were performed. For each repeat, ND diameter was measured with DLS just after production, and at 2 hours, 1, 2, 3 and 6 days after production.

3.1.2 Phase Transition of Nanodroplets

3.1.2.1 Acoustofluidic device

Nanodroplets can be considered as the precursors of microbubbles, and the transition can be achieved by applying either thermal or acoustic energy. During the transition, the liquid core of NDs vaporises and this leads to the formation of gas-filled MBs. Tests were thus performed to assess NDs ability to undergo phase transition.

In a first phase of the study, experiments were performed to study the phase transition of nanodroplets caused by an increase in temperature and an acoustofluidic device was designed to generate an ultrasonic standing wave within a fluid layer, as illustrated in Appendix A.

This first version of acoustofluidic device only allowed to perform the acoustic stimulation of nanodroplets; a second version of the device was then implemented to

combine thermal stimulation, acoustic stimulation, and imaging. The device therefore had to include a temperature controller, namely a Peltier element and a piezoelectric transducer (PZT) to generate the ultrasonic stimulus. The device also had to be integrated within a microscope to visualise and potentially measure the size of the generated microbubbles. To allow the integration with a microscope, the device was designed to have the classic dimension of a microscope glass slide, namely 75 x 25 mm.[1]

The acoustofluidic device designed consisted of 3 connected chambers. The first chamber is used to regulate the temperature of the nanodroplet solution thanks to a Peltier element; the second to stimulate NDs with ultrasound and detect their phase transition, thanks to a transducer and a passive cavitation detector; and the third to observe microbubbles obtained under a microscope, as shown in Figure 3.3.

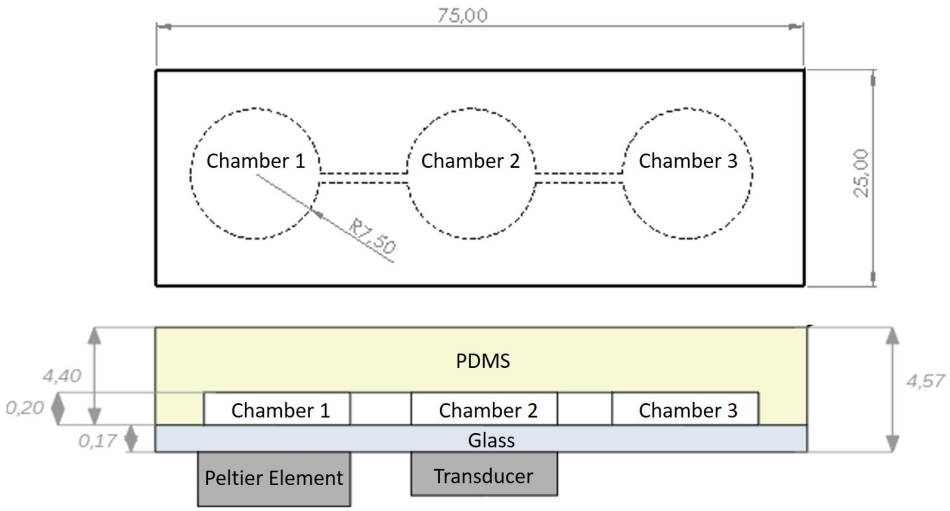

Figure 3.3: *Top and front plane of the device. The acoustofluidic device comprised three chambers: the first one is connected to a Peltier element and is used to control the temperature of the sample of NDs, the second one is connected to a transducer and a passive cavitation detector and is used to acoustically stimulate the sample and record its phase transition, the third one allows the visualisation of the sample with a microscope.*

Starting from chamber 1, the constitutive layers of the device are: a Peltier element, a 170 µm glass slide, a sample of nanodroplets and the PDMS external side of the chamber. A Peltier element is a heat pump which transfers heat from one side to the other, depending on the direction of the electrical current applied to it. COMSOL

[1]The device was designed and tested with the help of Mathieu Cabot.

simulations were performed by applying the 'Heat Transfer in Solids' study to check if the temperature of the Peltier surface could allow to obtain an homogeneous increase in temperature limited to chamber 1. To get an homogeneous and adjustable temperature in the chamber, the Peltier element should completely cover the chamber. For this purpose, a Peltier element was bought from European Thermodynamics Limited with dimensions of 15 x 15 mm (ET0311020, European Thermodynamics Limited, Leicestershire, United Kingdom).

As for chamber 2 and as shown in Figure 3.4, the constitutive layers of the device are: a piezoelectric transducer PZT, a carrier, the fluid and a reflector. The US wave emitted by the transducer travels into the fluid layer through a carrier, and is then reflected backwards by the reflecting layer, due to a mismatch in the acoustic impedance between fluid and reflector and due to the thickness of the reflector layer. The interaction between the emitted and reflected waves gives origin to a standing wave field.

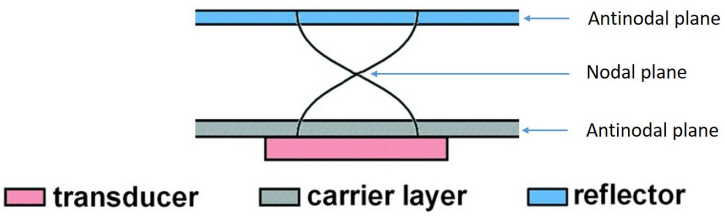

Figure 3.4: *The figure shows a schematic of the constitutive layers of the acoustofluidic device. The interaction between the emitted and reflected waves gives origin to a standing wave.*

The plane in which the incident and reflected waves intersect each other is called 'node' or 'nodal plane', and the acoustic pressure is the lowest in this region. Planes where the acoustic pressure reaches its maximum value are instead referred to as 'antinodes' or 'antinodal planes'. By changing the US frequency and the architecture of the device (i.e. thickness of its layers), it is possible to change the position and number of nodes and antinodes. Ultrasonic standing waves are often employed to manipulate particles in suspension, as they generate acoustic radiation forces that move particles at desired locations within the fluid layer. Since acoustic radiation forces are proportional to the third power of the particle radius; their effect on nanosocale droplets can be neglected. Thus, it can be assumed that nanodroplets remain homogeneously distributed upon exposure to an ultrasonic standing wave field within a fluid cavity [175].

The aim of this chamber is to achieve a high acoustic pressure, ideally without nodes and antinodes. The range of frequencies that can be used was between 1 and 2 MHz, as this is a range commonly used for therapeutic applications since such frequencies don't induce any physical or chemical changes in the stimulated environment, and thus avoid any physical damage.

The geometrical and physical parameters that were chosen to be varied in different computational simulation to find the best values for the application were: (i) the thickness of the PDMS layer (varied between 3 and 5 mm); (ii) the thickness of the chambers and channel where the nanodroplet solution circulated (varied between 0.2 and 0.5 mm); (iii) the frequency of ultrasound emitted by the piezoelectric transducer, (varied between 0.5 and 2MHz); (iv) the temperature induced by a voltage difference within the Peltier element.

The production of the device consisted of a simple assembly of the different materials and components. To create the PDMS section, it was first necessary to create a mold. The mold was designed with Solidworks and shown in Figure 3.5.

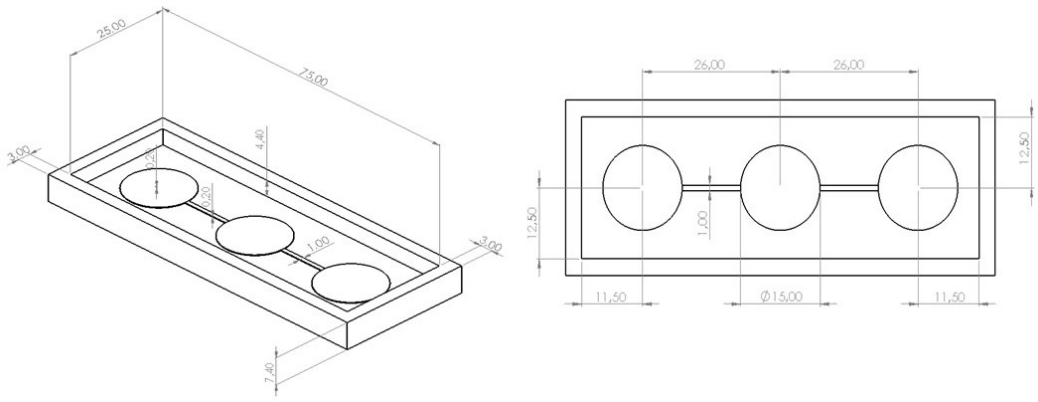

Figure 3.5: *Mold designed in Solidworks.*

This mold was 3D printed using the 3D printer Ultimaker^{2+} (Ultimaker, Utrecht, Netherlands). Figure 3.6 shows the printed mold to be used to produce the PDMS section of the device.

To produce the PDMS mold, silicon was mixed with the curing agent (1:10, Sylgard 184, Dowsil, Dow Way Midland, MI, USA) until a preparation full of air bubbles was obtained. Air bubbles were removed by placing the preparation in a vacuum pump. Degassed PDMS was poured onto the mold and left curing for 24 hours at room temperature. After having obtained the PDMS section, this needed to be connected

Figure 3.6: *A) Plasma bonding technique. B) Acoustofluidic device.*

to the glass coverslip (75 x 25 x 0.17 mm, Logitech, Glasgow, Scotland, UK) to create a sealed device. The binding was obtained by using the plasma bonding technique. Figure 3.7.A shows the plasma bonding technique on the PDMS section of the device and Figure 3.7.B shows the device at the end of its assembly. To make the binding permanent, the device was put in the oven at 65°C for 15 minutes.

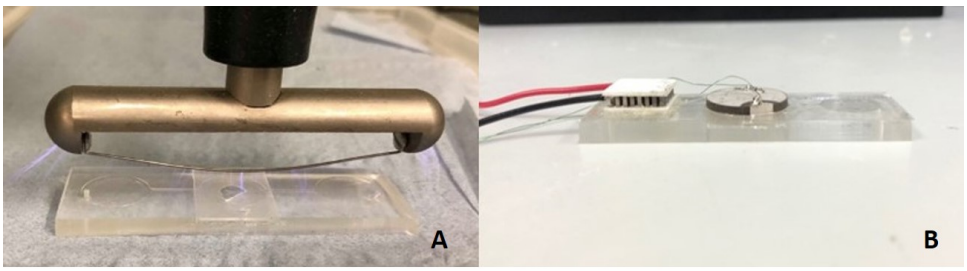

Figure 3.7: *Diagram under Solidworks of the mold for the PDMS silicone part.*

A piezoelectric transducer with a diameter of 10 mm (PZT26, Meggitt, Christchurch, Dorset, UK) was coupled to the glass slide using a layer of glycerol and the Peltier element was glued thanks to a thin layer of spray glue (CRC Fast Stick Spray Adhesive, CRC, Bridgwater, Somerset, United Kingdom). The glue was applied and let to dry overnight at room temperature.

The electronic circuit used to operate the device comprised of a signal generator (TG2000 20 MHz DDS function generator, Aim and Thurlby Thandar Instruments, Huntingdon, UK) connected to an amplifier (E&I-1040L-01, Rochester, New York, USA), which was then connected to an oscilloscope (DSO1102B 100 MHz, Keysight Technologies, Wokingham, UK) and to the PZT connected to the acoustofluidic device. The strongest resonance frequencies were determined experimentally using an impedance-amplitude-phase analyser (C60 Cypher Instrument, UK), with the maxima of conductivity. To verify the results, the signal generator was used to find the minima in the peak-to-peak voltage signal acquired through the oscilloscope. Resonance

frequency was around 2MHz.

To induce vaporisation of PFP NDs, the Peltier element was connected to a voltage generator, setting the intensity at 1 A, with a voltage of 0.7 V to reach a temperature of the nanodroplets solution of 37^{o}C. Different experiments were performed by changing the time of the sweep (5 s, 10 s, 15 s, 20 s, 25 s).

To study the size and concentration of MBs after vaporisation, microscope images of the sample within the acoustofluidic device were taken with 10x magnification.

3.1.2.2 Phase transition in a tissue mimicking flow phantom

NDs acoustic response depends on different factors, and the main ones to consider are as follows: chemical composition, size and boundary conditions. To check the influence of boundary conditions, the acoustic response of PFP nanodroplets (NDs) was measured in a tissue mimicking flow phantom with an embedded 1 mm channel through which the NDs were flowed. The setup used is shown in Figure 3.8.[2]

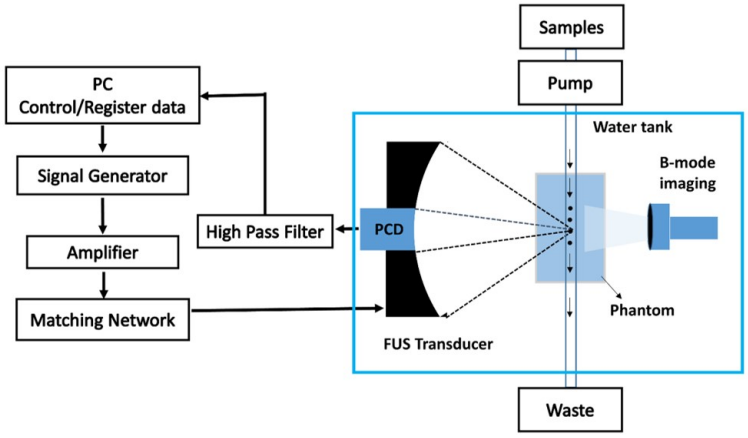

Figure 3.8: *Schematic diagram of the experimental setup.*

A focused ultrasound (FUS) transducer (H103, Sonic Concepts, Bothell, WA, USA) of fundamental frequency 0.5 MHz was used to excite PFP NDs, while a PCD transducer (V320 Panametrics, Olympus, Waltham, USA) was used to record any acoustic emissions. The flow phantom was created from a degassed biocompatible hydrogel composed of 2% (w/v) low melting point ultrapure agarose gel (Invitrogen, Carlsbad, CA, USA). FUS and PCD were coaxially and confocally aligned via a

[2]The experiment was performed with the help of Dr Qiang Wu at the University of Oxford.

central circular opening in the FUS which was in-turn aligned with the middle of the agarose channel. The FUS was previously calibrated using a 0.4 mm diameter needle hydrophone (ONDA 1056, Onda Corporation). Both FUS and PCD are fully controlled from custom-made software using graphical programming language (LabVIEW, National Instruments, Austin, TX, USA). The NDs degassed solution was infused through the flow phantom at 0.4 mL/min by syringe pump and exposed to 0.5 MHz ultrasound during the experiment. The frequency spectra of the emissions recorded by the PCD were used to determine the response of the PFP NDs to ultrasound as well as to determine the pressure threshold required to vaporisation activity. Two thousand-cycle FUS excitation pulses of increasing pressure were transmitted whilst a continuous flow of NDs passed through the phantom, allowing for complete replenishment of the exposed region between each pulse. A L12-5 (Philips, USA) linear array ultrasound probe was used to provide real-time B-mode imaging to detect NDs vaporisation process during the experiment. The imaging allowed to monitor the integrity of the channel, detect possible leaks, and make sure the flow was uniform and without any air bubbles. Harmonic imaging was used at a low, mechanical index in order to avoid any interference of the imaging with the therapeutic pulse and the response of the NDs.

Nanodroplets were produced following the protocol presented in Paragraph 3.1.1 and were subsequently centrifuged twice at 10000 rcf for 5 minutes with washing in between. ND size was checked with a DLS machine and was 400 nm. Half of the batch was subsequently passed through a 450 nm filter to obtain a final average size of 200 nm. Both sizes of samples were tested in this experiment to study how the size affects the acoustic pressure needed to phase transition NDs into MBs.

3.1.3 Intracellular Uptake of Nanodroplets

A preliminary test was performed to assess whether nanodroplets are likely to be taken up by cells and the result was then compared to the uptake of microbubbles by cells.[3]

Figure 3.9 illustrates the main steps taken in this experiment. Two flasks with 400.000 human osteosarcoma MG63 cells were prepared and maintained in Dulbecco's

[3]The experiment was performed with the help of Dr Antonio De Grazia, who performed the cell culture.

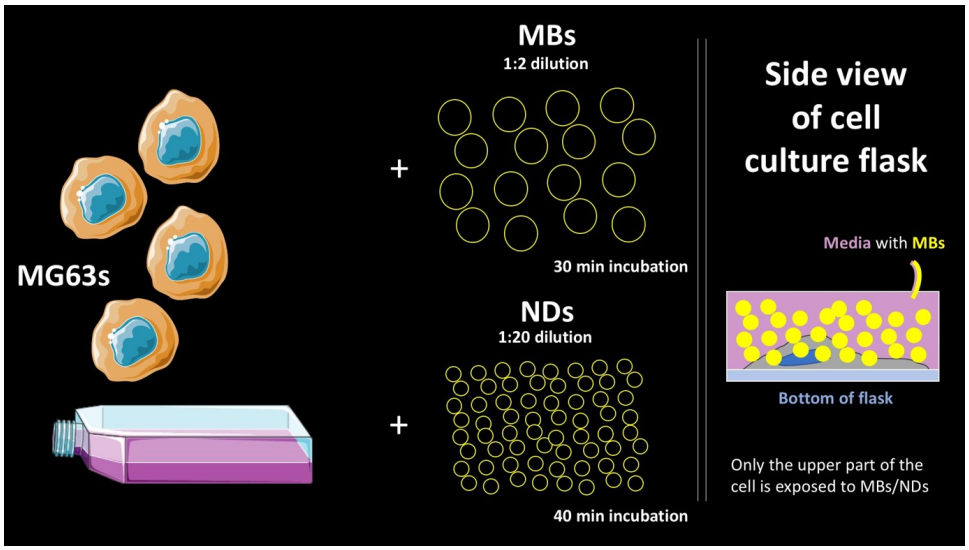

Figure 3.9: *MG63 cells were incubated with either microbubbles (1:2 dilution by volume) or nanodroplets (1:20 dilution by volume) to study their uptake by cells.*

Modified Eagle's medium (DMEM) supplemented with 5% (v/v) fetal bovine serum (FBS, Gibco, UK), 100 U/mL penicillin, and 100 μg/mL streptomycin. MG63 cells were chosen to be in line with other studies being undertaken within the wider research group. Cells were then incubated at 37°C and 5% CO_2 for 24 hours, to reach a confluence of around 1 million cells. After 24 hours, the medium was removed and discarded in Virkon, a multi-purpose disinfectant, and the two flasks were treated as follows:

- 5 mL of fresh medium, 5 mL of microbubble solution and cells were placed in the incubator for 30 minutes. After 30 minutes, the medium was removed and cells were washed twice with PBS and detached from the flask by the addition of 1% (v/v) trypsin-EDTA (5 minutes in the incubator). 10 mL of medium was added after trypsin incubation, to stop the enzymatic action. Cells were placed in a 15 mL tube and centrifuged at 300 rcf for 4 minutes. The supernatant was then discarded and cells were washed with PBS (i.e. resuspended by pipetting and centrifuged again). The pellet was then resuspended in 2 mL of PBS and 2 mL of 4% PFA were added to fix the cells (20 minutes at 4°C). Cells were then washed with PBS. Nuclear staining was performed by using 1 mL of a 0.1 μg/mL DAPI solution (10 minutes at room temperature). Cells were washed with PBS, and imaged on a glass slide.

- 9.5 mL of fresh medium was added along with 500 μL of nanodroplet solution, and cells were incubated for 40 minutes. After 4 minutes, the medium was removed, cells were washed twice with PBS and detached from the flask by the addition of 1% (v/v) trypsin-EDTA (5 minutes in incubator). 10 mL of medium was added after trypsin incubation, to stop the enzymatic action. Cells were placed in a 15 mL tube and centrifuged at 300 rcf for 4 minutes. The supernatant was discarded and cells were washed with PBS (i.e. resuspended by pipetting and centrifuged again). The pellet was then resuspended in 2 mL of PBS and 2 mL of 4% PFA were added to fix the cells (20 minutes at 4°C). Cells were then washed with PBS. Nuclear staining was performed by using 1 mL of a 0.1 μg/ml DAPI solution (10 minutes at room temperature). Cells were washed with PBS and imaged on a glass slide.

Microbubbles and nanodroplets were produced as previously described in Paragraphs 2.1.1 and 3.1.1. Both microbubbles and nanodroplets were stained with the fluorescent lipophilic dye DiI (molar ratio DSPC:PEG40s:DiI of 0.89:0.101:0.00025, 2.14 μM).

Cells were then pipetted onto a glass slide and a coverslip was placed on the top, to allow imaging with a fluorescence microscope (Axioimager M2m, Zeiss, Oberkochen, Germany), as shown in Figure 3.10. Cells were imaged at different positions along the z-axis, to determine the presence of internalised particles.

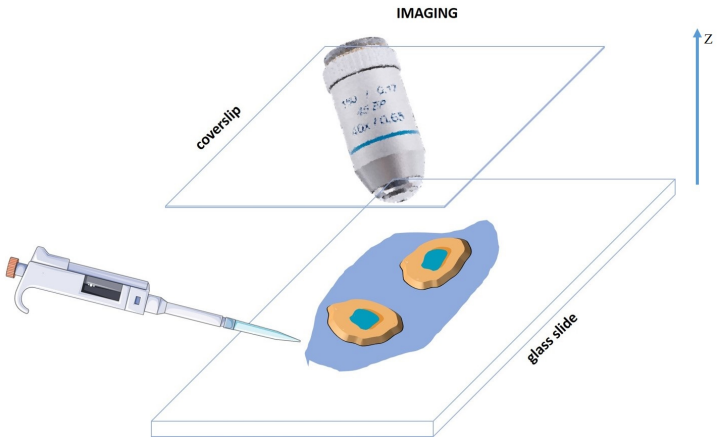

Figure 3.10: *MG63 cells were pipetted onto a glass slide, and a coverslip was placed at the top to allow imaging.*

3.2 Results

3.2.1 Generation of Nanodroplets

3.2.1.1 Effect of production parameters on nanodroplet dimension

3.2.1.1.1 Effect of the quantity of PFP

PFP nanodroplets were produced using the same coating formulation used for microbubbles. The hypothesis tested was that increasing the concentration of PFP would lead to an increase in the diameter of the emulsion droplets formed by sonication, due to the relative decrease in the concentration of phospholipid surfactant relative to the amount of PFP. The test described in Paragraph 3.1.1.1.1 was performed. Confirming the hypothesis, it was found that increasing the volumetric concentration of PFP from 5% to 15% (v/v) led to an increase in the mean ND diameter from 162.87 ± 49.42 μm to 308.7 ± 76.01 μm (Table 3.1, Figure 3.11 and Figure 3.12). The size dispersity of NDs also increased with increasing the concentration of PFP; i.e. the PdI increased from 0.23 to 0.32 ($p < 0.05$) when increasing the quantity of PFP from 5% to 15% (v/v).

Table 3.1: *The table shows the mean diameter and the standard deviation of nanodroplets (after production) obtained using different concentrations of PFP in the range 5-15% v/v in PBS.*

PFP v/v in PBS	Diameter [nm]	PdI
5%	162.87 ± 49.42	0.23 ± 0.03
10%	277.55 ± 60.69	0.27 ± 0.11
15%	308.17 ± 76.01	0.32 ± 0.11

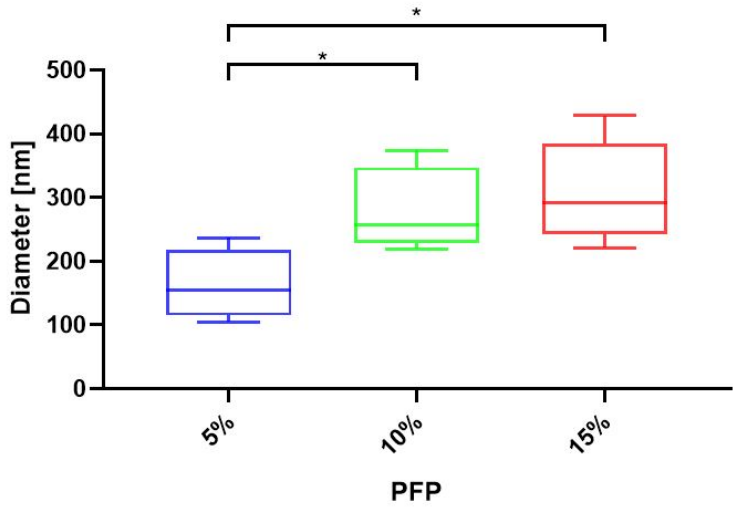

Figure 3.11: *The boxplots show the ND diameter distribution (after production) obtained using different quantities of PFP. NDs produced with 5% v/v of PFP in PBS were statistically different from the other two groups (*$p < 0.05$).*

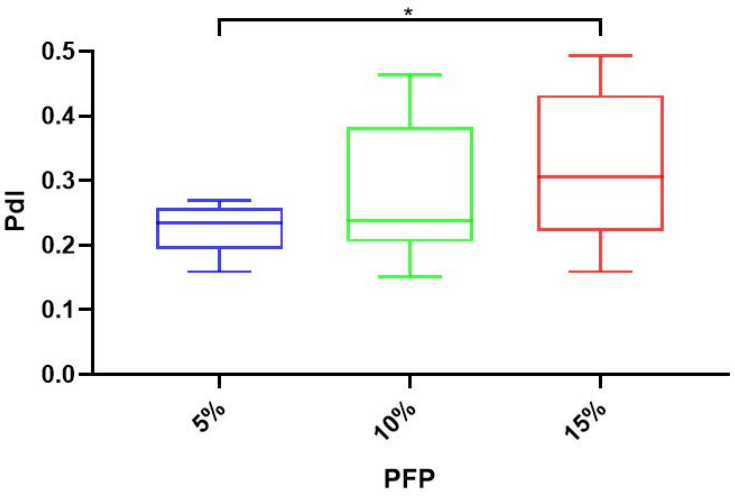

Figure 3.12: *The boxplots show the PdI of NDs (after production) obtained using different quantities of PFP. There is a statistical difference between the group produced with 5% v/v and 10% v/v of PFP in PBS (*$p < 0.05$).*

3.2.1.1.2 Effect of varying the sonication pulse length

Bulk PFP has a phase transition temperature of 29°C and this could represent a limitation during the sonication process, since ultrasound stimulation induces an increase in the local fluid temperature. If the temperature reaches the phase transition temperature of PFP, its evaporation may limit the efficacy of the ND production process. In order to prevent this, the lipid dispersion and PFP were maintained in ice in an Eppendorf chiller during sonication. In addition, nanodroplets were produced with a pulsed sonication to further avoid excessive temperature increase. The test described in Paragraph 3.1.1.1.2 was performed to determine whether the pulse length had an effect on the final ND size. Shorter pulses were anticipated to cause a lower increase in fluid temperature, hence a potential lower evaporation of PFP. Having more PFP available in the medium could lead to bigger nanodroplets in the final batch, this idea being based on previously presented results where higher amounts of PFP led to bigger nanodroplets.

A pulsed sonication with an active time of 20 seconds and a pulse length of 6 seconds and 15% duty cycle was applied. During each pulse, the ultrasound wave was active for 1 second, rather than 2 seconds (as the one reported in the previous Paragraph). Table 3.2, Figure 3.13 and Figure 3.14 show the diameter and polydispersity index of nanodroplets obtained by using different amounts of PFP, and sonicating the sample with a pulsation of 6 seconds and duty cycle of 15%. As for the case of a pulsation of 7 seconds with 30% duty cycle presented in the previous Paragraph, increasing the amount of PFP resulted in larger nanodroplets with a higher polydispersity index. One-way ANOVA tests demonstrated that there was a statistical difference between the dimensions of nanodroplets produced with 5% or 15% v/v of PFP in PBS ($p < 0.05$), but there was not enough evidence to demonstrate a difference between the two different pulsation regimes.

PFP v/v in PBS	Diameter [nm]	PdI
5%	215.80 ± 16.77	0.20 ± 0.03
10%	315.01 ± 100.56	0.33 ± 0.12
15%	408.95 ± 171.24	0.42 ± 0.17

Table 3.2: *The table shows the mean diameter and the standard deviation of nanodroplets (after production) obtained with different concentrations of PFP, and by performing a pulsed sonication of 20 seconds with a pulse of 6 seconds and 15% duty cycle.*

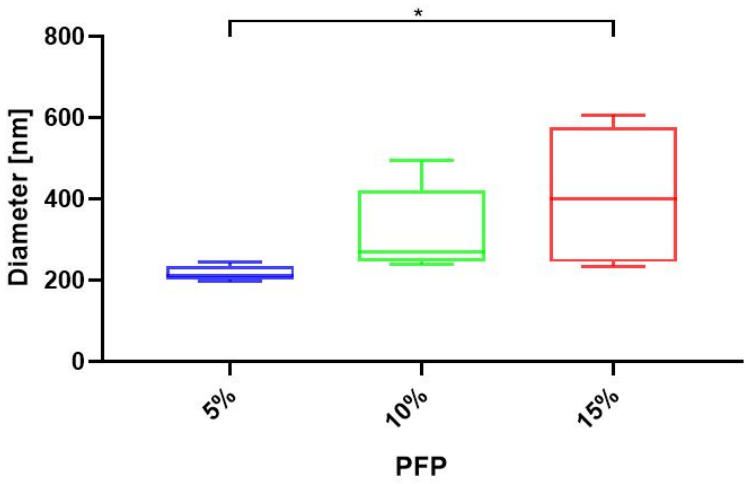

Figure 3.13: *The boxplots show the distribution of NDs diameter (after production) obtained with different concentrations of PFP and by performing a pulsed sonication of 20 seconds, with a pulse of 6 seconds and 15% duty cycle. NDs produced with 5% v/v of PFP in PBS were statistically different from the ones produced with 15% (*$p < 0.05$).*

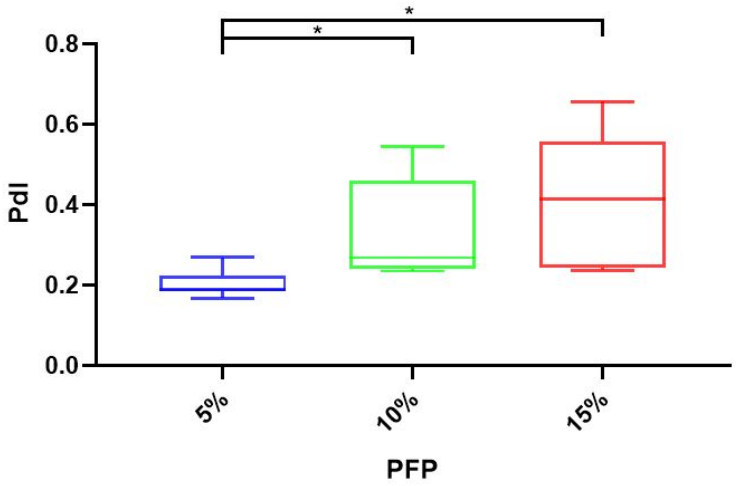

Figure 3.14: *The boxplots show the PdI of NDs (after production) obtained with different quantities of PFP and by performing a pulsed sonication of 20 seconds, with a pulse of 6 seconds and 15% duty cycle. NDs produced with 5% v/v PFP in PBS had a PdI which was statistically different from the other two groups (*$p < 0.05$).*

3.2.1.1.3 Effect of the intensity of the second sonication

After having investigated the influence of the quantity of PFP on the final ND size, another operational parameter was evaluated, namely the sonication power. It was hypothesised that increasing the sonication intensity would lead to a corresponding decrease in nanodroplet size and size dispersity, due to a more vigorous mechanical breakdown of NDs.

Confirming the hypothesis, Table 3.3, Figure 3.15 and Figure 3.16 show the diameter and PdI of nanodroplets obtained by performing a sonication at 48 and 72 W. Results obtained with a 24 W power are not reported, since the sample quality was too low (as reported by the DLS software). By increasing the power from 48 to 72 W, a reduction in both ND size and size dispersity was obtained from 354.65 $\pm$ 127.21 nm to 315.01 $\pm$ 100.56 nm. A one-way ANOVA was performed on the results and it showed that there was no statistical difference between the groups tested.

Intensity [W]	Diameter [nm]	PdI
48	354.65 ± 127.21	0.41 ± 0.20
72	315.01 ± 100.56	0.33 ± 0.12

Table 3.3: *The table shows the mean diameter and standard deviation of nanodroplets (after production) obtained using different sonication powers in the range 48 - 72 W.*

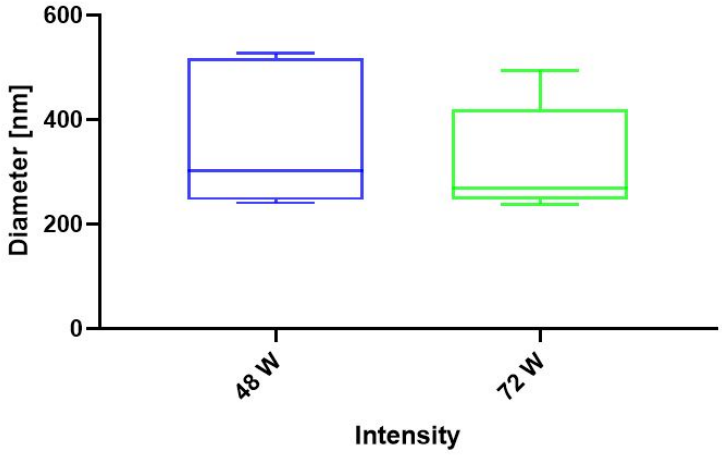

Figure 3.15: *The boxplots show the distribution of ND diameter after production, for NDs obtained with sonications of different power.*

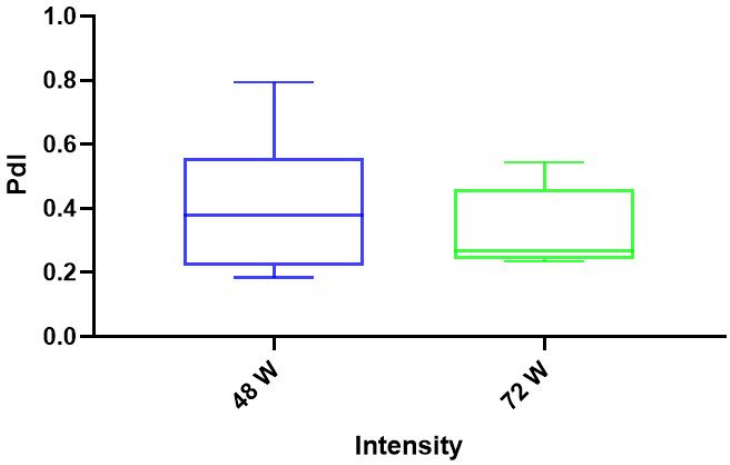

Figure 3.16: *The boxplots show the polydispersity index of ND diameter after production, for NDs obtained with sonications of different power.*

3.2.1.1.4 Effect of the length of the second sonication

The effect of the duration of the second sonication on ND size was evaluated following the protocol presented in Paragraph 3.1.1.1.4, and the results are presented in Table 3.4. The active time of the second sonication step was varied between 20 and 60 seconds. The hypothesis was that an increase in the sonication length would lead to smaller NDs with a lower size dispersity due to the longer mechanical action of ultrasound on the batch.

Table 3.4: *The table shows the mean diameter and standard deviation of nanodroplets produced with different sonication durations, and their corresponding polydispersity index.*

Time [s]	Diameter [nm]	PdI
20	277.55 ± 60.69	0.27 ± 0.11
40	314.03 ± 75.28	0.41 ± 0.12
60	249.74 ± 9.67	0.35 ± 0.04

Figures 3.17 and 3.18 show respectively the diameter and standard deviation of nanodroplets, and corresponding polydispersity index values.

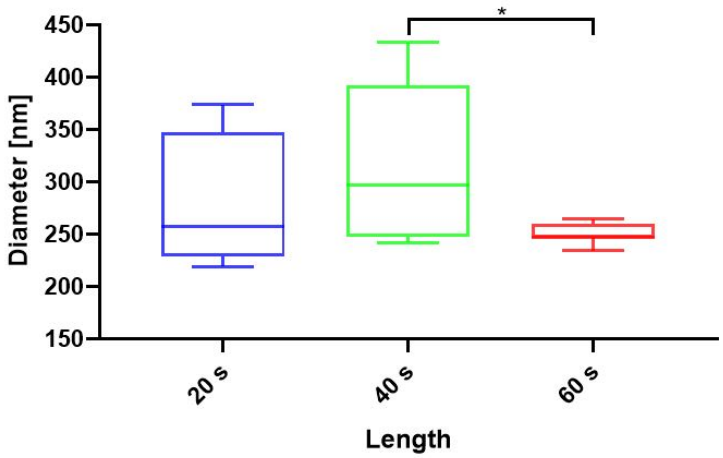

Figure 3.17: *The boxplots show the diameter distribution of nanodroplets produced varying the length of the second sonication. There was a statistical difference between nanodroplets produced with a sonication of 40 seconds and 60 seconds (*$p < 0.05$).*

A one-way ANOVA test showed that there was enough evidence to demonstrate a statistical difference between the diameters of nanodroplets produced with a sonication

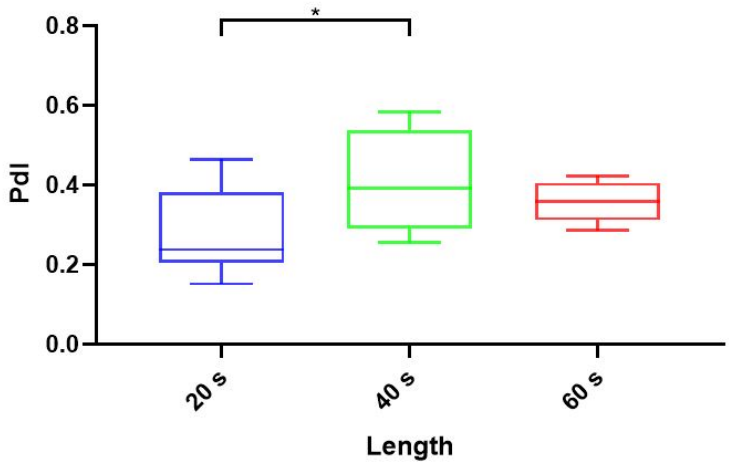

Figure 3.18: *polydispersity index of nanodroplets produced varying the length of the second sonication. There was a statistical difference between nanodroplets produced with a sonication of 20 seconds and 40 seconds ($^*p < 0.05$).*

of 40 seconds and 60 seconds ($p < 0.05$), while there was not enough evidence to prove that the other values were different. Nanodroplets produced with a second sonication of 60 seconds were the most reproducible since the standard deviation was only 9.26 nm.

3.2.1.1.5 Effect of production in cell medium

Nanodroplets were produced in cell medium instead of PBS, as described in Paragraph 3.1.1.1.5, to investigate whether this would impact on their properties and to assess whether direct administration of droplets could be performed, using a biologically relevant medium and without dilution. Bovine serum albumin (BSA) is a protein and a component of fetal bovine serum (FBS), and this could lead to the formation of protein-shelled droplets. Nanodroplets were produced either sonicating a solution containing only PFP and the chosen cell medium, and sonicating a solution containing PFP, the chosen cell medium and phospholipids.

Figure 3.19 and Table 3.5 show the diameter of the nanodroplets produced, while Figure 3.20 shows their PdI. When lipids were present in the suspension, the nanodroplets produced were comparable in size, suggesting that the presence of proteins or other chemicals in the suspension did not have a significant effect on the ND size. When only the enriched cell medium with PFP was sonicated, this led to the production of NDs which were different in size from the ones produced in the

presence of lipids. NDs produced in DMEM and BSA were slightly larger than their counterparts produced in the presence of lipids; but the main difference was between NDs produced in DMEM and FBS without lipids and the ones produced in DMEM and FBS with lipids. In the former case, there was a difference between mean values of 102.53 μm; in the latter, the difference was of 1130.96 μm.

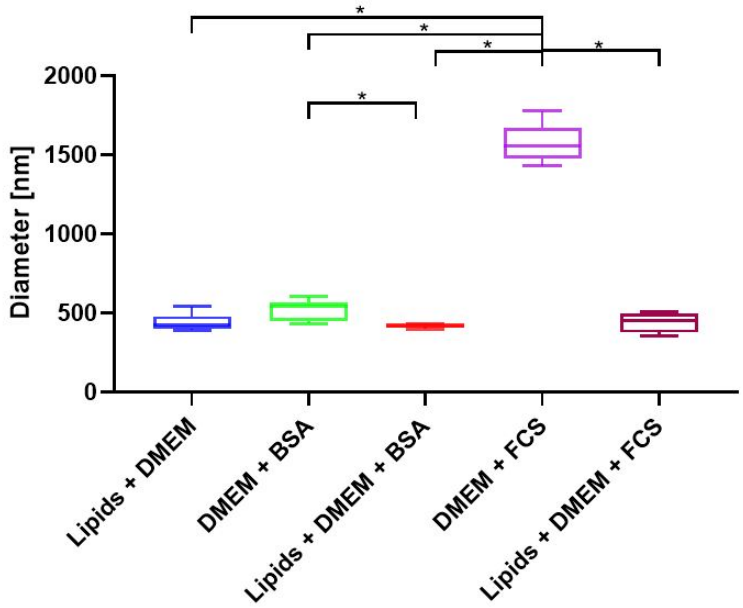

Figure 3.19: *Boxplots showing the diameter of nanodroplets produced in a medium composed of various formulations. There was a statistical difference between nanodroplets produced in DMEM and FBS without lipids and all the other groups, and between nanodroplets produced in DMEM and BSA with or without lipids (*$p < 0.05$).*

A statistical difference was present between the diameter of nanodroplets produced in DMEM and FBS without lipids and all the other groups ($p < 0.05$), and between nanodroplets produced in DMEM and BSA with or without lipids ($p < 0.05$). There is not enough evidence to conclude that there is a statistical difference between the other groups.

Table 3.5: *The table shows the mean diameter and PdI with their standard deviation of nanodroplets produced in different media.*

	Diameter [nm]	PdI
Lipids + DMEM	440.23 ± 54.07	0.6 ± 0.18
DMEM + BSA	520.94 ± 62.19	0.34 ± 0.06
Lipids + DMEM + BSA	418.41 ± 9.96	0.52 ± 0.04
DMEM + FBS	1570.67± 113.38	0.42 ± 0.09
Lipids + DMEM + FBS	439.71 ± 57.34	0.54 ± 0.08

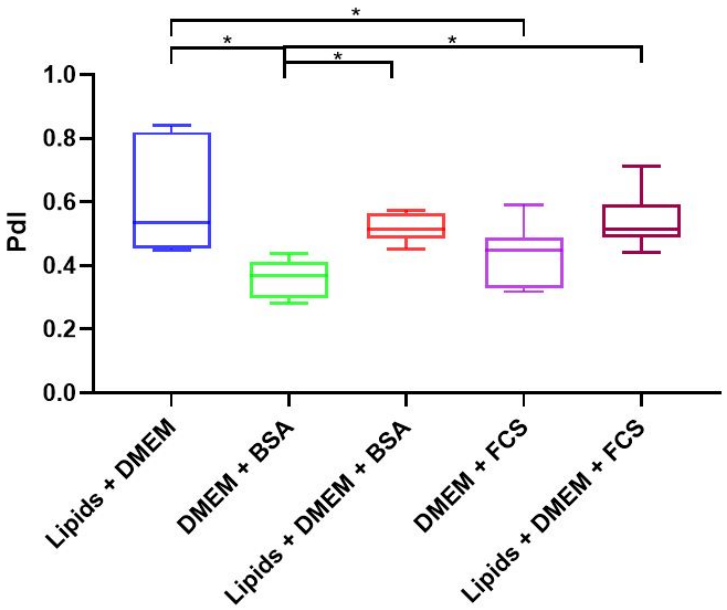

Figure 3.20: *Boxplots showing the polydispersity index of nanodroplets produced in media composed of different chemicals. The bars on the top of the graph indicate the groups that are statistically different (*$p < 0.05$).*

3.2.1.1.6 Effect of nanodroplet dilution in cell medium

Nanodroplets were produced in PBS and then diluted in different ratios of DMEM and DMEM with 10% FBS, as explained in Paragraph 3.1.1.1.6. It was hypothesised that: (i) the interaction between the lipids in the ND shell and the proteins and amino acids of DMEM could have an impact on the size of NDs by modifying the shell composition, and (ii) that different dilutions in cell medium could lead to different ND sizes. Figures 3.21 and 3.22 show the diameter and polydispersity index of nanodroplets, and Table 3.6 summarises these values.

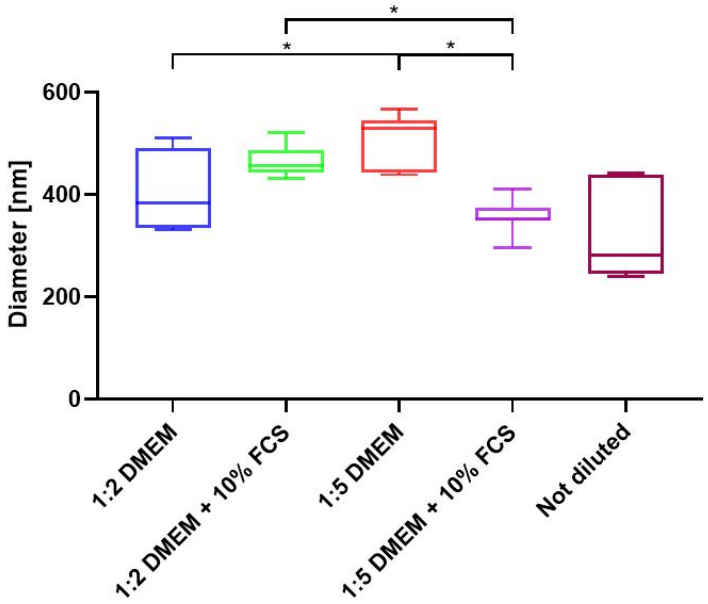

Figure 3.21: *Boxplots showing the diameter of nanodroplets produced in PBS and diluted 1:2 or 1:5 by volume, in a medium composed of different chemicals. there was a statistical difference between NDs diluted 1:5 in DMEM and both 1:2 in DMEM and 1:5 in DMEM and FBS and between ND diluted 1:2 and 1:5 in DMEM and FBS (*$p < 0.05$).*

Results show that ND dimension was not affected by dilution. While in the case of microbubbles sample dilution led to an increase in MB diameter, there was no sufficient evidence to suggest that dilution might have an impact on the size of NDs. A one-way ANOVA was performed on the results and it showed that there was a statistical difference between NDs diluted 1:5 in DMEM and both 1:2 in DMEM and 1:5 in DMEM and FBS and between ND diluted 1:2 and 1:5 in DMEM and FBS.

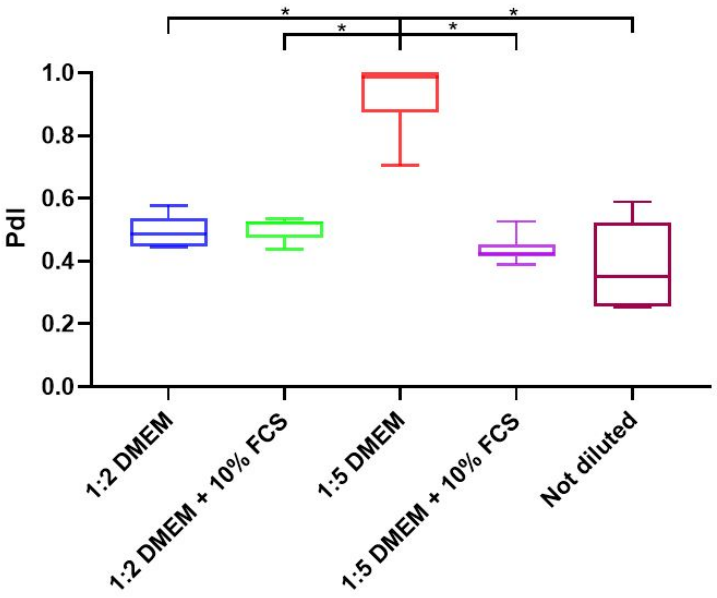

Figure 3.22: *Boxplots showing the polydispersity index of nanodroplets produced in PBS and diluted 1:2 or 1:5 by volume, in a medium composed of different chemicals. There was a statistical difference between NDs diluted 1:5 in DMEM and all the other cases (*$p < 0.05$).*

Table 3.6: *The table shows the mean diameter and standard deviation of nanodroplets diluted in different media.*

Dilution medium	Diameter [nm]	PdI
1:2 DMEM	406.02 ± 73.09	0.49 ± 0.05
1:2 DMEM + 10% FBS	464.08 ± 30.06	0.50 ± 0.03
1:5 DMEM	503.58 ± 51.60	0.93 ± 0.10
1:5 DMEM + 10% FBS	356.22 ± 31.22	0.44 ± 0.04
Not diluted	409.9 ± 176.66	0.42 ± 0.14

3.2.1.1.7 Effect of storage temperature

NDs were produced with a second sonication step of 60 seconds and stored at 37°C for two hours, to study their stability at conditions comparable to the ones present *in vitro* and *in vivo*, as explained in Paragraph 3.1.1.1.7.

Figures 3.23 and 3.24 show respectively the diameter and polydispersity index of NDs with respect to time, while Table 3.7 shows their values.

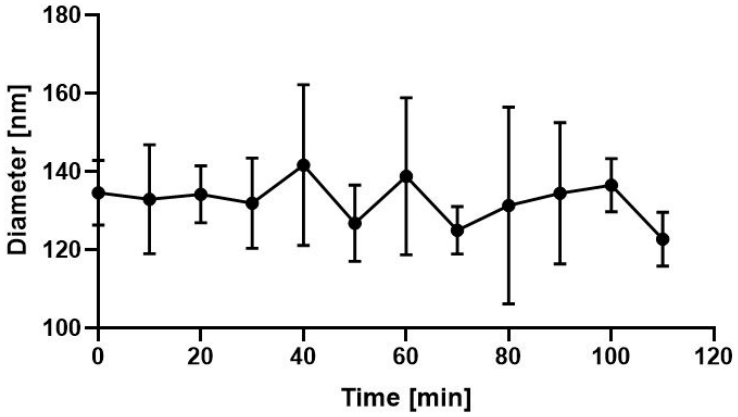

Figure 3.23: *The graph shows the mean diameter and standard deviation with respect to time of nanodroplets stored at 37°C and analysed at different time points up to 110 minutes.*

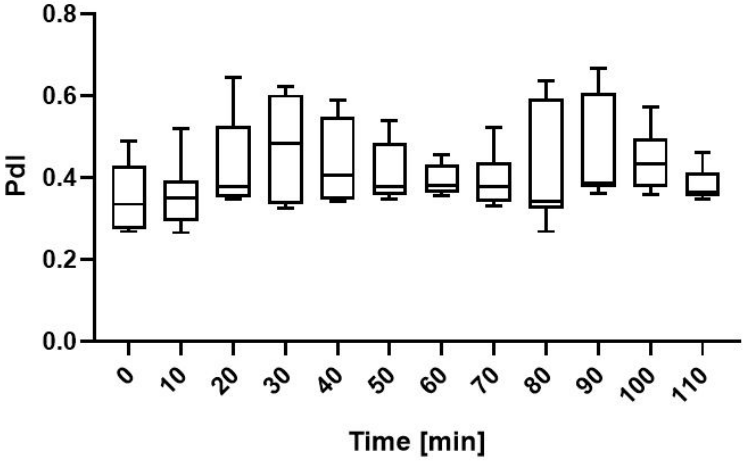

Figure 3.24: *The graph shows the PdI and its standard deviation of nanodroplets stored at 37°C and analysed at different time points up to 110 minutes.*

Table 3.7: *The table shows the mean diameter and the standard deviation of nanodroplets stored at 37°C and analysed at different time points up to 110 minutes.*

Time [min]	Diameter [nm]	PdI
0	134.58 ± 8.26	0.35 ± 0.08
10	132.90 ± 13.90	0.36 ± 0.08
20	134.14 ± 7.30	0.43 ± 0.11
30	131.86 ± 11.54	0.47 ± 0.12
40	174.98 ± 67.02	0.44 ± 0.10
50	126.8 ± 9.77	0.41 ± 0.07
60	138.74 ± 20.09	0.39 ± 0.04
70	124.98 ± 6.09	0.39 ± 0.06
80	131.26 ± 25.14	0.42 ± 0.14
90	134.45 ± 18.06	0.46 ± 0.12
100	136.48 ± 6.83	0.44 ± 0.07
110	122.68 ± 6.91	0.38 ± 0.04

The diameter of NDs did not change with respect to time even when they were stored at 37°C. There was no statistical difference between the diameters of the samples analysed ($p > 0.05$). Microscope images of the samples were also acquired at each time point analysed, and these showed the potential presence of some microbubbles, Figure 3.25, which could not be detected by the DLS machine because, being filled with air, they float in the cuvette.

Some small microbubbles were present just after production; from 40 minutes onwards, larger microbubbles were detected. Microbubbles present in the sample after production were measured and they had a mean diameter of 2.48 ± 1.06 μm, while the larger microbubble detected had a diameter equal to 10.5 μm. This demonstrates that the particle size in the sample is still below the critical value of 10 μm (95% of the microbubbles in batches used in the clinic have a size smaller than 10 μm, hence the reference to this value [56]); thus, the sample would be safe for intravascular usage.

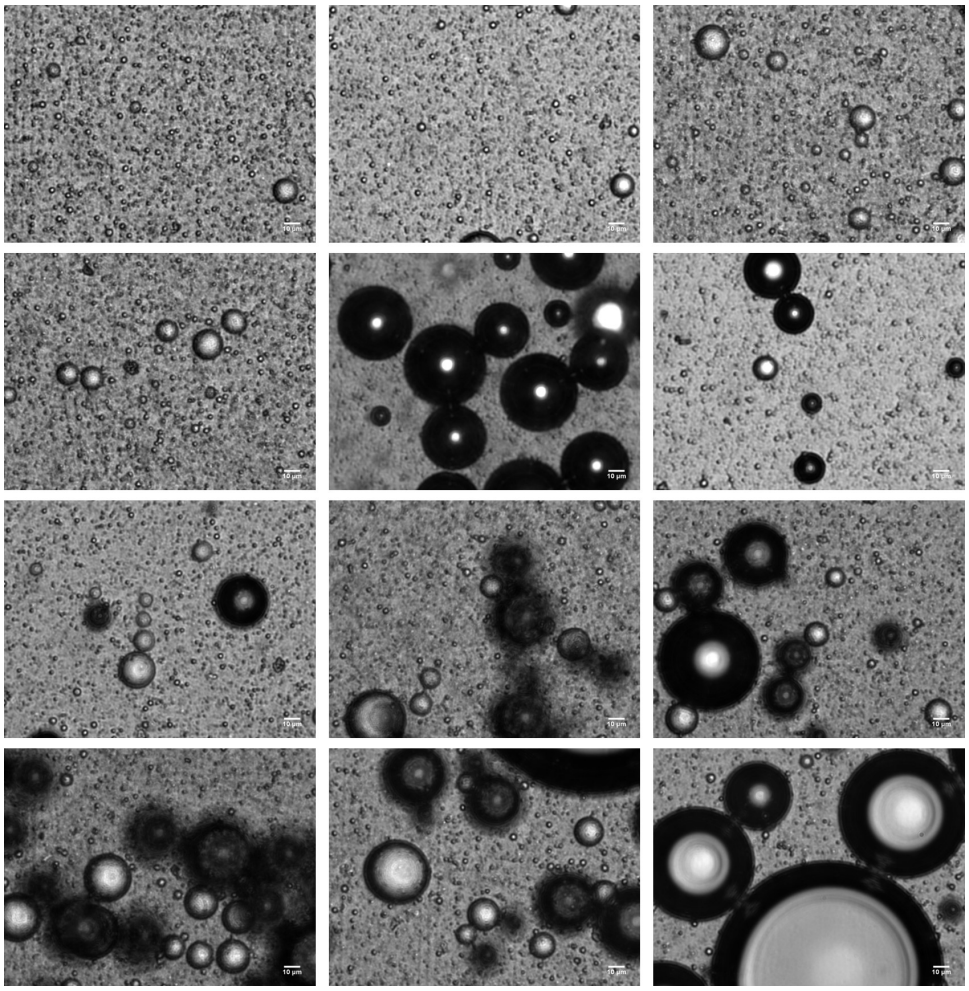

Figure 3.25: *The pictures shows microscope images of the sample of nanodroplets stored at 37°C. Pictures were taken every 10 minutes up to 110 minutes. Some small microbubbles were present just after production; from 40 minutes onwards, larger microbubbles were detected. The scale bar on the pictures indicates a length of 10 μm.*

3.2.1.1.8 Effect of the use of a fluorescent dye

Fluorescent labelling of nanodroplets is commonly performed for visualisation *in vivo* and *in vitro*. Nanodroplets were labelled with DiI at different molar ratios to assess if this could have and impact on their size. Three different final concentrations were used: 2.14 µM, 10.71 µM and 21.42 µM, corresponding to molar ratios DSPC:PEG40s:DiI of 0.89:0.101:0.00025, 0.9:0.101:0.0012, and 0.9:0.101:0.0025. Figures 3.26 and 3.27 show respectively the diameter and PdI of nanodroplets, and the corresponding values are shown in Table 3.8.

As described in Paragraph 2.2.1.2.3 for MBs, higher molar amounts of DiI led to bigger MBs soon after production. As for NDs, the use of DiI did not have an impact on their size; i.e. there was no statistical difference between the three groups analysed ($p > 0.05$).

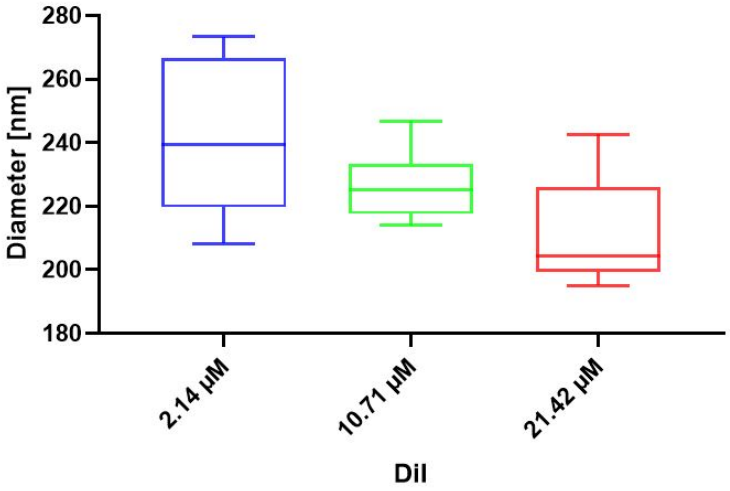

Figure 3.26: *The boxplots show the diameters of nanodroplets produced with different amounts of DiI. The use of DiI did not have a significant impact on ND size.*

Table 3.8: *The table shows the mean diameter and the standard deviation of nanodroplets produced with different concentrations of DiI.*

DiI concentration [µM]	Diameter [nm]	PdI
2.14	240.49 ± 23.74	0.35 ± 0.02
10.71	226.24 ± 10.37	0.44 ± 0.07
21.42	211.75 ± 16.74	0.41 ± 0.04

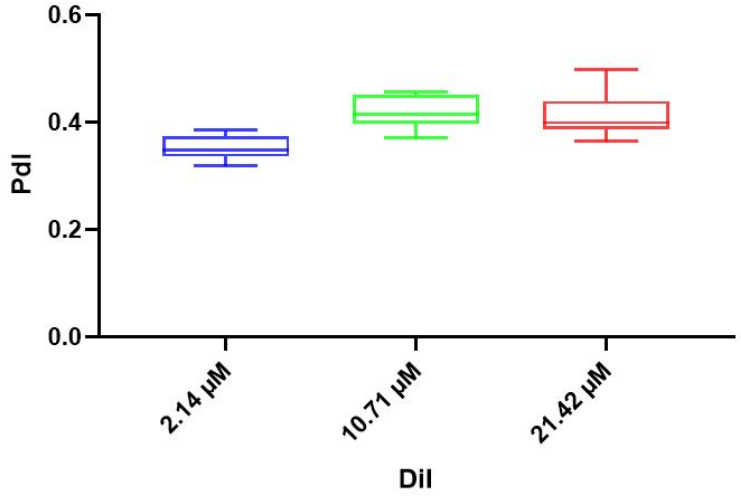

Figure 3.27: *Boxplots showing the polydispersity index of nanodroplets produced with different amounts of DiI. Changing the concentration of DiI did not affect the PdI.*

3.2.1.2 Stability of nanodroplets with respect to time

Following the production and storage of nanodroplets, as described in Paragraph 3.1.1.2, ND size was measured at different time points. Results are presented in Table 3.9. Figures 3.28 and 3.29 show respectively the ND diameter at different time points, and the corresponding polydispersity index.

Time [h]	Diameter [nm]	PdI
0	409.90 ± 176.65	0.42 ± 0.14
2	388.96 ± 164.36	0.41 ± 0.19
24	553.23 ± 155.21	0.70 ± 0.16
48	463.11 ± 160.22	0.61 ± 0.19
72	473.20 ± 55.17	0.75 ± 0.14
144	491.67 ± 119.31	0.61 ± 0.22

Table 3.9: *The table shows the mean diameter and the standard deviation of nanodroplets at the different time points tested, and corresponding polydispersity index.*

It should be noted that, while samples measured just after production and after 2 hours were of sufficient quality, samples tested at greater time points were of poorer quality in some cases, which required additional repeats.

There was no significant difference between the diameter of NDs at different time

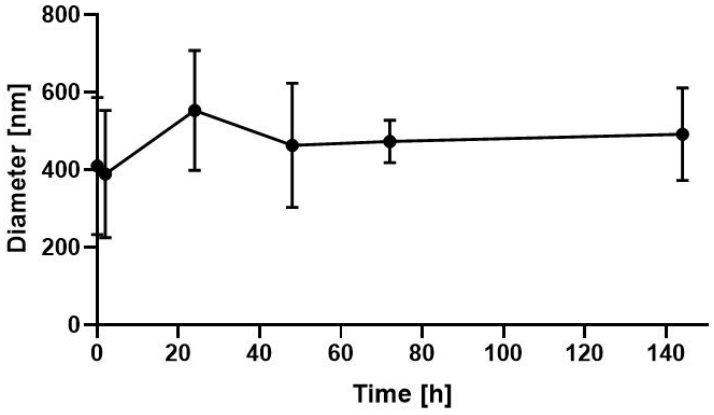

Figure 3.28: *The graph show the diameters of nanodroplets at the different time points tested.*

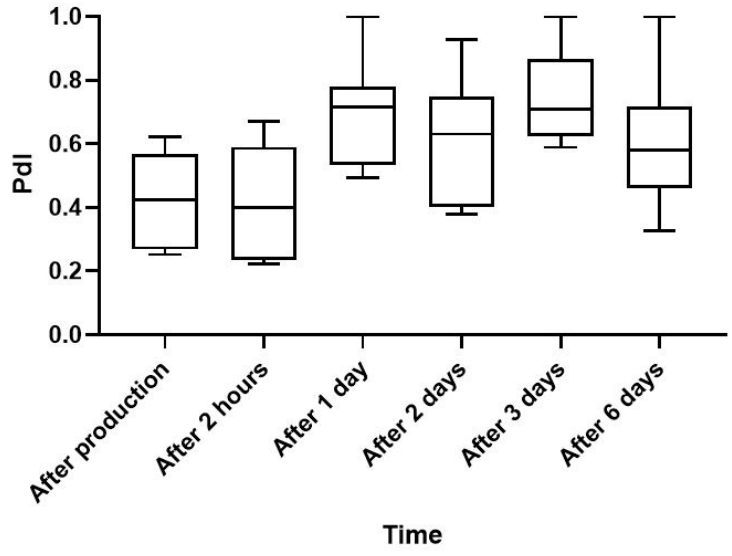

Figure 3.29: *Boxplots showing the polydispersity index of nanodroplets, at the different time points tested.*

points ($p > 0.05$). As for the PdI, values obtained after production and after 2 hours were different from the ones obtained after one and three days ($p < 0.05$), while the other values did not show a significant difference.

3.2.2 Phase Transition of Nanodroplets

3.2.2.1 Acoustofluidic device

Nanodroplets can transition into microbubbles on an increase in temperature or a change in pressure induced by ultrasound stimulation. Nanodroplets were produced following the protocol explained in Paragraph 3.1.1, and tests were performed as outlined in Paragraph 3.1.2.1.

As for the computational simulations to know the temperature in the device; Figure 3.30 shows that it is possible to obtain an increase in temperature limited in space in the chamber under study and that the Peltier element allows to have an homogeneous temperature of 37°C in the volume of the device containing the sample of NDs.

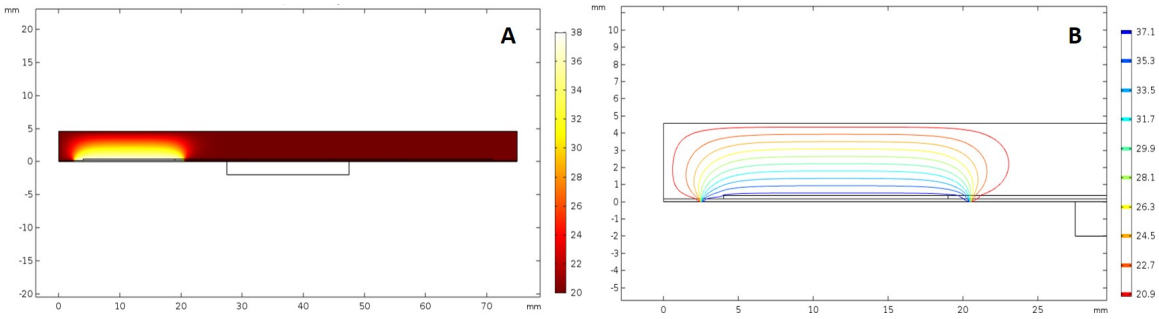

Figure 3.30: *A) Temperature evolution in the device. B) Isotherms in the device.*

To study the acoustic field inside chamber two, two different transducers (1 mm and 2 mm) have been implemented and four different thicknesses of the fluid layer have been tested for each transducer, namely 0.2, 0.3, 0.4 and 0.5 mm. Firstly, the resonance frequency of each model was defined and values are presented in Table 3.10.

The resonance frequency found for each case tested was then used to calculate the average value of the absolute acoustic pressure developed inside the volume of chamber two. Since it was found that the thickness of PDMS influences the standard deviation of such value, simulations were run to find the thickness connected to the lowest standard deviation of the absolute acoustic pressure. Having a limited standard deviation of this value means that the acoustic field developed inside the volume of the

Table 3.10: *The table shows the resonance frequency of every combination of thickness of transducer and thickness of fluid layer tested.*

Thickness fluid [mm]	PZT 1 mm [MHz]	PZT 2 mm [MHz]
0.2	0.855	1.705
0.3	1.147	1.195
0.4	0.879	0.437
0.5	0.855	0.746

chamber is homogeneous, hence the number of nodes and antinodes is limited, hence nanodroplets are stimulated homogeneously throughout the volume. The optimal thicknesses of PDMS for each case tested are presented in Table 3.11.

Table 3.11: *The table shows the thickness of PDMS minimising the standard deviation of the absolute acoustic pressure in chamber two for every combination of transducer and thickness of fluid previously defined.*

Model	Resonance frequency [MHz]	Optimal PDMS thickness [mm]
PZT: 1 mm, t: 0.2 mm	0.855	5
PZT: 1 mm, t: 0.3 mm	1.147	3.4
PZT: 1 mm, t: 0.4 mm	0.879	5
PZT: 1 mm, t: 0.5 mm	0.855	3
PZT: 2 mm, t: 0.2 mm	1.705	4.2
PZT: 2 mm, t: 0.3 mm	1.195	3.8
PZT: 2 mm, t: 0.4 mm	0.437	5
PZT: 2 mm, t: 0.5 mm	1.746	5

The values presented in Table 3.10 and Table 3.11 were then used to plot the mean absolute acoustic pressure and standard deviation for each model tested to select the best one to use. Such values are shown in Figure 3.31.

Thus the model that will stimulate the nanodroplets most strongly is model 3, but its absolute pressure may not be homogeneous due to its high standard deviation. On the contrary, model 7 seems to have a very homogeneous pressure but less intense sound pressure than the other models. The rationale for condition selection was the standard deviation of the acoustic pressure field measurements as an indication of field uniformity. By taking into consideration both the absolute acoustic pressure value and its standard deviation, model 1 was chosen to carry on all the following

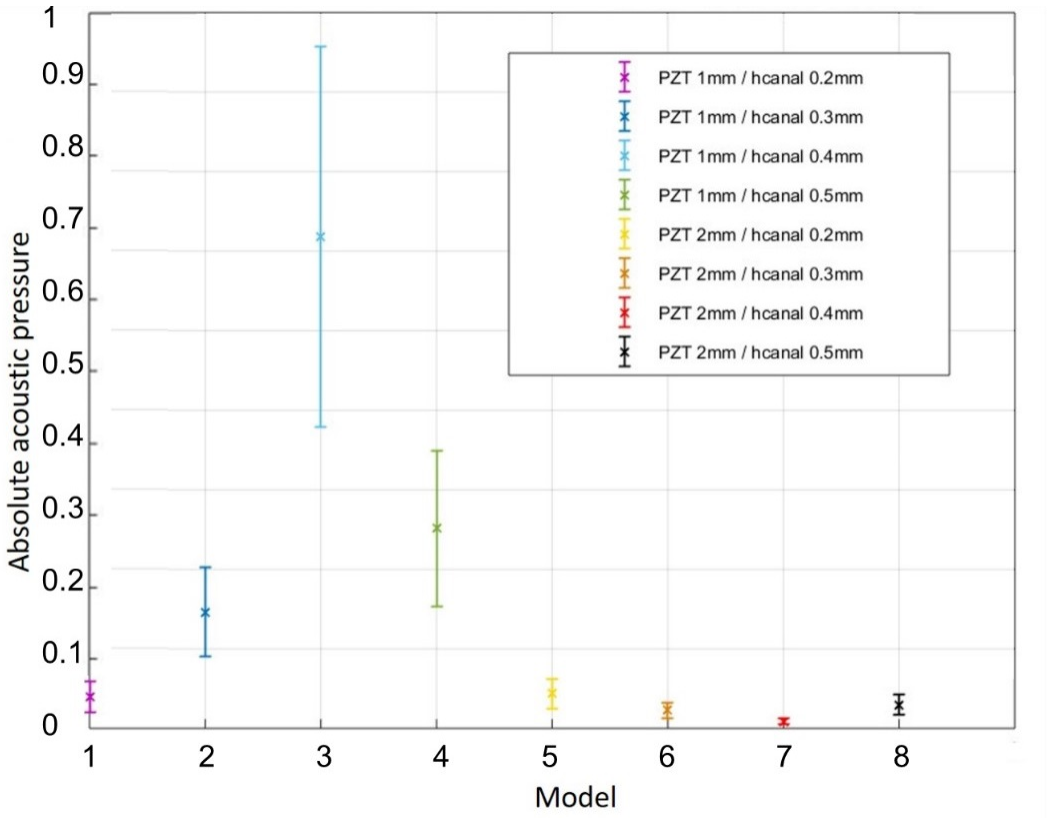

Figure 3.31: *Normalised mean absolute acoustic pressure and standard deviation of the acoustic pressure field developed in the volume of chamber two for every model tested.*

simulations and experiments. The absolute acoustic pressure field developed in this model is shown in Figure 3.32.

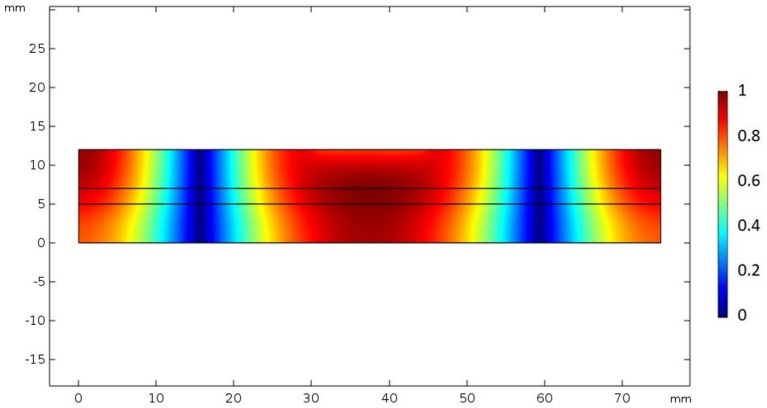

Figure 3.32: *Absolute acoustic pressure field developed in the volume of chamber two in model 1.*

The following step was to manufacture the acoustofluidic device corresponding to the model selected and perform phase transition tests of nanodroplets. After having produced the device, it was possible to ensure that they flowed into the device. It had to meet different constraints. The first constraint was about having a laminar flow throughout the channel; and the second one was that, after filling the entire first chamber, injecting the same amount of nanodroplets into chamber 1 pushed the first injection into the second chamber. To verify this, the second injection of NDs was coloured to observe its flow. Thus the flow responded well to the constraints, as shown in the Figure 3.33.

The first chamber into which the nanodroplets are introduced aims to fix the solution at a desired temperature. This is variable using a Peltier element which, at a fixed intensity, varies the temperature by varying its voltage. However, it was first necessary to determine the temperature at the surface of the Peltier element as a function of the voltage, for a current of 1 A. For this purpose, a thermal camera and a voltage generator were used. The voltage applied to the Peltier element was varied and the temperature generated was measured using the thermal camera. Figure 3.34 shows the evolution of temperature (^{o}C) as a function of voltage (V).

Thus, to reach a temperature of 37^{o}C in the fluid, a temperature of 39^{o}C was obtained in simulation on the surface of the Peltier element. It was therefore necessary to supply the Peltier with a voltage of 0.7 V. The temperature of the fluid in chamber

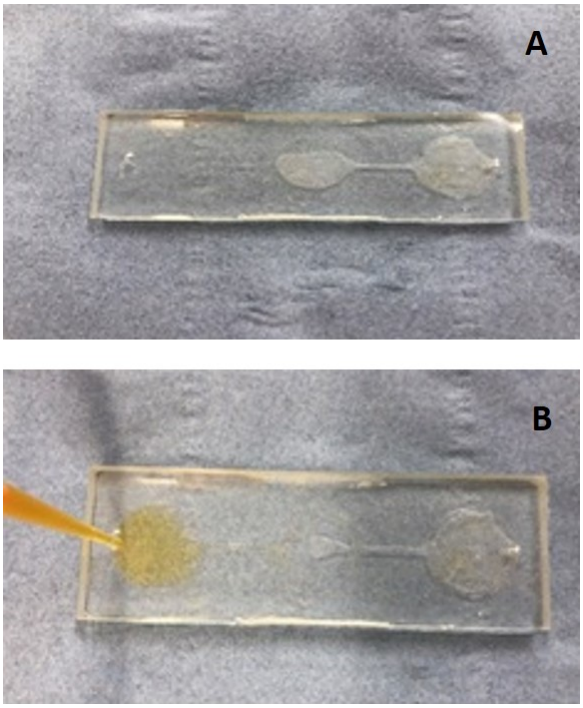

Figure 3.33: *Photo of the device with nanodroplets in the first chamber (A) and then after injection of coloured nanodroplets in the same chamber (B).*

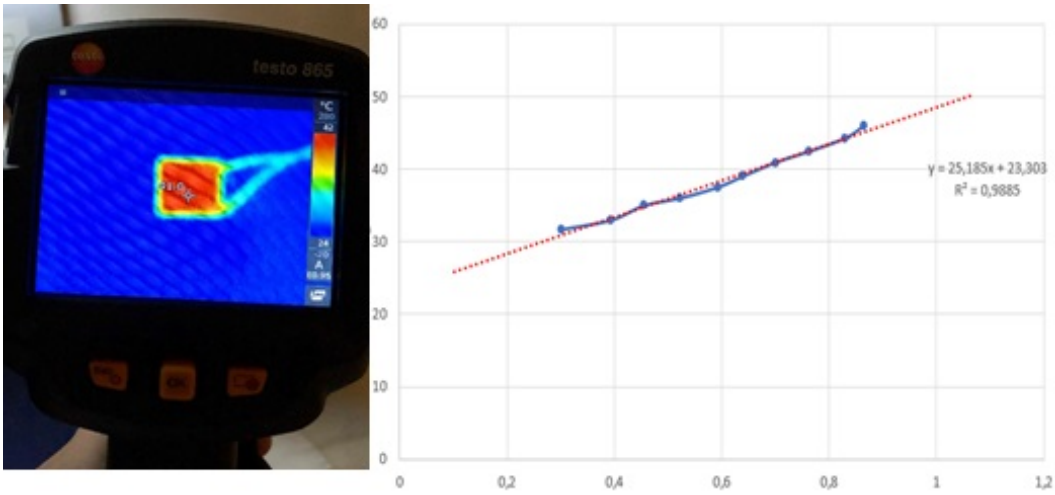

Figure 3.34: *a) Thermal image of a Peltier element powered at 0.7 V and 1 A. b) Temperature evolution as a function of the Peltier element voltage.*

1 was checked by using the thermal camera.

The experiment then involved the vaporisation of nanodroplets by means of both thermal and ultrasound stimulation, by following the protocol previously presented. Regardless of the time of exposure to ultrasound, microbubbles were obtained, as shown in Figure 3.35. One of the main problems identified is that the microbubbles produced were unstable, their size continued to grow after cavitation.

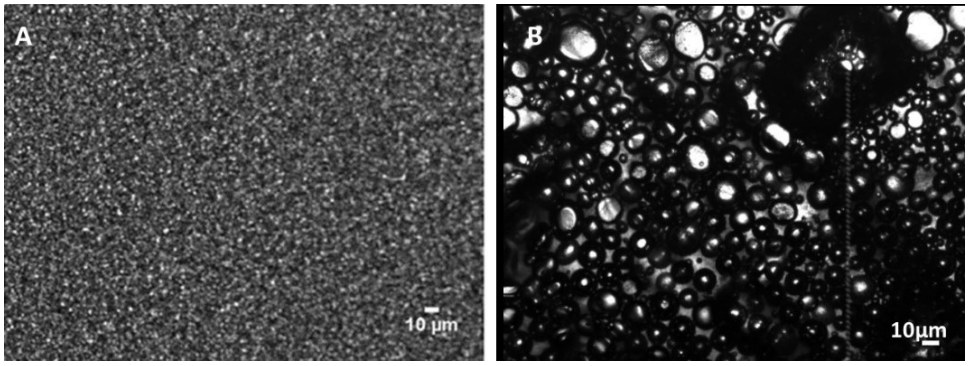

Figure 3.35: *Phase transition of NDs within an acoustofluidic device. A) Microscope image, taken with a 50x magnification objective, of NDs produced with a second pulsed sonication of 20 s. B) Microscopic image, taken with a 50x magnification, of the same sample after it was conveyed through both chamber 1, where the temperature of the sample was risen to 37°C, and chamber 2, where the US stimulation was applied. NDs phase transitioned to MBs.*

3.2.2.2 Phase transition in a tissue mimicking flow phantom

To study the phase transition of PFP NDs in a tissue mimicking flow phantom, the experiments presented in Paragraph 3.1.2.2 were performed and real-time B-mode imaging was used to visualise phase transition.

Figure 3.36 shows a real-time picture of the channel containing a sample of NDs prior to any US stimulation.

Both 400 nm and 200 nm NDs were tested and the acoustic pressure at which phase transition occurred was recorded. As for the sample containing the bigger NDs, namely with a diameter of 400 nm, Figure 3.37.a shows the moment at which phase transition from NDs to MBs occurred and Figure 3.37.b shows the channel filled with MBs obtained thanks to phase transition.

The first phase transition was obtained when an acoustic pressure of 3 MPa was applied to the sample constrained in the channel.

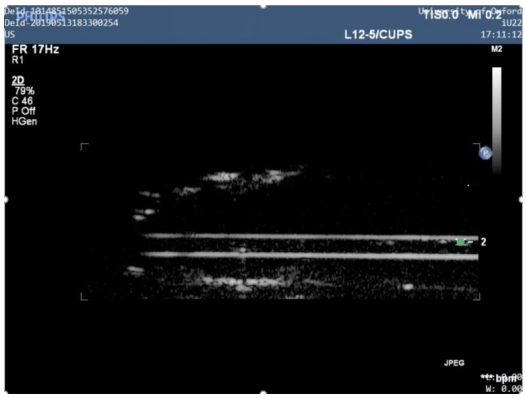

Figure 3.36: *Real-time B-mode image of the channel containing PFP NDs prior to any US stimulation.*

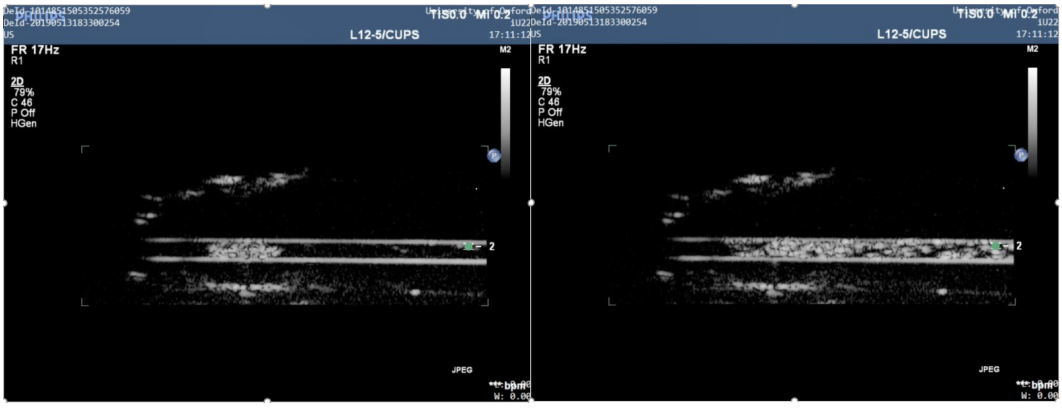

Figure 3.37: *a) Real-time B-mode image of the channel containing PFP NDs with a mean diameter of 400 nm at the moment when the first phase transition occurred. b) Real-time B-mode image of the channel containing MBs obtained from the phase transition of PFP NDs with a mean diameter of 400 nm.*

As for the sample containing the NDs with a mean diameter of 200 nm, phase transition was firstly obtained when an acoustic pressure of 3.87 MPa was applied. Figure 3.38.a shows the channel when the first phase transition was visualised while Figure 3.38.b shows the channel containing MBs obtained from phase transition.

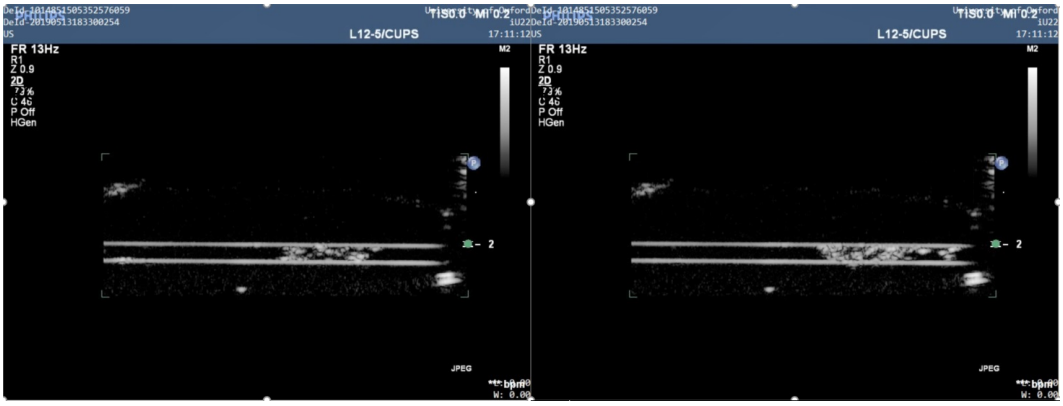

Figure 3.38: *a) Real-time B-mode image of the channel containing PFP NDs with a mean diameter of 200 nm at the moment when the first phase transition occurred. b) Real-time B-mode image of the channel containing MBs obtained from the phase transition of PFP NDs with a mean diameter of 200 nm.*

3.2.3 Intracellular Uptake of Nanodroplets

Figures 3.39 and 3.40 show preliminary observations from the cellular uptake experiment described in Paragraph 3.1.3.

Figure 3.39 shows four microscope pictures of MG63 cells incubated with MBs. The two blue areas are the nuclei of two cells stained with DAPI. The halos around the nuclei are external membranes and cytoplasm of the cells. The four pictures were taken at increasing z values, from the glass slide at the bottom to the coverslip at the top. These different focal positions were set to assess whether it was possible to detect uptake of microbubbles by cells and, in the presence of uptake, to assess the level of penetration of the bubble into the cytoplasm. The small yellow regions (< 1 μm in diameter) around the nuclei and the cell membrane represent DiI-labelled structures.

Similarly to Figure 3.39, Figure 3.40 shows cells incubated with labelled nanodroplets. Again, yellow staining indicates areas where DiI is present. Staining is visible both within the cell cytoplasm and outside the cells, in particular in picture A. Additional DiI staining could be detected inside the cells. As for the microbubble experiments,

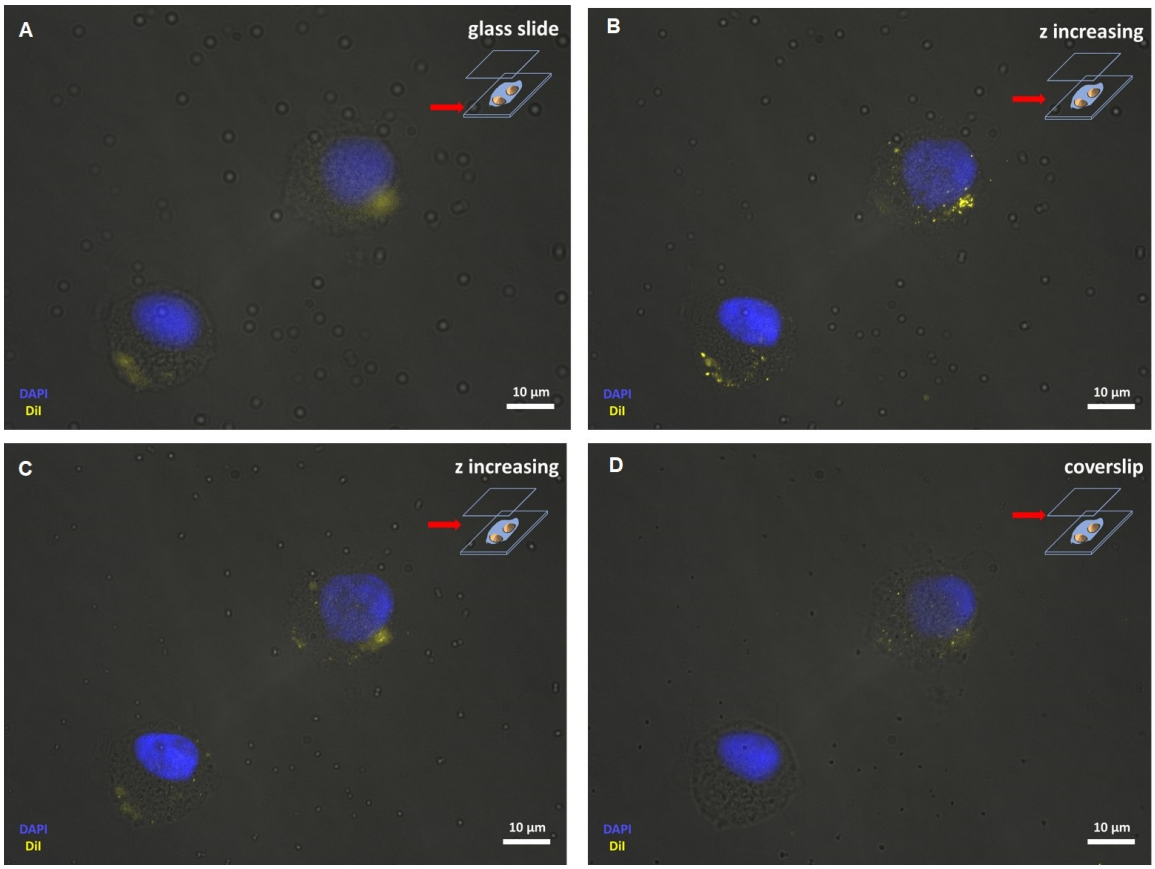

Figure 3.39: *The microscope images show two representative cells, where the blue circle is the nucleus stained with DAPI dye, while the yellow spots are the DiI-labelled structures stained with the fluorescent dye DiI. The four pictures were taken at different z values: A was taken on the glass slide, B and C were taken at increasing z levels, and D was taken on the coverslip. The scale bar on the pictures indicates a length of 10 µm.*

these could be the result of the interaction or uptake of DiI-labelled lipids by cells. Due to the small size of the dots, they could be entire nanodroplets taken up by cells or agglomerations of NDs present inside endosomes or lysosomes. In picture D there are some larger dots; notably, this picture was acquired in proximity to the upper coverslip, thus these dots may represent floating microbubbles or coalesced nanodroplets.

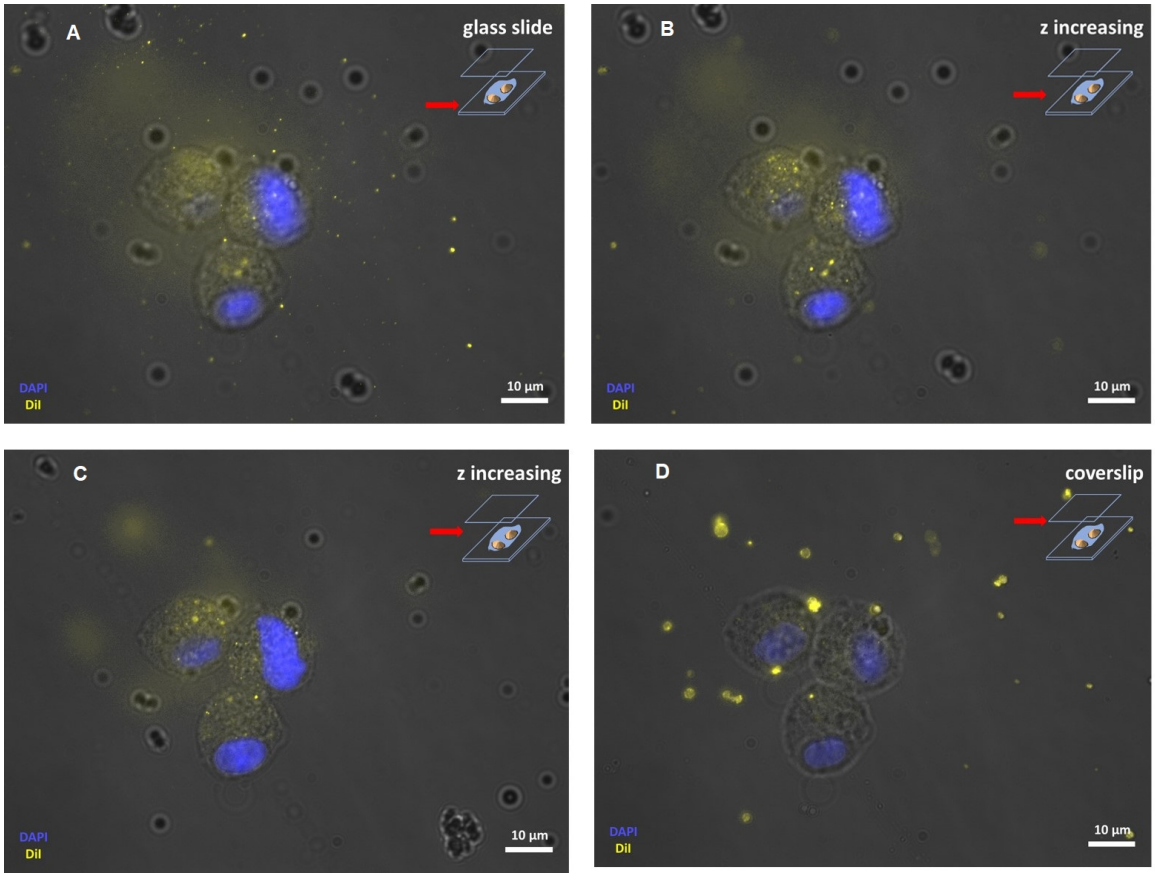

Figure 3.40: *The pictures show three cells, where the blue circle is the nucleus stained with the DAPI dye, while the yellow spots are the nanodroplets stained with the fluorescent dye DiI. The four pictures were taken at different z values: A was taken on the glass slide, B and C were taken at increasing z levels and D was taken on the coverslip. The scale bar on the pictures indicates a length of 10 µm.*

3.3 Discussion

3.3.1 Generation of Nanodroplets

Nanodroplets can be used as an alternative to microbubbles, or in combination with microbubbles, to enhance extravasation and therapeutic effects. Different parameters related to the production and storage of nanodroplets have been evaluated, to investigate their influence on nanodroplet size.

3.3.1.1 Effect of production parameters on nanodroplet size and dispersity

In order to achieve the production of a batch of ND with the desired characteristics in terms of size and small size dispersity, different experiments investigating the effects of production parameters were performed. Both the chemical composition of the medium used to produce NDs and the sonication step parameters were investigated.

As for the chemical composition used to produce NDs, two tests were performed; the former looked into the effect of varying the quantity of PFP used onto the size of NDs, while the latter investigated whether the use of the lipophilic dye DiI could have an impact on ND size.

The size of nanodroplets is an important factor for their use in *in vivo* application; as a matter of fact, it's important to find a trade-off between having a nanodroplet small enough to extravasate through the bone vasculature and a nanodroplet big enough to vaporise into a microbubble without using too high acoustic pressures (it is known that smaller NDs require higher acoustic pressures to extravasate) [42]. Previous work by Wang et al. [70], Stride et al. [26] and Rapoport et al. [169] reported the extravasation of particles with a diameter smaller than 200 nm to a bone fracture, and extravasation of paclitaxel loaded PFP PEG-PDLA nanodroplets with an average size of 250-300 nm to a tumour. It is also known that bone vessels are fenestrated with a pore size of 80 nm and that ultrasound and cavitation can increase the permeability of vessels allowing bigger particles to extravasate. For these reasons, a mean size around 200-300 nm is thought to be acceptable. Different concentrations of PFP, ranging between 5% and 15% v/v in PBS were used to produce different batches of NDs and results reported in Paragraph 3.2.1.1.1, Table 3.1 and Figure 3.11 (page 139), show that an increase in the concentration of PFP resulted in larger NDs. Notably, PFP is immiscible in the saline dispersion of DSPC and PEG40s; thus, when

it is added to PBS, it forms a separate layer on the bottom of the vial. The vial is subsequently stirred (for two seconds) to break this layer into droplets. During the sonication step, these droplets are broken down into nanodroplets. Therefore, it is likely that a greater amount of PFP results in larger precursor droplets that in turn generate larger nanodroplets upon sonication, as illustrated schematically in Figure 3.41.

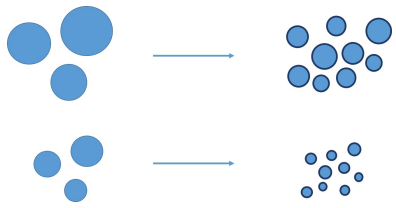

Figure 3.41: *A higher amount of PFP leads to larger precursor lipid-shelled droplets that - upon sonication - break down into larger nanodroplets.*

In addition to this, in this experiment, higher amount of PFP are associated with a decrease in the relative concentration of phospholipid surfactant. Less surfactant is available to surround PFP giving origin to the lipid shell and produced nanodroplets may be bigger to optimise the surface-area-to-volume ratio with respect to the available surfactant. In conclusion, adjusting the quantity of PFP in the solution offers a means to control the final mean size of the batch. Since our ND target diameter is in the range 200-300 nm, 10% PFP (v/v in PBS) is the amount that leads to the preferable outcome.

The possibility of labelling nanodroplets using fluorophores provides a means to detect them *in vitro* and *in vivo*. Figure 3.26 in Paragraph 3.2.1.1.8 (page 154) shows that an increase in the volume of DiI used led to a small decrease in the size of nanodroplets; however, there was no statistical difference between groups ($p > 0.05$). This result is in contrast with the microbubble labelling tests; Figure 2.16 in Paragraph 2.2.1.2.3 (page 93) shows that an increase in the quantity of dye led to larger microbubbles. It is thought that, in the case of microbubbles, the dye intercalates within the shell and, due to its molecular structure, it stretches the membrane and alters its gas permeability. On the other hand, in the case of nanodroplets, the dye could be in the liquid core and not in the membrane, hence it does not have an impact on NDs size [176]. DiI is commonly used to stain nanoparticles [171] [176], but, similarly to MBs, there is no study available looking into the effect that this might have on ND size, hence the results of this experiments represent a novelty in this area.

As for the tests looking into the effects of the second sonication step (namely the one leading to the production of nanodroplets); the sonication pulse, intensity and length were varied and their effect on ND size quantified.

Regarding the sonication pulse, Table 3.2 and Figure 3.13 presented in Paragraph 3.2.1.1.2 (page 142) show that there was no statistical difference between nanodroplets produced with a pulsation of 6 seconds and 15% duty cycle or a pulsation of 7 seconds and 30% duty cycle. This may suggest that the difference between the two pulsation regimes is not high enough to cause significant differences in size between the different generated NDs. Although there was no statistical difference between groups obtained with the two sonication regimes, it can be noticed that nanodroplets produced with a longer pulse were slightly smaller and less dispersed. This might be due to two reasons: the more persistent mechanical action of the sonication on one side and a lower evaporation of PFP (hence more PFP available when shorter pulses are used) on the other. Indeed, as previously observed in Paragraph 2.2.2.2, pulsed sonication led to larger and more dispersed bubbles compared to continuous sonication. As a consequence, there is a trade-off between the desired size and the dispersity associated. The size distribution of droplets influences their acoustical response upon ultrasound stimulation; a less dispersed suspension is preferable as it leads to a predictable acoustic response [140]. Considering these results, all nanodroplets used in the following studies of this work were produced with a pulsation of 7 seconds and 30% duty cycle.

Regarding the intensity of the second sonication, results reported in Paragraph 3.2.1.1.3, Figure 3.15 and Table 3.3 (page 144), show that a higher sonication power led to smaller and less dispersed nanodroplets. At 48 W, the mean diameter of nanodroplets was 346.65 $\pm$ 127.21 nm with a PdI of 0.41 $\pm$ 0.2; while a sonication of 72 W led to a mean diameter of 315.01 $\pm$ 100.56 nm with a PdI of 0.33 $\pm$ 0.12. This could be be due to the greater mechanical effects associated with higher ultrasound intensity, and this is further shown by the fact that a sonication intensity of 24 W led to a low-quality sample that could not be measured by the DLS machine. These results are in line with what had been previously shown by Bilati et al. [170]; in this work, a higher intensity led to smaller polymer-shelled nanodroplets. This shows that the sonication intensity has similar effects both on lipid-shelled and polymer-shelled nanodroplets. Based on these findings, a sonication power of 72 W was selected for further tests.

Finally, as for the length of the second sonication, Figures 3.17 and 3.18 in

Paragraph 3.2.1.1.4 (page 145) show that both diameter and dispersity of nanodroplets produced with a second sonication of 60 seconds had a smaller standard deviation in comparison with the other sonication lengths investigated. This results are in line with what had been previously shown by Bilati et al. [170]; in his work, a longer duration led to smaller polymer-shelled nanodroplets. As for lipid-shelled nanodroplets, this could have two explanations; on one hand, the effect of an increase in the length of the second sonication could be predominant with respect to the effect related to possible differences between different samples. The mechanical effects of a longer sonication could allow overcoming the variability between multiple repeats, as suggested by the standard deviation of the different samples, suggesting that the stochastic nature of the process is averaged out over longer times. Based on the previous results obtained and shown, another possible reason for obtaining smaller lipid-shelled NDs could be due to the evaporation of PFP. Having a longer active sonication could subject the sample to higher temperatures leading to a higher evaporation of PFP and having less PFP in the medium could result in smaller nanodroplets. For the 20-second sonication, the standard deviation is 60.69 nm; while the mean diameter obtained with the 60-second sonication has a standard deviation of 9.67 nm. On the other hand, since an increase in sonication length leads to an increase in fluid temperature, this may have caused some PFP to evaporate resulting in the production of liposomes rather than nanodroplets. Since there is not a similar study in literature, a droplet vaporisation test was performed to assess whether the obtained sample contained nanodroplets or liposomes.

Since the research about nanodroplets is relatively new in comparison to MBs, there are less available studies quantitatively evaluating the effects of production parameters onto ND size and size dispersity. Knowing the quantitative effects of changing different parameters on the final product allows to have control on the characteristics of the produced batch. To the best of the author's knowledge, no study in literature has quantitatively looked into the effect of the quantitaty of PFP and DiI, the sonication pulse, intensity and length on the final size of NDs; hence this represent a new addition to the field of nanodroplets.

3.3.1.2 Effect of cell medium on nanodroplets

Experiments were performed to investigate the effect of cell medium on ND size, to study if and how the presence of amino acids and proteins influence ND characteristics

and whether direct administration of droplets could be performed, using a biologically relevant medium and without dilution. The underlying hypothesis was that producing NDs in cell medium could have an impact on their size, due to the interaction with chemicals present in the medium. The results are shown in Paragraph 3.2.1.1.5. In a first step of the test, the dilution medium and PFP were sonicated in the absence of lipids, while - in a second step - lipids were added to the medium. Figure 3.19 (page 147) shows that there is no difference between all the groups tested, except for the case where PFP, DMEM and FBS were sonicated in absence of lipids. While the similar groups tested displayed a mean diameter of 454.82 μm, the different one had a mean size of 1570.67 μm. This could be a consequence of the composition of the medium.

Three media had been tested: DMEM, DMEM with 4 mg/mL of BSA, and DMEM supplemented with 10% FBS. DMEM is the basic cell medium and it is composed of 1 g/L of glucose, amino acids and vitamins, to provide cell with metabolites during culturing *in vitro* [177]. It can be supplemented with proteins, growth factors, antibiotics and other components to provide cells in the culture with a favourable environment; here the use of BSA and FBS was tested. BSA is a globular protein that is used in numerous biochemical applications due to its stability and low biological reactivity [178]; FBS is the liquid fraction of clotted blood from fetal bovine, depleted of cells, fibrin and clotting factors, but containing a large number of nutritional and macromolecular factors essential for cell growth. Bovine serum albumin is the major component of the fetal bovine serum. Growth factors are very important in fetal bovine serum, essential for the maintenance and growth of cultured cells. Fetal bovine serum also contains small molecules like amino acids, sugars, lipids, and hormones. [179]

Nanodroplets produced in DMEM and FBS had the biggest diameter, which was statistically different from all other groups ($p < 0.05$), and this is thought to be due to the chemicals present in FBS. When sonication is performed, it is possible that the proteins coat the surface of PFP emulsions, resulting in larger droplets. Interestingly, when the same process was repeated in the presence of lipids, the final nanodroplets were smaller and had comparable size to the ones produced with the other media. It is thought that the stabilising effects of lipids prevails on other medium constituents.

Other two groups displayed a statistical difference ($p < 0.05$): particles produced with or without lipids. Similarly to the previous case, the presence of lipids led to smaller and more monodispersed particles. Also in this case, the presence of lipids and

their behaviour and organisation upon US stimulation had an impact on the membrane of the droplets which is thought to be less influenced by the other components in the solution and hence smaller.

Nanodroplets were also analysed in their preparation medium or upon dilution in different media (with different dilution factors), as described in Paragraph 3.2.1.1.6. When the same test was performed with microbubbles, it was found that higher dilutions led to larger microbubbles (Paragraph 2.2.1.2.5). As illustrated in Figure 3.21 (page 149), the size of nanodroplets instead was not affected by dilution of the suspension medium. This could be due to the different compositions of MBs and NDs. MBs are filled with gas and there could be exchanges of gas between the inside and the outside of the lipid shell by diffusion. When already formed MBs are diluted in a fresh medium, this could have a different saturation of gases with respect to the one in which MBs have been produced; hence this could lead to an enhanced diffusion of gases to reach a concentration equilibrium resulting in an altered stability with respect to time. ND, instead, are filled with liquid and this could provide them with more resistance against the Ostwald ripening effect.

3.3.1.3 Stability of nanodroplets

Knowing the storage and *in vivo* stability of ND is fundamental to assess the maximum allowed time between production and use and to guarantee the efficacy of the treatment.

NDs were produced and stored either at 4^{o}C and at 37^{o}C and their size was checked with respect to time to assess their stability.

As for the storage stability, the results presented in Paragraph 3.2.1.2 show that ND diameter did not undergo significant changes with respect to time. Values taken after 1, 2, 3 and 6 days had a higher polydispersity index compared to the ones taken after production and after 2 hours. In addition, samples tested after 1 day (or more) showed a poor quality, meaning that more samples were needed to obtain at least three repeats of sufficient quality to be analysed. This suggests that, even if there is not enough evidence to prove that there is a statistical difference between the diameter of nanodroplets at different time points, their size dispersity increased with respect to time. This may be connected to the fact that coalescence or spontaneous phase transition to MBs happened. The monodispersity of nanodroplets is decreasing and the fact that the

DLS technique was not able to provide reliable results about certain sample suggests that those samples are not good and safe enough to be used for clinical applications. The sooner NDs are used after production, the better for their safety. According to data, if NDs are used up to two hours after production, their polydispersity index is maintained almost constant, allowing safe administration. In the literature, there is no available quantitative study using the same ND formulation to directly compare and validate these results, however Zhang et al. [180] studied the acoustic stability of PEGylated PLGA-based NDs at 4^{o}C for 5 days. The solution didn't show any echo in US imaging for two days, meaning that all NDs were maintaining their conformation. From the third day some echo appeared and it became stronger and stronger with the passing of time, indicating that phase transition to microbubbles had occurred without any stimulation applied.

The final aim of this study is to use nanodroplets as a drug carrier in the body to reach the site of a fracture, hence it was fundamental to characterise their stability at body temperature. Figure 3.23 (page 151) shows that nanodroplets were stable when stored at 37^{o}C for 110 minutes. The behaviour of nanodroplets at body temperature was thus different from the one of microbubbles, which displayed a marked increase in size when stored at 37^{o}C (Paragraph 2.2.1.2.4). This could be due to an enhanced stability of the liquid of NDs core made of PFP with respect to the gaseous one of microbubbles made of room air. As a matter of fact, the stability of microbubbles and nanodroplets relies on two different processes; MB stability strongly depends on gas diffusion from the gas core to the surrounding medium, while ND stability depends on the phase transition temperature of the liquid core. An increase in the storage temperature leads, consequently, to different behaviours. In the case of MB, the increased temperature results in an increased rate of diffusion. In the case of ND, if the temperature is higher than the phase transition temperature, then NDs vaporise into MBs; if it's lower, the liquid core maintains its phase and stability is not affected.

Interestingly, microscope images of the sample taken every 10 minutes (Figure 3.25, page 153) revealed some characteristics of the sample that could not be determined through DLS. Indeed, just after production, the sample was made of nanodroplets and bigger particles, which could correspond to microbubbles. After production, the microbubbles seen in the microscope picture were measured and they displayed a mean diameter or 2.48 $\pm$ 1.06 μm and the biggest microbubbles was 10.5 μm in size. Overall, these results demonstrate that the sample was safe for intravascular usage.

With increasing the storage time, the number of microbubbles in the sample increased and, from 40 minutes onward, it was possible to observe large microbubbles in the sample (which were not detected by DLS). It is thought that these large microbubbles are the result of coalescence of microbubbles present from the very beginning in the sample. Since microbubbles have a gas core, they float in a suspension; this is the reason why, even if they are present, the DLS device is not able to detect them. In addition to this, the maximum particle size that the DLS can capture is 10 μm; this means that some small microbubbles could be detected if they were not floating, but the bigger one wouldn't be detected anyway.

There is no available study using the same chemical composition to compare the results and stability at 37°C is composition-dependent: Lee et al. [71] showed that the average size of magnetic particle-loaded DTAB PFP NDs increased with respect to time at 37°C, and their concentration halved after 6 hours from production, while the concentration of Albumin–PEG hybrid nanoparticles encapsulating superparamagnetic iron oxide and PFP reduced by just 3.5% in the first 6 hours, denoting a huge difference in terms of stability.

3.3.2 Phase Transition of Nanodroplets

3.3.2.1 Acoustofluidic device

The results presented in Paragraph 3.2.2.1 demonstrate that it is possible to obtain MBs from NDs, confirming that the production protocol used results in a stimuli-responsive agent.

Acoustic droplet vaporisation was assessed using a custom-built acoustofluidic device composed of three chambers; where the first one was used to increase the temperature of the sample to body temperature (37°C), the second one was used to perform an acoustic stimulation and the third one was used to visualise the sample by means of a microscope. Thanks to the device, it was possible to reach an homogeneous temperature in the first chamber, as shown in Figure 3.30 (page 157). As for the acoustic stimulation, the device was designed to minimise the presence of standing waves in the sample volume and provide a stimulation as homogeneous as possible and maximise the areas of high acoustic pressure, as shown in Figure 3.32 (page 160). The rationale for condition selection was the standard deviation of the acoustic pressure field measurements as an indication of field uniformity.

The device was then tested experimentally and phase transition was achieved, demonstrating the effectiveness of the device. A main limitation of the device used is that microbubbles obtained as a result of phase transition were not stable and their diameter was not controllable. This is in line with what has been observed in the literature: after vaporisation, the resulting MB is in theory approximately 5 times bigger than the original ND; but larger MBs appear too, and these are secondary bubble developing due to different phenomena like: coalescence between newly formed MBs or between MBs and NDs and diffusion of dissolved air from small bubbles into larger bubbles (i.e. Oswald ripening). The expansion is, hence, hard to control and some bubbles become larger than expected [93] [82]. The rationale of the study is that US is applied a first time at low intensity to induce extravasation of ND thanks to the radiation forces applied on NDs and the increase in permeability of blood vessels usually associated with US; and a second time at high intensity to stimulate phase transition. Phase transition is, then, expected to happen after ND extravasation and, as a consequence, having big microbubbles should not be hazardous since they are not in the bloodstream where they could occlude vessels.

3.3.2.2 Phase transition in a tissue mimicking flow phantom

The experiments presented in Paragraph 3.2.2.2 were performed to visualise phase transition from NDs to MBs and quantitatively check the required acoustic pressure to achieve vaporisation for batches containing different sizes of NDs. Two dimensions of NDs were tested: 200 and 400 nm, building on the knowledge that the smaller the droplet, the higher the acoustic pressure needed to trigger phase transition, as shown in Figure 1.17 (page 42) presented in Paragraph 1.4.1 [43].

For the bigger NDs (mean diameter of 400 nm), phase transition was obtained when an acoustic pressure of 3 MPa applied (MI: 4.2), while for the smaller NDs (mean diameter of 200 nm) vaporisation was recorded for acoustic pressures higher than 3.87 MPa (MI: 5.5). The boiling point of nanoscale particles is related to the acoustic energy required to vaporise them and the Clausius-Clapeyron Equation shows that the smaller is the droplet, the higher is the phase transition temperature, hence the higher is the acoustic pressure required to vaporise it [43]. This is outside the standard clinical imaging safety guideline of 1.9 MI, but it is not unusual for studies where short pulses are used to activate NDs. These results are, hence, in line with what expected, but having the possibility to achieving phase transition at lower acoustic

pressures would be preferable to avoid any side effects in the human body.

3.3.3 Intracellular Uptake of Nanodroplets

The final aim of this work is ND and MB use *in vivo*; at this stage of the work a preliminary test was performed to assess whether drug carriers are likely to be taken up by cells. The results shown in Paragraph 3.2.3 show that both MB and ND were stained by DiI. Assuming that all DiI is incorporated into the lipids and there is no free DiI left in the solution, there seems to be internalisation of particles and lipids, but further tests are needed to confirm this theory.

In the case of the incubation of MG63 cells with microbubbles, the yellow dots present in Figure 3.39 (page 165) are likely not microbubbles, due to their small size (< 1 μm). Dots are present both on the membrane and in the cytoplasm and their presence could be attributed to two different phenomena: (i) they could be labelled lipid aggregates that have been internalised by the cell or that have stained the membrane of the cell, since the sample was washed, these are not aggregated of DiI alone; on the other hand, (ii) they could be the result of the interaction between the cell membrane and the microbubble shell. Since the lipid membrane of MBs was stained with DiI, transfer of material from the MB shell to the cell membrane could have happened. [166]

The main aim of the project is to deliver drug to cells in a fracture site to enhance its healing, therefore being able to assess an interaction between drug carriers and cells just by incubation and without ultrasound stimulation is a promising result. Moreover, no cytotoxicity was observed during the experiment, showing the biocompatibility of this treatment. It should be noted that a cancer cell line was used, which is notably more resistant than primary cell lines. Before moving to the clinic, studies should be performed to look into the interaction between MBs and NDs on one side and primary cells on the other.

3.3.4 Conclusions

All the experiments done have helped in establishing a protocol to produce nanodroplets with an acceptable size. In addition to this, nanodroplets were proved to be stable with respect to time, their phase transition to microbubbles was assessed

and their interaction with cells showed.

To obtain nanodroplets with the desired size around 200-300 nm and a small size dispersity, it is advisable to add 100 μL/mL of PFP to the lipid solution prior the second sonication. The second sonication parameters are fundamental to achieve the desired characteristics, these are the ones included in the protocol used in this work: pulsed second sonication of 7 seconds and 30% duty cycle, total active duration of 60 seconds, intensity of 72 W. Nanodroplets should be produced in a protein-free medium, like PBS, to avoid the interaction between proteins or amino acids and the shell of nanodroplets. In addition to this, NDs should be diluted only if necessary and just prior to their use *in vitro* and *in vivo* to avoid any changes in the size and size dispersity of the batch. When needed, NDs can be stained with DiI and this does not alter their size.

Nanodroplets produced with this protocol were stable at storage temperature, 4^{o}C, for one week and at body temperature, 37^{o}C, for 110 minutes. In addition to this, it was possible to observe phase transition to MBs upon US stimulation and interaction with cells, staining of the cell membrane and possible internalisation of particles, when fluorescently-labelled NDs and cells were incubated together.

The quantitative relation between different production parameters and the size and size dispersity of nanodroplets represents a novel contribution to the field since, to our best knowledge, no published study has looked into these effects in a quantitative and systematic way.

Chapter 4

Development of an *in vitro* model for the acoustic characterisation of microbubbles and nanodroplets in a bone fracture

It is well known that the response of ultrasound-sensitive agents (such as gas microbubbles and perfluorocarbon nanodroplets) depends on the acoustic stimulation conditions, as well as the physical properties of the surrounding environment [181] [182]. This study aims to investigate ultrasound stimulation of MBs and NDs at the site of a bone fracture, in order to ultimately control the release of biologically active compounds and induce therapeutically favourable mechanostimulatory effects. To achieve this, it is of fundamental importance to understand how MBs and NDs respond to different US stimulation settings, and how their behaviour may change in the presence of fractures with different (clinically-relevant) geometries.

Passive cavitation detection (or PCD) is one of the most common methods used to characterise the acoustic behaviour of ultrasound-responsive agents. A typical PCD system comprises a transducer to stimulate the sample, and another transducer that passively 'listens' to the acoustic emissions generated by the sample, analogous to a speaker and a microphone respectively [106]. Notably, the US-induced oscillation of microbubbles results in the generation of acoustic waves. The cavitation detector

records the change in pressure as the acoustic wave emitted by the oscillating microbubbles passes the transducer. These waves provide information about the frequency content and stability of the microbubble response, and the pressure recorded is proportional to the second temporal derivative of the volume of the microbubble (thus an indicator of its oscillation amplitude). As a consequence, spectral peaks in the pressure emissions are correlated to spectral peaks in the volumetric oscillation [107]. Overall, PCD is a useful technique to determine the threshold between stable cavitation, inertial cavitation, and destruction of microbubbles, as well as the phase transition pressure of nanodroplets (and the cavitation dynamics of microbubbles formed by ND vaporisation). Acoustic stimulation and cavitation detection are normally performed within large water tanks [183] [184], which are difficult to couple with optical microscopes for real-time imaging and are not easily transportable. These two features could be relevant additions to this project as real time imaging performed with a ultra high speed camera could provide more insights into MBs and NDs acoustic behaviour; and having an easily transportable device could allow easiness of use and coupling with different kinds of microscopes and cameras.

There are some studies in the literature showing that the propagation of US waves in fractured bones can be used to assess the state of healing of a bone fracture, by applying the so-called 'axial transmission technique'. This technique is based on the principle that the US propagation properties of bone (i.e. the US propagation velocity) change during tissue healing. This can be associated to changes in the mechanical characteristics of a bone fracture gap with respect to time, as it progresses through the healing process and undergoes remineralisation. Healing is typically associated with a gradual increase in tissue's stiffness, load at failure and Young's modulus and, hence, increase in US propagation velocity [38]. By studying how the speed of US and the signal amplitude change with respect to time, it is possible to determine the stages of fracture's healing. Gheduzzi et al. [185] performed numerical and experimental tests to determine a relationship between the healing stage of a fracture and the ultrasound transmission loss. Moreover, Catelani et al. [186] used 2D numerical simulations to investigate how US propagates within fractures, in the presence and absence of a metal rod inserted in the medullary cavity (a procedure called intramedullary nailing used to treat comminuted and displaced fractures).

When trying to develop a bone fracture model for acoustic studies, it's important to simulate the same acoustic characteristics that bone and soft tissue in the fracture

gap have. In previous studies by Dodd et al. [137], Sawbones material, consisting of E-glass fibre epoxy resin, was used to simulate a cortical bone as they have comparable acoustic impedance. As for soft tissue, Maxwell et al. [131] showed that the acoustic and mechanical properties of agarose gel were comparable to real tissue and that US responsive agents embedded within real tissue or within the gel had comparable acoustic responses when stimulated.

To the best of the author's knowledge, no previous study has designed a model platform to study how the propagation of US in bone is affected by fractures with different geometries, and how this in turn affects the acoustic behaviour of ultrasound-responsive agents present in the fractured area. It is of fundamental importance to address this knowledge gap, as the efficacy of the treatment under development in our research group strongly relies on the ability to achieve a controllable and desired acoustic response from ultrasound-responsive agents. If these agents do not receive appropriate acoustic stimulation, it could lead to the drug not being delivered to the fracture and to the tissue not being mechanically stimulated. The novelty and contribution of this study lies on the development of a compact experimental setup that enables *in vitro* characterisation of the interaction between US-responsive agents, bone fractures, and ultrasound. By using the setup, both in the presence and absence of a fracture model, it was possible to quantify the effect of the presence of a fracture on the acoustic behaviour of microbubbles and nanodroplets. Findings from this study will help defining the characteristics of a novel treatment to improve the bone fracture healing process by using US-responsive drug-loaded agents.

This chapter is divided into two sections. After an introduction to the design and construction of the setup for acoustic characterisation of ultrasound-responsive agents, the first section describes the numerical simulations performed to characterise the upon-mentioned setup and the acoustic field it generates. The second section instead presents the *in vitro* experiments performed to study the acoustic behaviour of MBs and NDs in a bone fracture model.

4.1 Materials and Methods

4.1.1 Design and construction of a setup for the acoustic characterisation of ultrasound-responsive agents in a bone fracture model

To perform acoustic characterisation of microbubbles and nanodroplets in the presence and absence of a bone fracture, a passive cavitation detection method was chosen and an arrangement of apparatus (hereafter referred to as 'setup') was designed in Solidworks (Solidworks Applications Limited, Oldbury, West Midlands, United Kingdom) and 3D-printed using the Prusa i3 MK3 printer (Prusa Research s.r.o., Partyzánská, Praha Czech Republic).

To characterise the cavitation activity of US-responsive agents, a system comprising a passive cavitation detector (PCD) element and a transducer to acoustically stimulate the sample were needed. Other design criteria included: (i) the possibility to integrate the setup with an optical microscope, in order to visualise the sample during acoustic stimulation; (ii) the ability to position bone fracture models of different clinically-relevant sizes at the US target position, to assess whether this could influence the acoustic response of the sample; and (iii) the ability to deliver a uniform acoustic pressure field at the target site, to provide repeatable acoustic stimulation conditions for assessment of different treatment approaches.

Figure 4.1 shows a schematic of the device. A tank (190 x 110 x 60 mm) was designed for integration with an optical microscope; i.e. a circular hole was fabricated on the tank lid, allowing illumination of samples placed at the basal surface of the tank. The sample will sit on a glass slide with a thickness of 1 mm to meet the criteria for optical imaging. A 2 MHz unfocused transducer (Precision Acoustics, Dorchester, UK) or a 1 MHz unfocused transducer (Camasonic, Batley, West Yorkshire, UK) were integrated with the lid, generating the US wave that stimulated the sample. Both transducers had a focal distance of 76 mm. The choice of transducers was made based on the fact that lipid-shelled MBs with a small diameter (few μm) resonate at frequencies in the range 1-10 MHz, which is the same range used in biomedical imaging [60]. MBs with a mean size around 3 μm usually resonate with frequencies in the range 1-2 MHz, hence our choice [187]. Moreover, the lid had a squared hole to accommodate an acoustically absorbing material (polyurethane Aptflex, Precision

Acoustics, Dorchester, Dorset, UK), in order to absorb the incident acoustic wave reflected by the sample or its substrate. One of the side-walls of the tank contained a circular hole to accommodate a passive cavitation detector (V320-SU 7.5 MHz immersion transducer, Olympus Industrial, Southend-on-Sea, Essex, UK), employed to capture the signal generated by MBs or NDs upon stimulation.

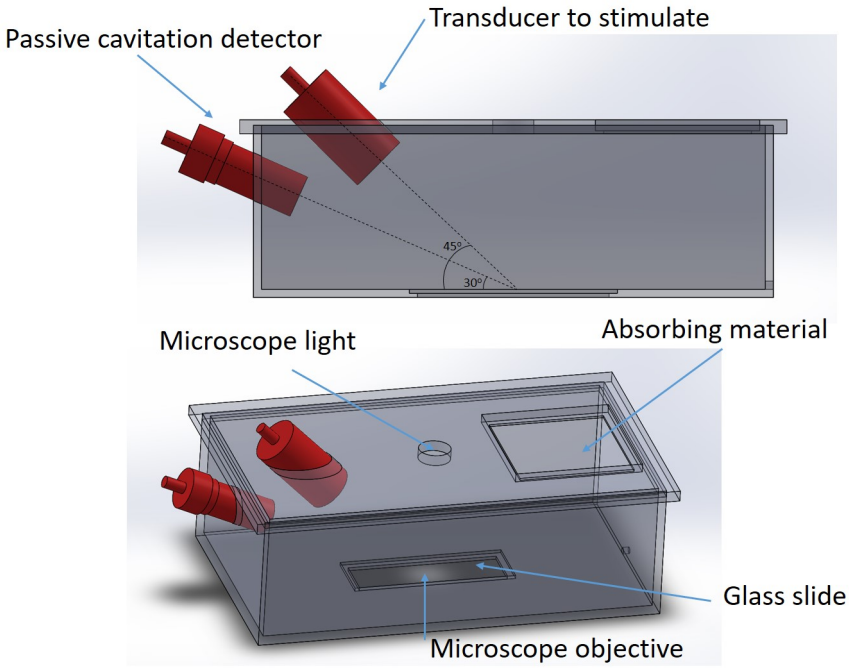

Figure 4.1: *A tank (190 x 110 x 60 mm) was designed in Solidworks and 3D-printed to allow acoustic stimulation of NDs and MBs. The tank accommodates two transducers, one for stimulating the sample (either 1 MHz or 2 MHz unfocused transducers) and one for detecting cavitation activity from the sample. Both transducers are oriented towards a glass slide placed at the bottom of the tank; the transducer emitting US has a 45° inclination angle, while the PCD element has a 30° inclination angle. Both angles are considered with respect to the base of the tank. On the top lid, a squared hole accommodates an acoustic absorbing material and a circular hole allows illumination of the sample for optical imaging using a microscope.*

A slightly modified water tank design was generated to enable the integration of a 1 MHz focused transducer (31 mm outer diameter, 23 mm transducer diameter, 5.58 mm radius of curvature, Precision Acoustics, Dorchester, UK). Using the 1 MHz focused transducer, instead of the unfocused ones, allows achieving greater acoustic pressure at the target site whilst still operating at the resonance frequency of the sample. Such higher acoustic pressure is anticipated to be required to achieve ND phase transition. Figure 4.2 shows the new tank geometry, with overall dimensions of 200 x 120 x 60 mm. The tank is larger than the the previous one, reported in Figure 4.1, as it accommodates the slightly bigger focused transducer. Transducer and PCD are not placed on the same side of the tank to avoid their physical interaction and to avoid the potential blocking of some of the signal generated by the sample before it reached the PCD.

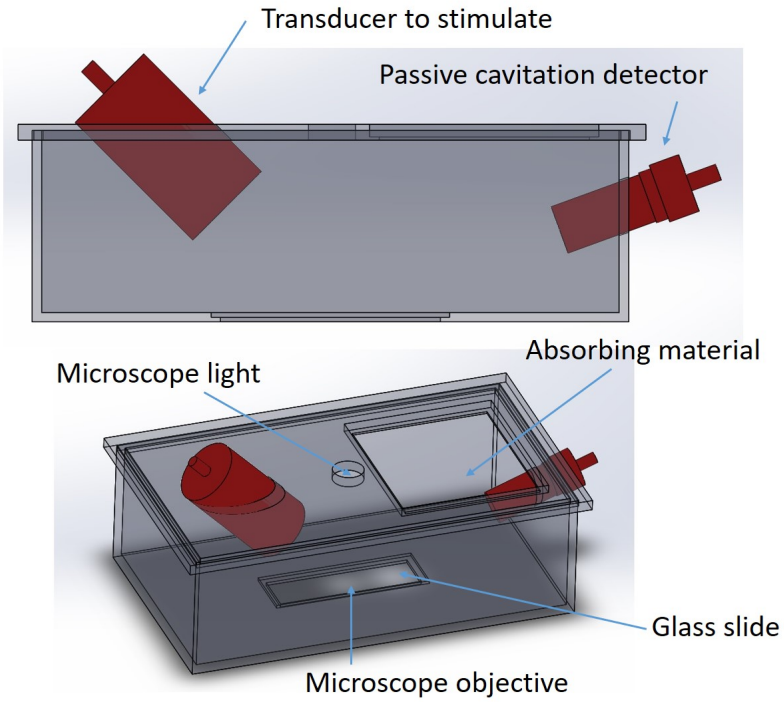

Figure 4.2: *A tank (200 x 120 x 60 mm) was designed in Solidworks and 3D-printed to allow acoustic stimulation of NDs and MBs. The tank accommodates two transducers, a 1 MHz focused transducer stimulating the sample and a transducer detecting cavitation activity from the sample. Both transducers are oriented towards a glass coverslip placed at the bottom of the tank; the transducer emitting US has a 45^{o} inclination angle, while the PCD has a 30^{o} inclination angle. On the top lid, a squared hole accommodates an acoustic absorbing material and a circular hole allows illumination of the sample for visualisation through optical microscopy.*

4.1.2 Numerical simulations

4.1.2.1 Computational characterisation of the acoustic field developed in the experimental setup

Before performing *in vitro* tests with microbubbles and nanodroplets, it is important to determine the properties of the acoustic field within the tank, and particularly at the target point, corresponding to the place where the glass slide is placed (i.e. at the bottom of the tank), which is where the sample of particles will be placed during experiments. For this purpose, numerical simulations were performed using COMSOL Multiphysics (COMSOL Inc., Burlington, MA, USA). Figure 4.3 shows the geometry of the tank that was modelled in COMSOL. This is a 2D model representing the frontal plane of the tank. By determining the acoustic pressure distribution over this plane, it is possible to investigate how the US wave emitted by the transducer is reflected by the tank. As previously discussed, an absorbing material is placed on the lid of the tank, to absorb most of the incident acoustic wave that is reflected by the glass slide. A large proportion of the incident wave will be reflected at a 45^{o} inclination angle (with respect to the substrate), but reflection in other directions may also occur. Therefore, a first series of simulations was performed by placing absorbing material at different locations within the tank.

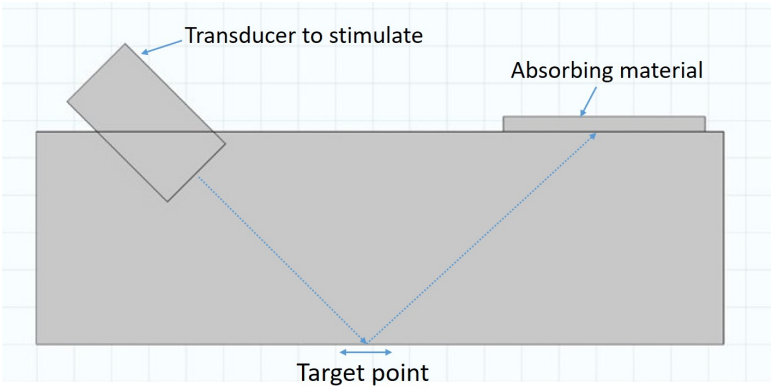

Figure 4.3: *The geometry of the tank previously designed in Solidworks was subsequently modelled in COMSOL. This is a 2D section of the frontal plane, namely the one where it is possible to study the US wave being emitted by the transducer and reflected by the surfaces of the tank. The transducer has a 45^{o} inclination and it is positioned in such a way to allow the US wave to be focused at the centre of the glass slide, where the sample of MBs or NDs is placed.*

Figure 4.4 shows a schematic of the three different simulations that were run, in

which the absorbing material was placed either: (i) on the lid only, (ii) on the lid and on the lateral walls, (iii) on the lid, the lateral walls, and the bottom surface of the tank (i.e. next to the glass slide).

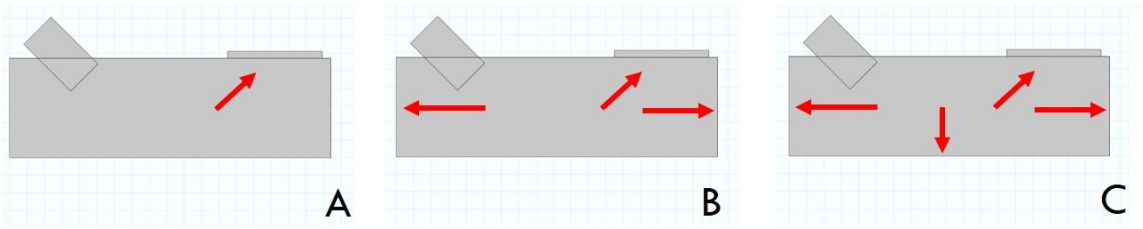

Figure 4.4: *The figure shows the three different configurations tested. The absorbing material was placed A) on the lid; B) on the lid and the lateral walls; or C) on the lid, the lateral walls, and the bottom surface of the tank, i.e. in the region next to the glass slide. The red arrows indicate the position of the absorbing layers.*

Numerical simulations were performed in COMSOL using the 'Pressure Acoustics, Frequency Domain' module and performing a 'Frequency Domain' study. A 'Sound Hard Boundary' condition was set on the blue lines shown in Figure 4.5.A, corresponding to the inner boundaries of the tank. An initial acoustic pressure value relative to atmospheric pressure of 0 Pa was set within the volume of the tank in the liquid phase (Figure 4.5.B); a normal acceleration of 1 m/s^2 was set on the surface of the transducer submerged in the fluid (Figure 4.5.C) and a 'Plane Wave Radiation' boundary condition was set on the absorbing material boundary (Figure 4.5.D) to simulate total absorption of the incident acoustic waves. Finally, a triangular shaped mesh was defined, with a maximum element size of 1.4 x $10^{-3/6}$ m.

Simulations were run to study the absolute acoustic pressure field developed at the target site; and pressure values along the bottom line were plotted. Subsequently, the absolute acoustic pressure was quantified both over an area at the target site and over an area out of the region of interest, for all of the three different configurations of absorbing material tested. A one-way ANOVA statistical test was applied to detect any statistical difference between the different configurations of absorbing material. The same steps reported above were applied to the version of the tank designed to accommodate the 1 MHz focused transducer.

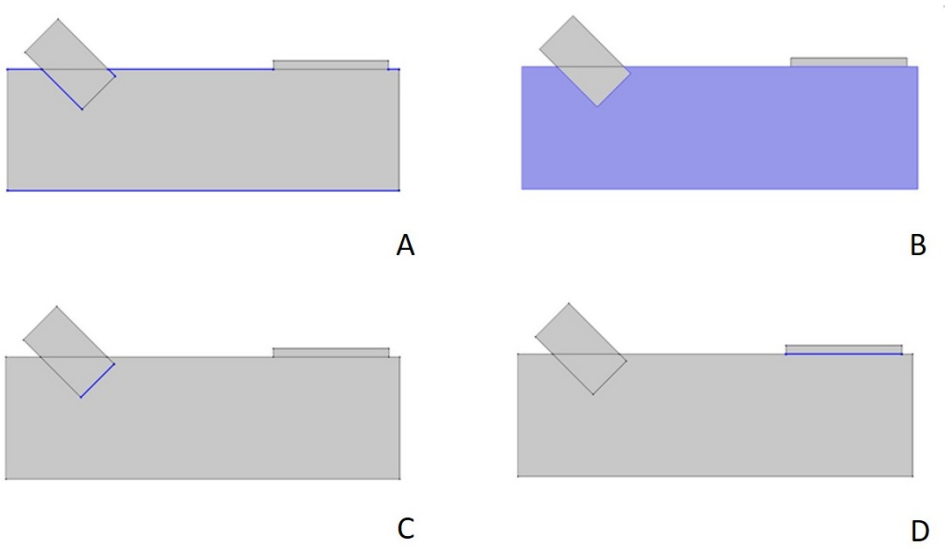

Figure 4.5: *The figure shows how the simulation was implemented in COMSOL. A) A 'Sound Hard Boundary' condition was set at the lines labelled in blue; B) an initial acoustic pressure value equal to 0 Pa was defined within the area of the tank; C) a normal acceleration of 1 m/s^2 was set an the surface of the transducer, and D) a 'Plane Wave Radiation' boundary condition was set on the absorbing material.*

4.1.2.2 Computational characterisation of the acoustic field developed in the experimental setup in the presence of a bone fracture model

While ultrasound propagates effectively through soft tissue, with minimal reflections occurring, the presence of hard tissue (such as bone) can affect the properties of the travelling wave [38]. Indeed, bone has a different impedance with respect to surrounding soft tissues, and this leads to the acoustic wave being reflected and refracted at the interface between soft tissue and bone. If the acoustic field to which microbubbles and nanodroplets are subject changes, then their acoustic response changes too. For these reasons, numerical simulations were performed to study how the acoustic field changes when it interacts with a simplified bone model. Specifically, a bone fracture model was designed for integration within the stimulation tank described earlier. The two bone fragments in the model have a length of 4 cm each and a thickness that can be varied between 2 and 4 mm. The thickness values were chosen to be similar to the size of mice femurs, which will be used in a complementary phase of this project, while the length was chosen for ease of use and it has been assumed that the selected length does not impact the final results (i.e. the acoustic pressure within the fracture gap). The impedance of bone (5.41 x 10^6 kg/m^{2}s) was defined as a material property at

the edges of the bone. The geometry designed in COMSOL is shown in Figure 4.6.A, where the red arrows indicate the presence of an absorbing material, as discussed in Paragraph 4.1.2.1.

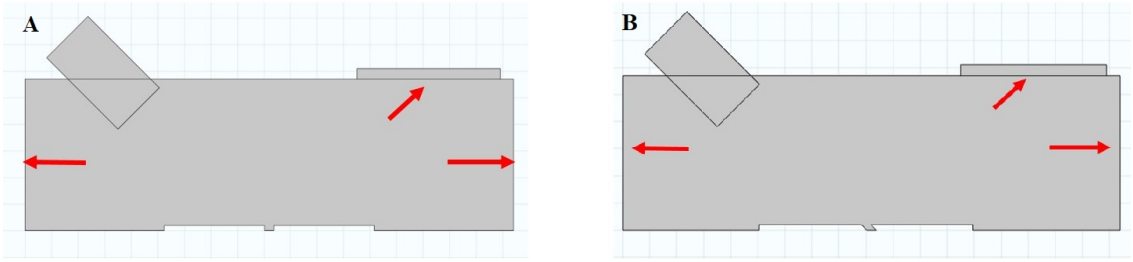

Figure 4.6: *The geometry of the tank was modified to accommodate the presence of the bone model. The gap at the bottom of the tank represents the bone fracture and the red arrows indicate the position of an acoustic absorbing material. The bone is simulated by defining its acoustic impedance in the material properties. A) The fracture gap has a 45^{o} inclination angle with respect to the acoustic wave coming from the transducer. B) The fracture gap is aligned to the acoustic wave coming from the transducer.*

Using this model, it was possible to study how different physical properties of the fracture affect the acoustic field. Particular attention was devoted to the following parameters: fracture's gap size, bone thickness, and gap inclination with respect to the incident wave. Three different gap sizes were tested: 3.5, 4.5 and 5.5 mm. As for the thickness, both 2 mm and 4 mm thick models were investigated. These values were chosen to be comparable to other studies in the literature [137] [188]. These design parameters would reflect cases in which the fracture is only partial (i.e. not total), since the US wave will be reflected by the glass substrate placed at the bottom of the tank. In order to also model conditions relevant to a total fracture, a 'Plane Wave Radiation' boundary condition was set at the bottom surface of the tank between the two bone segments. In this modelling scenario, it was assumed that the incident wave would travel through the fracture gap and subsequently be attenuated by soft tissues. Finally, two different inclinations of the fracture were tested with respect to the incident US wave: 0^{o} (i.e. the fracture gap was aligned with respect to the incident US wave), and 45^{o} (i.e. the fracture gap was inclined with respect to the incident US wave). Figure 4.6.B shows a schematic of the geometry with a 0^{o} inclination angle.

Simulations were run to evaluate the absolute acoustic pressure field developed at the target point, and its values along the bottom line of the tank were plotted. Subsequently, the absolute acoustic pressure was quantified in the fracture gap for all

of the different fracture gap geometries tested. A one-way ANOVA test was applied to detect any statistical difference in the absolute acoustic pressure values between fracture gap sizes. The same steps were applied to the version of the tank designed to accommodate the 1 MHz focused transducer.

4.1.3 *In vitro* tests

4.1.3.1 Acoustic calibration of the experimental setup

Before performing further experimental investigations, a calibration test was carried out to characterise the acoustic field generated by the transducers used, both in the absence and presence of the experimental tank setup[1].

The setup used to calibrate the US field is shown in Figure 4.7; a plastic tank was filled with degassed water and either the transducer alone, or the transducer coupled with the microscope-compatible tank previously designed, were fully submerged in water. All the transducers used for the acoustic characterisation of ultrasound-responsive agents were calibrated, namely the 1 MHz unfocused, the 2 MHz unfocused and the 1 MHz focused transducers. A needle hydrophone (ONDA HNC-0200, Sunnyvale, California, USA) was fully submerged in the tank and aligned to the transducer. A signal generator (Agilent 33220A, Santa Clara, California, USA) was connected to an amplifier (Electronics & Innovation 1140LA, Rochester, New York, USA), which was then connected to an oscilloscope (LeCroy 64Xi-A, Chestnut Ridge, New York, USA). The oscilloscope was then connected to both the transducer and the hydrophone.

The transducer was driven at its working frequency (either 1 MHz or 2 MHz) and the following experiments were performed, as shown in Figure 4.8:

- Measurement of the spatial distribution of the acoustic pressure generated by the transducer alone driven at a voltage of 28 Vpp, on the XZ plane at a distance of 8 cm from the transducer. The distance was chosen to be equal to the distance between the transducer and the sample within the microscope-compatible tank. The area studied was 2x2 cm; this area was chosen to assess the acoustic field and its variation at the target plane, and determine whether the setup could provide an acoustic pressure which was high enough to stimulate MBs and NDs

[1]The calibration test was performed at the Institute of Biomedical Engineering of the University of Oxford, under the supervision of Luke Alex Richards.

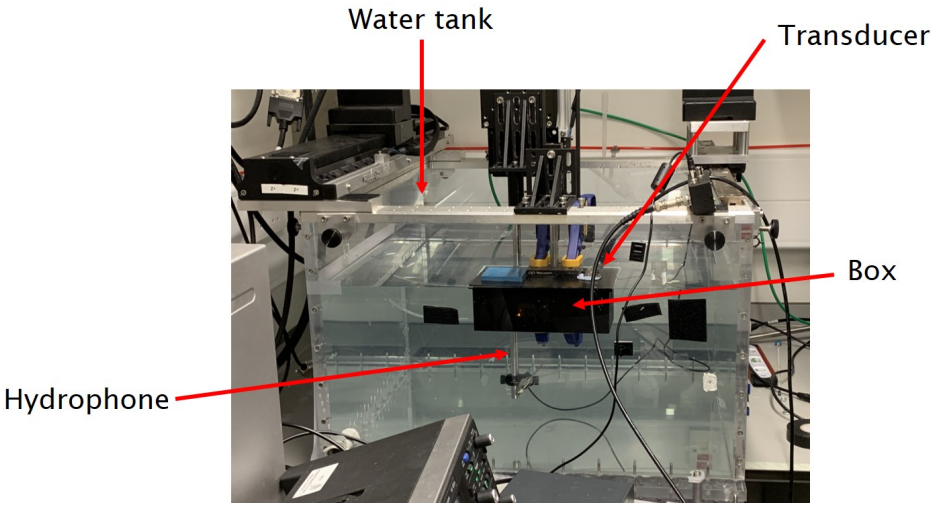

Figure 4.7: *Setup used to calibrate the transducers and characterise the acoustic field in the experimental tank setup. A water tank was filled with water, the transducer alone - or the transducer coupled with the tank setup - was partially submerged in water and a hydrophone was aligned to the transducer to measure the acoustic pressure.*

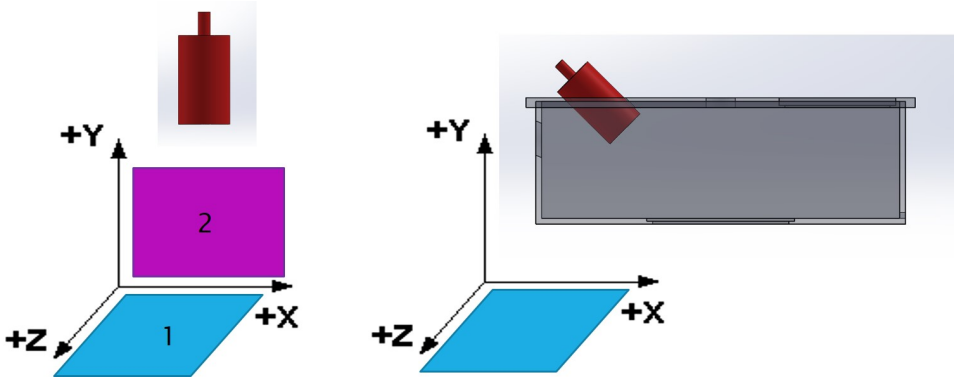

Figure 4.8: *The figure shows the different calibration steps performed to determine the acoustic field at regions of interest. The acoustic field was measured at a distance of 8 cm from the transducer on the XZ and XY planes. The transducer coupled with the microscope-compatible tank was also tested, by measuring the acoustic field on the XZ plane, at a distance of 8 cm from the transducer. When the transducer was coupled with the tank, the glass slide was removed to allow the hydrophone to record the acoustic field.*

and achieve cavitation for the former and vaporisation for the latter. The aim of this test was to study the acoustic pressure at which the sample would be subject to during *in vitro* experiments.

- The measurements reported above were performed on the XY plane, with the transducer driven at 28 Vpp. The area studied in this case was 2x4 cm. The aim of this test was to determine the spatial variation of acoustic pressure in the Y directions, hence the bigger area studied with respect to the previous case. Determining the level of pressure variation allows to assess the importance of transducer's position in the tank; if the acoustic pressure is constant over several mm in the Y direction, it is anticipated that minor accidental displacements of the transducer would not significantly alter the stimulation conditions.

- Measurement of the acoustic pressure at increasing driving voltages (from 15 Vpp to 200 Vpp) at 8 cm from the transducer, taken in a central position on the target plane (XZ plane). The aim of this test was to determine the relationship between driving voltage applied to the transducer and acoustic pressure developed at the target site; this information is necessary to determine the acoustic stimulation conditions to which particles are subject and evaluate their response to stimulation.

- Measurement of the spatial distribution of the acoustic pressure generated by the transducer coupled with the microscope-compatible tank, on the target plane (XZ plane) at a distance of 8 cm from the transducer. Similarly to the first case, the area studied was 2x2 cm. When the transducer was coupled with the tank, the glass slide was removed to allow the hydrophone to record the acoustic field. The aim of this test was to assess whether the addition of the tank altered the acoustic field developed at the target site.

4.1.3.2 Experimental validation of the setup

After having characterised the acoustic field in the microscope-compatible tank, subsequent tests were carried out to experimentally validate the functioning of the tank *in vitro*, in particular it was fundamental to evaluate whether the acoustic field developed in the tank could be recorded by the PCD, and whether the presence of microbubbles could be detected in the recorded signal and their acoustic response

quantified. Figure 4.9 shows the setup used to perform the experiment. A signal generator (TG2000 20 MHz DDS function generator, Aim and Thurlby Thandar Instruments, Huntingdon, UK) generated a sinusoidal signal that was then amplified by a power amplifier (E&I-1040L-01, Rochester, New York, USA). The signal was monitored through an oscilloscope (DSO1102B 100 MHz, Keysight Technologies, Wokingham, UK). The oscilloscope was connected to a 1 MHz transducer (Camasonics, Batley, West Yorkshire, UK) used to stimulate the sample. The tank was filled with water so that both surfaces of the stimulation transducer and the PCD were submerged. The passive cavitator detector (V320-SU 7.5 MHz immersion transducer, Olympus Industrial, Southend-on-Sea, Essex, UK) inserted through the lateral wall of the tank, acted as a passive listener. The signal recorded from the PCD was conveyed to a pre-amplifier (SR445A, Stanford Research Systems, Sunnyvale, California, USA) and then to an oscilloscope (DSO1102B 100 MHz, Keysight Technologies, Wokingham, UK), through which it could be saved for post-processing.

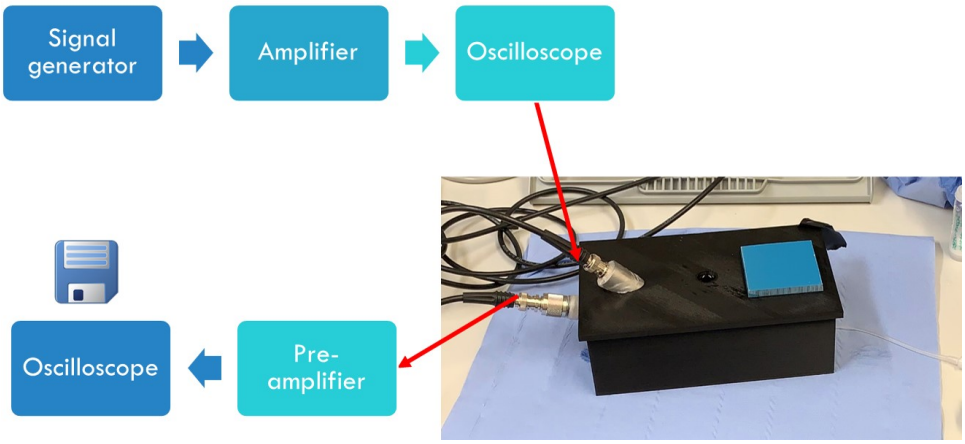

Figure 4.9: *Setup designed to assess the efficacy of the absorbing material placed in the tank. A signal generator generates a sinusoidal wave, which is amplified by a power amplifier. The signal can be visualised through an oscilloscope, and is then delivered to a transducer that stimulates the target site within the tank. Another transducer acts as a passive cavitation detector; it records the signal emitted by the sample and sends it to a pre-amplifier, and finally to another oscilloscope used to save the recorded signal.*

In a first set of experiments, four peak-to-peak input voltages were tested: 50, 100, 150 and 200 mV resulting in peak-to-peak output voltages of 28, 56, 84 and 112 V. For every voltage, two different cases were tested (in the absence of ultrasound-responsive agents):

- Without absorbing material.
- With absorbing material on the lid and on the lateral walls of the tank.

The aim of the test was to determine the content in frequency of the recorded signal, to study the effect of the addition of an absorbing material on the acoustic field developed in the tank and assess whether this effect was consistent with the computational simulations, which showed greater field uniformity upon inclusion of absorbing layers. In order to achieve these objectives, a fast Fourier transform (FFT) was performed on the recorded signal using a script implemented in Matlab (Matlab, Natick, Massachusetts, USA), reported in Appendix B.1.

A second set of experiments was then performed to assess whether the presence of MBs could be detected by the embedded PCD. Microbubbles were added to the tank within a PDMS chamber placed at the bottom of the tank, which would keep the MB suspension in a fixed position. PDMS was chosen as it can be considered an acoustically transparent material, sharing similar speed of sound and acoustic impedance to water [189]; hence, it does not macroscopically alter the acoustic wave stimulating the sample and the acoustic response from the sample itself. The chamber was manufactured in PDMS using a replica moulding technique; briefly, a positive master mould was designed in Solidworks and 3D printed using an Ultimaker 2^+ printer. The mould, shown in Figure 4.10, is composed of a rectangular chamber that accommodates the PDMS during the curing phase, and contains a cylindrical structure with radius of 1 cm and height of 2 mm, which will give origin to the PDMS chamber where MBs are placed.

To produce the PDMS device, the PDMS monomer was mixed with a curing agent (1:10 by weight, Sylgard 184, Dowsil, Dow Way Midland, MI, USA). Any air bubble was then removed by placing the preparation in a vacuum chamber connected to a vacuum pump. The degassed mixture was poured onto the mould and left to cure for 24 hours at room temperature to form a solid PDMS layer. Microbubbles were produced as described in Paragraph 2.1.1, mixed in a 2% agarose gel (1:2 by volume, Sigma-Aldrich, Saint Louis, Missouri, USA) and were subsequently placed in the chamber. Agarose hydrogel (AG) was obtained by thermal crosslinking of an agarose solution and was prepared by dissolving agarose (2% wt) in water by microwaving, with manual mixing every ten seconds. The melting point of 2% agarose gel is around 48^{o}C [136]. During cooling, and before liquid-gel transition, MBs were mixed with

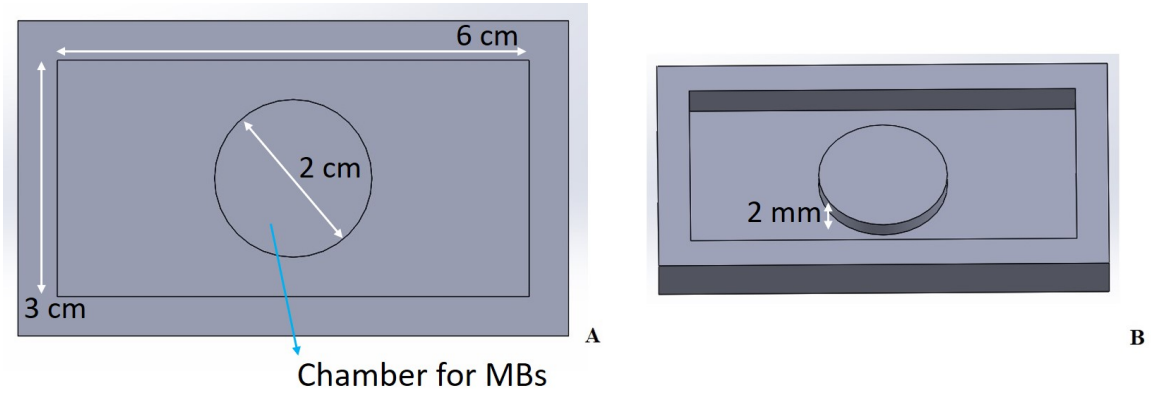

Figure 4.10: *Manifold designed in Solidworks and 3D printed in PLA to create a PDMS chamber keeping the MB suspension in place during the experiment. A) Top view. B) 3D projection.*

the liquid. The liquid solution containing MBs and agarose was placed in the PDMS chamber and the device was then placed at -4°C to ensure quick gelification. After gelification and before usage, MBs embedded in the agarose gel underwent microscope inspection.

Microbubbles were stimulated with a pulsed ultrasound wave. To record the acoustic response from the microbubble suspension, the USB Handyscope HS3 (TiePie, Sneek, The Netherlands) and its built-in software Multi Channel (TiePie, Sneek, The Netherlands) were used. The Handyscope was set to work with two channels (to allow MBs stimulation and cavitation detection at the same time) and with a recording frequency of 1 ms/div. The Handyscope was used to produce a square wave (PRF: 1 Hz, amplitude: 1 V, duty cycle: 1-5%) that triggered another signal generator (TG2000 20 MHz DDS function generator, Aim and Thurlby Thandar Instruments, Huntingdon, UK) producing a sinusoidal signal (Vpp = 25-575 mV, f = 1 MHz). The resulting pulsed sinusoidal wave was then amplified by a power amplifier (E&I-1040L-01, Rochester, New York, USA), resulting in output Vpp of 8-218 V. The signal recorded from the PCD was conveyed to a pre-amplifier (SR445A, Stanford Research Systems, Sunnyvale, California, USA) and then to the Handyscope, through which it could be saved. A schematic of the electrical setup is shown in Figure 4.11. An FFT was then performed on the recorded signal to determine its content in frequency. The same experiment was repeated without MBs, as a control test.

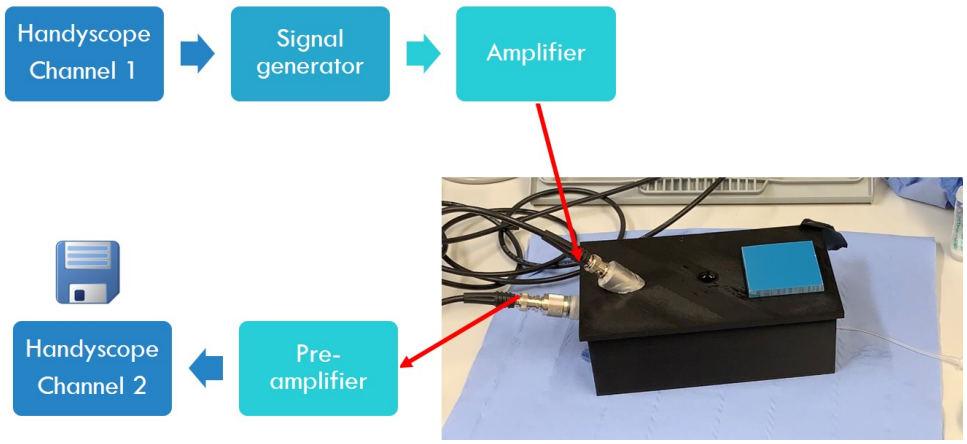

Figure 4.11: *Setup designed to stimulate MBs and NDs with ultrasound, and characterise their acoustic response. An handyscope generates a squared wave that triggers a signal generator to produce a pulsed sinusoidal wave, which is then amplified by a power amplifier. The signal is subsequently delivered to a transducer that stimulates a sample placed on a glass coverslip at the bottom of the tank. Another transducer acts as a passive cavitation detector; it records the signal and directs it to a pre-amplifier, and finally back to the handyscope where it is stored for post-processing.*

4.1.3.3 Characterisation of the acoustic response of MBs in a bone fracture model

After having evaluated the effect of adding absorbing material to the tank and the setup ability to detect MBs response, further tests were carried out to investigate the acoustic behaviour of microbubbles under a range of different experimental conditions. A new PDMS manifold was created to simulate a bone fracture model and evaluate its effect on the acoustic behaviour of MBs. Figure 4.12 shows how the bone fracture model was manufactured.

Firstly, a PLA 3D printed mould was created (Figure 4.12.A); it displayed a central chamber to accommodate MBs (corresponding to the fracture gap) and two lateral channels to keep the bone in place. The mould was used to manufacture a PDMS manifold; PDMS was produced as previously described in Paragraph 4.1.3.2 (Figure 4.12.B). To simulate the presence of a bone fracture, a material with a similar acoustic impedance as the one of real bone was chosen (Z = 5.41 x 10^6 kg/m^2s, Sawbones, Washington, USA; vs a bone acoustic impedance of 5.32 x 10^6 kg/m^2s [190]). Sections of the material were cut and inserted in the lateral channels of the manifold (Figures 4.12.C and 4.12.D). Finally, MBs were embedded in a 2% agarose gel and placed in

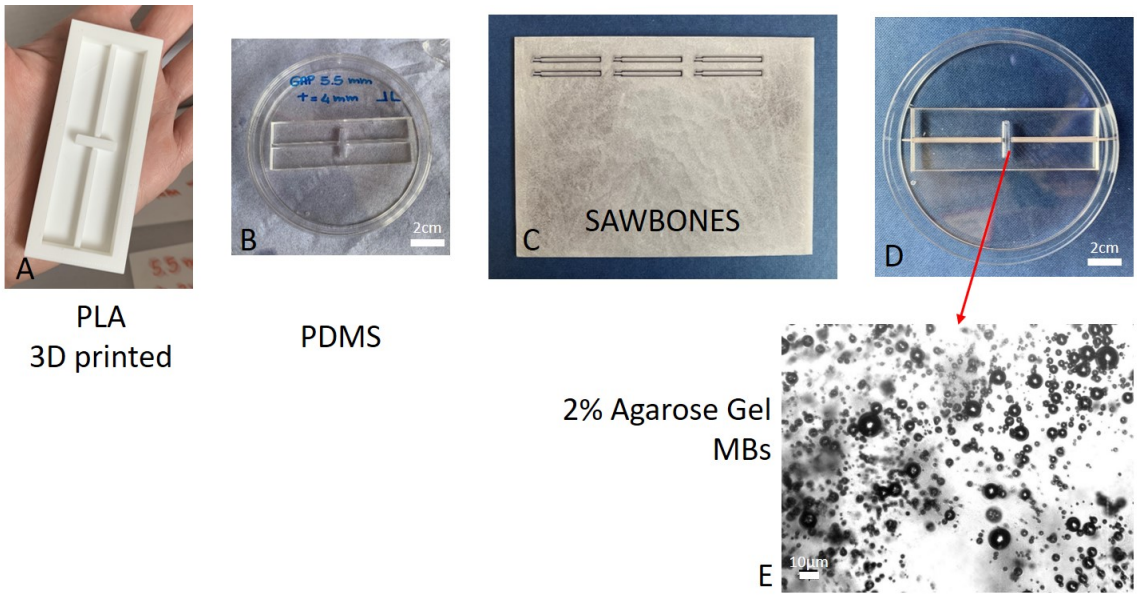

Figure 4.12: *Setup designed to stimulate MBs and NDs with ultrasound and characterise their acoustic response in a model fracture. A) PLA 3D printed mould. B) PDMS manifold with a central chamber (i.e. the fracture gap model) to accommodate MBs and two lateral channels for insertion of bone segments. C) Sawbones material, simulating the acoustic impedance of bone. D) Bone fracture model assembled. E) Bright field microscope picture (magnification lens 10x) of MBs embedded in a 2% agarose gel and placed in the central chamber of the fracture model.*

the central chamber. Figure 4.12.E shows a microscope image of DPSC-PEG40s MBs embedded in the gel.

The PDMS manifold, accommodating two Sawbones segments and MBs in a 2% agarose gel, was placed at the target position within the tank. A total of six different geometries of bone fracture were produced, with the thickness of the fracture varying between 2 and 4 mm and a fracture gap of 3.5, 4.5 and 5.5 mm. These values were in line with the geometries previously simulated numerically, as reported in Paragraph 4.1.2.2.

For each model's geometry, four different cases were tested and compared:

- Absence of Sawbones, and fracture gap filled with 2% agarose gel,
- Absence of Sawbones, and fracture gap filled with 2% agarose gel containing MBs,
- Presence of Sawbones, and fracture gap filled with 2% agarose gel,
- Presence of Sawbones, and fracture gap filled with 2% agarose gel containing MBs.

For every case tested, three different independent repeats were performed (N=3). To stimulate MBs and record their acoustic response, the electronic setup described in Paragraph 4.1.3.2 was used. Experiments were carried out using two different US transducers (1 MHz and 2 MHz unfocused), to investigate different acoustic stimulation conditions.The choice of transducers was made based on the fact that lipid-shelled MBs with a small diameter (few μm) resonate at frequencies in the range 1-10 MHz, which is the same range used in biomedical imaging [60]. MBs with a mean size around 3 μm usually resonate with frequencies in the range 1-2 MHz, hence our choice [187]. The samples were stimulated for 30 seconds, with a pulse repetition frequency (PRF) of 1 Hz and duty cycle of 1-5%, and this values were chosen to be in line with other studies in the literature [191] [192]. The signal recorded by the passive cavitation detector was processed with a FFT algorithm to determine its frequency content over the stimulating time. The Welch method (pwelch) was applied on the recorded signal to determine the power spectral density of the signal, which describes the power present in the signal as a function of frequency. Harmonic (integer multiples of the stimulating frequency f0) and ultraharmonic (1.5 x f0) power values were extracted,

and integrated over the stimulating period (i.e. 30 seconds) to determine their energy. A script, reported in Appendix B.2, was implemented in Matlab to perform these steps. One way ANOVA and Tuckey post-hoc tests were applied to the results, to assess whether differences between experimental groups were statistically significant.

1 MHz unfocused transducer

When the 1 MHz unfocused transducer was employed, the voltage set on the signal generator was in the range 25-575 mVpp, where the maximum voltage was set based on the transducer's specifications. This allowed achieving an output driving voltage between 8 and 218 Vpp, corresponding to a peak-negative acoustic pressure at the target point between 0.06 and 0.33 MPa (MI: 0.06 - 0.7).

2 MHz unfocused transducer

When the 2 MHz unfocused transducer was used, the voltage set on the signal generator was in the range 50-600 mVpp, where the maximum voltage was again set based on the transducer's specifications. This corresponded to an output voltage to the transducer between 11 and 150 Vpp, and a peak-negative acoustic pressure at the target point between 0.03 and 0.7 MPa (MI: 0.02 - 0.49).

4.1.3.4 Characterisation of the acoustic response of NDs in a bone fracture model

The protocol used in Paragraph 4.1.3.3 to characterise the acoustic behaviour of microbubbles was employed to also characterise the behaviour of perfluorocarbon nanodroplets. The aim of this series of tests was to achieve phase transition from NDs to MBs in the fracture gap. Six gap geometries were tested (fracture gap width: 3.5, 4.5 or 5.5 mm; fracture thickness: 2 or 4 mm), and three different cases were tested for each one of them:

- Fracture gap filled with 2% low melting point (LMP) agarose gel,
- Fracture gap filled with 2% low melting point (LMP) agarose gel containing PFP NDs,
- Fracture gap filled with 2% low melting point (LMP) agarose gel containing PFB NDs.

For every case tested, five different independent repeats were performed (N=5). PFP NDs were produced following the protocol previously presented in Paragraph 3.1.1, while PFB NDs were received from Dr. Qiang Wu at the University of Oxford. Since the phase transition temperature of PFB is lower than that of PFP, it was anticipated that vaporisation of PFB NDs would occur at lower acoustic pressures. Similarly to MBs, three different stimulation conditions were investigated, corresponding to unfocused (1 and 2 MHz) and focused (1 MHz) ultrasound. The driving voltages applied to the unfocused transducers and the resulting acoustic pressures obtained at the target point are the same previously described for experiments involving MBs, as presented in Paragraph 4.1.3.3. Concerning the focused transducer, the voltage set on the signal generator was in the range 10-200 mVpp, leading to an output voltage to the transducer between 3-58 Vpp, corresponding to an acoustic pressure at the target site between 0.03 and 0.95 MPa (MI: 0.03 0.95). The ND suspension was embedded into low melting point agarose gel (rather than conventional agarose), to allow NDs incorporation at room temperature and avoid potential phase transition that may occur during gelification at higher temperatures. The signal recorded by the PCD was processed with an FFT algorithm in MATLAB, the script of which is reported in Appendix B.2. The Welch method was applied to determine the power density of the signal with respect to time. Harmonic and ultraharmonic power density values and the broadband level were extracted, and their values were integrated with respect to time to determine their energy. In the harmonic and ultraharmonic calculations, $\pm$ 2 frequency bins around each harmonic were included to capture the shoulders of these peaks and prevent them from being identified as broadband. All frequencies below 2.1 MHz were excluded, since they are highly affected by the noise generated by the stimulating sound wave and could bias the final energy measurements. One way ANOVA and Tukey post hoc tests were applied to the results, to investigate the presence of any statistical difference between the cases without NDs, with PFP NDs and with PFB NDs.

4.1.3.5 Ultra-high speed imaging of ND vaporisation in a tissue mimicking phantom

The acoustic response of PFP NDs was visualised through ND vaporisation in a tissue mimicking bone fracture phantom. All tests were conducted in an optically

transparent acrylic water tank, filled with degassed water at room temperature.[2]

The bone fracture phantom was manufactured following the protocol presented in Paragraph 4.1.3.2. PFP NDs were mixed in a 2% (w/v) agarose gel and the mixture was put in the bone fracture gap. The phantom was then put in the freezer to solidify for two minutes. PFP NDs were produced following the protocol presented in Paragraph 3.1.1.

A spherically-focused single-element FUS transducer with a centre frequency of 0.5 MHz was used (H107, Sonic Concepts, USA) to excite the PFP NDs, while a high speed camera (Hyper Vision HPV-X2, Shimadzu, Kyoto, Japan) was used to visualise (and record) the process of NDs vaporisation in the bone fracture phantom. The aperture and the geometric focus of the transducer were 64 mm and 60 mm, respectively. FUS were aligned with the fracture gap by performing pulse-echo measurements, and the camera field of view was positioned in the middle of the bone fracture gap itself. The acoustic pressure generated was previously calibrated in water using a 0.4 mm diameter needle hydrophone (ONDA 1056, Onda Corporation, USA). The excitation signal was provided by an arbitrary waveform generator (33220A, Agilent, USA), which was amplified by a 300W RF power amplifier (A-300, ENI, USA) and sent to the FUS via a 50 ω matching network.

An high speed camera was used to provide real-time imaging to detect and visualise ND vaporisation in the bone fracture phantom at 1 million frame rate per second.

In these tests, 2000-cycle FUS excitation pulses with 5% duty cycle were applied. The acoustic pressure was equal to 1.8 MPa peak negative at the fracture gap.

The recorded image sequences were post-processed in ImageJ (National Institute of Health, USA) to detect the occurrence of phase transition. The first image frame of every video was subtracted from all other frames to remove background noise. A threshold was subsequently applied to make the area occupied by microbubbles stand out with respect to the background, and a measure of the percentage of total area occupied by MBs was obtained for every pictures. These values were then plotted with respect to time to evaluate the phase transition phenomenon during US stimulation.

[2]The experiment was performed at the Institute of Biomedical Engineering of the University of Oxford, under the supervision of Dr Qiang Wu.

4.2 Results

4.2.1 Numerical simulations

4.2.1.1 Computational characterisation of the acoustic field developed in the experimental setup

The simulations described in Paragraph 4.1.2.1 were carried out to determine the influence of absorbing material on the acoustic pressure field developed in the experimental tank and minimise reflections of the incident wave by optimising the positioning of absorbing material. Both focused and unfocused transducers were simulated to assess the properties of the ultrasound field they developed in the tank. Transducers had a 45^{o} inclination angle with respect to the baseline of the tank; once the US incident wave was emitted, it travelled towards the baseline of the tank, where it got reflected. Waves were mainly reflected in an orthogonal way towards the upper side of the tank, where an absorbing material absorbed them; a small proportion of waves was expected to be reflected by the lateral walls of the tank in other directions as well. The tank was designed to be used in conjunction with a passive cavitation detector (PCD), to record the acoustic response of acoustically sensitive samples added into the tank, hence the importance of avoiding reflected components of the incident wave (i.e. not directly associated with the sample's response) being directed towards the PCD.

Unfocused ultrasound field

Figure 4.13 shows the absolute acoustic pressure fields developed in the fluid when unfocused transducers were used and corresponding to three different configurations (i.e. positioning) of the absorbing layers.

The addition of absorbing material on the lateral walls of the device (Figure 4.13.B) and the basal surface of the tank (Figure 4.13.C) reduced the intensity of reflected waves, which are visible in Figure 4.13.A as a higher absolute acoustic pressure in regions not within the main path of the US wave. Figure 4.14 shows how the absolute acoustic pressure varied along the bottom line of the tank and the red frame highlights the central region, where MBs and NDs will be placed. Line plots correspond respectively to the cases with absorbing material (i) on the top of the tank, (ii) on the top and on the lateral walls, and (iii) on the top, lateral walls and baseline

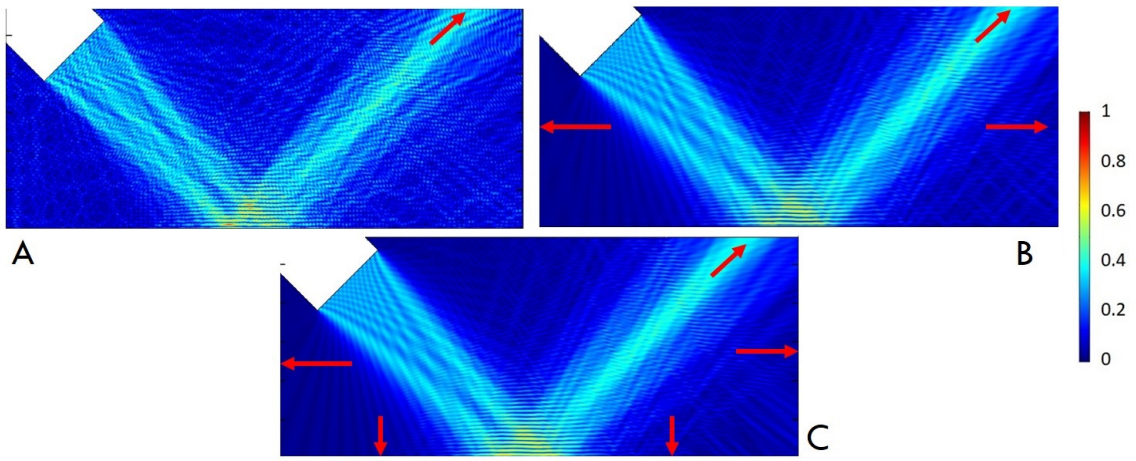

Figure 4.13: *Absolute acoustic pressure in the fluid within the tank. Values have been normalised to the maximum value. The red arrows indicate the position of the absorbing material: A) on the lid; B) on the lid and on the lateral walls; or C) on the lid, the lateral walls, and the basal surface of the tank next to the glass slide.*

of the tank. The graph shows that, in all cases, the maximum absolute pressure was in the central region of the tank, which was where the incident wave was directed to. The acoustic pressure here was approximately 5 times greater than in the lateral regions. By adding absorbing material in the tank, the acoustic pressure became more homogeneous (lower variations in intensity were detected) in the tank, while it did not significantly affect the field intensity at the target point.

The absolute acoustic pressure at the target area (defined as a rectangle with size 20 x 10 mm in the centre of the tank) was comparable in the three cases analysed, and did not present any statistical difference ($p > 0.05$), as shown in Figure 4.15. All values were normalised to the maximum value of absolute acoustic pressure obtained in the region of interest. However, the absolute acoustic pressure developed at the bottom of the tank (outside the target point) was influenced by the presence of absorbing material. The pressure was quantified in a rectangle with size 20 x 10 mm positioned in the first quarter of the baseline, on the left hand side, and normalised with respect to the maximum value; the boxplots in Figure 4.16 show that adding absorbing material led to a decrease both in the mean value and the standard deviation of the normalised absolute acoustic pressure.

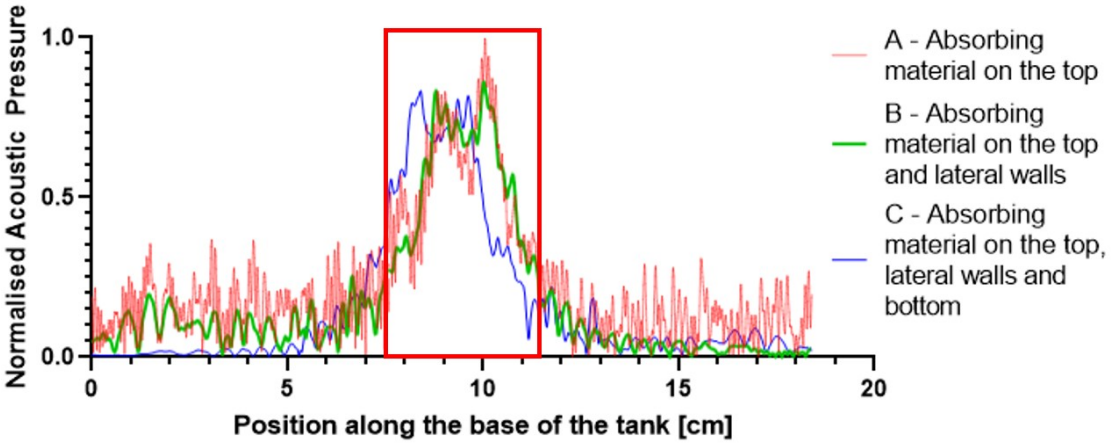

Figure 4.14: *The graph shows how the absolute acoustic pressure varied along the bottom line of the tank, which was the target area for the experiments. The red frame indicates the central area where MBs and NDs will be placed.*

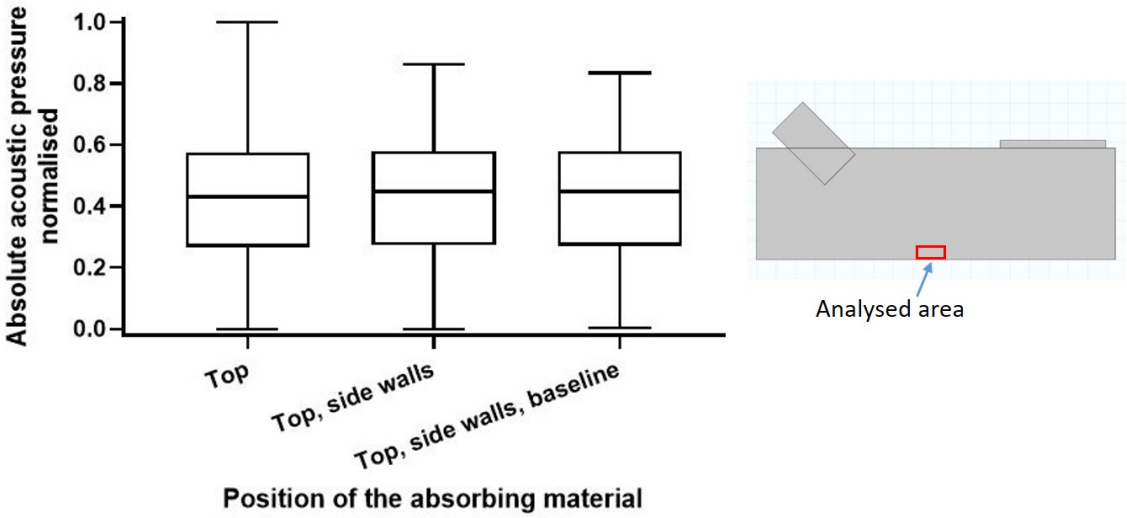

Figure 4.15: *The boxplots show how the normalised absolute acoustic pressure varied in the region of interest (red frame) when the absorbing material was placed in three different ways (corresponding to differences in the overall location). There is no statistical difference between groups ($p > 0.05$).*

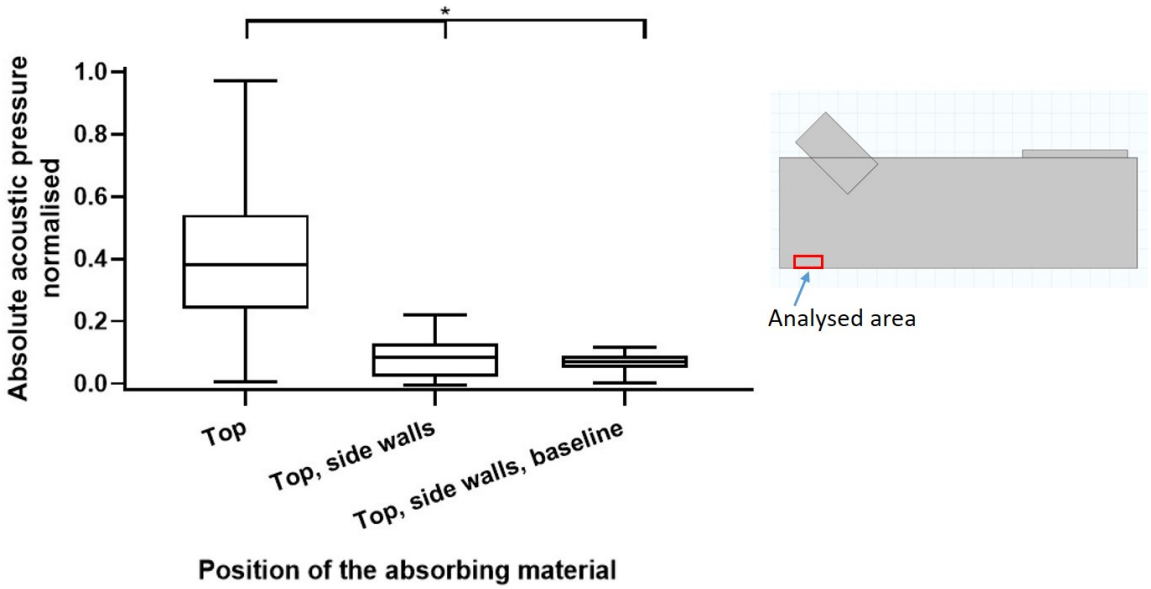

Figure 4.16: *The boxplots show how the absolute acoustic pressure varied in an area positioned at the baseline of the tank, but outside the central target area (highlighted by the red frame in the tank). While at the target point the absorbing material did not have a significant impact on the acoustic pressure field, it did affect the field properties in nearby areas. The addition of absorbing material led to less spatial variations in the acoustic pressure developed in those regions. The three cases presented, namely the addition of absorbing material on the top, on the top and lateral walls and on the top, lateral walls and baseline, are statistically different ($p < 0.05$).*

Even if the stimulation conditions at the target site are comparable between the three cases evaluated, it is important to minimise reflections in the tank to ensure that the signal recorded by the PCD originates predominately from the acoustic field emitted by NDs/MBs at the target point in the tank, and not from the reflected components of the incident wave. The best configuration would be the one with absorbing material positioned at the top, lateral walls and baseline of the tank, but, for ease of use and since there is not a marked difference between this case and the one where the absorbing material is placed only at the top and the lateral walls, this latter configuration was chosen for subsequent experiments.

Focused ultrasound field

The same set of simulations run for the tank accommodating an unfocused transducer, and described in Paragraph 4.1.2.1, were also carried out for focused transducer case. Figure 4.17 shows the absolute acoustic pressure fields in the fluid, obtained at three different position arrangements of the absorbing material.

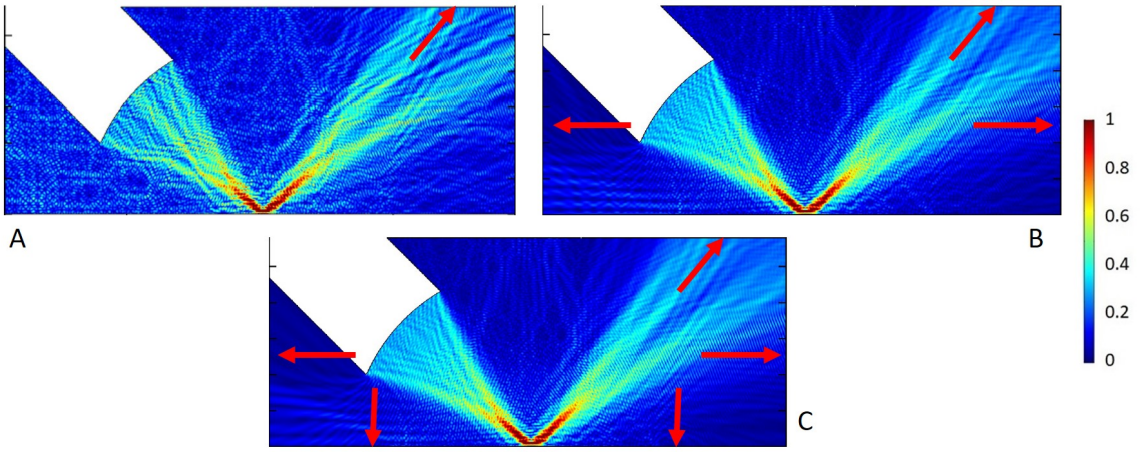

Figure 4.17: *Absolute acoustic pressure in the fluid within the tank. Values have been normalised to the maximum value. The red arrows indicate the position of the absorbing material: A) on the top; B) on the top and on the lateral walls; or C) on the top, the lateral walls, and the bottom of the tank next to the glass slide.*

The addition of absorbing material on the lateral walls (Figure 4.17.B) and the basal surface of the device (Figure 4.17.C) reduced the intensity of reflected waves throughout the fluid volume, as previously highlighted when unfocused transducers where modelled. The acoustic pressure developed at the central region of the tank

baseline was 8 times higher than in the lateral regions. Similarly to what has been reported in Figure 4.13 for the case with unfocused transducers, by adding absorbing material in the tank, the acoustic pressure became more and more homogeneous. The difference between the acoustic pressure at the target point and the surrounding area appeared to be more marked if compared to case with unfocused transducer.

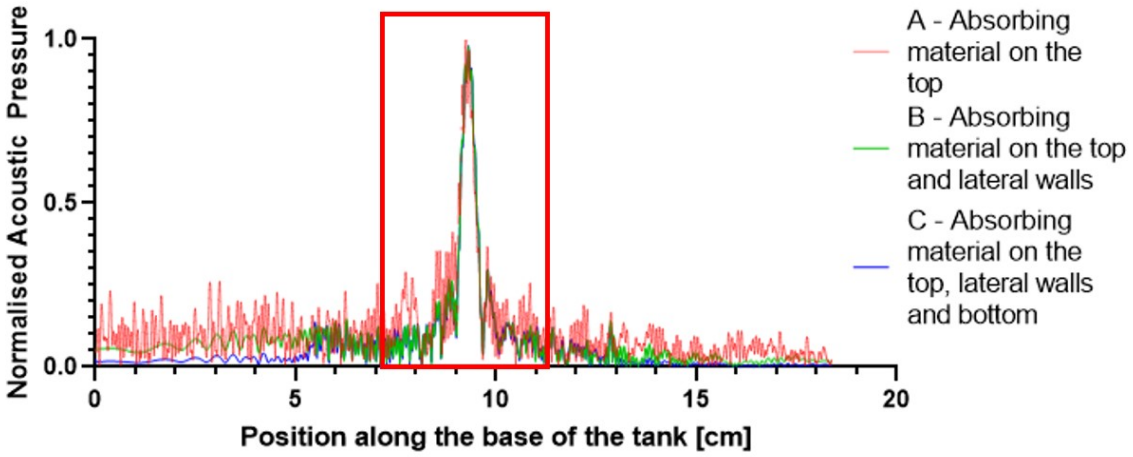

Figure 4.18: *The graph shows how the absolute acoustic pressure varied along the bottom line of the tank. The red box indicates the central region of the tank basal surface, where MBs and NDs will be placed.*

The magnitude of the absolute acoustic pressure at the target area (a rectangle with size 5 x 10 mm in the centre of the tank) was evaluated and, as shown in Figure 4.19, there is no statistical difference between the three absorbing material configurations ($p > 0.05$). However, the absolute acoustic pressure developed at the bottom line of the tank (outside the target area) was influenced by the presence of absorbing material. The pressure was quantified in a rectangle with size 5 x 10 mm positioned in the first quarter of the baseline, on the left hand side, and normalised with respect to the maximum value registered; the boxplots in Figure 4.20 show that adding absorbing material led to a decrease both in the mean value and the standard deviation of the normalised absolute acoustic pressure.

Similarly to the previous case when unfocused transducers were used, the best configuration would be the one with absorbing material placed at the top, lateral walls and baseline of the tank, as it corresponds to a situation whereby the reflected components of the incident wave are minimised. However, since there is not a marked

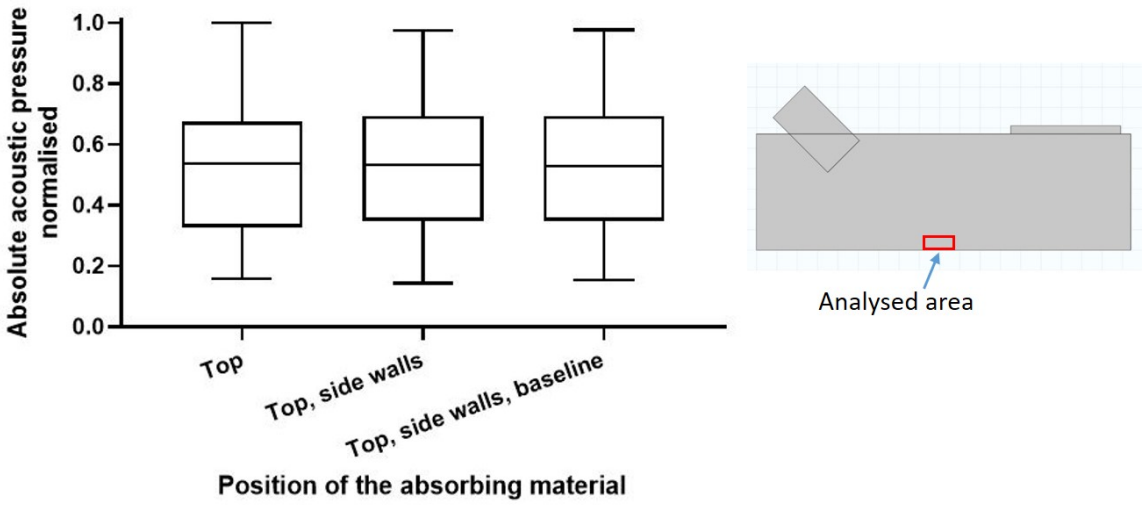

Figure 4.19: *The boxplots show how the absolute acoustic pressure varied in the region of interest (the red frame) when the absorbing material was placed as in the three different cases analysed.*

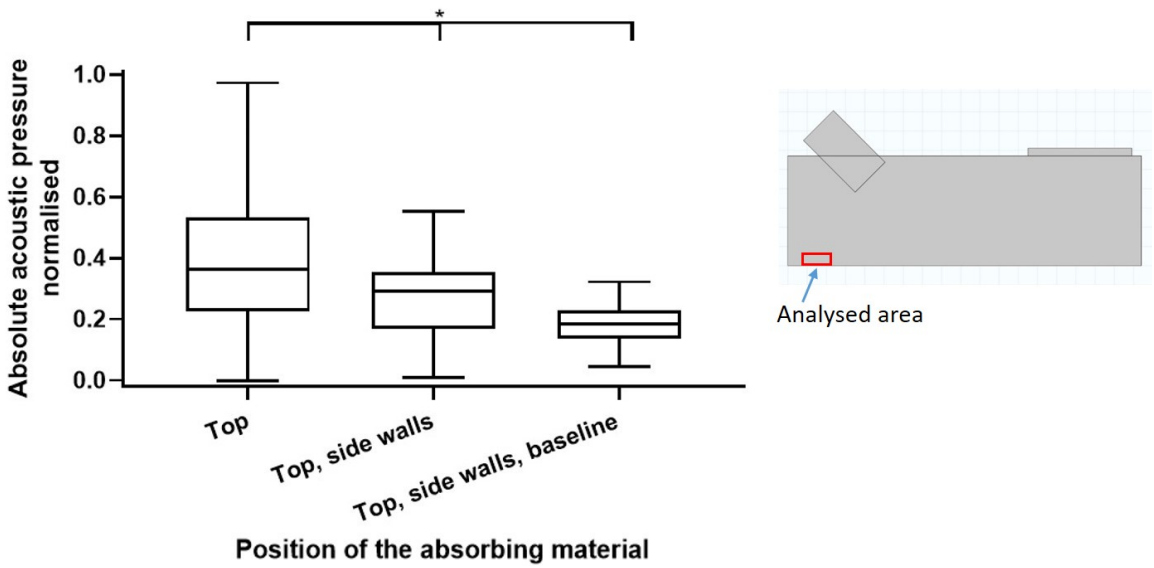

Figure 4.20: *The boxplots show how the absolute acoustic pressure varied in an area positioned at the baseline of the tank, outside the central target region, as highlighted by the red frame. While at the target region, the absorbing material did not have an impact on the acoustic pressure, it did in nearby areas. The addition of absorbing material led to less variations in the acoustic pressure developed. The three groups presented are statistically different ($p < 0.05$).*

difference between this case and the one with absorbing material positioned at the top and lateral walls, the latter configuration was chosen for subsequent experiments.

4.2.1.2 Computational characterisation of the acoustic field developed in the experimental setup in the presence of a bone fracture model

Unfocused ultrasound field

After having characterised the acoustic field developed in the tank, a further series of simulations was run to study the effect of the presence of a bone fracture model on the spatial distribution of the absolute acoustic pressure field within the tank, as described in Paragraph 4.1.2.2. Figure 4.21 shows the spatial distribution of the acoustic pressure field in the tank.

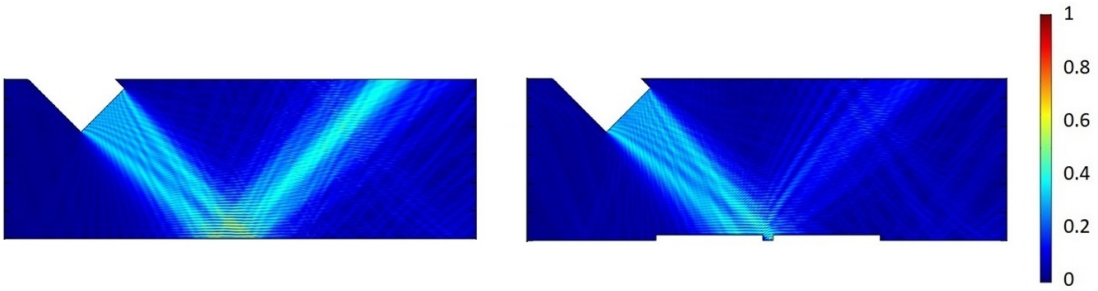

Figure 4.21: *The figure shows how the absolute acoustic pressure changed when a bone fracture model was added to the simulation. Absolute acoustic pressure values have been normalised to the maximum value detected. On the left image, the acoustic wave was reflected by the bottom surface of the tank and then absorbed by the absorbing material layer located on the lid of the tank. On the right image, part of the incident acoustic wave was reflected upwards while part of the acoustic energy led to the onset of reflections and a standing wave field.*

When the bone fracture was added to the model, the combined effect of the geometry of the bone and its acoustic impedance perturbed the characteristics of the acoustic pressure field. Without any fracture model, Figure 4.21 on the left, the acoustic wave was reflected by the bottom surface of the tank and then absorbed by the absorbing material layer located on the lid of the tank; while, in the presence of a fracture model, the reflected component showed a lower intensity. The region of interest in these simulations was the gap between the two fragments of bone, as this was the area where MBs/NDs will be administered. Figure 4.22 shows the absolute acoustic pressure distribution within the fracture gap, for different widths

and thicknesses of the gap (width: 3.5-5.5 mm; thickness: 2-4 mm). The last row refers to the condition of a total fracture (i.e. the wave travelling through the gap was completely absorbed).

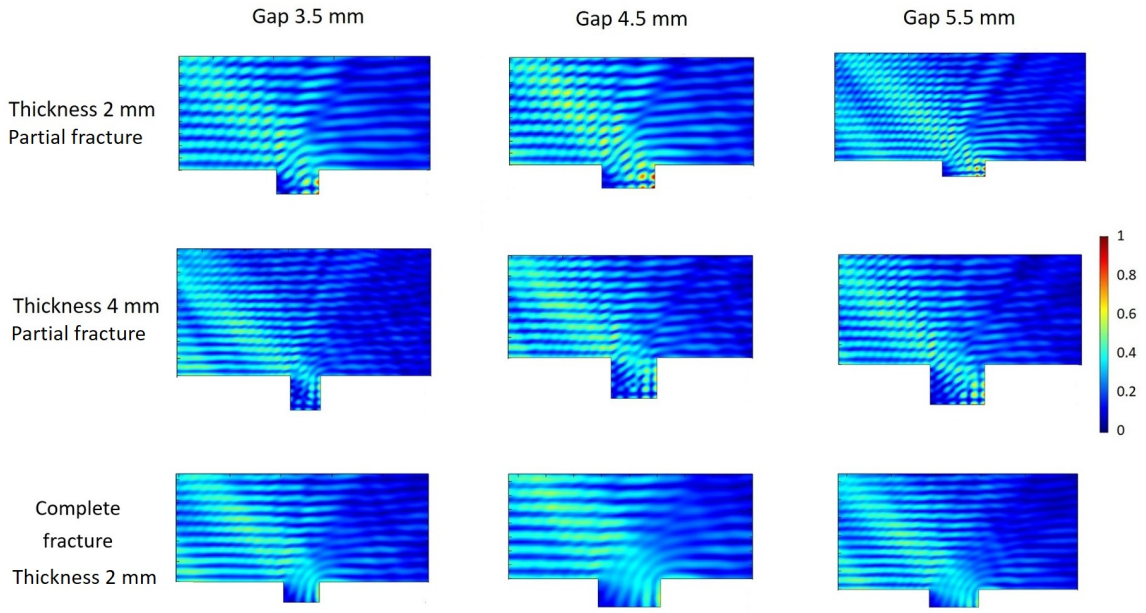

Figure 4.22: *The figure shows the contour of absolute acoustic pressure in fracture gaps having different geometries. The values have been normalised to the maximum value determined within the reported region.*

The architecture of the fracture gap affected the way in which the US wave propagated. In particular, the left edge of the fracture was characterised by a lower acoustic pressure compared to the right edge. The gap size did not have a marked impact on the magnitude and the spatial characteristics of the acoustic field, while having a 4 mm thickness instead of 2 mm increased the size of the gap's area characterised by low acoustic pressure (i.e., unstimulated area), since a greater portion of the fracture gap was hidden from the incident US field by the edges of the fracture itself. It is also possible to observe circular-like pressure hotspots in the gap (i.e. regions with greater acoustic pressure), which may be the result of a standing wave field setup in the fracture gap itself and may be caused by the interaction between the incident and the reflected waves from both the lateral and the bottom surfaces of the gap. Notably, these circular hotspots were not present in the case of a complete fracture (last row of Figure 4.22), since the wave did not get reflected by the bottom surface of the model. This behaviour can be better observed in Figure 4.23 where the

absolute acoustic pressure along the bottom line of the tank is plotted.

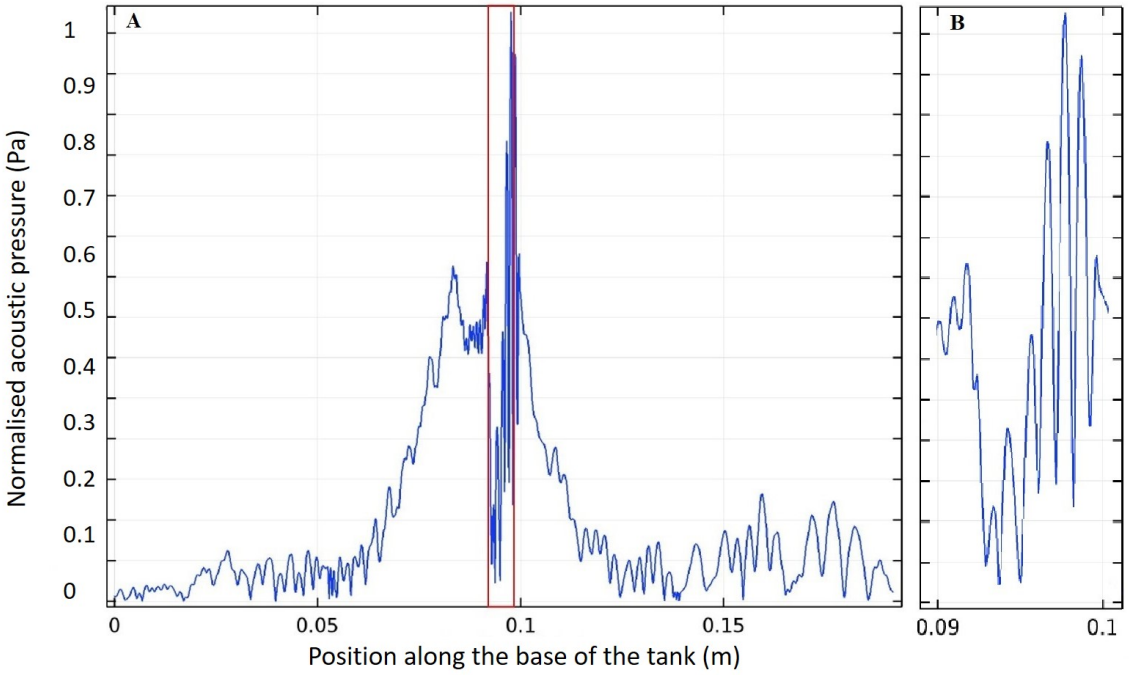

Figure 4.23: *A) The figure shows the absolute acoustic pressure along the bottom line of the tank. Values have been normalised to the maximum value. The gap was 4.5 mm wide and 2 mm thick, and the fracture was inclined with respect to the incoming US wave. The red window indicates the region of the fracture gap. B) Zoomed-in view of the acoustic pressure plot at the region of fracture gap.*

The red window indicates the region of the fracture gap; the acoustic pressure was lower on the left hand side, because this area was hidden from the incident US wave by the upper edge of the bone, and it increased moving towards the opposite edge of the fracture. Differently from the simulation performed in the absence of bone, it was not possible to achieve a relatively uniform acoustic pressure distribution at the target site.

To assess whether the intensity (and spatial distribution) of stimulation would vary as a function of width and thickness of the fracture gap, the absolute acoustic pressure developed in the gap was quantified and normalised with respect to the maximum value in all cases simulated. Results are shown in the boxplots of Figure 4.24.

There was statistical difference ($p < 0.05$) between the absolute acoustic pressure detected in the fracture gaps with a thickness of 2 mm and all other conditions modelled. The average acoustic pressure in the thinner gaps was greater, and its range

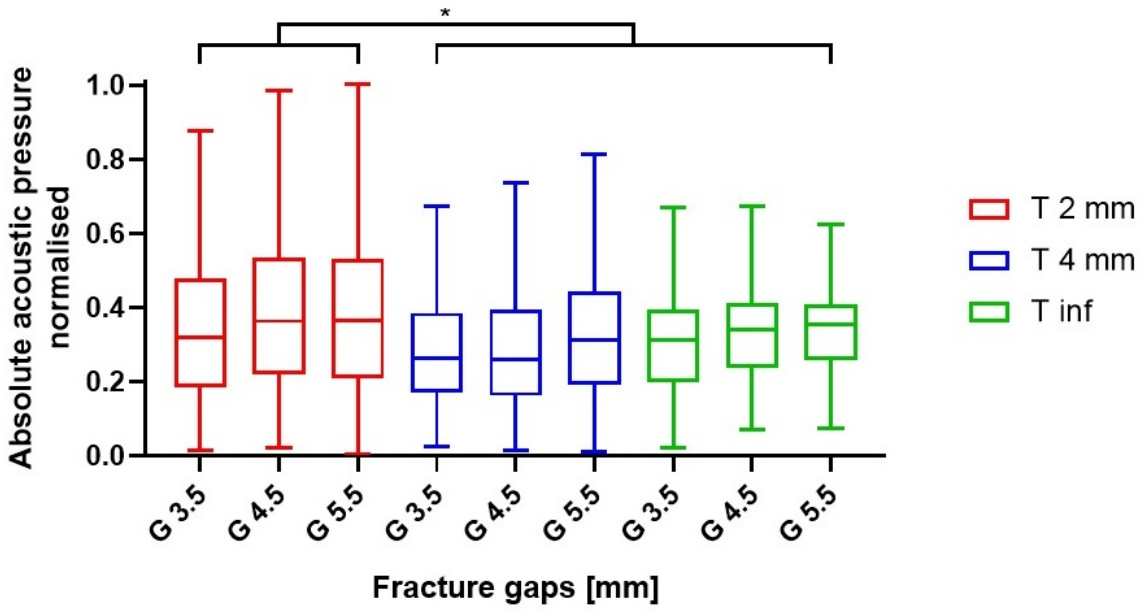

Figure 4.24: *The boxplots show how the absolute acoustic pressure varied in the region of interest (fracture gap) for the different geometries analysed (T: gap thickness, G: gap width, T inf refers to the case of a complete fracture of thickness 2 mm). There was statistical difference (*$p < 0.05$) between the absolute acoustic pressure detected in the fracture gaps with a thickness of 2 mm and all other conditions modelled.*

of variation was broader than the other cases. This could be due to the presence of hotspots with greater pressure amplitude - hotspots in the first line of Figure 4.24 were red and hence stronger than the ones in the second line that were yellow - which could potentially lead to more intense stimulation conditions within the fracture gap. Results suggested that increasing the gap from 3.5 to 5.5 mm led to greater acoustic pressure in the gap itself and a broader range of pressure values, but there is no statistical evidence to support this finding.

In the clinic, it can be challenging to align the transducer to the fracture, hence it's important to determine whether the alignment has an impact on the acoustic field developed at the point of treatment. A further simulation was thus performed with the fracture aligned to the incoming US wave. Figure 4.25 shows that the absolute acoustic pressure distribution changed with changing the fracture's inclination angle; when the fracture was aligned to the incident US wave, there were no areas of the gap 'hidden' from the incoming pressure field. Figure 4.26 shows the absolute acoustic pressure along the bottom line of the tank, and the red window indicates the position of the fracture gap. The acoustic field presented some spatial variations in the fracture

gap, but variations were less significant compared to the inclined fracture model.

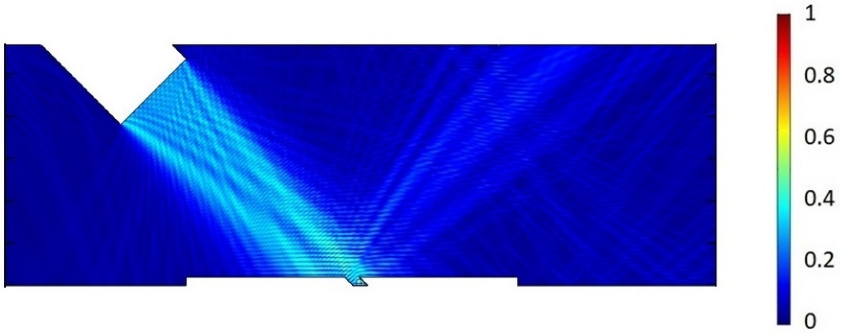

Figure 4.25: *The figure shows the absolute acoustic pressure field in the tank in the presence of a fracture aligned to the US wave. The values have been normalised to the maximum value.*

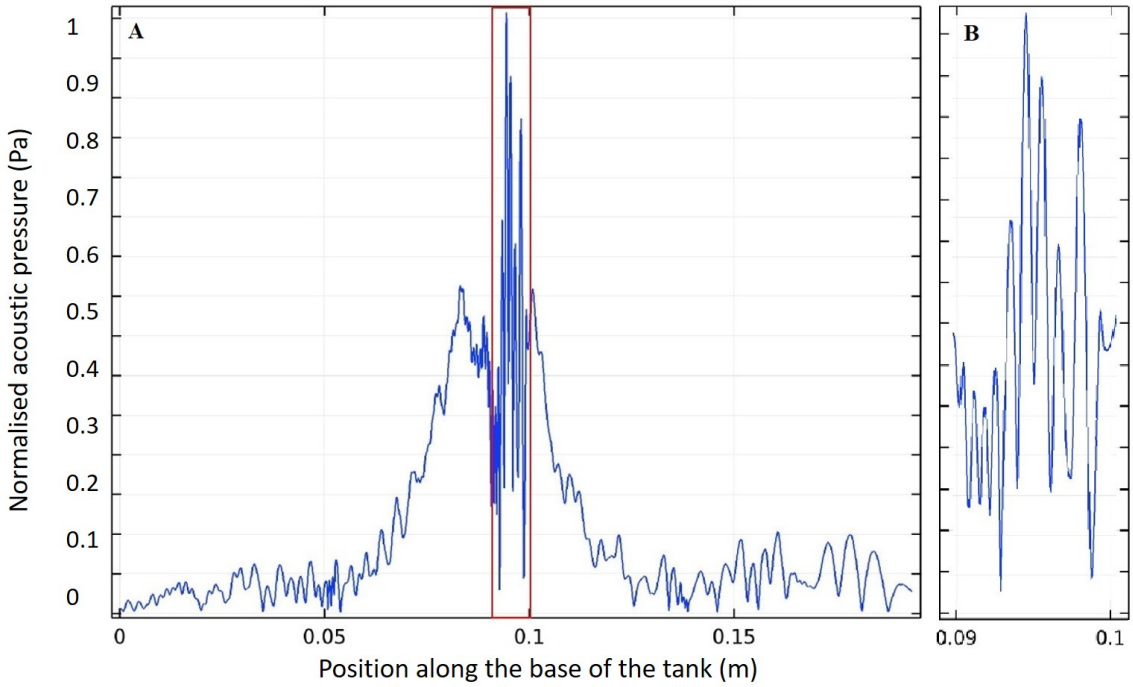

Figure 4.26: *A) The figure shows the absolute acoustic pressure along the bottom line of the tank. Values have been normalised to the maximum value. The gap was 4.5 mm wide and 2 mm thick and the fracture was aligned to the US wave. The red window indicates the region of the fracture. B) Zoomed-in view of the region of the fracture.*

The simulation was run for different gap sizes and thicknesses, and the results are shown in Figure 4.27. In the case of fracture aligned to the incident US field, the gap size and thickness of the fracture did not have a marked impact on the acoustic pressure field within the gap. Similarly to the observations made on the inclined fracture model, it was possible to notice some circular-like pressure hotspots in the gap, which may be attributed to a standing wave field set up within the gap itself. These circular hotspots were not present in the case of complete fracture (last row). There was no clear difference in the location of hotspots compared to the inclined model, while their number was greater in the aligned fracture gap, likely due to the larger area being exposed to the acoustic wave.

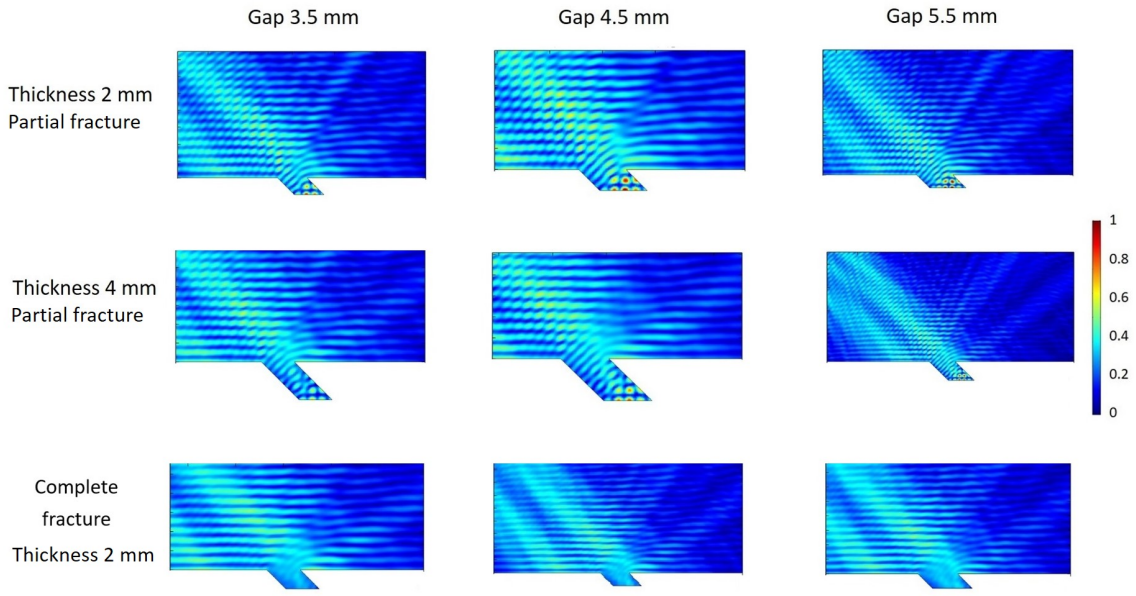

Figure 4.27: *The figure shows the contour of absolute acoustic pressure in fracture gaps aligned to the US wave and having different geometries. The values have been normalised to the maximum value determined within the reported region.*

Figure 4.28 shows the absolute acoustic pressure along the bottom line of the tank in the case of a complete fracture, and the red window indicates the position of the fracture gap. The magnitude of acoustic pressure was lower than the case of the partial fracture, potentially due to a weaker standing wave field established within the gap.

To numerically assess the influence of width and thickness of the gap on the acoustic field, the absolute acoustic pressure developed within each gap was quantified

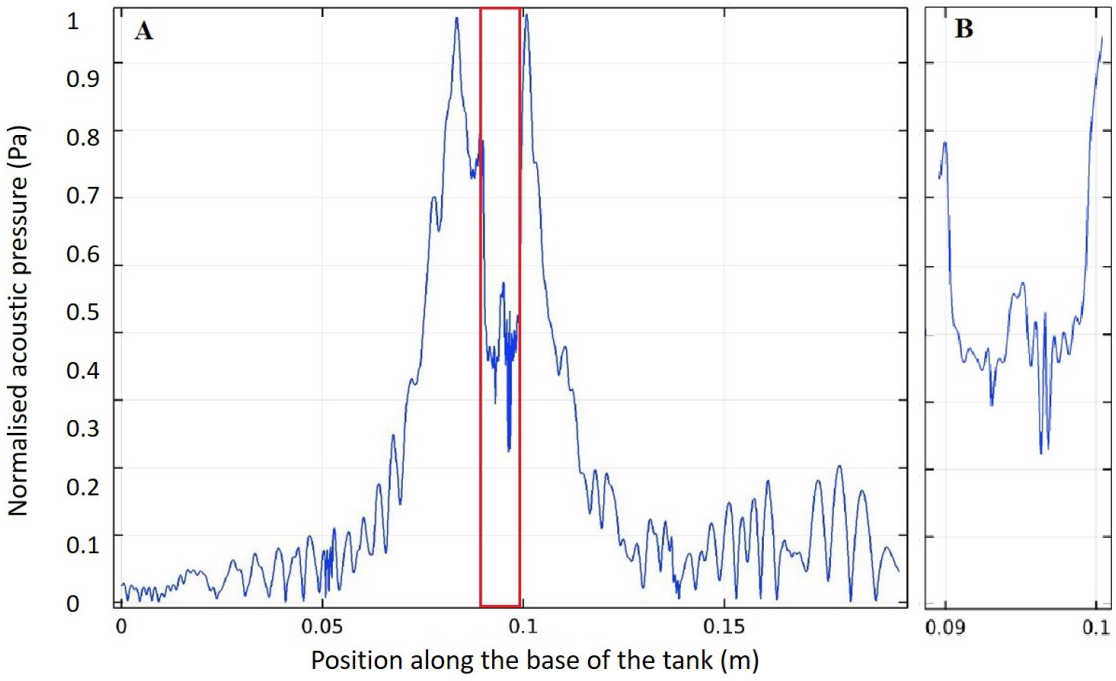

Figure 4.28: *A) The figure shows the absolute acoustic pressure along the bottom line of the tank. Values have been normalised to the maximum value. The gap was 4.5 mm wide, the fracture was modelled as complete and was aligned to the incident US wave. The red window indicates the region of the fracture gap. B) Zoomed-in view of the region of the fracture.*

and plotted in Figure 4.29.

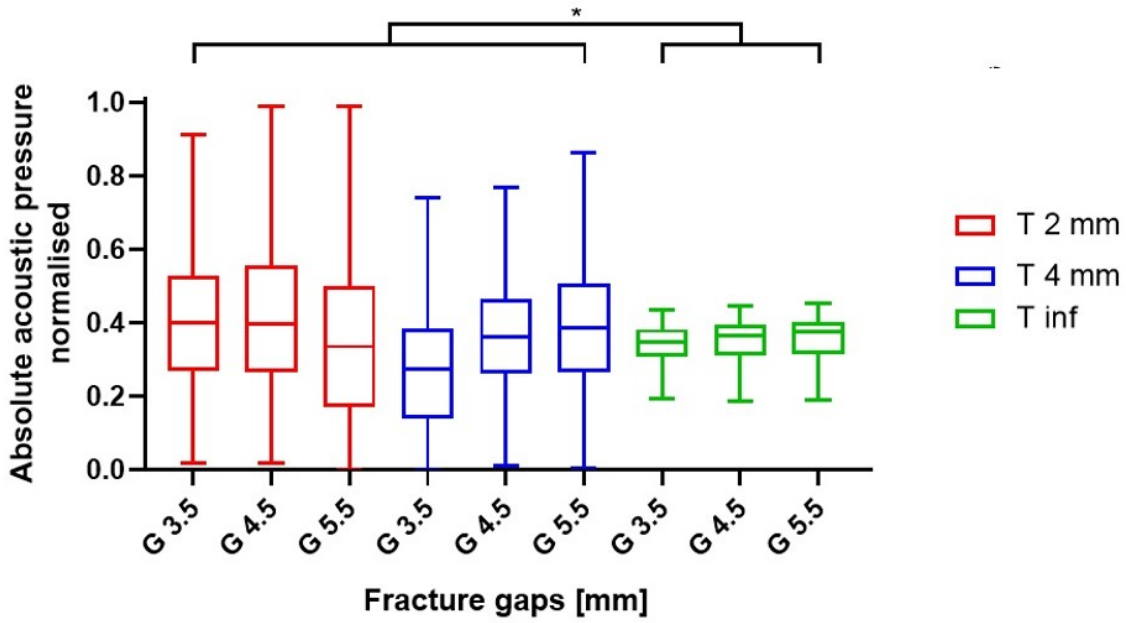

Figure 4.29: *The boxplots show how the normalised absolute acoustic pressure varied in the region of interest (the fracture gap) for different geometries simulated (T: gap thickness, G: gap width, T inf refers to the case of a complete fracture of thickness 2 mm). There was statistical difference (p¡ 0.05) between the absolute acoustic pressure detected in the passing through fracture and all the other conditions modelled.*

When a passing-through fracture was tested, the range of variation of the total acoustic pressure (defined by the first and fourth quartiles of the boxplots) was significantly narrower than the other cases examined. In the absence of US reflections at the baseline of the tank, pressure hotspots are not present in the gap, hence the spatial variation of acoustic pressure is reduced.

In conclusion, when the transducer is aligned to the fracture gap, a larger proportion of the gap region is likely to be stimulated by ultrasound; conversely, if the transducer is inclined, there are sections of the gap that may not receive sufficient stimulation. Therefore, the first configuration is to be preferred in order to ensure that a greater proportion of ultrasound-responsive agents administered to the fracture gap receive the desired acoustic pressure stimulation conditions, and hence provide the anticipated therapeutic action. In addition to this, the present work only analyses single element transducers, while multi element devices could be used in the clinic to overcome issues connected to the the inclination of the transducer with respect to the fracture.

Focused ultrasound field

The simulations were repeated for the tank containing the 1 MHz focused transducer, and the results obtained (in terms of acoustic pressure magnitude and its spatial distribution) were comparable to the ones obtained using a focused transducer. Figure 4.30 shows the spatial distribution of the acoustic pressure field in the tank.

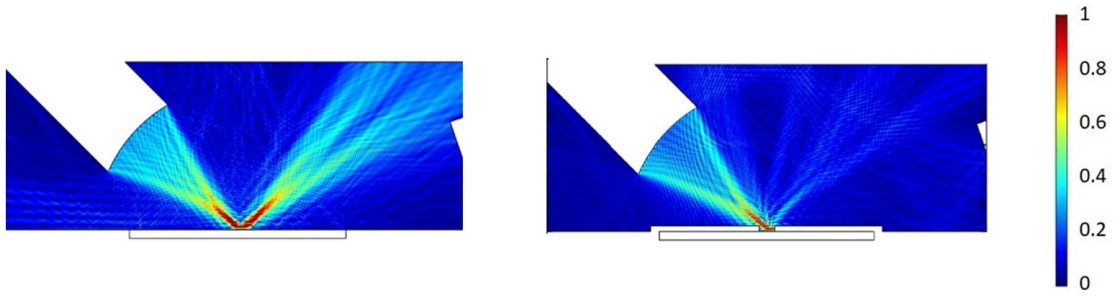

Figure 4.30: *The figure shows how the absolute acoustic pressure changed when a bone fracture model was added to the simulation. The values were normalised to the maximum value observed. On the left, the acoustic wave was totally reflected by the bottom surface of the tank, and then absorbed by the absorbing material layer located on the lid of the tank. Conversely, in the presence of a fracture model, only part of the acoustic wave was reflected upwards, while part of the acoustic energy was either stored in the gap likely due to the onset of a standing wave field and lost within the bone through standing waves.*

Figure 4.31 shows the absolute acoustic pressure within the fracture gap, for different widths and thicknesses of the gap (width: 3.5-5.5 mm; thickness: 2-4 mm). The last row refers to the condition of a total fracture (i.e. the wave travelling through the gap was completely absorbed).

Similarly to the results obtained using an unfocused transducer, the architecture of the fracture gap affected the way in which the US wave propagated and resulted in the formation of pressure hotspots in the gap where the acoustic pressure was higher. This behaviour can be better observed in Figure 4.32 where the absolute acoustic pressure along the bottom line of the tank is reported. The red window indicates the region of the fracture gap.

To assess whether the intensity of stimulation (in terms of acoustic pressure) could vary as a function of width and thickness of the fracture gap, the absolute acoustic pressure developed in the gap was quantified and normalised with respect to the maximum value detected in all cases modelled. Results are shown in the boxplots of Figure 4.33.

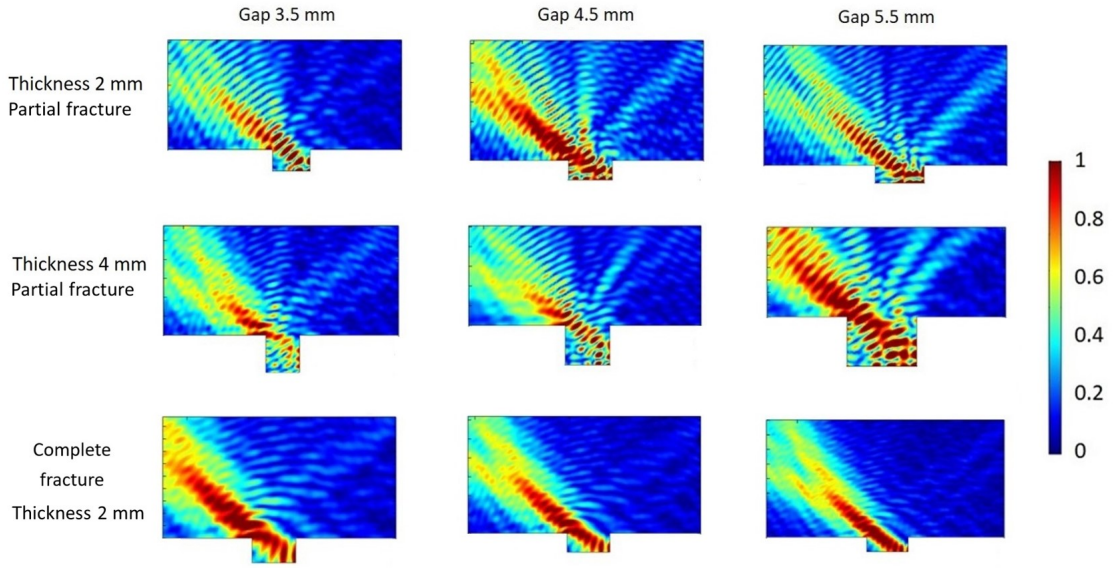

Figure 4.31: *The figure shows the absolute acoustic pressure in fracture gaps with different geometries. The values were normalised to the maximum value observed.*

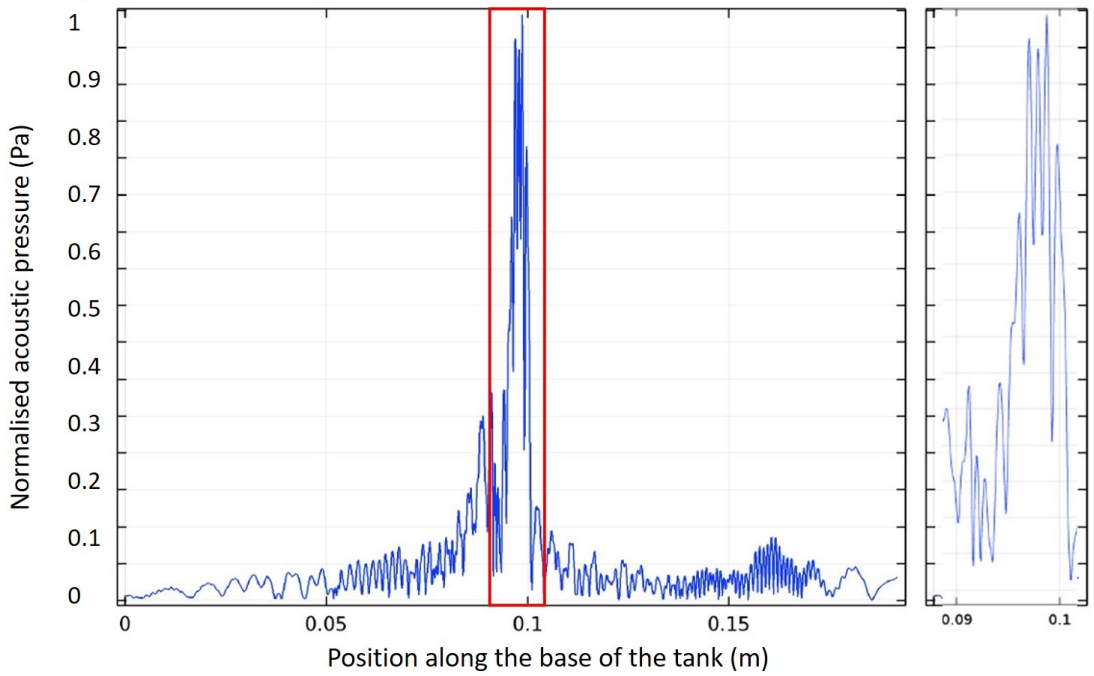

Figure 4.32: *A) The figure shows the absolute acoustic pressure along the bottom line of the tank. The gap was 5.5 mm wide and 2 mm thick, and the fracture was inclined with respect to the incoming US wave. The red window indicates the region of the fracture. B) Zoomed-in view of the region of the fracture.*

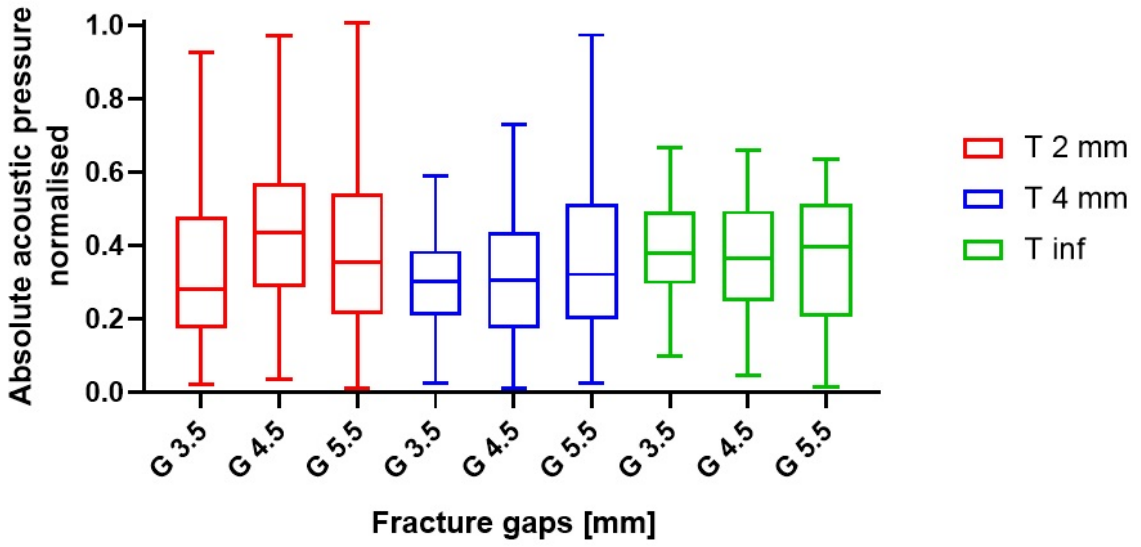

Figure 4.33: *The boxplots show how the normalised absolute acoustic pressure varied in the region of interest (the fracture gap) for different geometries simulated (T: gap thickness, G:gap width, T inf refers to the case of a complete fracture of thickness 2 mm).*

Statistical difference was found among the majority of cases modelled, but there was no specific trend suggesting that an increase in either the thickness or the width of the gap might have a proportional effect on the absolute acoustic pressure developed at the target region.

To take into consideration the difficulty in aligning the transducer with respect to the fracture gap (in a clinical context), a further series of simulations was performed with a fracture aligned to the incoming US wave. Figure 4.34 shows the absolute acoustic pressure developed in the tank in the presence of an aligned fracture.

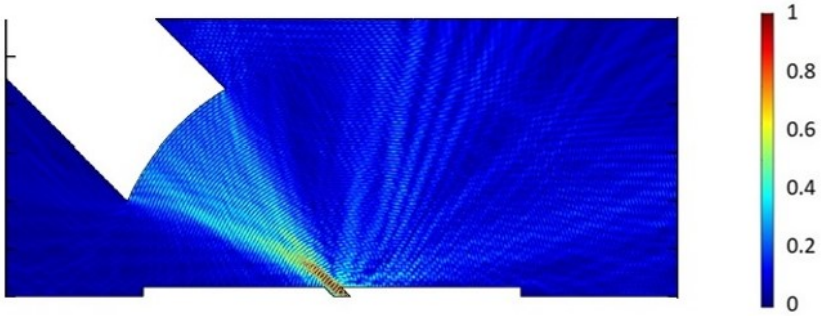

Figure 4.34: *The figure shows the contour of absolute acoustic pressure in fracture gaps having different geometries. The values have been normalised to the maximum value determined within the reported region.*

Figure 4.35 shows the absolute acoustic pressure along the baseline of the tank, and the red window indicates the position of the fracture gap. The acoustic field presented some variations in the fracture gap, but the magnitude of these variations was less significant when compared to the inclined fracture model.

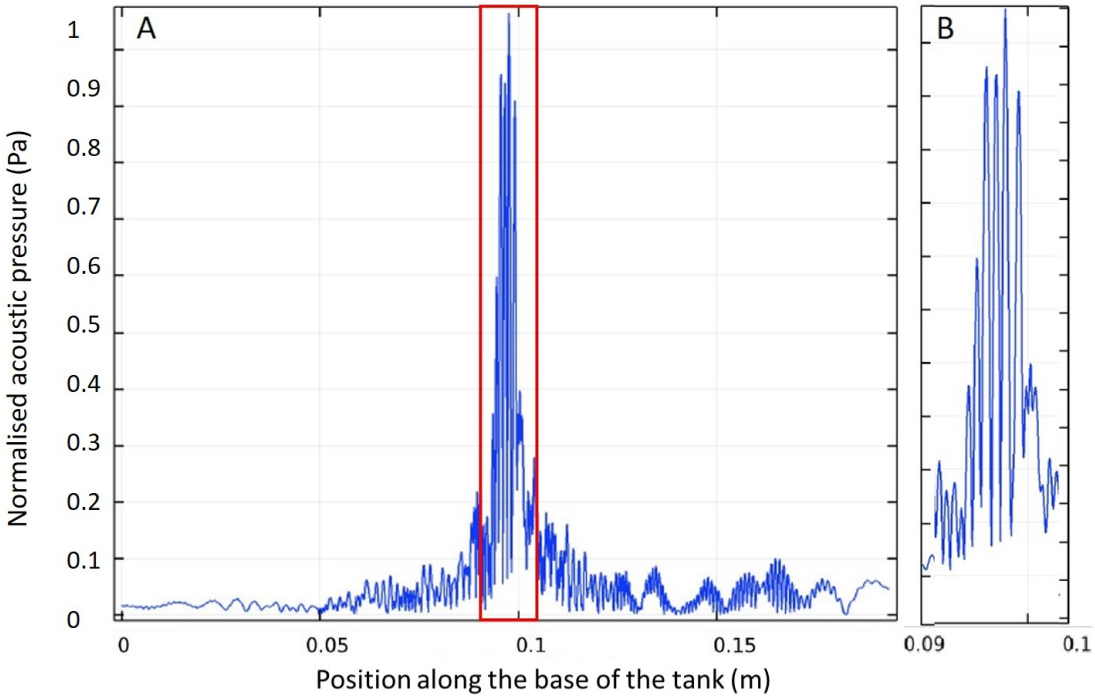

Figure 4.35: *A) The figure shows the absolute acoustic pressure along the baseline of the tank. The gap was 5.5 mm wide and 2 mm thick and the fracture was aligned with respect to the incident US wave. The red window indicates the region of the fracture. B) Zoomed-in view of the region of the fracture.*

Figure 4.36 shows the absolute acoustic pressure within the fracture gap, for different widths and thicknesses of the gap (width: 3.5-5.5 mm; thickness: 2-4 mm). The last row refers to the condition of a total fracture (i.e. the wave travelling through the gap is completely absorbed).

To assess whether the intensity of stimulation (in terms of acoustic pressure) could vary as a function of width and thickness of the fracture gap, the absolute acoustic pressure developed in the fracture gap was quantified and normalised with respect to the maximum value detected in all cases tested. Results are shown in the boxplots of Figure 4.37.

Statistical difference was found among the majority of the cases tested, but there

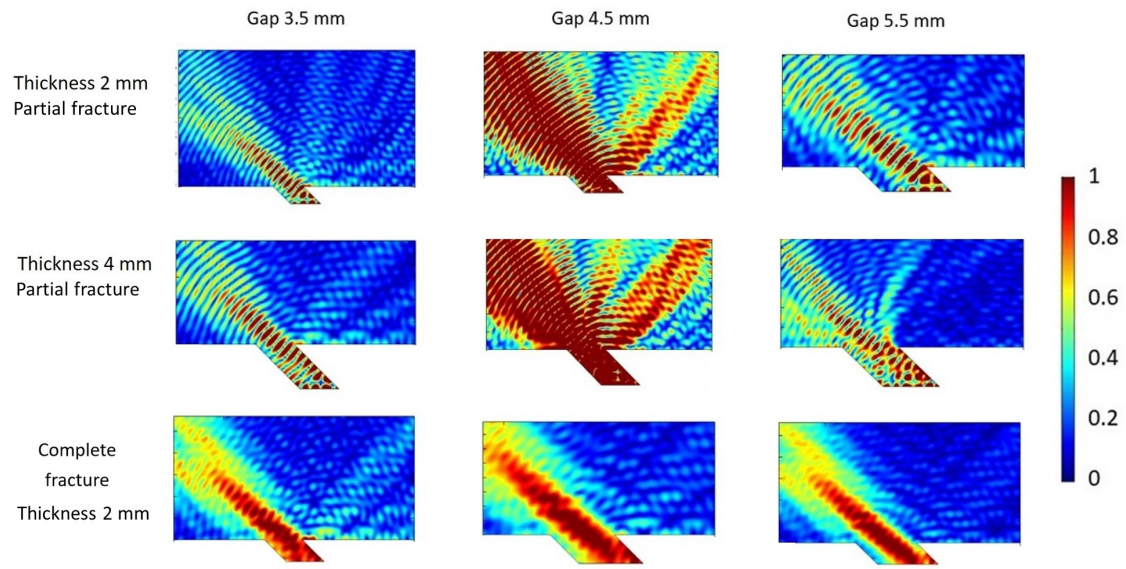

Figure 4.36: *The figure shows the contour of absolute acoustic pressure in fracture gaps aligned to the US and having different geometries. The values have been normalised to the maximum value determined within the reported region.*

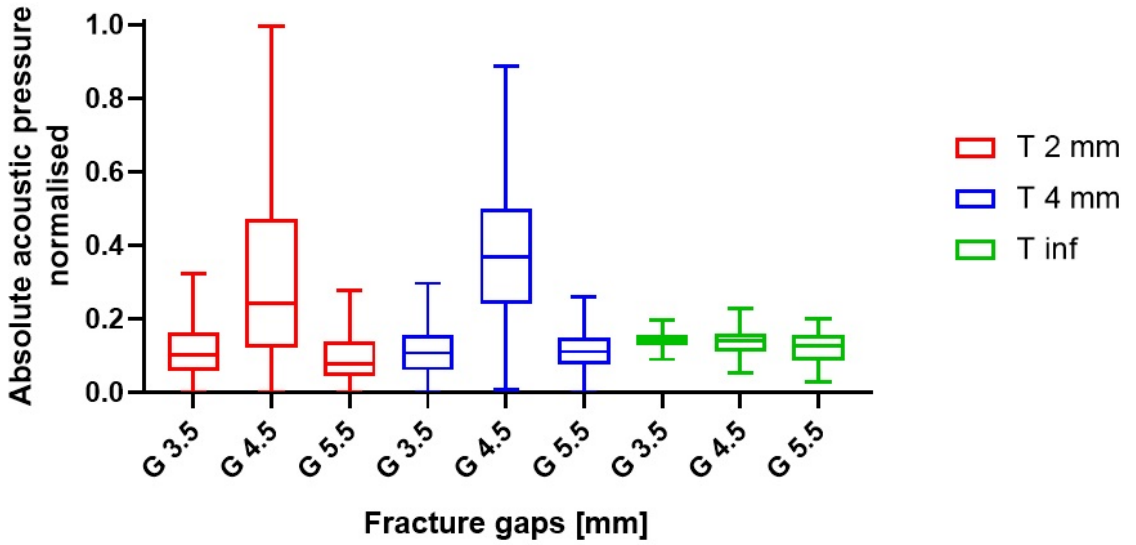

Figure 4.37: *The boxplots show how the normalised absolute acoustic pressure varied in the region of interest (the fracture gap) for different geometries simulated (T: gap thickness, G:gap width, T inf refers to the case of a complete fracture of thickness 2 mm).*

was no specific trend to suggest that an increase in either the thickness or the width of the gap might have a proportional effect on the absolute acoustic pressure developed at the target region.

In summary, numerical modelling of the acoustic field developed in the tank using different positioning of the absorbing material, different types of transducer, and different inclination angles of the fracture gap showed that: i) the presence of absorbing material is fundamental to attenuate reflection of the incident wave in the tank, while it does not compromise the stimulation conditions at the target region; ii) the focused transducer allows reaching higher acoustic pressures, hence a more intense stimulation, at the target region if compared to unfocused transducers; and iii) aligning the fracture with the direction of the US wave provides stimulations conditions that are more uniform over the fracture gap area.

4.2.2 *In vitro* tests

4.2.2.1 Acoustic calibration of the experimental setup

Prior to performing any experimental test using the developed tank, the transducers were calibrated to determine the relationship between the voltage applied to the transducer and the acoustic pressure developed at the target region in the tank.

2 MHz unfocused transducer

The experiments described in Paragraph 4.1.3.1 on page 189 were designed to study the acoustic pressure field at the set target plane placed at a distance of 8 cm from the transducer, when using the 2 MHz unfocused transducer. Figure 4.38.A shows the intensity of the signal recorded by the hydrophone over the XZ plane, which was the plane perpendicular to the direction of the US propagation. This signal was then processed to determine the acoustic pressure distribution. Figure 4.38.B shows the acoustic pressure over the XZ plane. It can be observed that the acoustic pressure was higher in the centre, and gradually reduced laterally. The transducer was driven with a frequency of 2 MHz and a voltage of 28 Vpp, and the maximum acoustic peak-negative pressure registered was equal to 0.14 MPa.

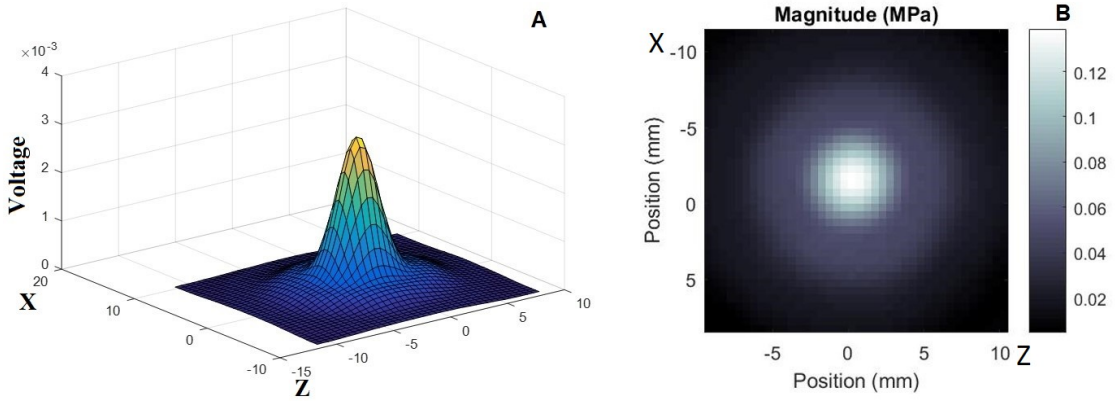

Figure 4.38: *A) Voltage recorded by the hydrophone on the XZ plane at a distance of 8 cm from the transducer. B) Acoustic pressure over a plane located at a distance of 8 cm from the transducer.*

The region where the acoustic pressure magnitude was greater than 50% of the maximum value covered an area of 5 mm^2. This was sufficiently large to cover the

total area of the analysed fracture gaps, indicating that the tank design was successful in stimulating the target region of interest, as shown in Figure 4.39.

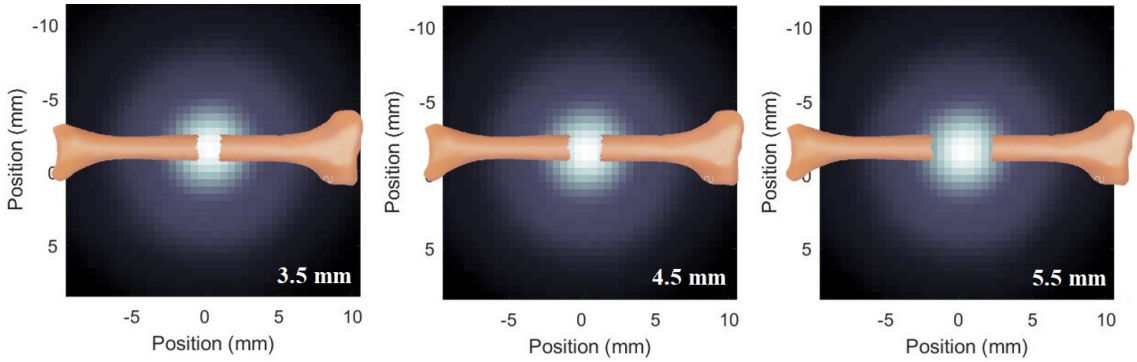

Figure 4.39: *The setup achieves a relatively homogeneous stimulation area of 5 mm^2, which is large enough to provide a sufficiently homogeneous incident acoustic pressure for the fracture gaps of namely 3.5, 4.5 and 5.5 mm width.*

The second series of measurements were performed over a XY plane, to determine the variation of the acoustic field while moving away from the transducer in order to determine whether small variations in the transducer's Y position could influence the stimulation conditions. Figure 4.40.A shows the voltage recorded by the hydrophone and Figure 4.40.B shows the corresponding acoustic pressure. It is possible to notice that the acoustic pressure decreased with increasing the distance from the transducer.

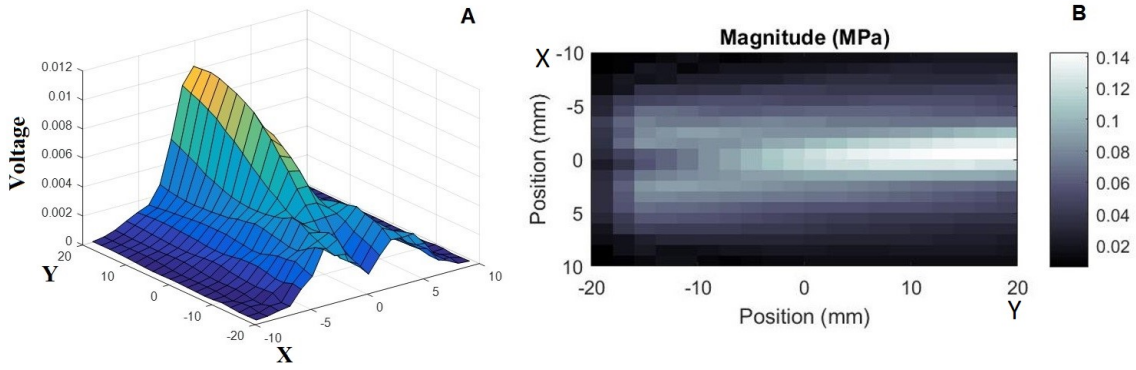

Figure 4.40: *A) Voltage recorded on the XY plane. B) Acoustic pressure along the XY plane of the transducer.*

A driving voltage ramp from 14 to 196 Vpp was applied in these tests. Figure 4.41 shows the relationship between driving voltage and maximum acoustic peak-negative pressure. This graph provides useful information about the acoustic pressure developed by the incident US wave at a distance from the transducer corresponding to the one where MBs/NDs will be positioned in the experiments. It should be noted that the peak acoustic pressure developed in the presence of a bone fracture model may be greater due to the onset of a standing wave field in the fracture gap.

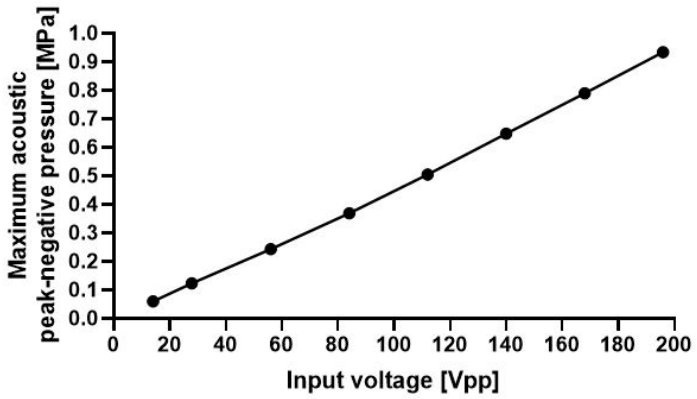

Figure 4.41: *A test was performed to determine the relationship between the voltage applied to the 2 MHz transducer and the peak-negative acoustic pressure developed at the target plane, placed at 8 cm from the transducer surface. The voltage ramp in the graph shows that the relationship between input voltage and acoustic pressure is linear.*

In addition to characterising the acoustic field generated by the transducer alone, it was also important to determine whether the acoustic field changed when the transducer was coupled with the microscope-compatible tank. Figure 4.42.A shows the voltage recorded at the target plane (at 8 cm from the transducer), while Figure 4.42.B shows the corresponding acoustic pressure. The spatial distribution of the acoustic pressure appeared to be slightly affected by the presence of the tank (i.e., likely due to reflections of the incident wave taking place within the tank); however, the maximum acoustic pressure recorded (0.14 MPa) and the area where such stimulation was applied were comparable to the ones measured for the transducer alone, suggesting that the presence of the tank does not significantly alter the acoustic stimulation at the target region.

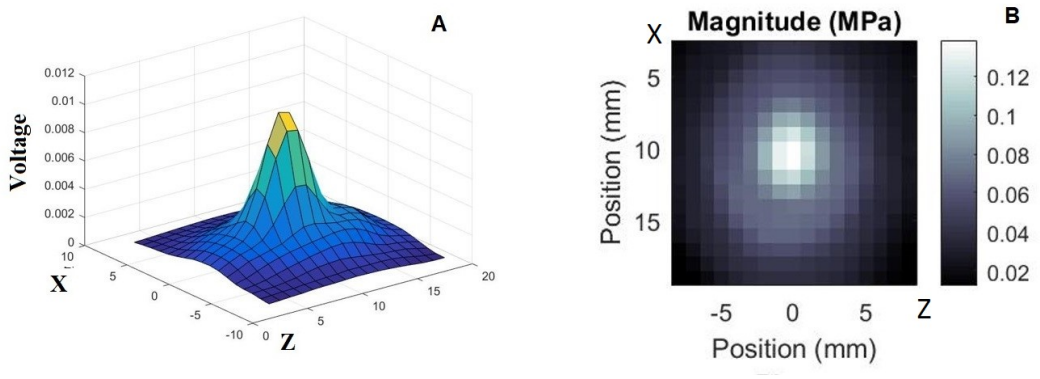

Figure 4.42: *A) Voltage recorded on the XZ plane at a distance of 8 cm from the transducer placed inside the microscope-compatible tank. B) Acoustic pressure over the XZ plane, at a distance of 8 cm from the transducer.*

1 MHz unfocused transducer

The same calibration was performed for the 1 MHz unfocused transducer to determine the acoustic pressure field at the set target plane.

Figure 4.43.A shows the intensity of the signal recorded by the hydrophone over the XZ plane. This signal was then processed to determine the acoustic pressure distribution. Figure 4.43.B shows the acoustic pressure over the XZ plane. It can be observed that the acoustic pressure was higher in the centre, and gradually reduced laterally. The transducer was driven with a frequency of 1 MHz and a voltage of 140 Vpp, and the maximum acoustic peak-negative pressure registered was equal to 0.21 MPa.

The second series of measurements were performed over a XY plane, to determine the variation of the acoustic pressure field while moving away from the transducer's surface. Figure 4.44.A shows the voltage recorded by the hydrophone and Figure 4.44.B shows the corresponding acoustic pressure. It is possible to notice that the acoustic pressure decreased with increasing the distance from the transducer.

A driving voltage ramp from 14 to 196 Vpp was applied and Figure 4.45 shows the relationship between driving voltage and maximum peak-negative acoustic pressure.

Overall, results showed that the presence of the tank did not significantly alter the acoustic pressure field (both peak amplitude and spatial distribution) developed at the target point.

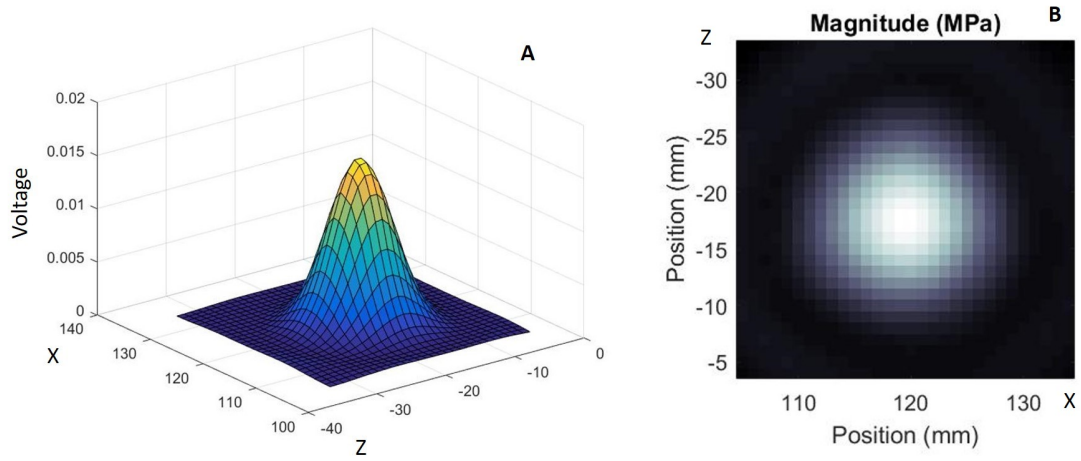

Figure 4.43: *A) Voltage recorded on the XZ plane. B) Acoustic pressure along the axis of the transducer.*

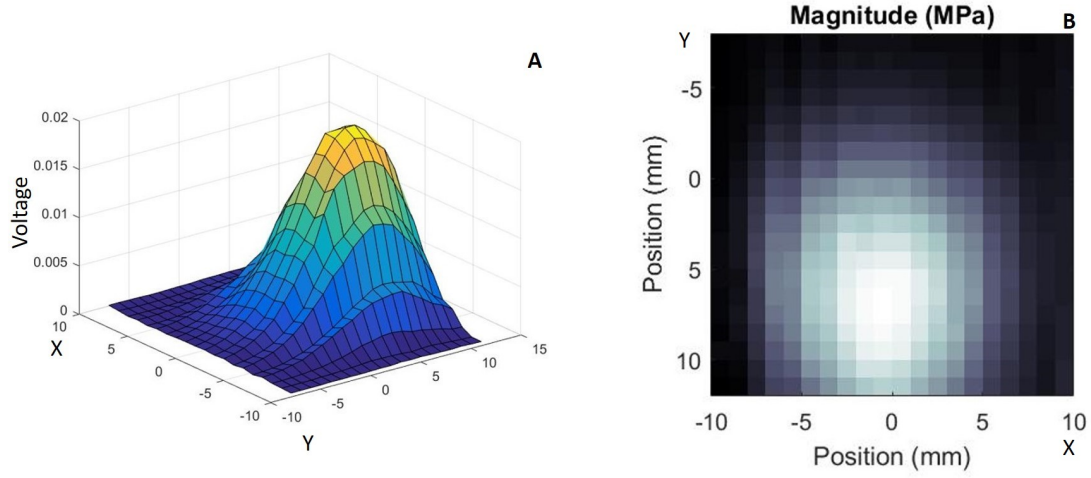

Figure 4.44: *A) Voltage recorded on the XY plane at a distance of 8 cm from the transducer placed inside the microscope-compatible tank. B) Acoustic pressure over the XY plane, at a distance of 8 cm from the transducer.*

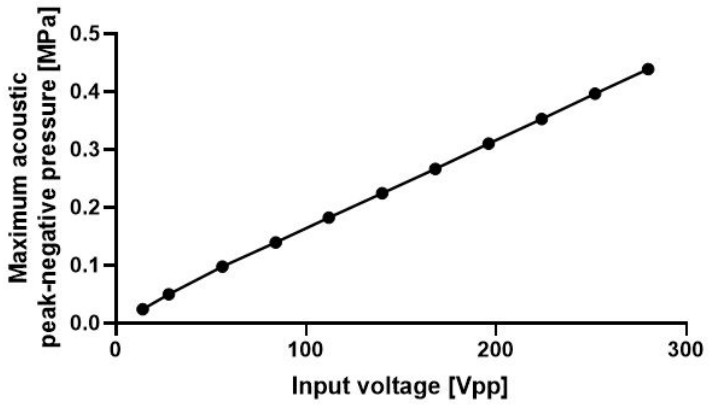

Figure 4.45: *A test was performed to determine the relationship between the voltage applied to the 1 MHz transducer and the peak-negative acoustic pressure developed at the target plane. The results show that the relationship between input voltage and acoustic pressure was linear.*

1 MHz focused transducer

The same calibration process was performed for the 1 MHz focused transducer. Figure 4.46 shows the voltages recorded along the x, y and z axes around the target region, while Figure 4.47 shows the relationship between driving voltage and maximum peak-negative acoustic pressure developed at the target point.

The calibration tests performed on the unfocused transducer showed that the presence of the tank did not alter the acoustic pressure field developed at the target site. It is anticipated that the same applies to the case of a focused transducer.

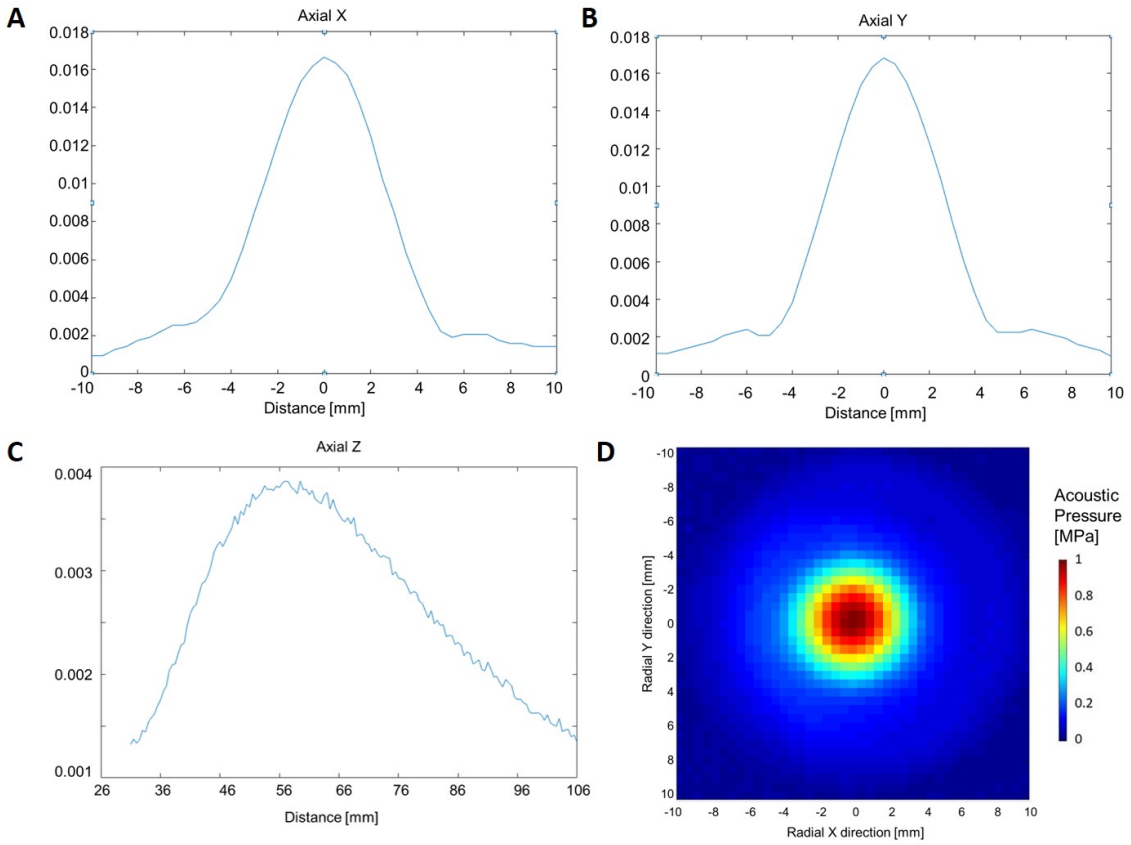

Figure 4.46: *Voltage recorded on the: a) x axis, b) y axis and c) z axis. D) Acoustic pressure developed on the XY plane.*

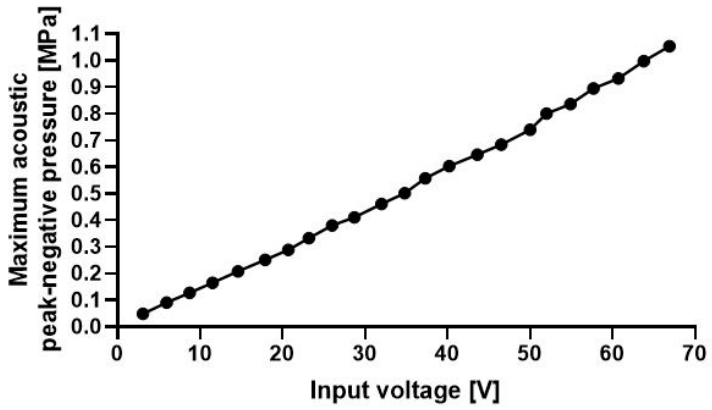

Figure 4.47: *A test was performed to determine the relationship between the voltage applied to the 1 MHz focused transducer and the peak-negative acoustic pressure developed at the target plane. The voltage ramp in the graph shows that the relationship between input voltage and acoustic pressure was linear.*

4.2.2.2 Experimental verification of the setup

After having calibrated the transducers employed for MB/ND stimulation, a subsequent step was a preliminary verification of the developed setup, which included a qualitative comparison with the computational modelling results. The experiment described in Paragraph 4.1.3.2 on page 191 was performed and the results are presented here. The aim was to assess whether the addition of absorbing material would reduce the wave amplitude detected by the PCD, due to a reduction in sound wave reflections within the setup.

Results from the numerical simulations reported in Paragraph 4.2.1.1 on page 201 showed that the addition of an acoustic absorbing material on the lateral walls of the tank and on the lid allowed reducing the extent of these reflections. A first *in vitro* test was thus performed to confirm this experimentally. The signal recorded by the PCD, either in the absence or presence of absorbing material, is shown in Figure 4.48.

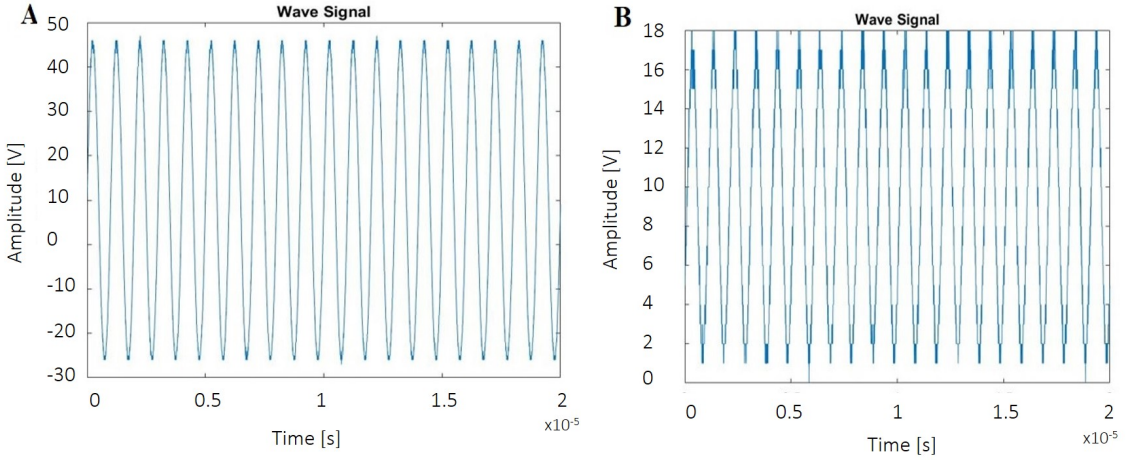

Figure 4.48: *Signal recorded by the PCD when an US stimulation of 84 Vpp and 1 MHz was applied. A) The tank did not have any acoustic absorbing material inside, and no MBs/NDs were added to the fluid. B) The acoustic absorbing material was added to the tank on the lateral walls and on the lid. No MBs/NDs were added to the fluid.*

The graphs in Figure 4.48 show that the signal recorded in the absence of absorbing material had a peak-to-peak value of 70 V (Figure 4.48.A), while the one recorded in the presence of absorbing material had a peak-to-peak value of 17 V (Figure 4.48.B). The absorbing material was thus able to reduce the amplitude of the reflected signal, and this finding was consistent with the numerical results.

The configuration with absorbing material on the top and on the lateral walls

was chosen and used for all experiments from here onward. A subsequent test was performed to determine whether MBs could be detected by the PCD. The frequency content of the detected signal is particularly relevant to the acoustic response of MBs, as it defines their cavitation regime. For this reason, an FFT was performed on the signals recorded and the results are shown in Figure 4.49.

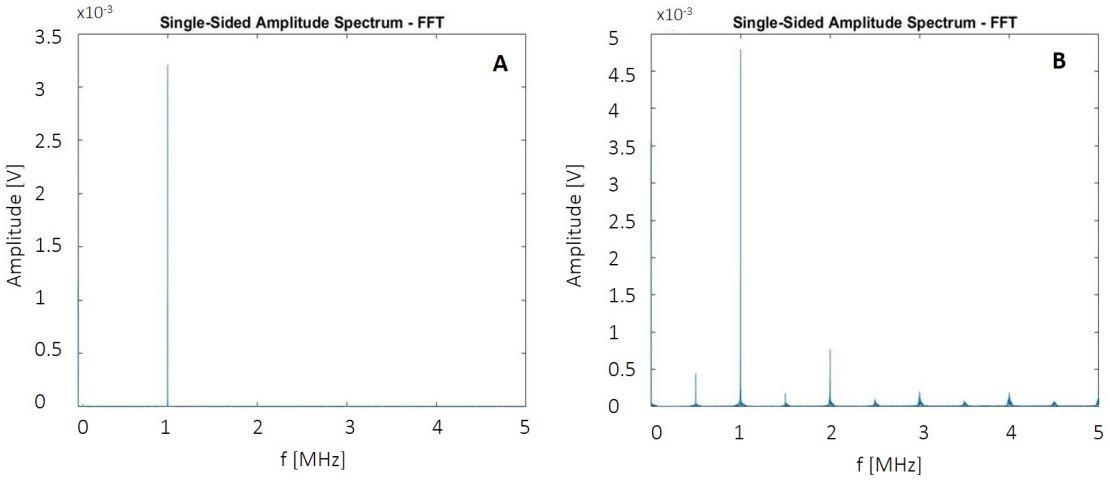

Figure 4.49: *FFT power spectrum of the signal recorded by the PCD in the absence (A) or presence (B) of microbubbles. A stimulation of 218 Vpp, PRF 1 Hz, duty cycle 1%, f 1 MHZ, peak-negative pressure 0.33 MPa was applied in both cases. When no MB was present at the target region, the frequency of the recorded signal only showed one peak at 1 MHz, which corresponded to the stimulation frequency. When MBs were added, the recorded signal presented harmonics, subharmonics and ultraharmonics.*

By comparing Figure 4.49.A and Figure 4.49.B, it is possible to notice that, when no MB was present at the target point, the frequency of the recorded signal only showed a peak at 1 MHz, which corresponded to the stimulation frequency. When MBs were added, the recorded signal presented harmonics, subharmonic and ultraharmonics, likely resulting from MB oscillations. It was hence demonstrated that the setup could detect the acoustic response of MBs.

4.2.2.3 Characterisation of the acoustic response of MBs in a bone fracture model

Upon validation of the experimental setup, subsequent experiments focused on the acoustic characterisation of microbubbles within the bone fracture model. This involves defining the relationship between the acoustic stimulation applied and the

acoustic response obtained from the MBs. These tests were performed by using two different transducers, which resulted in different frequencies and acoustic pressures at the target region.

1 MHz unfocused transducer

In these experiments, the 1 MHz unfocused transducer was used to apply an acoustic pressure at the target in the range 0.02-0.33 MPa. All experiments described were performed using all six geometries studied (gap: 3.5, 4.5 or 5.5 mm, thickness: 2 or 4 mm). However, only results obtained using a gap of 4.5 mm and thickness of 2 mm are reported, since there was no obvious difference in the characteristics of the experimental recorded signal between the different geometries tested.

Figure 4.50 shows the comparison between the FFT power spectra obtained in the absence (4.50.A) and presence of MBs (4.50.B), when no bone fracture model was added at the target point. MBs were suspended within a 2% agarose gel and positioned at the target point. In the absence of MBs, the acoustic response recorded was negligible. When MBs were present, their response could be detected, as indicated by the recorded signal having greater ultraharmonic intensity.

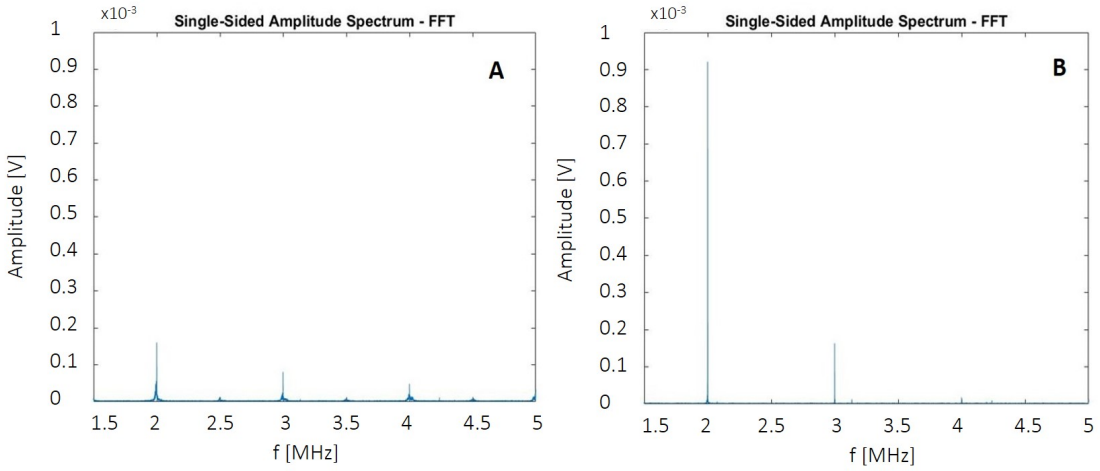

Figure 4.50: *FFT power spectrum of the signal recorded by the PCD in the absence of the bone fracture model (gap: 4.5 mm, thickness: 2 mm). A stimulation of 218 Vpp, PRF: 1 Hz, duty cycle: 1%, frequency: 1 MHZ, peak-negative pressure: 0.33 MPa was used. A) FFT of the signal recorded without MBs. B) FFT of the signal recorded when MBs were embedded in the 2% agarose gel. The presence of MBs was detectable by an increase in the amplitude of the FFT at harmonics.*

Figure 4.51 shows the comparison between FFTs of the PCD signals, obtained using the fracture gap model filled with 2% agarose gel (4.51.A) and filled with 2% agarose gel containing MBs (4.51.B). When only the bone was present, some harmonics appeared at the higher acoustic pressures tested, and this was probably due to vibrations of the Sawbones itself and reflections of the incident wave in between the walls of the bone fracture. When MBs were present, the intensity of the ultraharmonics was greater (i.e., the amplitude of the 2 MHz harmonic increased from approximately 0.3 mV to 0.5 mV), meaning that they were still detectable and likely undergoing volumetric oscillations.

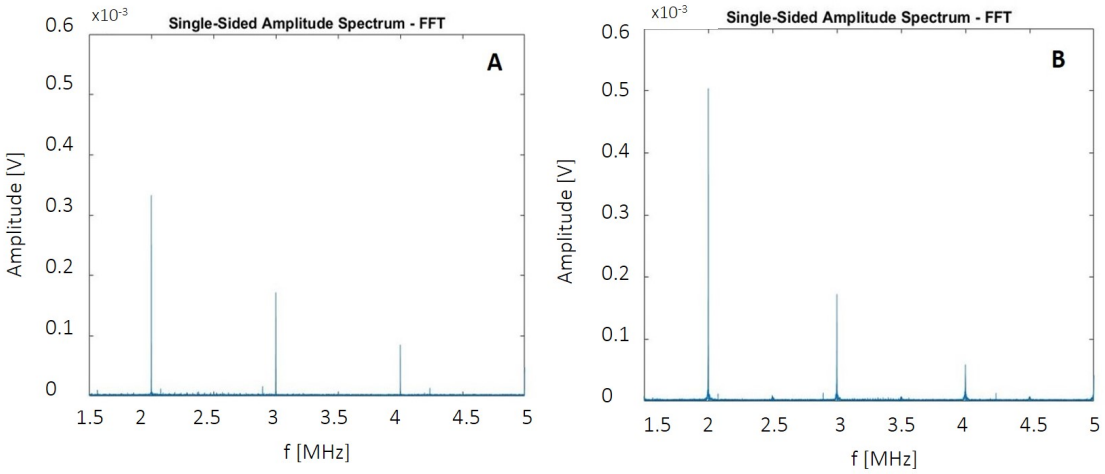

Figure 4.51: *FFT power spectrum of the signal recorded by the PCD in the presence of the bone fracture model (gap: 4.5 mm, thickness: 2mm). A stimulation of 218 Vpp, PRF: 1 Hz, duty cycle: 1%, frequency: 1 MHZ, peak-negative pressure: 0.33 MPa was used. A) FFT of the signal recorded when the PDMS manifold was filled with only 2% agarose gel and bone. B) FFT of the signal recorded when MBs were embedded in the 2% agarose gel and the bone was in place. The presence of MBs was detectable by an increase in the amplitude of the FFT at harmonics.*

The difference between the two cases in Figure 4.51 may not appear significant, but from the logarithmic FFT plot the effect of the presence of MBs in the setup appears evident. Figure 4.52 shows the logarithmic FFT of the recorded signal. It is possible to note that subharmonics and ultraharmonics were clearly present when MBs were added to the setup (4.52.B). When MBs were not present, the signal recorded only presented harmonics of the stimulation frequency (4.52.A) possibly due to reflections of the acoustic wave taking place in the tank.

The Welch method was applied to calculate the power spectral density of the signal,

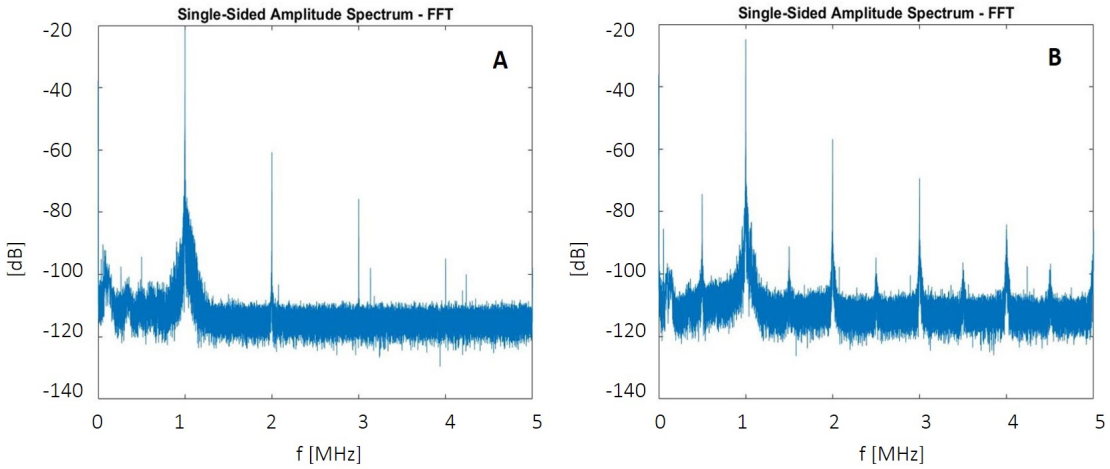

Figure 4.52: *Logarithmic FFT of the signal recorded by the PCD in the presence of the bone fracture model (gap: 4.5 mm, thickness: 2 mm). A stimulation of 218 Vpp, PRF: 1 Hz, duty cycle: 1%, frequency: 1 MHZ, peak-negative pressure: 0.33 MPa was used. A) FFT of the signal recorded when the mold was filled with only 2% agarose gel and bone. B) FFT of the signal recorded when MBs were embedded in the 2% agarose gel within the fracture gap, in the presence of Sawbones. MBs response to US is indicated in the presence of subharmonics and ultraharmonics.*

which was then integrated with respect to time to determine the energy associated with harmonics and ultraharmonics, as shown in Figure 4.53.

No statistical difference was found between the cases tested; however, when both MBs and Sawbones were present, the acoustic response registered at all acoustic pressures tested was the highest, and this may be due to the presence of pressure hotspots in the fracture gap, which resulted in more intense MB stimulation in these areas.

2 MHz unfocused transducer

The tests reported in the previous paragraph were repeated using the 2 MHz unfocused transducer. The aim was to assess whether greater acoustic pressures achieved by this transducer would elicit a more intense MB response at the fracture gap. In these experiments, agarose was added to the bone fracture gap model, either with or without MBs.

Consistently with the results obtained using the 1 MHz unfocused transducer, the logarithmic FFT of the recorded signal in the presence of Sawbones and MBs

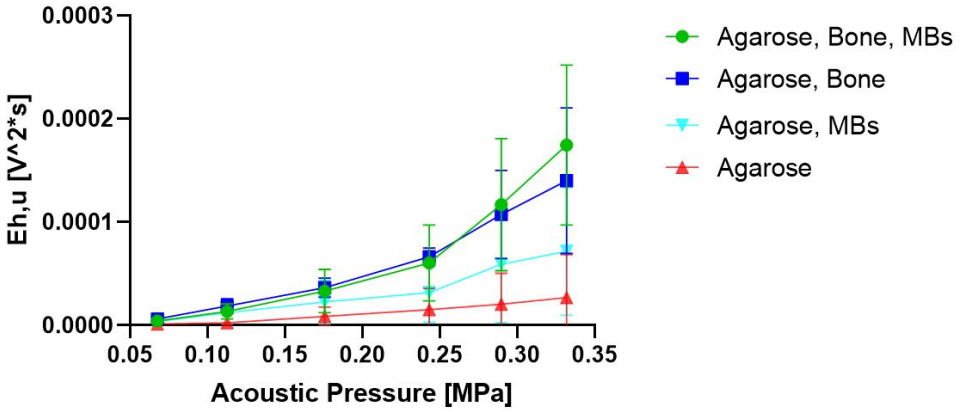

Figure 4.53: *Energy of harmonics and ultraharmonics of the recorded signal at the different acoustic pressures tested. Four cases are shown: model filled with 2% agarose, model filled with 2% agarose and Sawbones, model filled with 2% agarose and microbubbles, and model filled with 2% agarose, Sawbones and microbubbles. The latter case led to the highest energy content of the signal.*

contained sub- and ultra-harmonics that were not present in the absence of MBs. In the latter case, only harmonics were present, possibly resulting from the reflection of the sound wave in the tank due to the presence of the fracture gap. Figure 4.54 shows the two above mentioned cases.

Figure 4.55 shows the sum of the energies of harmonics and ultraharmonics, both in the presence and absence of MBs in the fracture gap, and determined over an acoustic pressure range of 0.09-0.7 MPa.

The signal recorded in the presence of MBs contained a higher energy than the case when no MBs were added. The greater the acoustic pressure, the larger was the difference in energy between the two cases investigated; the energy appeared to increase only marginally in the absence of MBs, while it increased more significantly (and non-linearly) in the presence of MBs.

4.2.2.4 Characterisation of the acoustic response of NDs in a bone fracture model

All the experiments reported earlier for microbubbles were repeated using PFP nanodroplets, with the aim of identifying acoustic stimulation conditions that would induce NDs to vaporise. NDs were mixed with low-melting point agarose in these experiments, and the hydrogel was placed within the fracture gap.

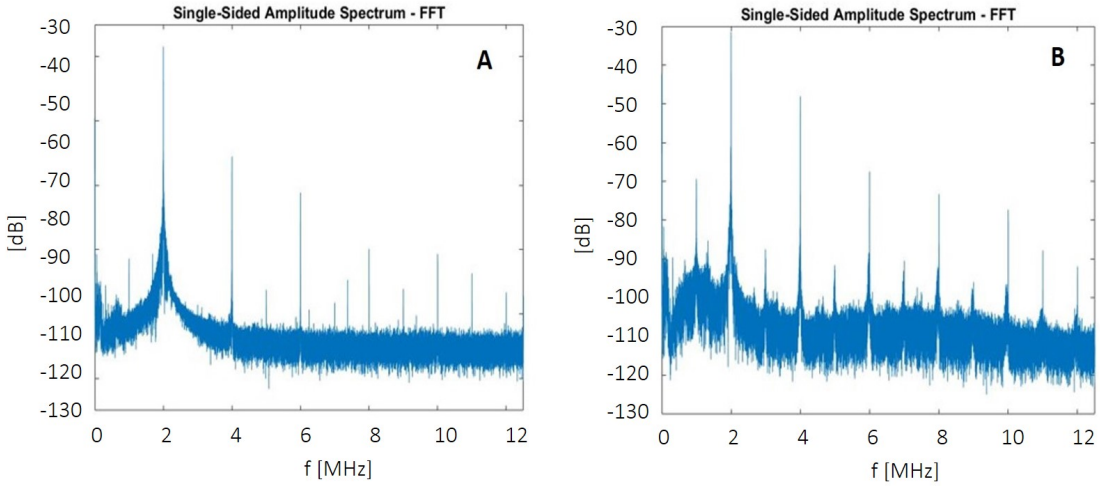

Figure 4.54: *Logarithmic FFT of the signal recorded by the PCD in the presence of the bone fracture model (gap: 4.5 mm, thickness: 2 mm). A stimulation of 150 Vpp, PRF: 1 Hz, duty cycle: 1%, frequency: 2 MHZ, peak-negative pressure: 0.7 MPa was used. A) FFT of the signal recorded when the Sawbones model was filled with only 2% agarose gel. B) FFT of the signal recorded when MBs were embedded in the 2% agarose gel and the Sawbones were in place. The presence of MBs could be identified by the presence of subharmonics and ultraharmonics in the signal.*

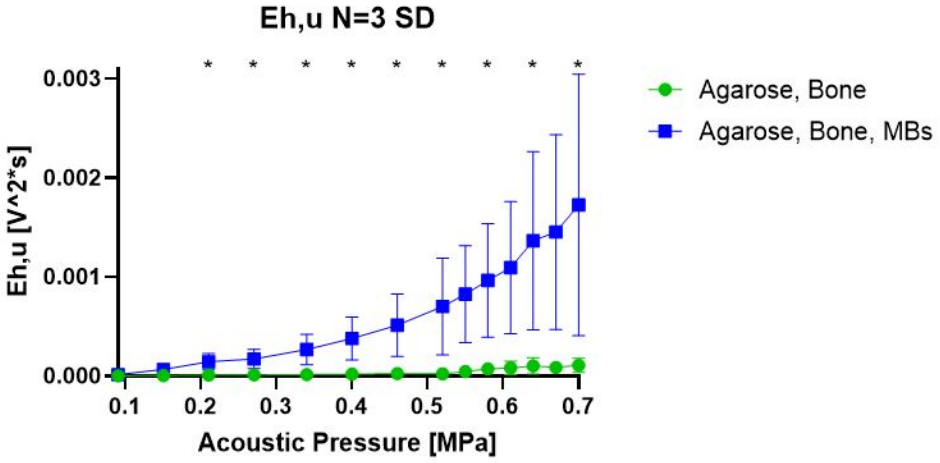

Figure 4.55: *Sum of the energy of harmonics and ultraharmonics of the recorded signal at different acoustic pressures investigated, for a fracture gap of 4.5 mm and a thickness of 2 mm. Statistical difference between the two groups was found for acoustic pressures greater than 0.2 MPa (*$p < 0.05$).*

1 MHz unfocused transducer

When the 1 MHz unfocused transducer was used, the additon of NDs did not cause any change in the recorded signal. The acoustic pressure reached at the target point (maximum of 0.33 MPa) was thus not high enough to induce phase transition of NDs.

Figure 4.56 shows the FFT power spectrum in the absence (4.56.A) and presence (4.56.B) of nanodroplets. There was no significant difference between the two cases. The signal intensity in the presence of NDs was slightly lower, potentially due to differences in the way in which the incident US wave was scattered at the fracture gap.

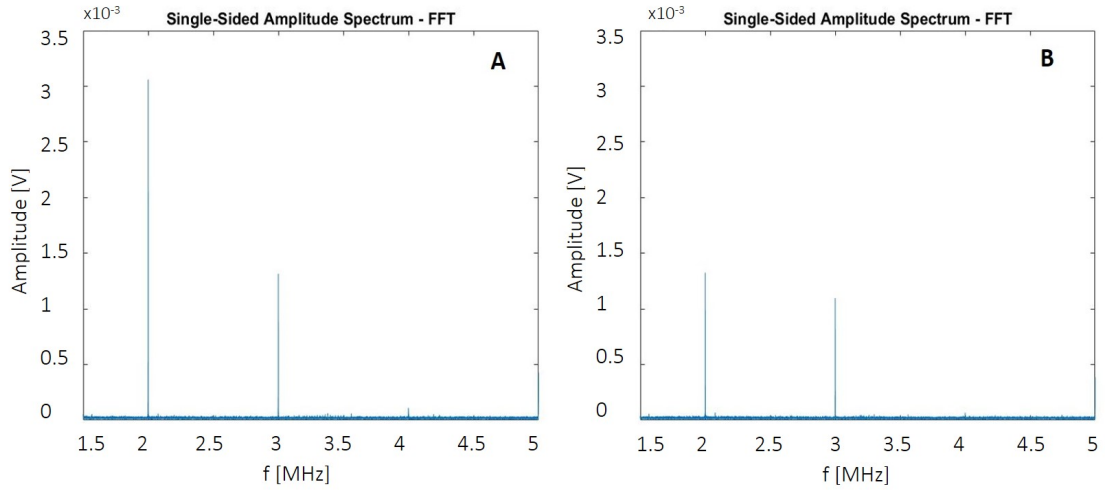

Figure 4.56: *FFT power spectrum of the signal recorded by the PCD in the presence of a bone fracture model (gap: 4.5 mm, thickness: 2 mm). A stimulation of 218 Vpp, PRF: 1 Hz, duty cycle: 1%, frequency: 1 MHZ, peak-negative pressure: 0.33 MPa was used. A) FFT of the signal recorded when the mold was filled with only 2% agarose gel. B) FFT of the signal recorded when NDs were embedded in the 2% agarose gel.*

Figure 4.57 shows the logarithmic FFT in the absence (4.57.A) or presence (4.57.B) of nanodroplets. The two graphs show comparable characteristics.

Further experiments using greater acoustic pressures were thus carried out in order to assess whether ND vaporisation could be achieved with increasing the intensity of stimulation.

2 MHz unfocused transducer

Figure 4.58 shows the FFT power spectrum in the absence (4.58.A) and presence (4.58.B) of nanodroplets. Similarly to the results obtained using the 1 MHz unfocused

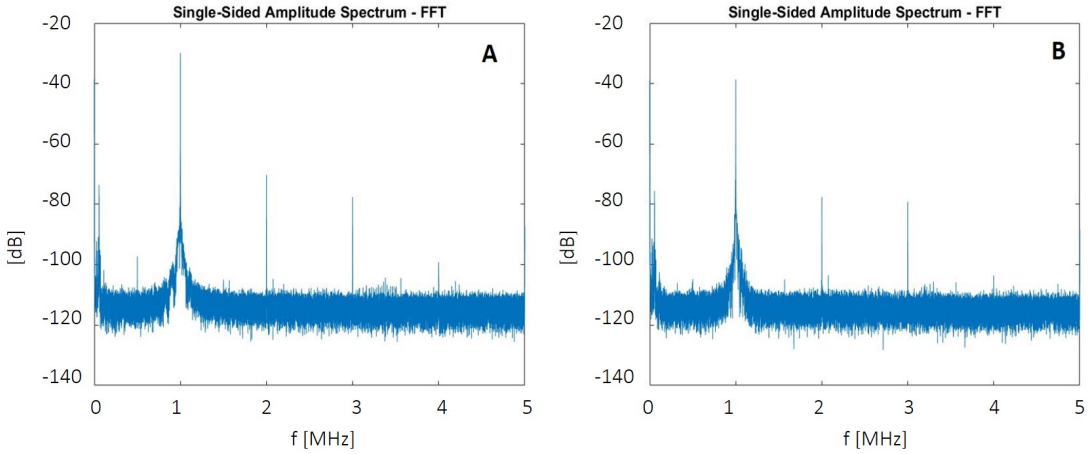

Figure 4.57: *Logarithmic FFT of the signal recorded by the PCD in the presence of the bone fracture model (gap: 4.5 mm, thickness: 2 mm). A stimulation of 218 Vpp, PRF: 1 Hz, duty cycle: 1%, frequency: 1 MHZ, peak-negative pressure: 0.33 MPa was used. A) FFT of the signal recorded when the Sawbones model was filled with only 2% agarose gel. B) FFT of the signal recorded when NDs were embedded in the 2% agarose gel and the Sawbones was in place. There was no obvious difference between the two cases.*

transducer, there was no difference between the two cases investigated. The peaks in Figure 4.58.B are lower that the ones in Figure 4.58.A, potentially due to different patterns of reflection of the acoustic wave associated with the presence of Sawbones.

Figure 4.59 shows the logarithmic FFT in the absence (4.59.A) and presence (4.59.B) of nanodroplets. The graphs show peaks at 1 MHz, which was the frequency of the stimulation wave, and some weak peaks at the first harmonic. The two graphs (Figures 4.59.A and 4.59.B) are overall comparable, suggesting that the acoustic pressure reached at the target point (maximum of 0.7 MPa) was not high enough to cause ND phase transition.

Given the results obtained in this series of experiments, further tests using greater acoustic pressures were thus performed in order to investigate whether increasing the intensity of stimulation further would induce ND vaporisation.

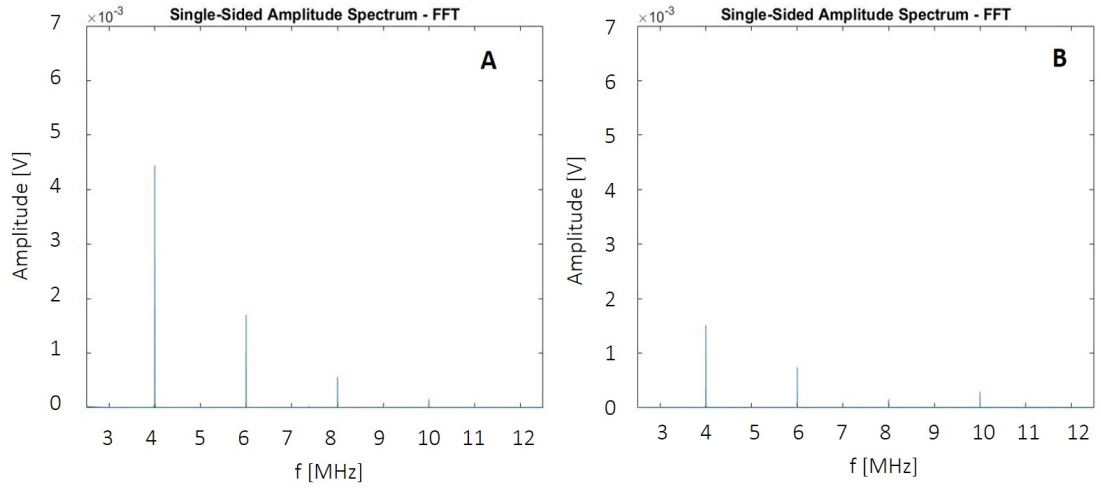

Figure 4.58: *FFT power spectrum of the signal recorded by the PCD in the presence of the bone fracture model (gap: 4.5 mm, thickness: 2 mm). A stimulation of 150 Vpp, PRF: 1 Hz, duty cycle: 1%, frequency: 2 MHZ, peak-negative pressure: 0.7 MPa was used. A) FFT of the signal recorded when the fracture gap was filled with only 2% agarose gel. B) FFT of the signal recorded when NDs were embedded in the 2% agarose gel.*

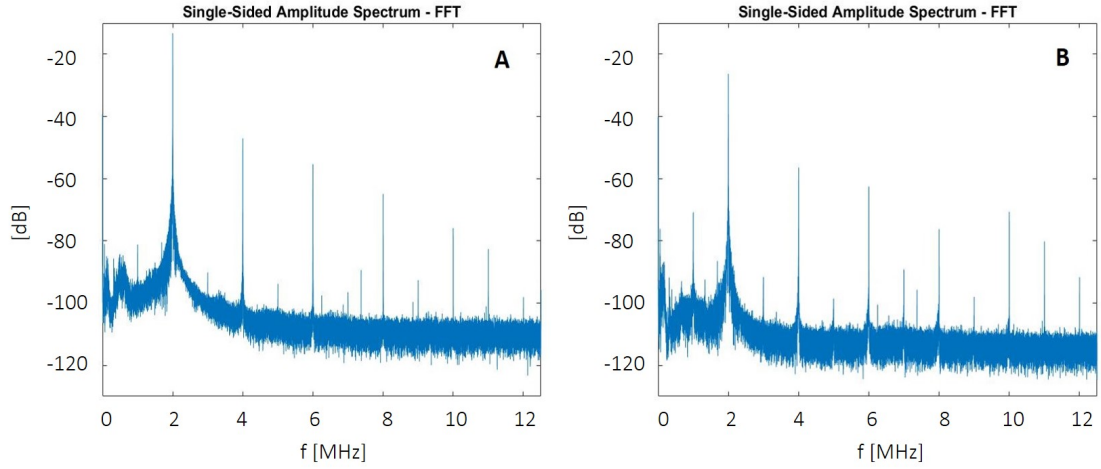

Figure 4.59: *Logarithmic FFT of the signal recorded by the PCD in the presence of the bone fracture model (gap: 4.5 mm, thickness: 2 mm). A stimulation of 150 Vpp, PRF: 1 Hz, duty cycle: 1%, frequency: 2 MHZ, peak-negative pressure: 0.7 MPa was applied. A) FFT of the signal recorded when the fracture gap was filled with only 2% agarose gel. B) FFT of the signal recorded when NDs were embedded in the 2% agarose gel and the Sawbones was in place. There is no obvious difference between the two cases.*

1 MHz focused transducer

When NDs were stimulated using the 1 MHz focused transducer, the recorded signal presented different characteristics when compared to the case in which NDs were not present. For this experiment, PFB NDs were tested too, in addition to PFP NDs. The rationale behind this experimental choice lies on the lower phase transition temperature for PFB NDs, which were thus expected to vaporise at lower acoustic pressures compared to PFP NDs. The mean FFT over 30 seconds of the recorded signal in the presence of NDs is shown in Figure 4.60.B. By comparing this with the plot in Figure 4.60.A (corresponding to a control experiment in which NDs were not present) it is possible to notice that NDs induced the appearance of harmonics, ultraharmonics, and broadband noise. These features were visible at the two highest acoustic pressures tested, namely 0.84 MPa and 0.94 MPa.

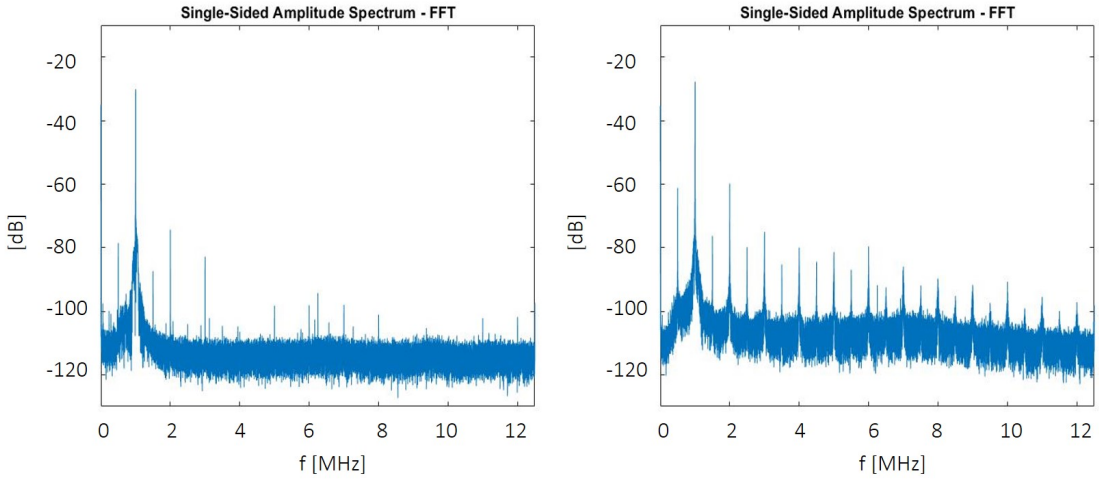

Figure 4.60: *Logarithmic FFT of the signal recorded by the PCD in the presence of the bone fracture model (gap: 4.5 mm, thickness: 2 mm). A stimulation of 55 Vpp, PRF: 1 Hz, duty cycle: 5%, frequency: 1 MHZ, peak-negative pressure: 0.84 MPa was applied. Graphs represent the mean behaviour over a 30 seconds stimulation. A) FFT of the signal recorded when the model was filled with 2% LMP agarose gel and bone. B) FFT of the signal recorded when NDs were embedded in the 2% LMP agarose gel and the Sawbones were in place. Harmonics, ultraharmonics and broadband noise are visible when NDs were present.*

The Welch method was applied to calculate the power spectral density of the recorded signal over the 30 seconds of stimulation, and the results are shown in Figure 4.61.A for the case without NDs and in Figure 4.61.B for the case with NDs. PFP NDs led to greater power spectral density at harmonics and ultraharmonics during

the whole stimulation. Values at harmonics and ultraharmonics are the highest (-115 dB re V^2/Hz for the case with NDs vs -140 dB re V^2/Hz for the case without NDs), but broadband noise is also present.

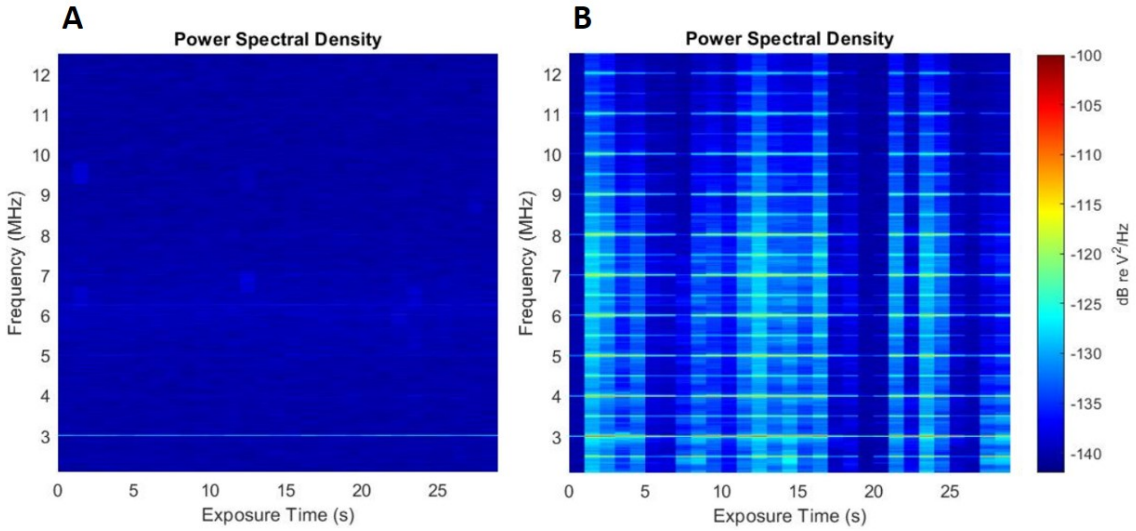

Figure 4.61: *Power spectral density over a 30 seconds stimulation in the presence of the bone fracture model (gap: 4.5 mm, thickness: 2 mm). A stimulation of 55 Vpp, PRF: 1 Hz, duty cycle: 5%, frequency: 1 MHZ, peak-negative pressure 0.84 MPa was applied. A) NDs were not present in the fracture gap. B) PFP NDs were embedded in the 2% LMP agarose gel and the Sawbones was in place. Harmonics, ultraharmonics and broadband noise are visible in the case with NDs.*

The power spectral density was integrated with respect to time (over 30 s) for each case tested and at each acoustic pressure used; results are shown in Figure 4.62.A. Power spectral density values for harmonics, ultraharmonics and broadband signal were determined and integrated with respect to time, and results are shown in Figures 4.62.B,C,D.

In the graphs, the red line corresponds to the case where the fracture model contained agarose gel only. The energy associated with this signal was always the lowest, meaning that the acoustic response was very low and could be associated to reflections of the stimulating acoustic wave or vibrations of the Sawbones structures. The harmonic energy and ultraharmonic energy graphs (Figures 4.62.B,C) suggest that PFB NDs have a greater energy content at these frequencies than PFP NDs. This behaviour does not hold for the total and broadband energies (Figures 4.62.A,D), as it appears that PFP NDs are associated with a greater energy level than the case

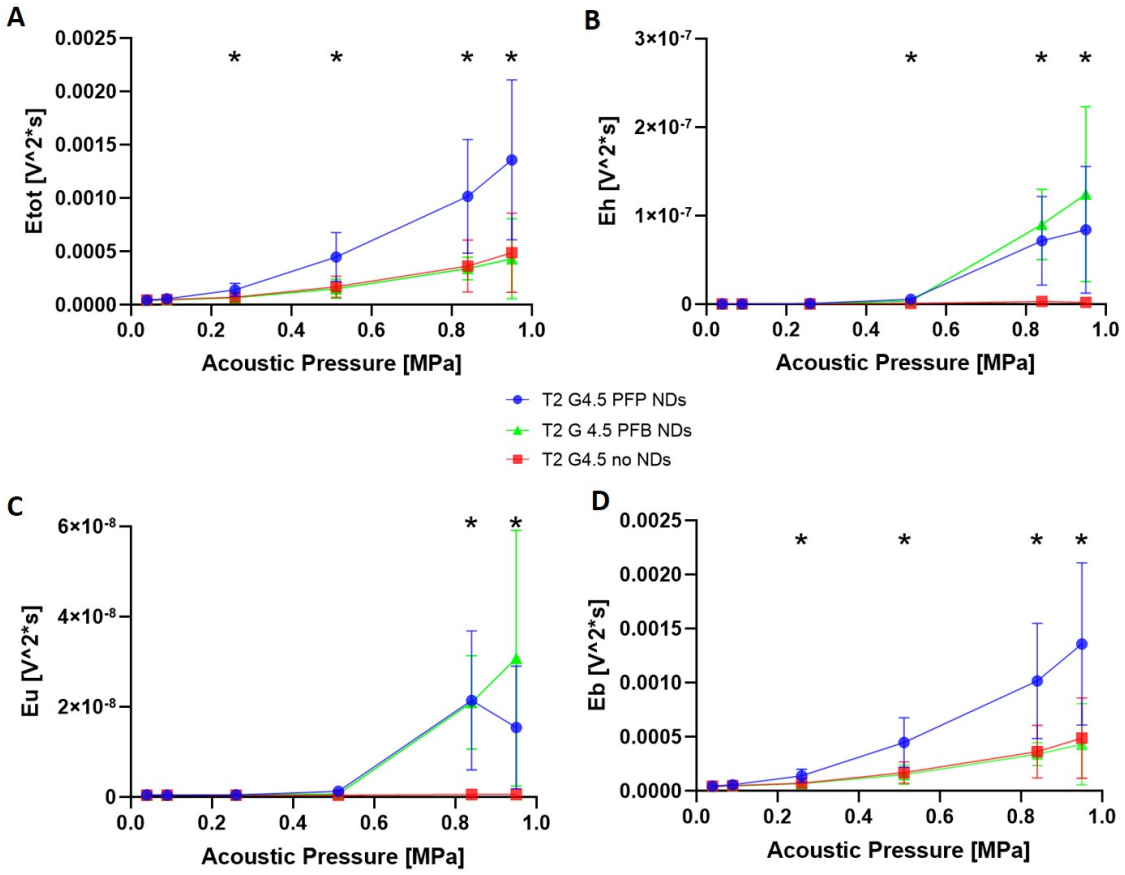

Figure 4.62: *Energy of the recorded signals, corresponding to the cases with a bone fracture model filled with LMP agarose gel (red line), PFP NDs embedded in LMP agarose gel (green line), and PFB NDs embedded in the LMP agarose gel (red line). The energy was obtained by integration of the power spectral density with respect to time. A) Total energy of the recorded signal. B) Harmonic energy. C) Ultraharmonic energy. D) Broadband energy. Stars in the graphs indicate statistical difference (*$p < 0.05$) between red and blue lines.*

without NDs, while the energy level of PFB NDs is comparable to the case without NDs. Such observation can be explained by looking at the power spectral density of PFB NDs over 30 s, stimulated with an acoustic pressure of 0.84 MPa in Figure 4.63 and by comparing it with the PFP NDs power spectral density in Figure 4.61.B.

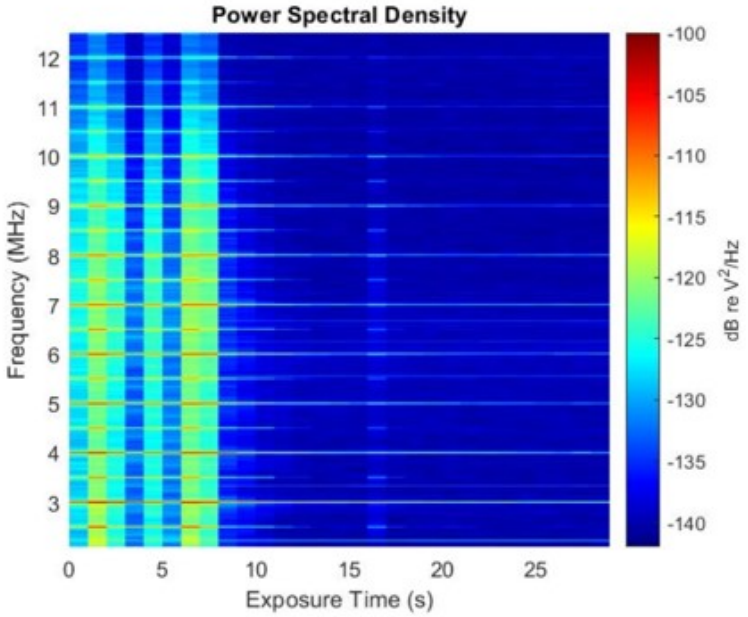

Figure 4.63: *Power spectral density over a 30 second stimulation in the presence of the bone fracture model (gap: 4.5 mm, thickness: 2 mm) with PFB NDs embedded in a LMP agarose gel. A stimulation of 55 Vpp, PRF: 1 Hz, duty cycle: 5%, frequency: 1 MHZ, peak-negative pressure: 0.84 MPa was applied.*

While PFP NDs emitted an acoustic signal during almost the whole duration of stimulation, PFB NDs mostly responded during the first ten seconds of stimulation, after which only harmonic components were present. The early acoustic response of PFB NDs is more intense than the one of PFP NDs (with values of approximately -105/-100 dB re V^2/Hz for harmonics in the PFB response vs values of approximately -115/-110 dB re V^2/Hz for harmonics in the PFP response); however, if energy content is integrated over the total stimulation time, the resulting value is lower. This different behaviour is a result of the different phase transition temperatures of PFP and PFB. Having a lower boiling point, PFB vaporises more easily and in a more intense way than PFP.

4.2.2.5 Ultra-High Speed Imaging of ND vaporisation in a tissue mimicking phantom

The vaporisation of NDs in a bone fracture model was assessed optically following the protocol presented in Paragraph 4.1.3.5 on page 199.

Before applying any US stimulation, it was possible to detect some microbubbles embedded in the 2% agarose gel. This may be due to the mixing step in which NDs are embedded in the gel. Notably, liquid agarose was produced by heating up to 80°C, which may have caused vaporisation of some NDs prior to stimulation.

After applying the US stimulation (2000-cycle FUS excitation pulses with 5% duty cycle and an acoustic pressure of 1.8 MPa peak negative), some channels appeared within the 2% agarose gel, as shown in Figure 4.64. It is thought that these channels were the result of the oscillation and translation of the embedded microbubbles, which applied mechanical stress on the gel and 'damaged' its structure. Once created, these channels were the preferable sites of accumulation of MBs formed by vaporisation since they offered a low mechanical resistance.

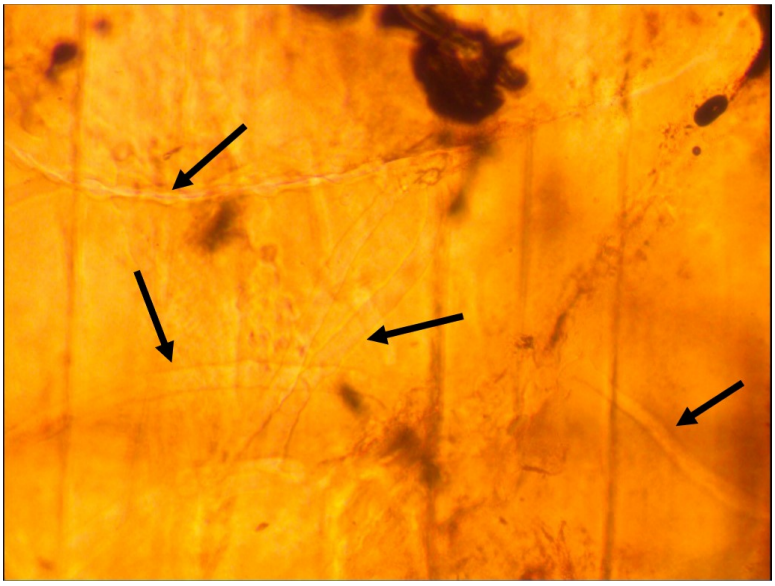

Figure 4.64: *2% agarose gel with MBs and NDs embedded after US stimulation. Some channels were present in the structure, highlighted by the black arrows, which may have been created by the oscillation and translation of MBs.*

Figure 4.65 shows six of the frames taken by the ultra-high speed camera at different time points while the US stimulation was being applied. Figure 4.65.A shows

an area of the agarose gel prior to any US stimulation. It is possible to observe the presence of some MBs, due to the premature vaporisation issue previously discussed. Figures 4.65.B-F show the appearance and and disappearance of MBs in the left bottom corner (yellow frame in the pictures), as a result of ND vaporisation induced by ultrasound stimulation.

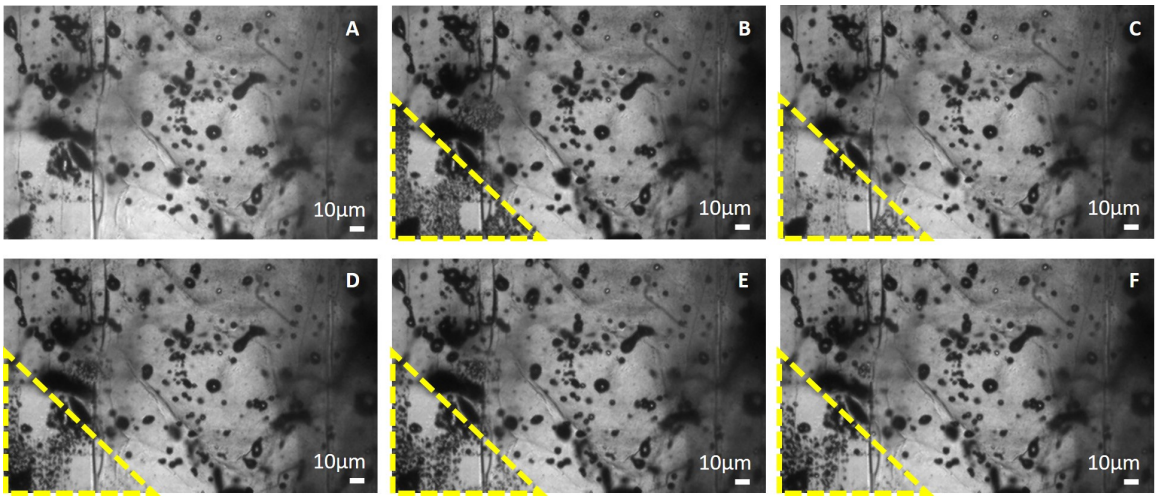

Figure 4.65: *Phase transition from NDs to MBs induced by US stimulation in the 2% agarose gel. A) Area of the gel prior to any US stimulation. B-F) Appearance and disappearance of MBs as a result of the US stimulation applied. The yellow frames in B-F show the area where MBs appear and disappear.*

To better visualise the phase transition, images were processed in ImageJ; briefly, the first frame was subtracted from all the others to show more clearly only the MBs obtained from the phase transition process. Figure 4.66 shows the result of this processing step. MBs appearing as a result of ND vaporisation are smaller than 4 µm, which is a good indicator of potential safety.

A total of three videos with the ultra-high speed camera were taken during these experiments, and Figures 4.67 and 4.68 show evidence of ND vaporisation achieved in the other two experiments performed.

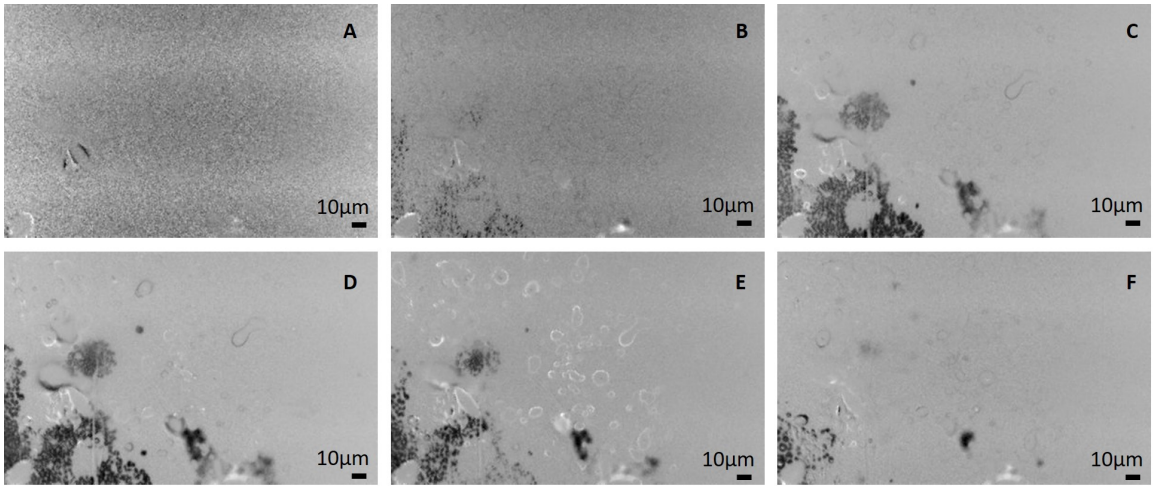

Figure 4.66: *Phase transition from NDs to MBs obtained from US stimulation in the 2% agarose gel. The images were processed with ImageJ, and the first frame was subtracted from all the others to highlight only the MBs appearing as a result of phase transition. A) Area of the gel prior to any US stimulation. B-F) Appearance and disappearance of MBs as a result of the US stimulation applied.*

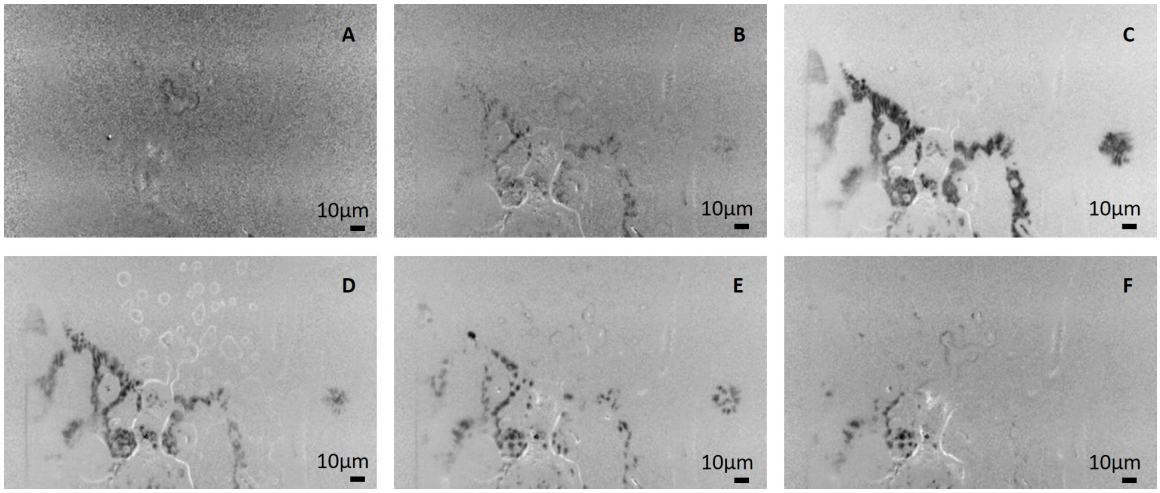

Figure 4.67: *Phase transition from NDs to MBs obtained from US stimulation in the 2% agarose gel. The images were processed with ImageJ, and the first frame was subtracted from all the others to clearly show only the MBs appearing as a result of phase transition. A) Area of the gel prior to any US stimulation. B-F) Appearance and disappearance of MBs as a result of the US stimulation applied.*

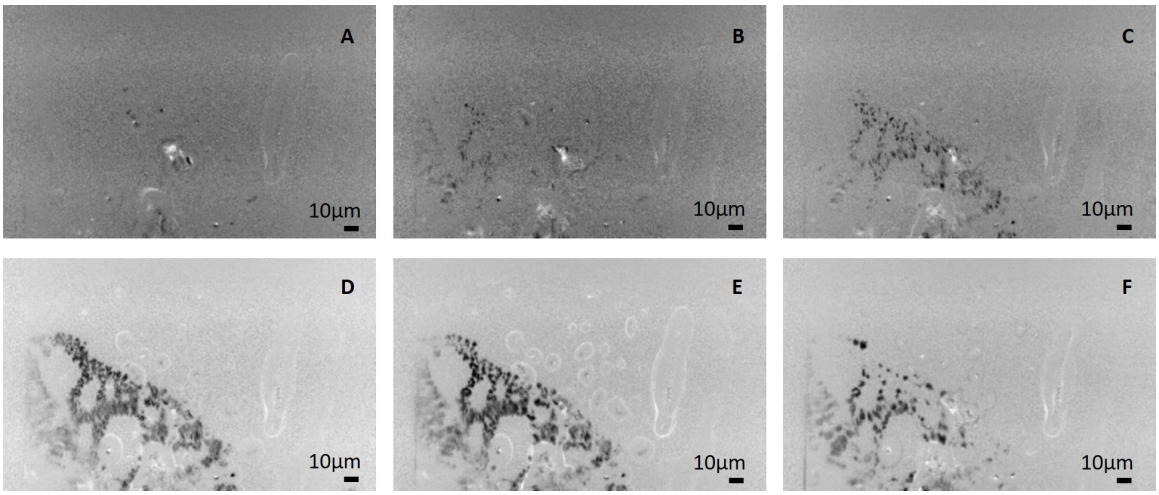

Figure 4.68: *Phase transition from NDs to MBs obtained from US stimulation in the 2% agarose gel. The images were processed with ImageJ and the first frame was subtracted from all the others to clearly show only the MBs appearing as a result of phase transition. A) Area of the gel prior to any US stimulation. B-F) Appearance and disappearance of MBs as a result of the US stimulation applied.*

ImageJ was also used to carry out a quantitative characterisation of the vaporisation process. For this purpose, the percentage area of each frame occupied by MBs was determined. Figure 4.69 shows that the percentage area occupied by MBs varied with respect to time in all three experiments performed. Graphs show two peaks, which corresponds to the two instants when the US stimulation was being applied. In every graph, the two peaks are comparable, both in shape and in height, suggesting that there was not a marked difference between the MBs appearing during the first cycle and the ones during the second cycle. Such behaviour could suggest that MBs developing during the first cycle recondensed to liquid NDs once the US stimulation terminated. These NDs, then, underwent a potential second vaporisation process and formed MBs again.

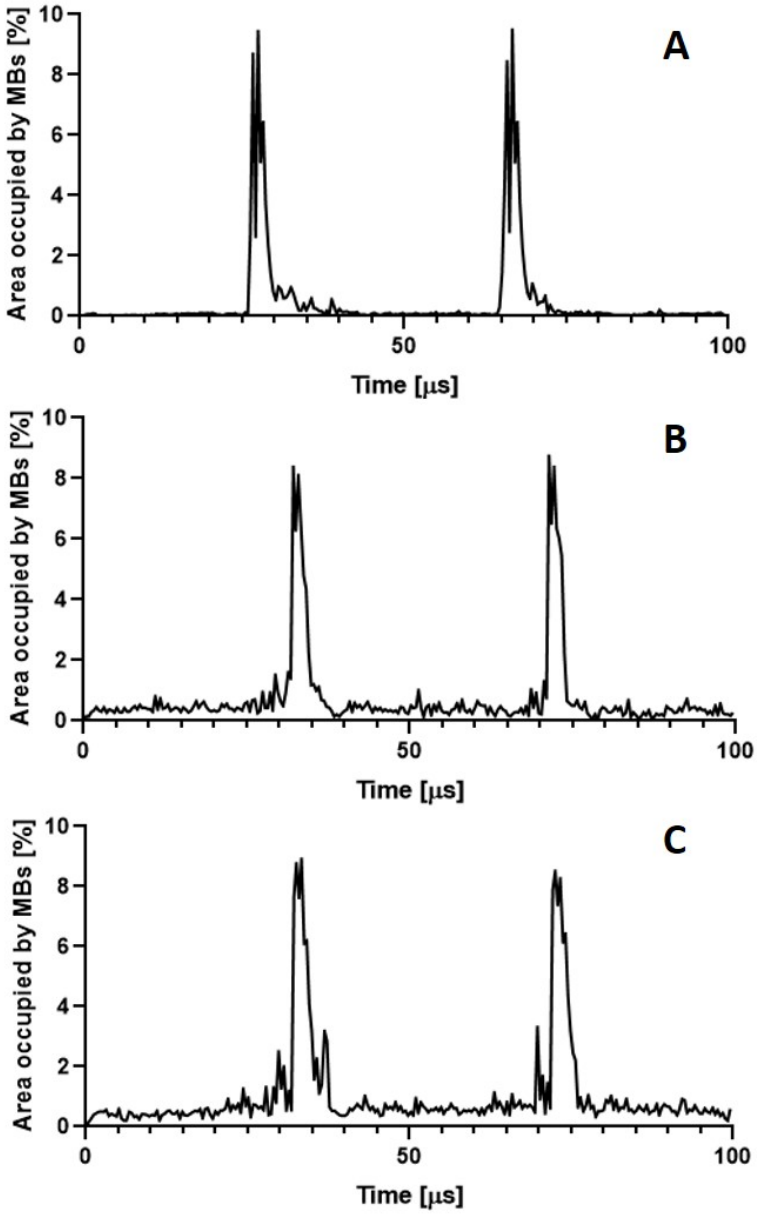

Figure 4.69: *Percentage area occupied by MBs with respect to time, in the three experiments performed. The two peaks in each graph correspond to the instants when US was applied. Peaks are comparable in height (around 9%) suggesting that: i) there was not a marked difference between the MBs appearing during the first cycle and the ones during the second cycle, and ii) ND vaporisation was comparable in the three different experiments.*

4.3 Discussion

This project aims to investigate ultrasound stimulation of MBs and NDs at the site of a bone fracture, in order to control the release of osteogenic or other bioactive compounds. To achieve this, it is of fundamental importance to understand how MBs and NDs respond to different US stimulation settings and how their behaviour may change in the presence of fractures with different, clinically-relevant geometries. MBs have been extensively studied for both diagnostic and therapeutic applications over the last 40 years [93], while the use of NDs for therapy has gained significant interest only over the last two decades [82]. Both agents are being studied for a range of different applications, but little is known about their use for bone fracture repair. US has been studied in conjunction with bones for two main purposes: LIPUS and the axial transmission technique. LIPUS is a treatment based on the evidence that ultrasound waves can generate micromechanical stresses within the fracture, thus stimulating and accelerating healing; however its efficacy is deemed controversial [19] [22]. The axial transmission technique is a method which evaluates propagation of US waves along the cortical shell of long bones to obtain information about the bone healing process of fractures. Recent studies by Gheduzzi et al. [185], Catelani et al. [186], Bossy et al [37] [38], Protopappas et al. [39] and Dodd et al. [137] analyse the axial transmission technique, but no study combines US, US-responsive agents and bone fractures. The acoustic field in the fracture gap and its interaction with potential US-responsive agents is not taken into account in neither of the aforementioned techniques, as their primary focus is on either the effect of US on bone healing or on US transmission along the bone axial direction.

To address the knowledge gap, a setup was built to allow the acoustic stimulation of a sample of MBs or NDs placed in a bone fracture model, and it consisted of a microscope-compatible water tank accommodating a transducer to stimulate the sample and a PCD to record its acoustic response. At first, the acoustic field developed within the tank at varying conditions (i.e. in the presence or absence of bone fractures with different geometries) were numerically simulated. Then, the tank was experimentally validated and the acoustic behaviour of MBs and NDs studied.

4.3.1 Numerical simulations

Numerical simulations were performed to assess the effects that adding acoustic absorbing material would have on the acoustic field developed within the tank. Results are presented in Paragraph 4.2.1.1 on page 201 and they show that the absorbing material had an impact on the acoustic field in the tank, both when the unfocused and focused transducers were used. When the absorbing material was placed only on the lid of the tank, then the absolute acoustic pressure in the fluid was affected by numerous reflections between the incident wave and the walls of the tank, as shown in Figure 4.13.A (page 202), for the unfocused transducers, and Figure 4.17.A (page 205), for the focused transducer. Since these reflected wave components could affect the wave recorded by the receiving transducer (i.e., the PCD), this design solution was rejected. Alternatively, when the absorbing material was placed on the top and on the lateral walls of the tank, the absolute acoustic pressure developed in the fluid was less affected by reflections, as shown in Figure 4.13.B (page 202), for the unfocused transducers, and in Figure 4.17.B (page 205), for the focused transducer. Since there was no major difference in the normalised absolute acoustic pressure at the target point (as shown by Figures 4.15 on page 203 and 4.19 on page 207, for the unfocused and focused transducer respectively) between this case and the one where the absorbing material was also added to the bottom of the tank (Figures 4.13.C - page 202 - for the unfocused transducers and Figure 4.17.C - page 205 - for the focused one) the configuration chosen for all subsequent tests was the one having absorbing layers placed on the top and on the lateral walls of the tank. It is also interesting to note the difference in stimulation conditions between the focused and unfocused transducers. Using a focused transducer allowed achieving an acoustic pressure at the target region which was 8 times the acoustic pressure applied in nearby regions, while the acoustic pressure generated at the target region by the unfocused transducers was only 5 times the one in nearby regions. However, the stimulated area at the target was smaller for the focused transducer than the unfocused ones, which did not represent an issue for this specific project as this area was still large enough to stimulate the fracture gaps investigated. Notably, the area at the target site where the absolute acoustic pressure was at least 50% of the maximum value was 2.5 cm^2 when using the unfocused transducer, as shown in Figure 4.14 (page 203), while it was 0.5 cm^2 when using the focused transducer, as shown in Figure 4.18 (page 206).

The influence of the presence of a bone fracture model on the acoustic field is presented in Paragraph 4.2.1.2 on page 208. Different fracture geometries were investigated, with the gap size ranging from 3.5 to 5.5 mm and the thickness ranging from 2 to 4 mm; the case of a complete fracture was also investigated. The gap width and thickness values are in line with fracture size used in other studies [188] [193] [137]. Both unfocused and focused transducers were modelled in these simulations.

When the fracture was inclined with respect to the incident US wave, as shown in Figure 4.22 (page 209) for the unfocused transducers and in Figure 4.31 (page 217) for the focused transducer, the fracture hid part of the fracture gap area from the incoming acoustic wave; this resulted in a significantly lower acoustic pressure in this region. The spatial distribution of the acoustic pressure was probably dictated by the interaction between reflections of the incident wave among the walls of the fracture gap. These interactions gave rise to standing waves and resulted in hotspots where the acoustic pressure was greater than in the surrounding regions. When a complete fracture was simulated, as shown in the last line of Figure 4.22 and Figure 4.31, the distribution of the absolute acoustic pressure changed. The incident wave interacted only with the reflected wave coming from the lateral walls of the fracture, while there was no reflection originating from the bottom surface of the model. This resulted in elongated nodal and antinodal regions, as opposed to the rounded ones previously observed.

A different inclination of the fracture was also modelled, and the results are shown in Figure 4.25 (page 212) for the unfocused transducers and in Figure 4.36 (page 220) for the focused one. In this case, the fracture was aligned with the direction of the incident acoustic wave, thus there were no areas of the gap hidden from the incident US wave. The acoustic pressure field in the fracture gap was thus more homogeneously distributed than the cases presented before. Despite there were still spatial variations in acoustic pressure, there was no area of the gap which was not stimulated. When a complete fracture was tested, the absence of reflections at the bottom of the tank resulted in an even more homogeneous acoustic field.

Overall, the parameter that more significantly affected the acoustic field was the inclination of the fracture with respect to the incident US wave. Changes in the acoustic pressure field resulting from different fracture architectures may thus cause microbubbles and nanodroplets to respond differently. If higher acoustic pressures are applied in certain areas of the fracture gap, MBs in those regions could undergo

oscillations of greater amplitude or potentially cavitate inertially. Similarly, NDs may vaporise only within regions of greater acoustic pressure in the fracture gap. A potential implication of the presence of spatial gradients in the acoustic pressure field is that MBs could be driven by acoustic radiation forces towards pressure nodes or antinodes of the standing wave field (similarly to what has been observed by Shi et al. [194]) within the fracture gap, resulting in MB clustering and uneven localisation of their therapeutic effects. To overcome this issue, multi element devices could be used instead of single element transducers to allow the acoustic stimulation to be more uniform at the target point.

Overall, the simulations also showed that it is possible to create a compact and microscope-compatible setup that allows achieving controlled acoustic stimulation at a target region, the properties of which can be tailored by changing the stimulating transducer used. Large water tanks are typically used for similar acoustic stimulation studies; these setups are bulky, need to be primed with large volumes of degassed water, are not easily transportable, and it is complex to couple them with optical microscopes for real-time imaging. For instance, Mannaris et al. [183] used a large tank filled with deionised water to compare the ability of MBs, polymer coated droplets and polymeric cups to achieve mass transport and extravasation of a co-administered, unencapsulated large macromolecular therapeutic agent into tumour-mimicking phantoms over a range of acoustic conditions. Moreover, Song et al. [184] used a large water tank to perform *in vitro* US characterisation of PFC NDs. In these more common water tank apparatuses, the lateral walls are sufficiently distant that they do not impact on the acoustic field developed at the target site; however, the simulations in this study demonstrate that a similar outcome can be achieved by adding absorbing material on the inner walls of a more compact tank. For these reasons, the proposed tank design potentially represents a useful addition to the research field, particularly for investigations requiring coupling of ultrasound stimulation with other analytical or detection systems. It should however be noted that simulations have been carried out over a 2D model of the tank. The development of a 3D model would have required significantly greater computation time and resources. It was instead decided that a 2D model of the ultrasound field was sufficient for the aim of this study, and also considering the primary direction of US propagation. This approach is normally employed to simulate sound fields in rectangular enclosed spaces. As Li et al. [195] highlighted, being able to predict the sound field in a real tank reasonably and effectively, mainly depends on the boundary

conditions set, rather than the use of a complete 3D model instead of a 2D model.

4.3.2 *In vitro* tests

4.3.3 Acoustic calibration and validation of the setup

Before performing the acoustic characterisation of microbubbles and nanodroplets, the tank apparatus was calibrated and validated experimentally. Calibration consisted in finding the relationship between the voltage applied to the transducers used and the acoustic pressure developed at the target region, while the validation consisted in assessing that microbubbles and their acoustic response (i.e., cavitation) could be detected in the setup.

Results shown in Paragraph 4.2.2.1 on page 222 demonstrate that both the unfocused transducers (2 MHz and 1 MHz) tested were able to uniformly stimulate an area large enough to cover the different fracture gaps tested. Moreover, the addition of the microscope-compatible tank designed for these experiments, did not affect the acoustic pressure field at the target.

The acoustic pressure needed in this project is anticipated to be in the range 0-1.5 MPa, to ensure that both different cavitation regimes of microbubbles and vaporisation of nanodroplets could be investigated. In the case of microbubbles, it's important to be able to distinguish between stable and inertial cavitation (the latter typically occurring at acoustic pressures greater than 300 kPa) and collapse (usually occurring at approximately 1 MPa) [45] [51]. Obtaining different MB cavitation regimes could lead to different types and magnitude of mechanical stimulation of the surrounding environment, and this could potentially affect the treatment efficacy. On the other hand, in the case of perfluorocarbon nanodroplets, it's important to define the acoustic pressure at which nanodroplets phase-transition to form microbubbles.

Results shown in Paragraph 4.2.2.2 on page 229 demonstrate that the setup developed in this study is suitable to characterise the acoustic response of microbubbles and, likely, nanodroplets. At first, both computational and experimental results confirmed that the addition of an acoustic absorbing material on the lateral and top walls of the tank led to a decrease in US wave reflections within the tank. This is an important feature of the setup, as it enables detection of a signal that is mainly

influenced by the response of the sample at the target site, rather than by reflections of the incident wave. Moreover, the addition of microbubbles led to a change in the recorded signal, namely the appearance of both subharmonic and ultraharmonic content, demonstrating that MB cavitation activity could be detected using the developed setup.

4.3.3.1 Characterisation of the acoustic response of MBs in a fracture model

The acoustic characterisation of microbubbles consisted in their acoustic stimulation at different acoustic pressures, as well as recording and processing of their acoustic response. Results presented in Paragraph 4.2.2.3 on page 230 show the acoustic response of microbubbles obtained after being stimulated with 1 MHz and 2 MHz unfocused transducers.

When the 1 MHz unfocused transducer was used, acoustic pressures in the range 0.06-0.33 MPa were applied at the target region, where microbubbles were placed. Fracture gaps in the range 3.5-5.5 mm with thickness between 2 and 4 mm were tested, and results show that there was no difference in the MB acoustic response between these cases, as expected from the simulated acoustic field at the fracture gap presented in Figure 4.22 (page 209) in Paragraph 4.2.1.2. Notably, having fracture gaps of different widths and thicknesses did not lead to significant differences in the acoustic field properties within the fracture gap, hence microbubbles were stimulated in a similar fashion and underwent a comparable response. Four different sets of experiments were carried out: in the presence/absence of microbubbles in the fracture gap and in the presence/absence of Sawbones. Figure 4.53 (page 234) summarises all the experiments performed.

When only agarose gel was present in the gap, the energy content of harmonics and ultraharmonics was low, indicating that there was no acoustic activity in the gap; only some reflections of the incident wave were detected by the PCD. This result offers a control for the other three cases tested. When microbubbles were added at the target region, the energy of harmonics and ultraharmonics increased, suggesting a mild MB oscillation of microbubbles. When the bone was tested without MBs, a greater level of acoustic energy was detected, probably resulting from reflections of the acoustic

wave taking place between the walls of the fracture gap and potential vibrations of the Sawbones structure. When both Sawbones and microbubbles were present, both harmonic and ultraharmonic energy increased even further. This demonstrated two important points: on one hand, microbubbles were detectable in the setup and provided a distinct signal compared to the control (i.e., bone model without microbubbles in the fracture gap); on the other hand, the power density of the signal generated from microbubbles was greater when the Sawbones was present, compared to the case in which it was removed. Importantly, the latter observation shows that the presence of bone enhances the response from microbubbles rather than hindering it, which could be helpful in a real life scenario since more acoustic response could lead to a higher mechanical stimulation of the surrounding environment and cells and, hence, an enhanced treatment efficiency. Such behaviour was foreseen considering the simulation's results, which showed the presence of a standing wave field within the fracture gap, which in turn potentially increases the acoustic energy within the gap itself. Acoustic pressure hotspots were also present within the gap; thus the intensity of MB response could have been greater in these regions. To achieve a more uniform acoustic stimulation in a real life scenario, a multi element device could be used instead of a single element transducer. To the best of the author's knowledge, there is no study in the literature showing how US propagates inside a bone fracture, therefore this investigation represents a novelty contribution to the field.

When the 2 MHz unfocused transducer was used, acoustic pressures in the range 0.03-0.7 MPa were applied. The signal recorded in the presence of MBs presented a greater response when compared to the case where no MBs were added. The greater the acoustic pressure, the larger was the difference in energy between the two cases investigated; the energy appeared to increase only marginally in the absence of MBs, while it increased more significantly (and non-linearly) in the presence of MBs. The highest acoustic pressure reached with this transducer was greater than the one reached with the 1 MHz unfocused transducer, and this led to a more intense MB response.

Overall, these results may have important therapeutic implications as they suggest that the presence of bone results in a more intense MB stimulation in the fracture gap, leading to enhanced acoustic response. Having materials of different acoustic impedance in the propagation path of an ultrasound wave gives origin to wave reflection, refraction and attenuation [34]. The resulting alterations in the wave path and intensity

could have had a potential negative impact on the MB response in the fracture gap because of a weaker or uneven acoustic pressure field; however, experiments in this study have shown that this was not the case and, in fact, wave reflections gave rise to standing waves and pressure hotspots that increased the maximum acoustic pressure in the fracture gap. Achieving enhanced MB acoustic response could potentially lead to greater mechanical stress applied on nearby cells, creating openings in cell membranes and thus leading to more effective uptake of drugs [45]. In addition, US stimulation was applied on MBs embedded in agarose gel within the fracture gap, which makes the physical experimental environment similar to the physiological one. It is well known that agarose gels can be employed as soft tissue substitutes; Maxwell et al. [131] used a mixture of agarose gel and canine red blood cells as a tissue phantom to study cavitation-induced damage to tissue, and the acoustic and mechanical properties of the gel phantom were found to be similar to soft tissue properties. The morphology of lesions generated in the phantom were also very similar to those generated in real tissue, at both macroscopic and cellular levels.

4.3.3.2 Characterisation of the acoustic response of NDs in a fracture model

The aim of this experiment was to achieve ND vaporisation in the bone fracture model. Nanodroplets were stimulated by applying different acoustic pressures and their acoustic response was recorded. Results presented in Paragraph 4.2.2.4 on page 234 show the acoustic response of nanodroplets obtained after being stimulated with 1 MHz and 2 MHz unfocused transducers, and with a 1 MHz focused transducer.

When using both the 1 MHz and 2 MHz unfocused transducers, it was not possible to detect any difference in the recorded signal upon addition of NDs to the fracture gap, which indicated that ND vaporisation did not occur. This could be due to the fact that the acoustic pressure applied to the target region was not high enough to induce acoustic droplet vaporisation. The highest acoustic pressure applied was 0.7 MPa. Notably, ND vaporisation depends on the vapour pressure (or boiling point) of the perfluorocarbon liquid core. When a sound wave is applied to a suspension of PFC nanodroplets, it generates a pressure wave (comprising compression and expansion phases) in the fluid. In the expansion phase of the wave, the pressure of the surrounding fluid decreases; when it becomes lower than the PFC vapour pressure,

phase transition can occur [94]. Further tests with higher acoustic pressure amplitude were thus performed to determine whether ND phase transition could be achieved.

When the 1 MHz focused transducer was used, it was possible to detect the presence of MBs from the acoustic response recorded during the experiment. In particular, when acoustic pressures greater than 0.84 MPa were applied to NDs (embedded in LMP agarose), harmonics, ultraharmonics and broadband noise appeared in the FFT of the recorded signal, which were not present in the absence of NDs. Such difference in behaviour suggested that ND vaporisation occurred, demonstrating that phase transition of NDs can be achieved in the bone fracture models tested. As previously discussed for MBs in Paragraph 4.3.3.1, reflections of the US wave in the fracture gap gave origin to pressure hotspots that allowed achieving a greater peak acoustic pressure compared to the case without fracture gap, promoting ND vaporisation. Notably, recent experiments [1] showed that lipid-shelled PFP NDs vaporised in a tissue-mimicking flow phantom only when acoustic pressures greater than 3 MPa were applied; while in this study, a lower pressure of 0.84 MPa induced ND vaporisation within a bone fracture model. In this study, two different ND formulations were used, containing either a PFP or a PFB core. The main difference between the two perfluorocarbons is their boiling point in bulk state, namely 29 ^{o}C for PFP and 3 ^{o}C for PFB. Once these PFCs are formulated as particles, the resulting surface tension increases the temperature and/or the vapour pressure magnitude needed to achieve phase transition [94]. PFB was thus expected to vaporise at lower acoustic pressure magnitudes than PFP. This hypothesis was confirmed experimentally, as shown in the power spectral energy with respect to time in Figures 4.61.B and 4.63 (pages 240 and 242). Interestingly, the harmonics, ultraharmonics and broadband power spectral energy obtained from PFP NDs were sustained during the whole 30 seconds of stimulation. PFB NDs instead gave a more intense response, but it was limited to the first 10 seconds of stimulation. These findings suggest that PFB NDs may have vaporised more readily and subsequently, the resulting MBs may have coalesced and dissolved in the first few seconds of stimulation. Conversely, the response of PFP NDs was weaker in terms of its energy content, but it was maintained over the total stimulation time (30 s), suggesting that phase transition events occurred throughout the whole stimulation. From a clinical point of view, choosing PFB NDs over PFP NDs could result in a stronger mechanical stimulation of the surrounding fracture gap area. Further biological experiments are however needed to determine whether

such enhanced mechanical stimulation would be beneficial for cells and tissues in the bone fracture. To the best of the author's knowledge, there is no previous study in the literature showing the different temporal behaviour between PFP and PFB NDs when subject to the same acoustic stimulation regime, and within a bone fracture a gap model.

4.3.3.2.1 Ultra high speed imaging of ND vaporisation in a tissue mimicking phantom

Ultra high speed imaging was used to investigate phase transition from PFP NDs to MBs, as presented in Paragraph 4.2.2.5 on page 243. Results showed that it was possible to achieve phase transition by applying an acoustic pressure of 1.8 MPa. Phase transition did not happen homogeneously in the whole volume of the gel, but only in some preferential regions of the fracture gap, as shown in Figures 4.66, 4.67 and 4.68 (page 245). This may be due to two aspects: (1) the mixing between agarose gel and NDs was not sufficiently homogeneous, since this step was performed quickly to avoid ND vaporisation due to the associated high temperatures. (2) After the first US cycle, some cracks and channels appeared in the gel likely due to the mechanical forces exerted by MBs. Such channels and tunnelling in gel phantoms have already been observed by Caskey et al. [196], mainly in the direction of propagation of the US wave. These channels represented regions where NDs and MBs would preferentially localise. As for possible therapeutic implications, channeling could promote a deeper penetration of the drug *in vivo*, leading to improved efficacy of the treatment.

Interestingly, if the percentage area occupied by MBs (with respect to time) is compared across three experimental repeats, as shown in Figure 4.69 (page 247), it is possible to notice that the peak value was of about 9% in all cases, and that values repeated themselves with comparable profiles. This suggests that the mixing between gel and ND suspensions was not as dishomogeneous as initially anticipated and that the experiment was sufficiently repeatable. Such finding could be useful from a therapeutic point of view as quantifying the amount of phase transition could help quantifying the amount of delivered drug to tissues, giving insights in how to adjust drug doses to achieve the efficacy of the treatment. The actual finding that only the 9% of area was occupied by MBs after US stimulation highlights that further tests should be done adjusting US parameters to allow achieving a higher phase transition percentage, which could then result in an enhanced efficiency of the treatment.

4.4 Conclusions

This chapter of the thesis focused on the development of a setup to perform acoustic characterisation of microbubbles and nanodroplets in a bone fracture model. Firstly, the setup was designed, simulated computationally and validated experimentally; then, it was used to perform acoustic characterisation of the US responsive agents developed in the previous chapters of the thesis.

Concerning the developed microscope-compatible tank, numerical simulations showed that it was possible to achieve a uniform acoustic field at the target plane of the setup when an absorbing material was placed on the top and on lateral walls of the tank and when the fracture was aligned to the incoming US wave. In addition to this, it was possible to experimentally detect changes in the signal recorded by the PCD when MBs were added at the target plane, demonstrating the conformity of the setup for the characterisation of the acoustic behaviour of MBs and NDs. As for the acoustic characterisation of MBs, it was shown that the presence of a bone fracture enhanced the acoustic response of MBs located in the fracture gap, likely due to the onset of a standing wave field caused by US reflections at the interfaces between soft and hard tissue. From a biological and therapeutic point of view, a greater MB response to ultrasound may result in a more intense mechanical stimulation of the surrounding tissue, potentially promoting intracellular drug uptake and overall treatment efficacy.

Findings from this study also demonstrated that it was possible to achieve phase transition of FPF nanodroplets in a bone fracture model. This has some important therapeutic implications, since NDs present greater stability and extravasation efficiency compared to MBs, and may thus be a preferred therapeutic candidate.

This work contributes to the research field of the acoustic characterisation of MBs and NDs since the model developed provides a compact tool to study the interaction between ultrasound, bone, and ultrasound-responsive agents. Other studies have previously focused on assessing how the US wave propagates in bone and how healing of a fracture can be monitored using US; however, to the best of the author's knowledge, no study has previously investigated the response of microbubbles and nanodroplets upon US stimulation in a fracture gap model. Moreover, from a therapeutic point of view, findings demonstrate that bone may not represent a barrier to US stimulation of a fracture gap, and - in some cases - it may enhance stimulation of US responsive agents and their acoustic response, which could improve treatment efficacy.

Chapter 5

Conclusions, Future Work and Research Outcomes

5.1 Conclusions

Bone fractures and nonunions impose an economic burden of £2 billions to the UK. Ten percent of bone fractures result in costly and debilitating conditions such as delayed healing or nonunion, where the bone fails to heal properly. Bone fractures are commonly treated with plaster casts, prostheses, or biological therapies. All these treatments have a major drawback: the immobilisation of the site of fracture that leads to a decrease in the quality of life of patients and possible side effects. To overcome these limitations, new treatments should aim at promoting faster bone mass production, in order to decrease the time of immobilisation. This study focuses on the development of a new treatment to enhance the bone fracture repair process by using drug-loaded microbubbles and/or nanodroplets. The ultimate goal is to deliver these drug-carriers to the site of fracture, and induce them to release the encapsulated drug in response to ultrasound stimulation. The main aim of this specific project was to develop stable microbubbles and nanodroplets and characterising their behaviour from an acoustic point of view in a bone fracture model, by using both computational modelling and experimental testing.

Specifically, the first step of the project was to study the production process and stability of phospholipid-shelled microbubbles, and to identify optimal production

parameters to create stable and safe drug-carriers. It was found that the storing conditions and temperature, the viscosity of the medium in which microbubbles are suspended and the labeling of microbubbles by means of fluorescent dyes all affect the stability of microbubbles in terms of their size and concentration with respect to time. Stability tests revealed that temperature had a significant effect on MBs mean diameter and concentration. At 37^{o}C, the diameter increased over two hours from 4.67 $\pm$ 1.45 to 18.24 $\pm$ 11.63 μm, while MB volumetric concentration decreased from 2.65 x 10^8 to 4 x 10^6 MBs/mL. In contrast, at 4^{o}C, the mean diameter increased from 3.9 $\pm$ 0.42 to 10.72 $\pm$ 0.7 μm while concentration decreased from 2 x 10^8 to 4 x 10^6 MBs/mL over six days. An increase in the viscosity of the medium (from 1.58 to 15.38 cP) led to smaller MBs, with mean diameter of 2.92 $\pm$ 2.88 vs 3.66 $\pm$ 2.89 μm (just after production) and 4.06 $\pm$ 4.49 to 6.26 $\pm$ 5.05 μm (after 1 day). Incorporation of the lipophilic dye, DiI, significantly affected MB size. The mean diameter increased, with increasing viscosity, from 4.99 $\pm$ 3.8 to 5.48 $\pm$ 2.99 μm, after production. Whereas, at day 6 the mean diameter increased from 13 $\pm$ 11.82 to 17.94 $\pm$ 14.74 μm with increasing DiI:MB ratio. To achieve maximum stability during storage, microbubbles should be produced in a biocompatible, viscous dilution medium, and stored at 4^{o}C until usage. Since there is an increase in the MB diameter and a decrease in their concentration over time, the storage time should be as short as possible (a maximum of 24 hours is advisable) to guarantee maximum safety. Finally, the visualisation of microbubbles *in vivo* and *in vitro* should be done by adding low concentration of dyes, i.e. a molar ratio of DSPC:PEG40s:DiI below 0.89:0.101:0.0002 (DiI $<$ 2.14 μM) should be used.

The second step of this project was an experimental investigation of the production and characterisation of lipid-shelled nanodroplets, leading to the identification of suitable manufacturing protocols. Concerning PFP DSPC:PEG40s nanodroplets, the findings from this research project suggest that parameters like the quantity of PFP used and the sonication regime both affect the properties of the final product. The production of phospholipid-coated nanodroplets involves two sonication steps: during the first one, lipid aggregates are dispersed in saline solution, while during the second one nanodroplets are formed. It was found that increasing the volumetric concentration of PFP from 5% to 15% v/v in PBS caused an increase in ND size from 215.8 $\pm$ 16.8 nm to 408.9 $\pm$ 171.2 nm; increasing intensity of sonication from 48 to 72 W led to a decrease in ND size from 354.6 $\pm$ 127.2 nm to 315.0 $\pm$ 100.5

nm, and, with an increase in the sonication time from 20 s to 60 s, the average ND diameter reduced to 249.7 ± 9.7 nm. NDs were also stained with a lipophilic dye (DiI, with a final concentration in the range 2.14 - 21.42 μM) and the effect of labelling on ND size was found to be negligible. Nanodroplets can be used as precursors of microbubbles; given their smaller size, they can penetrate more effectively through a blood vessel's wall and into a target tissue. Upon an increase in temperature above the boiling point of PFP, or a reduction in pressure (i.e. induced by an ultrasound wave propagation), nanodroplets produced in this study could be vaporised to form microbubbles, proving that the formulation and production methods used are suitable for this purpose. Finally, nanodroplets were proven to be able to maintain their mean size over a period of one-week when stored at 4^{o}C; however, it is recommended to use them within two hours from production, as within this time window they maintained the lowest size dispersity.

The third step of this project focused on the acoustic characterisation of microbubbles and nanodroplets. An experimental setup was specifically designed and manufactured for this purpose. The main design criteria included: enable simultaneous ultrasound stimulation and detection of acoustic response from a sample, possibility to integrate the setup with an optical microscope and fracture gap models of different clinically relevant sizes, and ability to achieve a predictable acoustic pressure field at a target site. Numerical simulations were initially carried out to determine the characteristics of the acoustic field to which US-responsive agents will be subject, followed by preliminary experiments to validate the conformity of the setup. It was shown, both numerically and experimentally, that it is possible to achieve a uniform acoustic field at a desired target plane within the setup when acoustically absorbing material was placed at specific locations in the setup. In addition, it was possible to detect changes in the signal recorded by a passive cavitation detector (PCD) when MBs were added at the target plane, demonstrating that the setup is suitable for characterising the acoustic behaviour of microbubbles and nanodroplets. The response of these agents to ultrasound stimulation was subsequently characterised, both in the presence and absence of a bone fracture model. In these experiments, the ultrasound-responsive agents were embedded in an hydrogel (mimicking soft tissue properties) and placed within the fracture gap. As for the acoustic characterisation of microbubbles, it was shown that the presence of a bone fracture enhanced their acoustic response when stimulated at 1 MHz for 30 seconds, with a PRF of 1 Hz, duty cycle of 1-5% and

peak negative acoustic pressures ranging between 0.06 and 0.33 MPa. The enhanced response was attributed to reflections of US taking place between the walls of the fracture gap and giving origin to standing waves and acoustic pressure hotspots. These findings have important therapeutic implications as they show that the presence of bone doesn't limit the ability to acoustically activate MBs within the fracture gap. When nanodroplets were acoustically stimulated at 1 MHz for 30 seconds, with a PRF of 1 Hz, duty cycle of 1-5% and peak negative acoustic pressures ranging between 0.03 and 0.95 MPa, the recorded signal confirmed occurrence of ND vaporisation within the bone fracture model at acoustic pressures higher than 0.84 MPa.

5.2 Contributions of Novelty

The research presented in this thesis provides several contributions of novelty, as reported below.

- There is no previous study that has systematically investigated how physico-chemical factors and production parameters affect MB characteristics. In Chapter 2, the effects of different parameters on lipid-shelled MB size and stability are presented for the first time. Moreover, fluorescent labelling of MBs is commonly used to detect them in applications *in vivo* and *in vitro*; Chapter 2 demonstrates the effect of shell labelling on MB size and stability.
- Although the use of PFC nanodroplets for therapy has gained significant interest over the last two decades, there are still open questions that may have hindered their clinical translation. For instance, no previous study has investigated the effect of varying production parameters and environmental condition on ND size. In Chapter 3, this knowledge gap was addressed and it was revealed that the perfluorocarbon concentration, sonication power and duration, and storage conditions affect ND size. Findings from this study could inform researchers aiming to produce batches of PFC NDs with a specific size range. In addition to this, to the best of the author's knowledge, this is the first study using a DSPC-PEG40s shell.
- There is no previous study that has investigated how the presence of a bone can affect the acoustic response of microbubbles and nanodroplets in a bone

fracture gap. Findings in Chapter 4 demonstrate that bone does not represent a barrier to US stimulation, but instead it may enhance the acoustic stimulation of US-responsive agents located within the fracture gap, due to the onset of an acoustic standing wave field. In addition, a compact system for investigating the response of ultrasound-responsive agents in a bone fracture model was developed for the first time, and may represent an alternative to bulkier water-tank apparatuses. The system is suitable for integration with different types of acoustic or optical detection technologies.

5.3 Limitations and Future Work

The research in this project led to the development of US-responsive MBs and NDs, and their acoustic characterisation within a bone fracture model. However, there are some limitations that could be addressed in future research. This study mainly focused on one type of MB/ND formulation, comprising a DSPC-PEG40s shell shell, a MB gas core made of room air, and a ND liquid core of PFP. Even if similar behaviours to the ones observed in this study are foreseen for other chemical formulations, a quantitative and comparative analysis of multiple formulations could provide useful insights, as agents with different characteristics may be preferred for different therapeutic indications. The numerical simulations performed to characterise the developed ultrasound tank were only two-dimensional; therefore, 3D computational modelling could be carried out to gain a more comprehensive characterisation of the acoustic field in the tank. Experimentally, only bone fracture models with a fracture inclination angle of 90^{o} (with respect to the base of the tank) were studied; future studies could focus on an experimental comparison with fracture models aligned to the incident wave. These may provide further information concerning the optimal transducer orientation for achieving desired therapeutic effects. Moreover, experiments were performed using Sawbones material as a model bone; the validity of this model could be assessed by using real bone fragment, potentially mice femurs, to investigate whether the architecture of a real fracture may impact on the acoustic behaviour of US-responsive agents. Finally, future work could be focused on performing additional microscopy-based assessment of MBs/NDs behaviour during/after US stimulation in the bone fracture mode, including a quantification of ND vaporisation efficiency, MB/ND radial and translational movements over time, and the release of fluorescent

drug models upon stimulation.

Another possible future development from this project relates to the study of the coupling between ultrasound-responsive carriers and bioactive compounds, which would include investigations of drug loading and release from these carriers. This future studies could be articulated in the following primary steps:

- Firstly, a choice should be made in terms of which drug to include in the carrier. Different drugs are available for different therapeutic aims, which include inducing stem cells to differentiate into bone cells, and decreasing immune response or inflammation. Our research group is investigating the use of BIO, a small molecule promoting the differentiation process.

- After having chosen the bioactive compound, research should be conducted on how to load it onto the carrier; the loading approach can vary according to the chemical characteristics of the drug itself. A protocol that has been already developed at the University of Oxford to produce BIO-PFB NDs may be employed in these experiments. Briefly, BIO is added to the lipid mixture (0.356 mg/mL), while the other steps of MB/ND production are kept almost unchanged. To remove excess free lipids and BIO, MB/ND suspensions will be centrifuged and resuspended in fresh PBS solution. Microbubbles and nanodroplets loaded with BIO will then be stimulated with ultrasound to assess their ability to release the drug in a controlled fashion, whilst maintaining its bioactivity.

- In the case of nanodroplets, a further experimental step will be required to assess whether vaporisation affects the efficacy, bioactivity and bioavailability of the drug.

- Tests will need to be performed *in vitro* to optimise the stimulation process parameters. These will include injection of the sample in a tissue phantom, stimulation with US, and quantification of drug release and potential mechanical effects. High performance liquid chromatography (HPLC) will be used to quantify release profiles.

5.4 Research Outcomes

5.4.1 Peer-reviewed research articles published

- Tailoring the size of ultrasound-responsive lipid-shelled nanodroplets by varying production parameters and environmental conditions. [1]

  Ultrasonics Sonochemistry, Volume 73, May 2021, 105482

  Sara Ferri, Qiang Wu, Antonio De Grazia, Anastasia Polydorou, Jonathan P. May, Eleanor Stride, Nicholas D. Evans, Dario Carugo

- Investigation of the acoustic vaporization threshold of lipid-coated perfluorobutane nanodroplets using both high speed optical imaging and acoustic methods.

  Ultrasound in Medicine & Biology

  Qiang Wu, Christophoros Mannaris, Jonathan P May, Luca Bau, Anastasia Polydorou, Sara Ferri, Dario Carugo, Nicholas D. Evans, Eleanor Stride

5.4.2 Peer-reviewed research articles under preparation

- Tailoring the size and stability of ultrasound-responsive lipid-shelled microbubble by varying production parameters and environmental conditions.

  Sara Ferri, Qiang Wu, Anastasia Polydorou, Jonathan P. May, Eleanor Stride, Nicholas D. Evans, Dario Carugo

- Design, characterisation and production of a microfluidic acoustofluidic device to perform acoustic and thermal stimulation and imaging of NDs and achieve phase transition.

  Sara Ferri, Mathieu Cabot, Qiang Wu, Anastasia Polydorou, Jonathan P. May, Eleanor Stride, Nicholas D. Evans, Dario Carugo

5.4.3 Conferences, presentations and prizes

- Bubbles for bone: acoustic stimulation for drug delivery in fracture repair

  VI FEE PG CONFERENCE - Southampton, 16^{th} January 2018 (oral presentation)

- Bubbles for bone: acoustic stimulation for drug delivery in fracture repair

  iPhD AND MRC DTP AWAY DAY - Southampton - 9th February 2018 (oral presentation)

- Acoustically stimulated microbubbles for bone fracture repair

  IfLS POSTER SESSION - Southampton, 18th May 2018 (poster)

- Bubbles for bone: acoustic stimulation for drug delivery in fracture repair

  FACULTY OF MEDICINE CONFERENCE - Southampton General Hospital, 6th June 2018 (oral presentation and poster, winner of "Best Poster Prize")

- Bubbles for bone: acoustic stimulation for drug delivery in fracture repair

  MODELLING AND EXPERIMENTS IN DRUG DELIVERY SYSTEMS (MEDDS) - University of Glasgow, 3rd-5th September 2018 (oral presentation)

- Acoustically stimulated microbubbles for bone fracture repair

  CARDIFF INSTITUTE FOR TISSUE ENGINEERING AND REPAIR (CITER) ANNUAL SCIENTIFIC MEETING - Cardiff University, 17th-18th September 2018 (oral presentation)

- Bubbles for bone: acoustic stimulation for drug delivery in fracture repair

  VII FEE PG CONFERENCE - Southampton, 15th January 2018 (oral presentation, winner of "Best Oral Presentation Prize")

- Acoustically-stimulated nanodroplets for bone fracture repair

  24th EUROPEAN SYMPOSIUM ON ULTRASOUND CONTRAST IMAGING - Rotterdam, 17th-18th January 2019 (poster)

- Bubbles for bone: acoustic stimulation for drug delivery in fracture repair

  iPhD AND MRC DTP AWAY DAY - Southampton - 8th February 2019 (oral presentation)

- Bubbles for bone: acoustic stimulation for drug delivery in fracture repair

  FACULTY OF MEDICINE CONFERENCE - Southampton General Hospital, 11th June 2019 (oral presentation)

- Engineering acoustically activated nanodroplets for bone fracture repair

  19 th INTERNATIONAL SYMPOSIUM OF ISTU - 5th EUROPEAN SYMPOSIUM OF EUFUS - Barcelona, 13th-15th June 2019

- Engineering acoustically activated nanodroplets for bone fracture repair

  IfLS POSTER SESSION - Southampton, 25th October 2019 (poster)

- A physical model to investigate the acoustic behaviour of microbubbles and nanodroplets within a bone fracture

  ACOUSTICAL SOCIETY OF AMERICA (ASA) ANNUAL MEETING - San Diego, 2nd-6th December 2019 (oral presentation)

- A physical model to investigate the acoustic behaviour of microbubbles and nanodroplets within a bone fracture

  25th EUROPEAN SYMPOSIUM ON ULTRASOUND CONTRAST IMAGING - Rotterdam, 16th-17th January 2020 (poster)

- A physical model to investigate the acoustic behaviour of microbubbles and nanodroplets within a bone fracture

  iPhD AND MRC DTP AWAY DAY - Southampton - 7th February 2020 (oral presentation)

- Investigation of the acoustic vaporization threshold of lipid-coated perfluorocarbon nanodroplets using simultaneous high-speed optical imaging and acoustic methods

  26th EUROPEAN SYMPOSIUM ON ULTRASOUND CONTRAST IMAGING - Rotterdam, 14th-15th January 2021 (poster)

Appendix A

Transition from nanodroplets to microbubbles

In Paragraph 3.1.2.1, an acoustofluidic device designed to study the combined effect of temperature and US stimulation on NDs is presented. In this Appendix, preliminary experiments and a first version of that device are shown.

A.1 Method

Nanodroplets can be considered as precursors of microbubbles, and the transition can be achieved by applying either thermal or acoustic energy. During the transition, the liquid core of NDs vaporises and this leads to the formation of gas-filled MBs. Tests were thus performed to assess NDs ability to undergo phase transition.

In a first phase of the study, vaporisation induced by thermal energy was investigated. After NDs were produced with the protocol described in Paragraph 3.1.1, a ND sample of 10 µL was placed on a glass slide (76 x 26 mm, thickness 1 mm) and covered with a coverslip (18 x 18 mm, thickness 0.17 mm, Menzel-Glaser). The glass slide was then placed on a hot plate. The hot plate temperature should be above the phase transition temperature of PFP, in order to promote liquid-to-gas phase transition and thus generate microbubbles. The phase transition temperature of PFP droplets is dependent upon the droplet size. Nanodroplets produced in this study have a diameter between 100 and 300 nm, so the corresponding phase transition temperature

is estimated to be around 70°C, as shown in Figure 1.17.

The hot plate was placed near a microscope, and microscope images of the sample with a magnification of either 10x and 50x were acquired every minute, until complete evaporation of PFP was observed.

In a second series of tests, ND vaporisation upon ultrasound stimulation was investigated. US stimulation combines pressure stimulation and heating effect to allow and facilitate phase transition. To perform this test, an acoustofluidic device was designed to generate an ultrasonic standing wave within a fluid layer. The constitutive layers of the device are: a piezoelectric transducer PZT, a carrier, the fluid and a reflector. The US wave emitted by the transducer travels into the fluid layer through a carrier, and is then reflected backwards by the reflecting layer, due to a mismatch in the acoustic impedance between fluid and reflector and due to the thickness of the reflector layer. The interaction between the emitted and reflected waves gives origin to a standing wave field. Figure A.1 shows a photograph of the acoustofluidic device employed for investigating acoustic droplet vaporisation in this study.

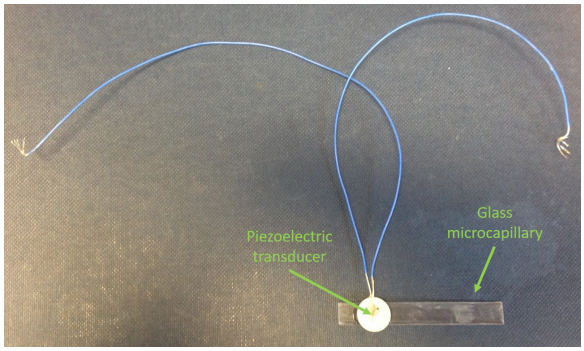

Figure A.1: *Acoustofluidic device used to stimulate nanodroplets with ultrasound, and phase transition them into microbubbles*

A glass microcapillary with an rectangular cross-section (0.3 x 6 x 50 mm, thickness 0.3 mm, VitroCom, West Yorkshire, United Kingdom) was coupled to a piezoelectric transducer with a diameter of 10 mm and thickness of 1 mm (PZT26, Meggitt, Christchurch, Dorset, UK) using a layer of epoxy glue (EpoTek 301, Epoxy Technology, Billerica, MA, USA). The glue was applied and let to dry overnight at room temperature. This specific device configuration will be referred to as acoustofluidic device from herein. The device could be primed with 100 µL of the nanodroplets suspension.

The electronic circuit used to operate the device comprised of a signal generator

(TG2000 20 MHz DDS function generator, Aim and Thurlby Thandar Instruments, Huntingdon, UK) connected to a custome-built amplifier, which was then connected to an oscilloscope (DSO1102B 100 MHz, Keysight Technologies, Wokingham, UK). The microcapillary was placed over the microscope stage (IX71 Olympus, Shinjuku, Tokyo, Japan). The strongest resonance frequencies were determined experimentally, and were associated with minima in the peak-to-peak voltage signal acquired through the oscilloscope; an half-wave resonance was established too. Resonance frequencies were 1.75, 2.22 and 2.36 MHz. To induce vaporisation of PFP NDs, an amplitude of 15 V (Vpp, peak-to-peak voltage) and a frequency of 1.75 MHz were set on the signal generator. Both continuous (stimulation of 10 seconds) and pulsed (total stimulation time of 10 seconds, with pulsation of 2 seconds and duty cycle of 50%) stimulations were performed. Microscope images of the sample within the acoustofluidic device were taken every ten seconds for one minute with magnifications of either 10x and 50x.

A.2 Results

Nanodroplets can transition into microbubbles because of an increase in temperature or upon ultrasound stimulation. Nanodroplets were produced following the protocol explained in Paragraph 3.1.1, and tests were performed as outlined in Appendix A.1.

Figure A.2 shows a microscope image of nanodroplets, prior to any form of stimulation. A first series of tests was performed by increasing the temperature of the hot plate to 90^{o}C and the resulting microbubbles are shown in Figure A.3. Since the transition occurred very rapidly, the test was repeated with a temperature of 80^{o}C. Both NDs produces with a second sonication of 20 and 60 seconds were tested and the resulting microbubbles are shown in Figures A.4 and A.4; lower temperatures did not lead to the transition from nanodroplets into microbubbles.

The second series of tests involved the vaporisation of nanodroplets by means of ultrasound stimulation. Nanodroplets were produced either with a second sonication of 20 seconds or 60 seconds and stimulated with continuous or pulsed ultrasound at 1.75 MHz using a custom-built acoustofluidic device. Microscope images were taken every 10 seconds, for one minute. Figures A.6, A.7 and A.8 show the microbubbles obtained by ultrasound simulation. In these images, it is possible to notice that the number of microbubbles and their size increased with respect to time upon US stimulation.

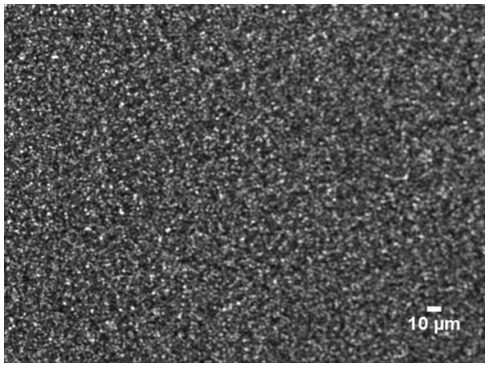

Figure A.2: *Microscope image taken with a 50x magnification lens of nanodroplets produced with a second pulsed sonication of 20 seconds.*

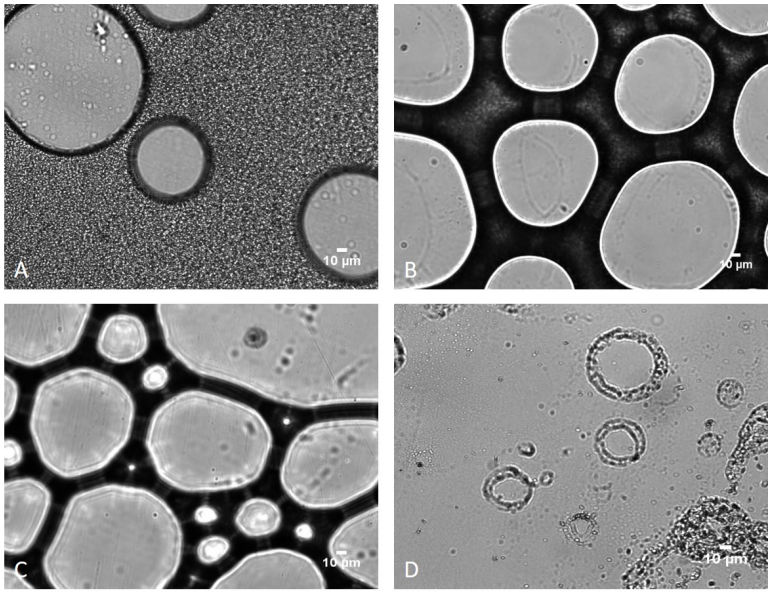

Figure A.3: *Transition from nanodroplets to microbubbles associated with an increase in temperature of the hot plate (from room temperature to 90°C). Nanodroplets were produced with a second pulsed sonication of 20 seconds. Microscope images correspond to different time points, namely A) 1 minute, B) 2 minutes, C) 3 minutes, and D) 4 minutes. The scale bar on the pictures indicates a length of 10 µm.*

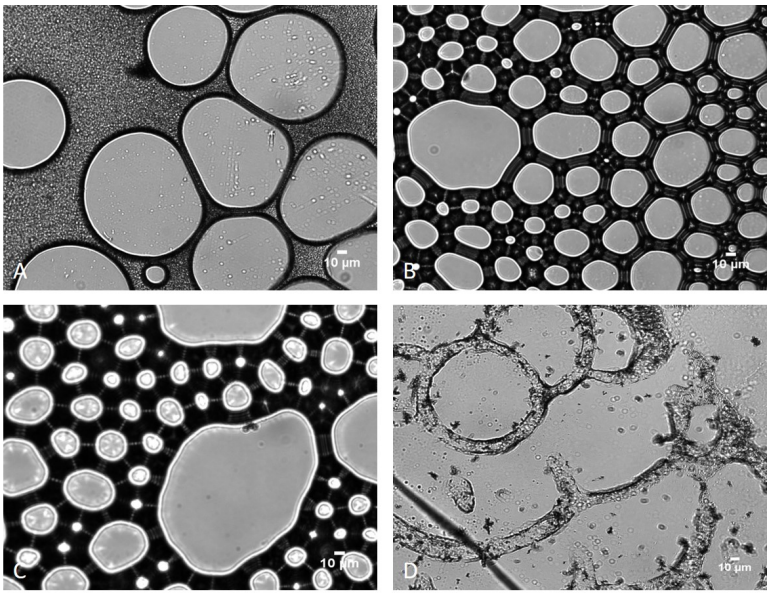

Figure A.4: *Transition from nanodroplets to microbubbles thanks to an increase in the temperature of the hot plate (from room temperature to 80°C). Nanodroplets were produced with a second pulsed sonication of 20 seconds. Microscope images correspond to different time points, namely A) 1 minute, B) 2 minutes, C) 3 minutes, and D) 4 minutes. The scale bar on the pictures indicates a length of 10 µm.*

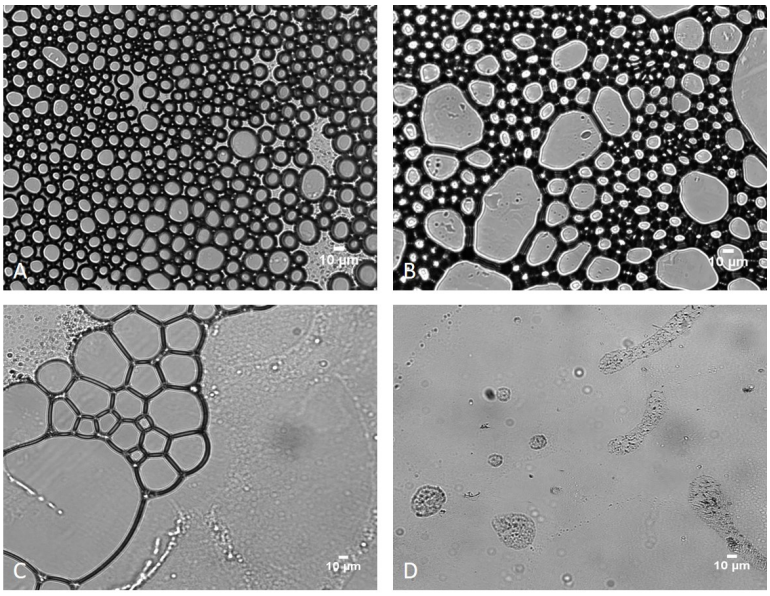

Figure A.5: *Transition from nanodroplets to microbubbles due to an increase in temperature of the hot plate (from room air to 80°C). Nanodroplets were produced with a second pulsed sonication of 60 seconds. Images correspond to different time points, namely A) 1 minute, B) 2 minutes, C) 3 minutes, and D) 4 minutes. The scale bar on the pictures indicates a length of 10 µm.*

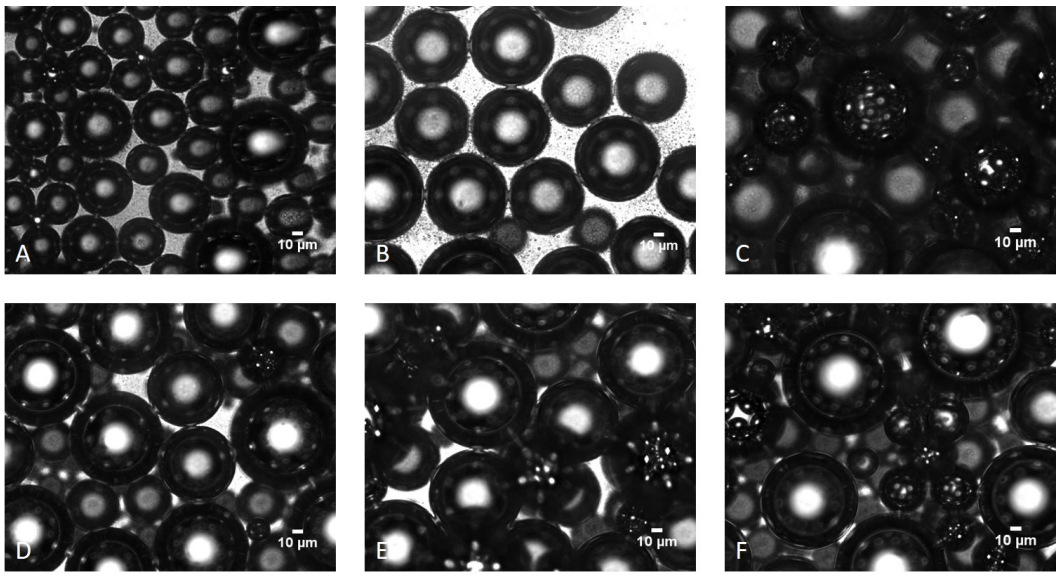

Figure A.6: *Transition from nanodroplets to microbubbles induced by ultrasound stimulation at 1.75* MHz*. Nanodroplets were produced with a second continuous sonication of 20 seconds. Images correspond to different time points, namely at A) 10 seconds, B) 20 seconds, C) 30 seconds, D) 40 seconds, E) 50 seconds, F) 60 seconds. The scale bar on the pictures indicates a length of 10* µ*m.*

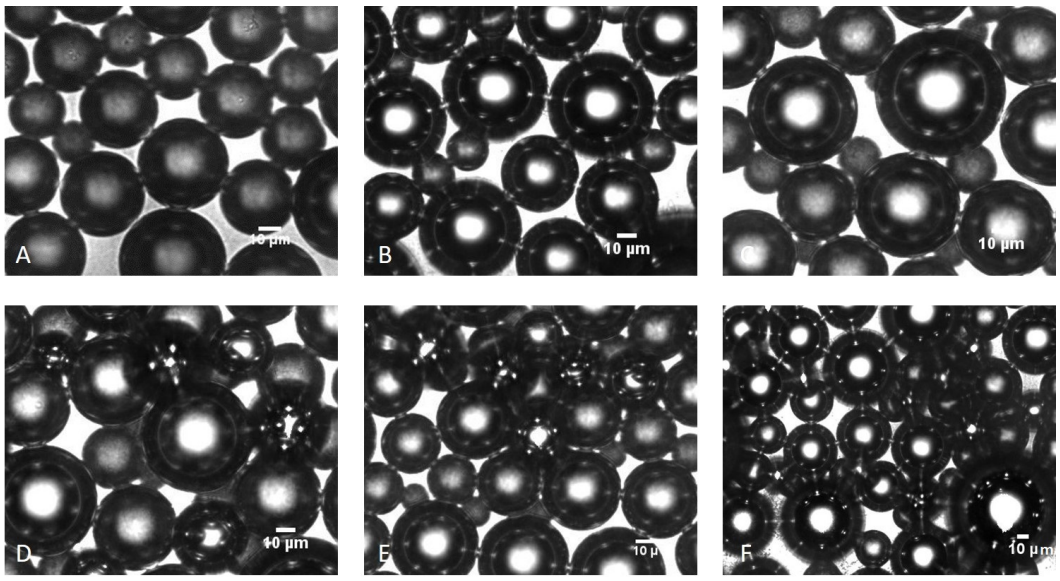

Figure A.7: *Transition from nanodroplets to microbubbles induced by a pulsed ultrasound stimulation (pulse of 2 seconds with 50% duty cycle). Nanodroplets were produced with a second pulsed sonication of 20 seconds. Microscope images correspond to different time points, namely A) 10 seconds, B) 20 seconds, C) 30 seconds, D) 40 seconds, E) 50 seconds, F) 60 seconds. The scale bar on the pictures indicates a length of 10* µ*m.*

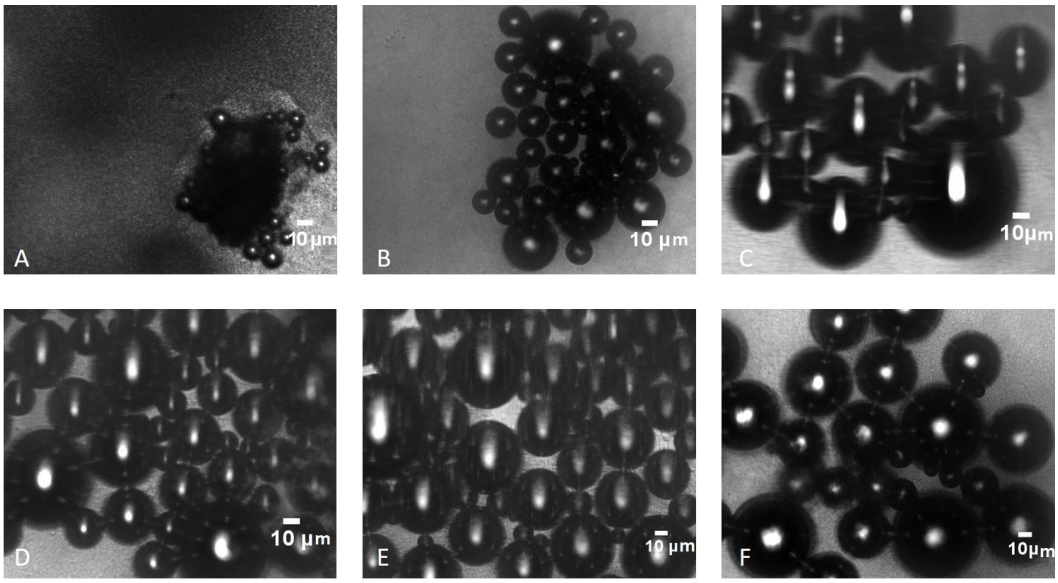

Figure A.8: *Transition from nanodroplets to microbubbles indiced by continuous ultrasound stimulation. Nanodroplets were produced with a second pulsed sonication of 60 seconds. Images correspond to different time points, namely A) 10 seconds, B) 20 seconds, C) 30 seconds, D) 40 seconds, E) 50 seconds, F) 60 seconds. The scale bar on the pictures indicates a length of 10 µm.*

Increasing the exposure time to ultrasound led to an increase in the mean diameter of microbubbles and their concentration.

A.3 Discussion

The results presented in Appendix A demonstrate that it is possible to obtain MBs from NDs, confirming that the production protocol used results in a stimuli-responsive agent. As a matter of fact, it was demonstrated that nanodroplets can transition into microbubbles when exposed to a temperature greater than the phase transition temperature of the perfluorocarbon used, for the specific ND size tested. In this study PFP was employed, which has a boiling temperature of 29°C at atmospheric pressure. This temperature drastically increases if PFP is in the form of a droplet, due to the presence of Laplace pressure. As a consequence, since the obtained nanodroplets had a mean diameter between 200 and 600 nm, their phase transition temperature was anticipated to be above 70°C, as shown in Figure 1.17.

Figure A.5 shows that it is possible to obtain microbubbles even when nanodroplets were produced with a second sonication step of 60 seconds. This demonstrates that, even if there was an increase in temperature during a longer sonication, this was not sufficient to cause PFP to evaporate. It is interesting to note that these microbubbles were smaller and less dispersed than the ones produced with a second sonication step of 20 seconds, the diameter after production ranged between 10 and 30 μm vs diameters > 60 μm with the shorter sonication. This finding suggests that using a second sonication step of 60 seconds leads to less size dispersed microbubbles, as anticipated in Paragraph 3.2.1.1.4.

The temperature used in these tests (80°C) was too high to be used for clinical purposes. For this reason, it was important to assess whether nanodroplets could be turned into microbubbles upon ultrasound stimulation.

Acoustic droplet vaporisation was assessed using a custom-built acoustofluidic device. A main limitation of the device used is that the acoustic pressure field is not uniform; however, it represents a cost-effective and compact device to perform rapid screening tests on different ND formulations. Figures A.6, A.7 and A.8 show that phase transition can be achieved with an ultrasound stimulation of 1.75 MHz and using relatively low acoustic pressures (< 1 MPa). Moreover, using a continuous or pulsed US stimulation did not lead to differences in the final product: the size and concentration of microbubbles in the two cases is comparable at all time points. Throughout the 1-minute observation, the observed MB size was between 20 and 80 μm.

Appendix B

This Appendix presents the codes implemented in Matlab to evaluate the FFT transform of the signals recorded by the PCD and to evaluate the energy associated to the signals recorded by the PCD.

B.1 FFT Matlab Code

```
%% Import data from spreadsheet
% Script for importing data from the following spreadsheet:
%
%    Workbook: \\filestore.soton.ac.uk\users\sf2e17\mydocuments
%    \Southampton\BioLab\3 - Acoustic characterization
%    \2018_11_30 - US tests\50mV\ALL0000\Sample0.xlsx
%    Worksheet: Sample0
%
% To extend the code for use with different selected data or a
% different spreadsheet, generate a function instead of
% a script.

% Auto-generated by MATLAB on 2018/12/03 10:17:22

%% Import the data
[~, ~, raw] = xlsread('\\filestore.soton.ac.uk\users...
\sf2e17\mydocuments\Southampton\BioLab\3 - Acoustic...
    characterization\2018_12_04 - TESTS - BOX+ ...
    absorbing mat 50,100,150,200\1_50mV, no MBs,...
    no abs\ALL0000\Sample0.xlsx','A0000CH1','C17:C4016');
```

```
%% Create output variable
Times = reshape([raw{:}],size(raw));

%% Clear temporary variables
clearvars raw;

%% Import the data
[~, ~, raw] = xlsread('\\filestore.soton.ac.uk\users...
\sf2e17\mydocuments\Southampton\BioLab\3 - Acoustic...
    characterization\2018_12_04 - TESTS - BOX+ ...
    absorbing mat 50,100,150,200\1_50mV, no MBs,...
    no abs\ALL0000\Sample0.xlsx','A0000CH1','C17:C4016');

%% Create output variable
WaveformData = reshape([raw{:}],size(raw));

%% Clear temporary variables
clearvars raw;

figure(1);
plot(Times,WaveformData);
title('Wave Signal');
xlabel('Time (s)');
ylabel('Amplitude (V)');

%%
Y = fft(WaveformData);
L = length(Y);
P2 = abs(Y/L);
P1 = P2(1:L/2+1);
P1(2:end-1) = 2*P1(2:end-1);
Fs = 1/0.000000005;
f = Fs*(0:(L/2))/L;

figure(2);
plot(f,20*log10(P1))
```

```
title('Single-Sided Amplitude Spectrum - FFT')
xlabel('f (Hz)')
ylabel('log(|P1(f)|)')

figure(3);
plot(f,P1)
title('Single-Sided Amplitude Spectrum - FFT')
xlabel('f (Hz)')
ylabel('|P1(f)|')
```

B.2 Energy Matlab Code

```
% process_pcd_06Nov2020.m
% Example script for processing pcd data from SAT-D
% MDG, 06Nov2020

for i=1:6


%% 1. SETUP: set paths and basic processing parameters
datadir = 'F:\Southampton - 2020_12_19 TUTTO\BioLab\...
3 - Acoustic characterization\2020_12_17 - PFB NDs...
    Qiang 1 MHz focused\N6\Processati Matlab\';

% filename front, used for file loading
if i == 1
    nmfrnt = '10mV';
elseif i == 2
    nmfrnt = '20mV';
elseif i == 3
    nmfrnt = '50mV';
elseif i == 4
    nmfrnt = '100mV';
elseif i == 5
    nmfrnt = '150mV';
```

```
elseif i == 6
    nmfrnt = '200mV';
end

% pcd preamp gain, if any.
gain = 1;

% file list
dd = dir([datadir,nmfrnt,'*.txt']);
% number of files
Nfiles = length(dd);

% FUS drive frequency, Hz
f0 = 1.0e6;
% spectrum bin width: 1/50th of f0, Hz
bin = f0/100;
% pulse repetition frequency
prf = 1;


%% 2. PROCESSING Loop
for qd = 1:Nfiles
    tmp = importdata([datadir,nmfrnt,num2str(qd),'.txt'],';',9)
    % columns are semicolon delimited, 9 header lines

    % extract data parameters needed for spectrum processing
    if qd==1
       % sample rate, Hz
       fs = 1/diff(tmp.data(1:2,1));
       % file length
       Npts = length(tmp.data(:,1));
       % number of fft points
       Nfft = round(fs/bin);
       % overlap size in pwelch
       Novr = round(Nfft/2);
       Nfrq = round(Nfft/2)+1;
       % number of points in pwelch spectrum (one-sided)
```

```
    P = zeros(Nfrq,Nfiles);
    % presize power spectral density matrix

    fharm = f0:f0:floor(0.9*fs/2);
    % drive harmonics below Nyquist
    % indices of harmonics
    iharm = round(fharm/bin) + 1;
    iharmselected = [iharm(1,3:11)];
    %nharm = length(iharm);
    nharm = length(iharmselected);

    fuhrm = f0/2:f0:floor(0.9*fs/2);
    % ultraharmonics below Nyquist
    % indices of harmonics
    iuhrm = round(fuhrm/bin) + 1;
    iuhrmselected = [iuhrm(1,3:11)];
    %nuhrm = length(iuhrm);
    nuhrm = length(iuhrmselected);

    % Presize harmonic data
    Pharm = zeros(nharm,Nfiles);
    % Presize ultraharmonic data
    Puhrm = zeros(nuhrm,Nfiles);
end

[P(:,qd),F] = pwelch(tmp.data(:,2)/gain,Nfft,Novr,Nfft,fs);
% run pwelch, P is units of V^2 / Hz

Pharm(:,qd) = P(iharmselected,qd)+P(iharmselected+1,qd)+...
    P(iharmselected+2,qd)+P(iharmselected-1,qd)+ ...
    P(iharmselected-2,qd);
% Harmonic power
Puhrm(:,qd) = P(iuhrmselected,qd)+P(iuhrmselected+1,qd)+...
    P(iuhrmselected+2,qd)+P(iuhrmselected-1,qd)+...
    P(iuhrmselected-2,qd);
% Ultraharmonic power
```

```
end

% Total power by signal type, units are V^2
Pwr(:,1) = sum(P,1)*bin;                    % total
Pwr(:,2) = sum(Pharm,1)*bin;                % harmonic
Pwr(:,3) = sum(Puhrm,1)*bin;                % ultraharmonic
Pwr(:,4) = Pwr(:,1) - sum(Pwr(:,2:3),2);    % broadband

% Energy: sum the powers and multiply by the record time
Trec = diff(tmp.data([1 end],1));           % data record length
E = sum(Pwr,1)*Trec;                        % energies (V^2*s)

if i == 1
    E10 = E;
elseif i == 2
    E20 = E;
elseif i == 3
    E50 = E;
elseif i == 4
    E100 = E;
elseif i == 5
    E150 = E;
elseif i == 6
    E200 = E;
end




%% 3. PLOT
t = (0:Nfiles-1)/prf;

if i == 1
    figure(1)
elseif i == 2
    figure(2)
elseif i == 3
```

```
    figure(3)
elseif i == 4
    figure(4)
elseif i == 5
    figure(5)
elseif i == 6
    figure(6)
end

limits = [-142 -100];

set(gcf,'position',[100 200 1200 400])
subplot(1,2,1)
    pcolor(t, F(211:1251,1)*1e-6, 0.5*db(P(211:1251,:))),...
        shading flat, ...
        h=colorbar('vert');
    caxis(limits);
    h.Label.String = 'dB re V^2/Hz'; colormap jet
    xlabel('Exposure Time (s)'), ylabel('Frequency (MHz)')
    title('Power Spectral Density')

subplot(1,2,2)
    plot(t, 0.5*db(Pwr))
    xlabel('Exposure Time (s)'), ylabel('Power, dB re V^2',...
        'interpreter','tex')
    title('Power By Signal Type')
    legend({['Total, ', num2str(0.5*db(E(1)),3),...
        ' dB re V^2 \bullet s'],...
            ['Harmonic, ', num2str(0.5*db(E(2)),3),...
            ' dB re V^2 \bullet s'],...
            ['Ultraharmonic, ', num2str(0.5*db(E(3)),3),...
            ' dB re V^2 \bullet s'],...
            ['Broadband ', num2str(0.5*db(E(4)),3),...
            ' dB re V^2 \bullet s']},...
            'location','se','fontsize',10)
    ylim([round(min(min(0.5*db(Pwr))))...
        -20 round(max(max(0.5*db(Pwr))))+10 ])
```

```
end

Etot = [E10; E20; E50; E100; E150; E200];
%Etotdb = 0.5*db*Etot;


% end mfile
```

Bibliography

[1] S. Ferri, Q. Wu, A. De Grazia, A. Polydorou, J. P. May, E. Stride, N. D. Evans, and D. Carugo, "Tailoring the size of ultrasound responsive lipid-shelled nanodroplets by varying production parameters and environmental conditions," *Ultrasonics Sonochemistry*, vol. 73, p. 105482, 2021.

[2] NICE, "Niceimpact falls and fragility fractures," 2018.

[3] M. Haffner-Luntzer, A. Liedert, and A. Ignatius, "Mechanobiology of bone remodeling and fracture healing in the aged organism," *Innov Surg Sci*, vol. 1, no. 2, pp. 57–63, 2016.

[4] P. Lavrador, V. M. Gaspar, and J. F. Mano, "Stimuli-responsive nanocarriers for delivery of bone therapeutics – barriers and progresses," *Journal of Controlled Release*, vol. 273, pp. 51–67, 2018.

[5] M. J. K. Blomley, J. C. Cooke, E. C. Unger, M. J. Monaghan, and D. O. Cosgrove, "Microbubble contrast agents: a new era in ultrasound," *British Medical Journal*, vol. 322, no. 7296, p. 1222, 2001.

[6] I. Lentacker, S. C. De Smedt, and N. N. Sanders, "Drug loaded microbubble design for ultrasound triggered delivery," *Soft Matter*, vol. 5, no. 11, pp. 2161–2170, 2009.

[7] L. F. Bonewald, "Mechanosensation and transduction in osteocytes," *BoneKEy osteovision*, vol. 3, no. 10, pp. 7–15, 2006.

[8] U. Kini and B. N. Nandeesh, *Physiology of Bone Formation, Remodeling, and Metabolism*, pp. 29–57. Berlin, Heidelberg: Springer Berlin Heidelberg, 2012.

[9] J. Bilezikian, L. Raisz, and G. Rodan, *Principles of Bone Biology*. Harcourt Academic, 2001.

[10] V. W. Bunker, "The role of nutrition in osteoporosis," *British journal of biomedical science*, vol. 51, no. 3, pp. 228–240, 1994.

[11] Osteoporosis, *Medical conditions that can cause bone loss, falls and/or fractures - Retrieved from: https://osteoporosis.ca/about-the-disease/what-is-osteoporosis/secondary -osteoporosis/medical-conditions-that-can-cause-bone-loss-falls-andor-fractures/.* 2020.

[12] M. R. Newman and D. S. W. Benoit, "Local and targeted drug delivery for bone regeneration," *Current opinion in biotechnology*, vol. 40, pp. 125–132, 2016.

[13] D. J. Hak, D. Fitzpatrick, J. A. Bishop, J. L. Marsh, S. Tilp, R. Schnettler, H. Simpson, and V. Alt, "Delayed union and nonunions: Epidemiology, clinical issues, and financial aspects," *Injury*, vol. 45, no. Supplement 2, pp. S3–S7, 2014.

[14] J. E. Corrarino, "Fracture repair: Mechanisms and management," *The Journal for Nurse Practitioners*, vol. 11, no. 10, pp. 960–967, 2015.

[15] H. Nieto and C. Baroan, "Limits of internal fixation in long-bone fracture," *Orthopaedics Traumatology: Surgery Research*, vol. 103, no. 1, Supplement, pp. S61–S66, 2017.

[16] P. Kuzyk and E. Schemitsch, "The science of electrical stimulation therapy for fracture healing," *Indian Journal of Orthopaedics*, vol. 43, no. 2, pp. 127–131, 2009.

[17] J. A. F. Tassinary, A. Lunardelli, B. d. S. Basso, H. B. Dias, A. V. Catarina, S. Stülp, G. V. Haute, B. A. Martha, D. A. d. S. Melo, F. B. Nunes, M. V. F. Donadio, and J. R. d. Oliveira, "Low-intensity pulsed ultrasound (lipus) stimulates mineralization of mc3t3-e1 cells through calcium and phosphate uptake," *Ultrasonics*, vol. 84, pp. 290–295, 2018.

[18] N. Itaya, Y. Yabe, Y. Hagiwara, K. Kanazawa, M. Koide, T. Sekiguchi, S. Yoshida, Y. Sogi, T. Yano, M. Tsuchiya, Y. Saijo, and E. Itoi, *Effects*

of Low-Intensity Pulsed Ultrasound for Preventing Joint Stiffness in Immobilized Knee Model in Rats, vol. 44. 2018.

[19] M. Aliabouzar, L. G. Zhang, and K. Sarkar, "Lipid coated microbubbles and low intensity pulsed ultrasound enhance chondrogenesis of human mesenchymal stem cells in 3d printed scaffolds," *Scientific Reports*, vol. 6, p. 37728, 2016.

[20] A. Harrison, S. Lin, N. Pounder, and Y. Mikuni-Takagaki, "Mode and mechanism of low intensity pulsed ultrasound (lipus) in fracture repair," *Ultrasonics*, vol. 70, pp. 45–52, 2016.

[21] NICE, "Low-intensity pulsed ultrasound to promote healing of delayed-union and non-union fractures," 2018.

[22] S. Schandelmaier, A. Kaushal, L. Lytvyn, D. Heels-Ansdell, R. A. C. Siemieniuk, T. Agoritsas, G. H. Guyatt, P. O. Vandvik, R. Couban, B. Mollon, and J. W. Busse, "Low intensity pulsed ultrasound for bone healing: systematic review of randomized controlled trials," *BMJ*, vol. 356, p. j656, 2017.

[23] J. A. Buza and T. Einhorn, *Bone healing in 2016*, vol. 13. 2016.

[24] V. Campana, G. Milano, E. Pagano, M. Barba, C. Cicione, G. Salonna, W. Lattanzi, and G. Logroscino, "Bone substitutes in orthopaedic surgery: from basic science to clinical practice," *Journal of Materials Science: Materials in Medicine*, vol. 25, no. 10, pp. 2445–2461, 2014.

[25] M. Bez, D. Sheyn, W. Tawackoli, P. Avalos, G. Shapiro, J. C. Giaconi, X. Da, S. Ben David, J. Gavrity, H. A. Awad, H. W. Bae, E. J. Ley, T. J. Kremen, Z. Gazit, K. W. Ferrara, G. Pelled, and D. Gazit, "In situ bone tissue engineering via ultrasound-mediated gene delivery to endogenous progenitor cells in mini-pigs," *Science Translational Medicine*, vol. 9, p. 3128, 2017.

[26] E. Stride, N. Evans, and D. Carugo, "Case for support combined nds 030517," 2017.

[27] E. J. Carbone, K. Rajpura, B. N. Allen, E. Cheng, B. D. Ulery, and K. W. H. Lo, "Osteotropic nanoscale drug delivery systems based on small molecule bone-targeting moieties," *Nanomedicine: Nanotechnology, Biology and Medicine*, vol. 13, no. 1, pp. 37–47, 2017.

[28] I. Alencastre, D. Sousa, C. Alves, L. Leitão, E. Neto, P. Aguiar, and M. Lamghari, "Delivery of pharmaceutics to bone: nanotechnologies, high-throughput processing and in silico mathematical models," *European Cells and Materials*, vol. 30, pp. 355–381, 2016.

[29] W. Gu, C. Wu, J. Chen, and Y. Xiao, "Nanotechnology in the targeted drug delivery for bone diseases and bone regeneration," *International Journal of Nanomedicine*, vol. 8, pp. 2305–2317, 2013.

[30] H. Cheng, A. Chawla, Y. Yang, Y. Li, J. Zhang, H. L. Jang, and A. Khademhosseini, "Development of nanomaterials for bone-targeted drug delivery," *Drug Discovery Today*, vol. 22, no. 9, pp. 1336–1350, 2017.

[31] Olympus, *What is Ultrasound? - Retrieved from: https://www.olympus-ims.com/en/ndt-tutorials/flaw-detection/ultrasound/.* 2020.

[32] M. Shiwa and T. Kishi, *NDT-based Assessment of Damage: An Overview*, pp. 1–8. Oxford: Elsevier, 2005.

[33] J. E. Wilhjelm, A. Illum, M. Kristensson, and O. T. Anderson, "Medical diagnostic ultrasound - physical principles and imaging," *Biomedical Engineering, DTU Elektro, Technical University of Denmark*, 2016.

[34] Khayyam, *Reflective Water with GLSL, Part II - Retrieved from: http://khayyam.kaplinski.com/2011/10/reflective-water-with-glsl-part-ii.html.* 2011.

[35] J. Erb, *Basic principles of physics in echocardiographic imaging and Doppler techniques*, pp. 13–33. Cambridge: Cambridge University Press, 2010.

[36] WHO, *Manual of Diagnostic Ultrasound*. Malta: Gutemberg Press Ltd, 2011.

[37] E. Bossy, M. Talmant, and P. Laugier, "Effect of bone cortical thickness on velocity measurements using ultrasonic axial transmission: A 2d simulation study," *The Journal of the Acoustical Society of America*, vol. 112, no. 1, pp. 297–307, 2002.

[38] E. Bossy, M. Talmant, and P. Laugier, "Three-dimensional simulations of ultrasonic axial transmission velocity measurement on cortical bone models," *The Journal of the Acoustical Society of America*, vol. 115, no. 5, pp. 2314–2324, 2004.

[39] V. C. Protopappas, M. G. Vavva, D. I. Fotiadis, and K. N. Malizos, "Ultrasonic monitoring of bone fracture healing," *IEEE Transactions on Ultrasonics, Ferroelectrics, and Frequency Control*, vol. 55, no. 6, pp. 1243–1255, 2008.

[40] C. McEwan, J. Owen, E. Stride, C. Fowley, H. Nesbitt, D. Cochrane, C. C. Coussios, M. Borden, N. Nomikou, A. P. McHale, and J. F. Callan, "Oxygen carrying microbubbles for enhanced sonodynamic therapy of hypoxic tumours," *Journal of Controlled Release*, vol. 203, pp. 51–56, 2015.

[41] M. A. Elnaggar, R. Subbiah, D. K. Han, and Y. K. Joung, "Lipid-based carriers for controlled delivery of nitric oxide," *Expert Opinion on Drug Delivery*, vol. 14, no. 12, pp. 1341–1353, 2017.

[42] E. Stride and M. Edirisinghe, "Novel microbubble preparation technologies," *Soft Matter*, vol. 4, no. 12, pp. 2350–2359, 2008.

[43] J.-M. Escoffre and A. Bouakaz, *Therapeutic Ultrasound*. Springer International Publishing, 1 ed., 2016.

[44] E. Stride, T. Segers, G. Lajoinie, S. Cherkaoui, T. Bettinger, M. Versluis, and M. Borden, "Microbubble agents: New directions," *Ultrasound in Medicine Biology*, vol. 46, no. 6, pp. 1326–1343, 2020.

[45] S. Roovers, T. Segers, G. Lajoinie, J. Deprez, M. Versluis, S. C. De Smedt, and I. Lentacker, "The role of ultrasound-driven microbubble dynamics in drug delivery: from microbubble fundamentals to clinical translation," *Langmuir*, vol. 35, no. 31, pp. 10173–10191, 2019.

[46] M. B. Callens, E. Verboven, and K. Van Den Abeele, "Investigation of microbubble composition on ultrasonic dispersion properties for biosensing applications," *Physics Procedia*, vol. 70, pp. 1237–1240, 2015.

[47] S. M. Fix, A. G. Nyankima, M. D. McSweeney, J. K. Tsuruta, S. K. Lai, and P. A. Dayton, "Accelerated clearance of ultrasound contrast agents containing

polyethylene glycol is associated with the generation of anti-polyethylene glycol antibodies," *Ultrasound in Medicine and Biology*, vol. 44, no. 6, pp. 1266–1280, 2018.

[48] M. Kaya, T. S. Gregory, and P. A. Dayton, "Changes in lipid-encapsulated microbubble population during continuous infusion and methods to maintain consistency," *Ultrasound in medicine and biology*, vol. 35, no. 10, pp. 1748–1755, 2009.

[49] R. Cavalli, M. Soster, and M. Argenziano, "Nanobubbles: a promising efficienft tool for therapeutic delivery," *Therapeutic Delivery*, vol. 7, no. 2, pp. 117–138, 2016.

[50] T. Biosonics, *Microbubble contrast Agent - Retrieved from: http://www.trust-biosonics.com/technology.* 2021.

[51] S. R. Sirsi and M. A. Borden, "Microbubble compositions, properties and biomedical applications," *Bubble Science, Engineering and Technology*, vol. 1, no. 1-2, pp. 3–17, 2009.

[52] M. A. Borden, *Lipid-Coated Nanodrops and Microbubbles*, pp. 1–26. Singapore: Springer Singapore, 2015.

[53] M. Parhizkar, M. Edirisinghe, and E. Stride, "The effect of surfactant type and concentration on the size and stability of microbubbles produced in a capillary embedded t-junction device," *RSC Advances*, vol. 5, no. 14, pp. 10751–10762, 2015.

[54] R. P. Garay, R. El-Gewely, J. K. Armstrong, G. Garratty, and P. Richette, "Antibodies against polyethylene glycol in healthy subjects and in patients treated with peg-conjugated agents," *Expert Opinion on Drug Delivery*, vol. 9, no. 11, pp. 1319–1323, 2012.

[55] P. Grenier, I. M. d. O. Viana, E. M. Lima, and N. Bertrand, "Anti-polyethylene glycol antibodies alter the protein corona deposited on nanoparticles and the physiological pathways regulating their fate in vivo," *Journal of Controlled Release*, vol. 287, pp. 121–131, 2018.

[56] N. De Jong, *Microbubbles*, pp. 1138–1139. Berlin, Heidelberg: Springer Berlin Heidelberg, 2008.

[57] Z. Fan, R. E. Kumon, and C. X. Deng, "Mechanisms of microbubble-facilitated sonoporation for drug and gene delivery," *Therapeutic delivery*, vol. 5, no. 4, pp. 467–486, 2014.

[58] Z. Izadifar, P. Babyn, and D. Chapman, "Mechanical and biological effects of ultrasound: A review of present knowledge," *Ultrasound in Medicine and Biology*, vol. 43, no. 6, pp. 1085–1104, 2017.

[59] M. Shankar, Hariharan and M. P. Pagel, Paul S., "Potential adverse ultrasound-related biological effects: A critical review," *Anesthesiology: The Journal of the American Society of Anesthesiologists*, vol. 115, no. 5, pp. 1109–1124, 2011.

[60] T. G. Leighton, *The Acoustic Bubble. Chapter 4 - The Forced Bubble*, pp. 287–438. Academic Press, 1994.

[61] M. Wiklund, R. Green, and M. Ohlin, "Acoustofluidics 14: Applications of acoustic streaming in microfluidic devices," *Lab on a Chip*, vol. 12, no. 14, pp. 2438–2451, 2012.

[62] V. Pereno, M. Aron, O. Vince, C. Mannaris, A. Seth, M. de Saint Victor, G. Lajoinie, M. Versluis, C. Coussios, D. Carugo, and E. Stride, "Layered acoustofluidic resonators for the simultaneous optical and acoustic characterisation of cavitation dynamics, microstreaming, and biological effects," *Biomicrofluidics*, vol. 12, no. 3, p. 034109, 2018.

[63] C. Yang, Y. Li, M. Du, and Z. Chen, "Recent advances in ultrasound-triggered therapy," *Journal of Drug Targeting*, vol. 27, no. 1, pp. 33–50, 2019.

[64] P. A. Dayton, S. Zhao, S. H. Bloch, P. Schumann, K. Penrose, T. O. Matsunaga, R. Zutshi, A. Doinikov, and K. W. Ferrara, "Application of ultrasound to selectively localize nanodroplets for targeted imaging and therapy," *Molecular imaging*, vol. 5, no. 3, pp. 160–174, 2006.

[65] N. Rapoport, "Phase-shift, stimuli-responsive perfluorocarbon nanodroplets for drug delivery to cancer," *Wiley interdisciplinary reviews. Nanomedicine and nanobiotechnology*, vol. 4, no. 5, pp. 492–510, 2012.

[66] H. Sarin, "Physiologic upper limits of pore size of different blood capillary types and another perspective on the dual pore theory of microvascular permeability," *Journal of angiogenesis research*, vol. 2, pp. 14–14, 2010.

[67] C. Hong, A. A. Brayman, and T. J. Matula, "Microbubble dynamics in microvessels: Observations of microvessel dilation, invagination and rupture," in *2008 IEEE Ultrasonics Symposium*, pp. 1163–1166.

[68] Dreamstime, *Étapes de la réparation de fracture - Retrieved from: https://fr.dreamstime.com/illustration-stock-etapes-de-la-reparation-de-fracture-image79043755.* 2020.

[69] M. Marenzana and T. R. Arnett, "The key role of the blood supply to bone," *Bone Research*, vol. 1, no. 3, pp. 203–215, 2013.

[70] Y. Wang, M. R. Newman, M. Ackun-Farmmer, M. P. Baranello, T.-J. Sheu, J. E. Puzas, and D. S. W. Benoit, "Fracture-targeted delivery of beta-catenin agonists via peptide-functionalized nanoparticles augments fracture healing," *ACS Nano*, vol. 11, no. 9, pp. 9445–9458, 2017.

[71] J. Y. Lee, D. Carugo, C. Crake, J. Owen, M. de Saint Victor, A. Seth, C. Coussios, and E. Stride, "Nanoparticle-loaded protein-polymer nanodroplets for improved stability and conversion efficiency in ultrasound imaging and drug delivery," *Adv Mater*, vol. 27, no. 37, pp. 5484–92, 2015.

[72] J. Feshitan, C. Chen, J. J Kwan, and M. A Borden, "Microbubble size isolation by differential centrifugation," *Journal of Colloid and Interface Science*, vol. 329, pp. 316–24, 2008.

[73] J. J. Kwan and M. A. Borden, "Lipid monolayer collapse and microbubble stability," *Advances in Colloid and Interface Science*, vol. 183-184, no. Supplement C, pp. 82–99, 2012.

[74] Y. Luan, G. Lajoinie, E. Gelderblom, I. Skachkov, A. F. W. van der Steen, H. J. Vos, M. Versluis, and N. De Jong, "Lipid shedding from single oscillating

microbubbles," *Ultrasound in Medicine and Biology*, vol. 40, no. 8, pp. 1834–1846, 2014.

[75] E. C. Unger, T. Porter, W. Culp, R. Labell, T. Matsunaga, and R. Zutshi, "Therapeutic applications of lipid-coated microbubbles," *Advanced Drug Delivery Reviews*, vol. 56, no. 9, pp. 1291–1314, 2004.

[76] Y. Shen, M. L. Longo, and R. L. Powell, "Stability and rheological behavior of concentrated monodisperse food emulsifier coated microbubble suspensions," *Journal of Colloid and Interface Science*, vol. 327, no. 1, pp. 204–210, 2008.

[77] P. Taylor, "Ostwald ripening in emulsions," *Advances in Colloid and Interface Science*, vol. 75, no. 2, pp. 107–163, 1998.

[78] M. A. Borden and M. Longo, "Dissolution behavior of lipid monolayer-coated, air-filled microbubbles: Effect of lipid hydrophobic chain length," *Langmuir*, vol. 18, 2002.

[79] M. A. Borden and M. L. Longo, "Oxygen permeability of fully condensed lipid monolayers," *The Journal of Physical Chemistry B*, vol. 108, no. 19, pp. 6009–6016, 2004.

[80] T. Segers, L. de Rond, N. de Jong, M. Borden, and M. Versluis, "Stability of monodisperse phospholipid-coated microbubbles formed by flow-focusing at high production rates," *Langmuir*, vol. 32, no. 16, pp. 3937–3944, 2016.

[81] N. Pagureva, S. Tcholakova, K. Rusanova, N. Denkov, and T. Dimitrova, "Factors affecting the coalescence stability of microbubbles," *Colloids and Surfaces A: Physicochemical and Engineering Aspects*, vol. 508, pp. 21–29, 2016.

[82] A. L. Y. Kee and B. M. Teo, "Biomedical applications of acoustically responsive phase shift nanodroplets: current status and future directions," *Ultrasonics Sonochemistry*, vol. 56, pp. 37–45, 2019.

[83] S. Mullick Chowdhury, T. Lee, and J. K. Willmann, "Ultrasound-guided drug delivery in cancer," *Ultrasonography*, vol. 36, no. 3, pp. 171–184, 2017.

[84] K. Loskutova, D. Grishenkov, and M. Ghorbani, "Review on acoustic droplet vaporization in ultrasound diagnostics and therapeutics," *Biomed Res Int*, vol. 2019, p. 9480193, 2019.

[85] Y. Zhou, "Application of acoustic droplet vaporization in ultrasound therapy," *Journal of Therapeutic Ultrasound*, vol. 3, no. 20, 2015.

[86] K.-i. Kawabata, N. Sugita, H. Yoshikawa, T. Azuma, and S.-I. Umemura, *Nanoparticles with Multiple Perfluorocarbons for Controllable Ultrasonically Induced Phase Shifting*, vol. 44. 2005.

[87] S. Zullino, M. Argenziano, I. Stura, C. Guiot, and R. Cavalli, "From micro- to nano-multifunctional theranostic platform: Effective ultrasound imaging is not just a matter of scale," *Molecular imaging*, vol. 17, 2018.

[88] H. Lea-Banks, M. A. O'Reilly, and K. Hynynen, "Ultrasound-responsive droplets for therapy: A review," *Journal of Controlled Release*, vol. 293, pp. 144–154, 2019.

[89] N. Rapoport, "Drug-loaded perfluorocarbon nanodroplets for ultrasound-mediated drug delivery," *Adv Exp Med Biol*, vol. 880, pp. 221–41, 2016.

[90] T. Şen, O. Tüfekçioğlu, and Y. Koza, "Mechanical index," *Anatolian journal of cardiology*, vol. 15, no. 4, pp. 334–336, 2015.

[91] P. S. Sheeran and P. A. Dayton, "Improving the performance of phase-change perfluorocarbon droplets for medical ultrasonography: Current progress, challenges, and prospects," *Scientifica*, vol. 2014, p. 579684, 2014.

[92] P. S. Sheeran, S. Luois, L. Mullin, T. O. Matsunaga, and P. A. Dayton, "Design of ultrasonically-activatable nanoparticles using low boiling point perfluorocarbons," *Biomaterials*, vol. 33, no. 11, pp. 3262–3269, 2012.

[93] P. S. Sheeran, T. O. Matsunaga, and P. A. Dayton, "Phase-transition thresholds and vaporization phenomena for ultrasound phase-change nanoemulsions assessed via high-speed optical microscopy," *Phys Med Biol*, vol. 58, no. 13, pp. 4513–34, 2013.

[94] C.-Y. Lin and W. G. Pitt, "Acoustic droplet vaporization in biology and medicine," *BioMed Research International*, vol. 2013, p. 13, 2013.

[95] K. Kooiman, S. Roovers, S. A. G. Langeveld, R. T. Kleven, H. Dewitte, M. A. O'Reilly, J.-M. Escoffre, A. Bouakaz, M. D. Verweij, K. Hynynen, I. Lentacker, E. Stride, and C. K. Holland, "Ultrasound-responsive cavitation nuclei for therapy and drug delivery," *Ultrasound in Medicine Biology*, vol. 46, no. 6, pp. 1296–1325, 2020.

[96] O. Shpak, M. Verweij, H. J. Vos, N. de Jong, D. Lohse, and M. Versluis, "Acoustic droplet vaporization is initiated by superharmonic focusing," *Proc Natl Acad Sci U S A*, vol. 111, no. 5, pp. 1697–702, 2014.

[97] S. Yarmoska, H. Yoon, and S. Emelianov, "Lipid shell composition plays a critical role in the stable size reduction of perfluorocarbon nanodroplets," *Ultrasound in medicine biology*, vol. 45, pp. 1489–1499, 2019.

[98] N. Anton, F. Hallouard, M. F. Attia, and T. F. Vandamme, *Nano-emulsions for Drug Delivery and Biomedical Imaging*, pp. 273–300. Cham: Springer International Publishing, 2016.

[99] X. Xu, R. Song, M. He, C. Peng, M. Yu, Y. Hou, H. Qiu, R. Zou, and S. Yao, "Microfluidic production of nanoscale perfluorocarbon droplets as liquid contrast agents for ultrasound imaging," *Lab on a Chip*, vol. 17, no. 20, pp. 3504–3513, 2017.

[100] T. D. Martz, D. Bardin, P. S. Sheeran, A. P. Lee, and P. A. Dayton, "Microfluidic generation of acoustically active nanodroplets," *Small (Weinheim an der Bergstrasse, Germany)*, vol. 8, no. 12, pp. 1876–1879, 2012.

[101] P. S. Sheeran, V. P. Wong, S. Luois, R. J. McFarland, W. D. Ross, S. Feingold, T. O. Matsunaga, and P. A. Dayton, "Decafluorobutane as a phase-change contrast agent for low-energy extravascular ultrasonic imaging," *Ultrasound in medicine and biology*, vol. 37, no. 9, pp. 1518–1530, 2011.

[102] K. Yoo, W. R. Walker, R. Williams, C. Tremblay-Darveau, P. N. Burns, and P. S. Sheeran, "Impact of encapsulation on in vitro and in vivo performance of volatile nanoscale phase-shift perfluorocarbon droplets," *Ultrasound in Medicine Biology*, vol. 44, no. 8, pp. 1836–1852, 2018.

[103] Z. Gao, A. M. Kennedy, D. A. Christensen, and N. Y. Rapoport, "Drug-loaded nano/microbubbles for combining ultrasonography and targeted chemotherapy," *Ultrasonics*, vol. 48, no. 4, pp. 260–70, 2008.

[104] A. Ishijima, J. Tanaka, T. Azuma, K. Minamihata, S. Yamaguchi, E. Kobayashi, T. Nagamune, and I. Sakuma, "The lifetime evaluation of vapourised phase-change nano-droplets," *Ultrasonics*, vol. 69, pp. 97–105, 2016.

[105] M. Wan, Y. Feng, and G. t. Haar, *Cavitation in Biomedicine*. Springer Netherlands, 2015.

[106] D. A. King, M. J. Malloy, A. C. Roberts, A. Haak, C. C. Yoder, and W. D. O'Brien, "Determination of postexcitation thresholds for single ultrasound contrast agent microbubbles using double passive cavitation detection," *The Journal of the Acoustical Society of America*, vol. 127, no. 6, pp. 3449–3455, 2010.

[107] M. Gyöngy and C.-C. Coussios, "Passive cavitation mapping for localization and tracking of bubble dynamics," *The Journal of the Acoustical Society of America*, vol. 128, no. 4, pp. EL175–EL180, 2010.

[108] Y. Gu, C. Chen, J. Tu, X. Guo, H. Wu, and D. Zhang, *Harmonic responses and cavitation activity of encapsulated microbubbles coupled with magnetic nanoparticles*, vol. 29. 2016.

[109] T. Giesecke and K. Hynynen, "Ultrasound-mediated cavitation thresholds of liquid perfluorocarbon droplets in vitro," *Ultrasound in Medicine and Biology*, vol. 29, no. 9, pp. 1359–1365, 2003.

[110] W.-S. Chen, T. J. Matula, A. A. Brayman, and L. A. Crum, "A comparison of the fragmentation thresholds and inertial cavitation doses of different ultrasound contrast agents," *The Journal of the Acoustical Society of America*, vol. 113, no. 1, pp. 643–651, 2003.

[111] P. Chang, W.-S. Chen, P. Mourad, S. L. Poliachik, and L. Crum, *Thresholds for inertial cavitation in Albunex suspensions under pulsed ultrasound conditions*, vol. 48. 2001.

[112] A. Y. Ammi, R. O. Cleveland, J. Mamou, G. I. Wang, S. L. Bridal, and W. D. O'Brien, "Ultrasonic contrast agent shell rupture detected by inertial cavitation and rebound signals," *IEEE transactions on ultrasonics, ferroelectrics, and frequency control*, vol. 53, no. 1, pp. 126–136, 2006.

[113] D. A. King, M. Santin, M. J. Malloy, A. C. Roberts, A. Haak, J. Foiret, S. Haupert, S. Jafari, L. Bridal, and W. D. O. Brien, "Using passive cavitation detection to observe postexcitation response of ultrasound contrast agents," in *2009 IEEE International Ultrasonics Symposium*, pp. 1286–1289.

[114] N. Audio, *Fast Fourier Transform FFT - Basics - Retrieved from: https://www.nti-audio.com/en/support/know-how/fast-fourier-transform-fft.* 2020.

[115] P. Kumar, *Fundamentals and Techniques of Biophysics and Molecular Biology - Chapter 6: Microscopy*, book section Chapter 6. 2018.

[116] J. Vangindertael, R. Camacho, W. Sempels, H. Mizuno, P. Dedecker, and K. P. F. Janssen, "An introduction to optical super-resolution microscopy for the adventurous biologist," *Methods Appl Fluoresc*, vol. 6, no. 2, p. 022003, 2018.

[117] A. S. Holik, *Optical Microscopy*, pp. 6458–6463. Oxford: Elsevier, 2001.

[118] M. Ali, D. Magee, and U. Dasgupta, "Texas instruments: Signal processing overview of ultrasound systems for medical imaging," Optional.

[119] J. Jensen, *Ultrasound Imaging and Its Modeling*, vol. 84, pp. 135–166. 2002.

[120] Nysora, *Physics of Ultrasound - Retrieved from: https://www.nysora.com/foundations-of-regional-anesthesia/equipment/physics-of-ultrasound/.* 2020.

[121] M. Versluis, "High-speed imaging in fluids," *Experiments in Fluids*, vol. 54, no. 2, p. 1458, 2013.

[122] S. T. Thoroddsen, T. G. Etoh, and K. Takehara, "High-speed imaging of drops and bubbles," *Annual Review of Fluid Mechanics*, vol. 40, no. 1, pp. 257–285, 2008.

[123] G. Lajoinie, I. De Cock, C. C. Coussios, I. Lentacker, S. Le Gac, E. Stride, and M. Versluis, "In vitro methods to study bubble-cell interactions: Fundamentals and therapeutic applications," *Biomicrofluidics*, vol. 10, no. 1, p. 011501, 2016.

[124] S. M. van der Meer, B. Dollet, M. M. Voormolen, C. T. Chin, A. Bouakaz, N. de Jong, M. Versluis, and D. Lohse, "Microbubble spectroscopy of ultrasound contrast agents," *The Journal of the Acoustical Society of America*, vol. 121, no. 1, pp. 648–656, 2007.

[125] P. Marmottant, S. van der Meer, M. Emmer, M. Versluis, N. de Jong, S. Hilgenfeldt, and D. Lohse, "A model for large amplitude oscillations of coated bubbles accounting for buckling and rupture," *The Journal of the Acoustical Society of America*, vol. 118, no. 6, pp. 3499–3505, 2005.

[126] B. Dollet, S. M. van der Meer, V. Garbin, N. de Jong, D. Lohse, and M. Versluis, "Nonspherical oscillations of ultrasound contrast agent microbubbles," *Ultrasound Med Biol*, vol. 34, no. 9, pp. 1465–73, 2008.

[127] J. Sijl, B. Dollet, M. Overvelde, V. Garbin, T. Rozendal, N. de Jong, D. Lohse, and M. Versluis, "Subharmonic behavior of phospholipid-coated ultrasound contrast agent microbubbles," *The Journal of the Acoustical Society of America*, vol. 128, no. 5, pp. 3239–3252, 2010.

[128] E. C. Gelderblom, H. J. Vos, F. Mastik, T. Faez, Y. Luan, T. J. A. Kokhuis, A. F. W. van der Steen, D. Lohse, N. de Jong, and M. Versluis, "Brandaris 128 ultra-high-speed imaging facility: 10 years of operation, updates, and enhanced features," *Review of Scientific Instruments*, vol. 83, no. 10, p. 103706, 2012.

[129] G. Menikou and C. Damianou, "Acoustic and thermal characterization of agar based phantoms used for evaluating focused ultrasound exposures," *J Ther Ultrasound*, vol. 5, p. 14, 2017.

[130] M. O. Culjat, D. Goldenberg, P. Tewari, and R. S. Singh, "A review of tissue substitutes for ultrasound imaging," *Ultrasound Med Biol*, vol. 36, no. 6, pp. 861–73, 2010.

[131] A. D. Maxwell, T.-Y. Wang, L. Yuan, A. P. Duryea, Z. Xu, and C. A. Cain, "A tissue phantom for visualization and measurement of ultrasound-induced

cavitation damage," *Ultrasound in medicine biology*, vol. 36, no. 12, pp. 2132–2143, 2010.

[132] S. Yang, Y. J. Chen, R. Cui, H. X. Zhao, Y. Zhao, Z. Q. Liu, Y. Yu, X. Y. Shao, and Q. Xu, "High-intensity focused ultrasound ablation: An in vitro agarose gel model," *International Journal of Clinical and Experimental Medicine*, vol. 10, pp. 15302–15308, 2017.

[133] L. Nolting, P. Hunt, T. Cook, and B. Douglas, "An inexpensive and easy ultrasound phantom: A novel use for spam," *J Ultrasound Med*, vol. 35, no. 4, pp. 819–22, 2016.

[134] E. Varoni, M. Tschon, B. Palazzo, P. Nitti, L. Martini, and L. Rimondini, "Agarose gel as biomaterial or scaffold for implantation surgery: characterization, histological and histomorphometric study on soft tissue response," *Connect Tissue Res*, vol. 53, no. 6, pp. 548–54, 2012.

[135] V. Normand, D. L. Lootens, E. Amici, K. P. Plucknett, and P. Aymard, "New insight into agarose gel mechanical properties," *Biomacromolecules*, vol. 1, no. 4, pp. 730–738, 2000.

[136] T. Morita, T. Narita, S.-a. Mukai, M. Yanagisawa, and M. Tokita, "Phase behaviors of agarose gel," *AIP Advances*, vol. 3, no. 4, p. 042128, 2013.

[137] S. P. Dodd, A. W. Miles, S. Gheduzzi, V. F. Humphrey, and J. L. Cunningham, "Modelling the effects of different fracture geometries and healing stages on ultrasound signal loss across a long bone fracture," *Computer Methods in Biomechanics and Biomedical Engineering*, vol. 10, no. 5, pp. 371–375, 2007.

[138] R. Gramiak and P. M. Shah, "Echocardiography of the aortic root," *Investigative Radiology*, vol. 3, no. 5, pp. 356–366, 1968.

[139] V. A. Salgaonkar, S. Datta, C. K. Holland, and T. D. Mast, "Passive cavitation imaging with ultrasound arrays," *The Journal of the Acoustical Society of America*, vol. 126, no. 6, pp. 3071–3083, 2009.

[140] E. Stride and M. Edirisinghe, "Novel preparation techniques for controlling microbubble uniformity: a comparison," *Medical and Biological Engineering and Computing*, vol. 47, no. 8, pp. 883–892, 2009.

[141] R. Shih and A. P. Lee, "Post-formation shrinkage and stabilization of microfluidic bubbles in lipid solution," *Langmuir*, vol. 32, no. 8, pp. 1939–1946, 2016.

[142] T. A. M. Rovers, G. Sala, E. van der Linden, and M. B. J. Meinders, "Effect of temperature and pressure on the stability of protein microbubbles," *ACS Applied Materials and Interfaces*, vol. 8, no. 1, pp. 333–340, 2016.

[143] J. Owen, S. Kamila, S. Shrivastava, D. Carugo, J. Bernardino de la Serna, C. Mannaris, V. Pereno, R. Browning, E. Beguin, A. P. McHale, J. F. Callan, and E. Stride, "The role of peg-40-stearate in the production, morphology, and stability of microbubbles," *Langmuir*, vol. 35, no. 31, pp. 10014–10024, 2018.

[144] E. Talu, M. M. Lozano, R. L. Powell, P. A. Dayton, and M. L. Longo, "Long-term stability by lipid coating monodisperse microbubbles formed by a flow-focusing device," *Langmuir*, vol. 22, no. 23, pp. 9487–9490, 2006.

[145] S. Kilic and E. S. Bolukcu, "Phase behavior of dspc/peg40st mixtures at higher emulsifier contents," *Colloids and Surfaces B: Biointerfaces*, vol. 171, pp. 368–376, 2018.

[146] R. Abdalkader, S. Kawakami, J. Unga, Y. Higuchi, R. Suzuki, K. Maruyama, F. Yamashita, and M. Hashida, "The development of mechanically formed stable nanobubbles intended for sonoporation-mediated gene transfection," *Drug Delivery*, vol. 24, no. 1, pp. 320–327, 2017.

[147] S. Ross, M. Gasparini, and L. Pistone, *Introduzione alla statistica*. Apogeo, 2008.

[148] Laerd, *Statistics - Retrieved from: https://statistics.laerd.com/*. 2020.

[149] G. D. Ruxton and G. Beauchamp, "Time for some a priori thinking about post hoc testing," *Behavioral Ecology*, vol. 19, no. 3, pp. 690–693, 2008. 10.1093/beheco/arn020.

[150] P. A. Dayton, H. Nguyen, E. Talu, K. Hettiarachchi, A. P. Lee, R. L. Powell, and M. L. Longo, "P2a-8 lipid-stabilized monodisperse microbubbles produced by flow focusing for use as ultrasound contrast agents," in *2006 IEEE Ultrasonics Symposium*, pp. 1568–1571.

[151] J. L. Chen, A. H. Dhanaliwala, A. J. Dixon, A. L. Klibanov, and J. A. Hossack, "Synthesis and characterization of transiently stable albumin-coated microbubbles via a flow-focusing microfluidic device," *Ultrasound in medicine and biology*, vol. 40, no. 2, pp. 400–409, 2014.

[152] M. Borden, D. Kruse, C. Caskey, S. Zhao, P. Dayton, and K. Ferrara, "Influence of lipid shell physicochemical properties on ultrasound-induced destruction," *IEEE transactions on ultrasonics, ferroelectrics, and frequency control*, vol. 52, pp. 1992–2002, 2005.

[153] Y. Sheng, E. Beguin, H. Nesbitt, S. Kamila, J. Owen, L. C. Barnsley, B. Callan, C. O'Kane, N. Nomikou, R. Hamoudi, M. A. Taylor, M. Love, P. Kelly, D. O'Rourke, E. Stride, A. P. McHale, and J. F. Callan, "Magnetically responsive microbubbles as delivery vehicles for targeted sonodynamic and antimetabolite therapy of pancreatic cancer," *Journal of Controlled Release*, vol. 262, pp. 192–200, 2017.

[154] J. Esmaeili, F. S. Rezaei, F. M. Beram, and A. Barati, "Integration of microbubbles with biomaterials in tissue engineering for pharmaceutical purposes," *Heliyon*, vol. 6, no. 6, p. e04189, 2020.

[155] H. Lin, J. Chen, and C. Chen, "A novel technology: microfluidic devices for microbubble ultrasound contrast agent generation," *Medical and Biological Engineering and Computing*, vol. 54, no. 9, pp. 1317–1330, 2016.

[156] S. B. Feinstein, M. W. Keller, R. E. Kerber, B. Vandenberg, J. Hoyte, C. Kutruff, J. Bingle, T. D. Fraker, R. Chappell, and A. H. Welsh, "Sonicated echocardiographic contrast agents: Reproducibility studies," *Journal of the American Society of Echocardiography*, vol. 2, no. 2, pp. 125–131, 1989.

[157] K. Pancholi, E. Stride, and M. Edirisinghe, "Dynamics of bubble formation in highly viscous liquids," *Langmuir*, vol. 24, no. 8, pp. 4388–4393, 2008.

[158] Drug, *Glycerin - Retrieved from: http://drug.pharmacy.psu.ac.th/article/file/239GLYCERIN20Glycerol.pdf*. 2020.

[159] A. Barrefelt, Y. Zhao, M. K. Larsson, G. Egri, R. V. Kuiper, J. Hamm, M. Saghafian, K. Caidahl, T. B. Brismar, P. Aspelin, R. Heuchel, M. Muhammed,

L. Dähne, and M. Hassan, "Fluorescence labeled microbubbles for multimodal imaging," *Biochemical and Biophysical Research Communications*, vol. 464, no. 3, pp. 737–742, 2015.

[160] C. E. Schutt, S. D. Ibsen, M. J. Benchimol, M. J. Hsu, and S. C. Esener, "Manipulating nanoscale features on the surface of dye-loaded microbubbles to increase their ultrasound-modulated fluorescence output," *Small (Weinheim an der Bergstrasse, Germany)*, vol. 10, no. 16, pp. 3316–3324, 2014.

[161] C. A. Grant, J. E. McKendry, and S. D. Evans, "Temperature dependent stiffness and visco-elastic behaviour of lipid coated microbubbles using atomic force microscopy," *Soft Matter*, vol. 8, no. 5, pp. 1321–1326, 2012.

[162] H. Shekhar, N. J. Smith, J. L. Raymond, and C. K. Holland, "Effect of temperature on the size distribution, shell properties, and stability of definity(®)," *Ultrasound in medicine and biology*, vol. 44, no. 2, pp. 434–446, 2018.

[163] J. Eisenbrey, A. Daecher, M. R. Kramer, and F. Forsberg, "Effects of needle and catheter size on commercially available ultrasound contrast agent enhancement in vitro," *Ultrasound in Medicine and Biology*, vol. 41, no. 4, p. S134, 2015.

[164] S. Garg, A. A. Thomas, and M. A. Borden, "The effect of lipid monolayer in-plane rigidity on in vivo microbubble circulation persistence," *Biomaterials*, vol. 34, no. 28, pp. 6862–6870, 2013.

[165] T. van Rooij, Y. Luan, G. Renaud, A. F. W. van der Steen, M. Versluis, N. de Jong, and K. Kooiman, "Non-linear response and viscoelastic properties of lipid-coated microbubbles: Dspc versus dppc," *Ultrasound in Medicine and Biology*, vol. 41, no. 5, pp. 1432–1445, 2015.

[166] D. Carugo, M. Aron, E. Sezgin, J. Bernardino de la Serna, M. K. Kuimova, C. Eggeling, and E. Stride, "Modulation of the molecular arrangement in artificial and biological membranes by phospholipid-shelled microbubbles," *Biomaterials*, vol. 113, pp. 105–117, 2017.

[167] R. J. Paproski and R. J. Zemp, "Comparing nanodroplets and microbubbles for enhancing ultrasound-mediated gene transfection," *2013 IEEE International Ultrasonics Symposium (IUS)*, 2013.

[168] N. Y. Rapoport, A. L. Efros, D. A. Christensen, A. M. Kennedy, and K.-H. Nam, "Microbubble generation in phase-shift nanoemulsions used as anticancer drug carriers," *Bubble science engineering and technology*, vol. 1, no. 1-2, pp. 31–39, 2009.

[169] N. Rapoport, A. Payne, C. Dillon, J. Shea, C. Scaife, and R. Gupta, "Focused ultrasound-mediated drug delivery to pancreatic cancer in a mouse model," *Journal of therapeutic ultrasound*, vol. 1, pp. 11–11, 2013.

[170] U. Bilati, E. Allémann, and E. Doelker, "Sonication parameters for the preparation of biodegradable nanocapsules of controlled size by the double emulsion method," *Pharmaceutical Development and Technology*, vol. 8, no. 1, pp. 1–9, 2003.

[171] J. Liu, T. Shang, F. Wang, Y. Cao, L. Hao, J. Ren, H. Ran, Z. Wang, P. Li, and Z. Du, "Low-intensity focused ultrasound (lifu)-induced acoustic droplet vaporization in phase-transition perfluoropentane nanodroplets modified by folate for ultrasound molecular imaging," *International journal of nanomedicine*, vol. 12, pp. 911–923, 2017.

[172] M. Fabiilli, *Ultrasound-triggered Drug Delivery Using Acoustic Droplet Vaporization*. PhD Thesis, 2010.

[173] S. Guo, A. Shi, S. Xu, X. Du, X. Wang, Y. Zong, A. Bouakaz, and M. Wan, *Lowering of acoustic droplet vaporization threshold via aggregation*, vol. 111. Applied Physics Letters, 2017.

[174] W. University, *Introduction to DLS - Retrieved from: https://warwick.ac.uk/fac/crossfac/sciencecity/programmes/internal/themes/am2/booking/particlesize/introtodls.pdf*. 2018.

[175] P. Glynne-Jones, R. J. Boltryk, and M. Hill, "Acoustofluidics 9: Modelling and applications of planar resonant devices for acoustic particle manipulation," *Lab on a Chip*, vol. 12, no. 8, pp. 1417–1426, 2012.

[176] A. S. Klymchenko, E. Roger, N. Anton, H. Anton, I. Shulov, J. Vermot, Y. Mely, and T. F. Vandamme, "Highly lipophilic fluorescent dyes in nano-emulsions: towards bright non-leaking nano-droplets," *RSC Advances*, vol. 2, no. 31, pp. 11876–11886, 2012.

[177] Lonza, *DMEM - Retrieved from: https://bioscience.lonza.com/lonzabs/US/en/Culture-Media-and-Reagents/p/0000000000181546/Dulbecco27s-Modified-Eagle-Medium-28DMEM29*. 2018.

[178] Merck, *Bovine Serum Albumins - Retrieved from: https://www.sigmaaldrich.com/life-science/biochemicals/biochemical-products.html?TablePage=103994915*. 2018.

[179] Labome, *Fetal Bovine Serum - Retrieved from: https://www.labome.com/method/Fetal-Bovine-Serum.html*. 2012.

[180] X. Zhang, J. Hu, G. Zhao, N. Huang, Y. Tan, L. Pi, Q. Huang, F. Wang, Z. Wang, Z. Wang, and Y. Cheng, "Pegylated plga-based phase shift nanodroplets combined with focused ultrasound for blood brain barrier opening in rats," *Oncotarget*, vol. 8, no. 24, pp. 38927–38936, 2017.

[181] C. J. Harfield, G. Memoli, P. Jones, N. Ovenden, and E. Stride, "Investigating the sensitivity of microbubble acoustic response for biosensing applications," *Proceedings of Meetings on Acoustics*, vol. 19, no. 1, p. 075043, 2013.

[182] R. Asami, T. Ikeda, T. Azuma, S. Umemura, and K.-i. Kawabata, "Acoustic signal characterization of phase change nanodroplets in tissue-mimicking phantom gels," *Japanese Journal of Applied Physics*, vol. 49, no. 7, p. 07HF16, 2010.

[183] C. Mannaris, L. Bau, M. Grundy, M. Gray, H. Lea-Banks, A. Seth, B. Teo, R. Carlisle, E. Stride, and C. C. Coussios, "Microbubbles, nanodroplets and gas-stabilizing solid particles for ultrasound-mediated extravasation of unencapsulated drugs: An exposure parameter optimization study," *Ultrasound Med Biol*, vol. 45, no. 4, pp. 954–967, 2019.

[184] R. Song, C. Peng, X. Xu, R. Zou, and S. Yao, "Facile fabrication of uniform nanoscale perfluorocarbon droplets as ultrasound contrast agents," *Microfluidics and Nanofluidics*, vol. 23, no. 1, p. 12, 2019.

[185] S. Gheduzzi, S. P. Dodd, A. W. Miles, V. F. Humphrey, and J. L. Cunningham, "Numerical and experimental simulation of the effect of long bone fracture healing stages on ultrasound transmission across an idealized fracture," *The Journal of the Acoustical Society of America*, vol. 126, no. 2, pp. 887–894, 2009.

[186] F. Catelani, A. P. M. Ribeiro, C. A. V. Melo, W. C. Pereira, and C. B. Machado, "Ultrasound propagation through bone fractures with reamed intramedullary nailing: results from numerical simulations," *Proceedings of Meetings on Acoustics*, vol. 19, no. 1, p. 075093, 2013.

[187] A. A. Doinikov, J. F. Haac, and P. A. Dayton, "Resonance frequencies of lipid-shelled microbubbles in the regime of nonlinear oscillations," *Ultrasonics*, vol. 49, no. 2, pp. 263–268, 2009.

[188] P. Garcia, T. Histing, J. H. Holstein, M. Klein, M. W. Laschke, R. Matthys, A. Ignatius, B. Wildemann, J. Lienau, A. Peters, B. Willie, G. Duda, L. Claes, T. Pohlemann, and M. D. Menger, "Rodent animal models of delayed bone healing and non-union formation: a comprehensive review," *Eur Cell Mater*, vol. 26, pp. 1–12; discussion 12–4, 2013.

[189] A. Cafarelli, A. Verbeni, A. Poliziani, P. Dario, A. Menciassi, and L. Ricotti, "Tuning acoustic and mechanical properties of materials for ultrasound phantoms and smart substrates for cell cultures," *Acta Biomaterialia*, vol. 49, pp. 368–378, 2017.

[190] H. Azhari, *Basics of Biomedical Ultrasound for Engineers, Appendix A: Typical Acoustic Properties of Tissues*, pp. 313–314. 2010.

[191] Z. Fan, Y. Sun, C. Di, D. Tay, W. Chen, C. X. Deng, and J. Fu, "Acoustic tweezing cytometry for live-cell subcellular modulation of intracellular cytoskeleton contractility," *Scientific Reports*, vol. 3, no. 1, p. 2176, 2013.

[192] C.-H. Wu, H.-L. Liu, C.-T. Ho, P.-H. Hsu, C.-H. Fan, C.-K. Yeh, S.-T. Kang, W.-S. Chen, F.-N. Wang, and H.-H. Peng, "Monitoring of acoustic cavitation in microbubble-presented focused ultrasound exposure using gradient-echo mri," *Journal of Magnetic Resonance Imaging*, vol. 51, no. 1, pp. 311–318, 2020. https://doi.org/10.1002/jmri.26801.

[193] C. C. Danielsen, L. Mosekilde, and B. Svenstrup, "Cortical bone mass, composition, and mechanical properties in female rats in relation to age, long-term ovariectomy, and estrogen substitution," *Calcified Tissue International*, vol. 52, no. 1, pp. 26–33, 1993.

[194] A. Shi, Y. Min, and M. Wan, "Flowing microbubble manipulation in blood vessel phantom using ultrasonic standing wave with stepwise frequency," *Applied Physics Letters*, vol. 103, no. 17, p. 174105, 2013.

[195] Q. Li, J. Xing, R. Tang, and Y. Zhang, "Finite-element method for calculating the sound field in a tank with impedance boundaries," *Mathematical Problems in Engineering*, vol. 2020, p. 6794760, 2020.

[196] C. F. Caskey, S. Qin, P. A. Dayton, and K. W. Ferrara, "Microbubble tunneling in gel phantoms," *The Journal of the Acoustical Society of America*, vol. 125, no. 5, pp. EL183–EL189, 2009.